Development of new generation receivers for experimental cosmology with the Cosmic Microwave Background and systematic effect studies

Tommaso Ghigna
Exeter College
University of Oxford

A thesis submitted for the degree of
Doctor of Philosophy

Trinity 2020

Acknowledgements

I thank everyone I met during these past 4 years who made this journey less of a burden, as well as all my older friends who had the patience of keeping contacts during my wandering of the Earth.

In particular I thank my parents Giancarla and Maurizio and my sister Martina who have always been very supportive, even though in the past 4 years we have been far apart for most of the time. I also thank immensely Yin, whom I met after moving to Japan. Every moment together has been memorable.

I am extremely grateful for all my friends in Milan because they have always been very close even from far apart. In particular I have to thank Francesco, Dario and Ilaria who came to visit me in the UK during the first year in Oxford. Francesco and Arianna deserve a special mention for coming all the way to Tokyo.

I will always remember the friends I made in Oxford who helped me a lot during my first year away from my home-country. A special mention goes to my Italian-family-away-from-Italy Giulia, Valeria and Cristian, my flat mates Carla, Matthew, Roderic, Aakashi and Nick, as well as Anggarara because we keep meeting in every possible corner of the globe after we both left Oxford. I will always be grateful to Alex and Bob for the help they provided during my first year of research in Oxford. Alex has also been a great climbing and slack-lining partner during our free-time.

I am really grateful for meeting Dominik, Yuri, Matet, Tomislav and Xianchong in Japan and for the wonderful memories of our hikes and trips around this great and beautiful country.

A special thank goes to my Oxford supervisors Mike and Angela for giving me this opportunity. I would have never had all these experiences if they had not offered me this position in Oxford. I will always be indebted to Masashi and Tomo for welcoming me at Kavli IPMU and providing extremely useful guidance throughout my DPhil. Tomo's constant stream of research ideas (from now on known as Tomo's brainwavery) has been at time a blessing and a curse throughout my 3 years as a graduate student at Kavli IPMU.

I owe a debt of gratitude for helping and enabling my research to Mario, Guillaume, Hirokazu, Toki, Yuki, Josquin, Davide, Maurizio, Giuiseppe, Carlo, Eiichiro, Tijmen and many more. Of all these wonderful researchers a special mention goes to Samantha who has helped a lot with the detector modelling, and has also become a good friend during the time she spent at IPMU.

Finally, a special thank goes to all the Japanese students and postdocs in the IPMU CMB group for speaking English when I was the only non-Japanese at gatherings and parties. In particular, I appreciated a lot all the efforts made by Kunimoto, Shinya and Ryota to make me feel part of the group.

Statement of Originality

This is to certify that this thesis was written by myself, and that all intellectual content within this thesis is my own, unless explicitly stated otherwise.

The work in this thesis has not been submitted for a degree to any other university, institution or professional body.

The work in this thesis is based on material from the following publications or submitted papers, completed during the course of my time studying at the University of Oxford:

1. Tommaso Ghigna et al. "Permittivity and permeability of epoxy-magnetite powder composites at microwave frequencies". In: *Journal of Applied Physics* 127.4 (2020), p. 045102. URL: `https://doi.org/10.1063/1.5128519`,

2. Tommaso Ghigna et al. "Design of a Testbed for the Study of System Interference in Space CMB Polarimetry". In: *Journal of Low Temperature Physics* (Jan. 2020). URL: `10.1007/s10909-020-02359-9`,

3. Tommaso Ghigna et al. *Requirements for future CMB satellite missions: photometric and band-pass response calibration.* 2020. arXiv: `2004.11601 [astro-ph.IM]` submitted to JCAP at the time of submission of this thesis.

I certify that the work in this thesis is entirely my own, with the following exceptions and clarifications:

Chapter 1 is a review of the current status of cosmology and CMB observation based on the literature.

Chapter 2 is an overview of the status of technology employed by CMB experiments based on the literature. The Half-Wave Plate (HWP) parameters reported in this chapter have been derived independently by the author following the recipe described in [4] (see Appendix E). The LiteBIRD overview given in this chapter is based on [5], of which the author of this thesis is a coauthor.

Chapter 3 is partially based on paper number 3 (Section 3.2). All the analyses presented in this chapter have been carried out by the author. Helpful comments have been received from Tomotake Matsumura, Guillaume Patanchon, Hirokazu Ishino, Masashi Hazumi and others inside the LiteBIRD collaboration. Part of the analysis relies on the component separation code *FgBuster*, which is a publicly available tool (the author thanks Josquin Errard and Davide Poletti for making the code available). CO intrinsic polarization maps for the analysis presented in Section 3.3 were prepared by Giuseppe Puglisi, while the notch-filters response was provided by Aritoki Suzuki. The code to generate hit and cross-linking maps has been written by the author (Appendix D). The author thanks Kunimoto Komatsu and Guillaume Patanchon for productive discussions that led to the definition of the formalism in Section 3.4 for the HWP phase.

For what concerns **Chapter 4**, the author thanks Aritoki Suzuki for the data in Figure 4.2 left. The author wrote the code that simulates the detector response (the code is now publicly available on *github*). The detector non-linearity analysis carried out by the author benefited greatly from comments from Aritoki Suzuki, Tijmen de Haan, Tomotake Matsumura, Samantha Stever and Adrian Lee.

Chapter 5 is based on work presented in paper 1 and paper 2. The entirety of the work was carried out by the author. However, this work would have been much harder without helpful advice from Tomotake Matsumura, Kunimoto Komatsu and Yuki Sakurai for the rescaling of the Polarization Modulator Unit (PMU) for the test-bed cryostat. The author thanks Mario Zannoni for help with the fabrication process and measurements of the absorber samples, as well as for making available the VNA (Vector Network Analyzer) set-up in his lab at Milano-Bicocca University. Finally, paper 2 would not exist without the detectors provided by Aritoki Suzuki, Ben Westbrook and Adrian Lee.

Abstract

Most of current and future Cosmic Microwave Background (CMB) Radiation experiments are targeting the polarized B-mode signal. The small amplitude of this signal makes a successful measurement challenging for current technologies. Therefore, very accurate studies to mitigate and control possible systematic effects are vital to achieve a successful observation. An additional challenge is coming from the presence of polarized Galactic foreground signals that contaminate the cosmological signal. When they are combined, the foreground signals dominate the polarized CMB signal at almost every relevant frequency. Future experiments, like the LiteBIRD space-borne mission, aim at measuring the CMB B-mode signal with high accuracy to measure the tensor-to-scalar ratio r at the 10^{-3} level.

In this thesis, after briefly introducing the science case, the LiteBIRD mission and some of its key technologies, we focus on a few systematic effects concerning mostly the band-pass response. In this context we present novel studies to determine the impact of band-pass uncertainties on the data.

Good control over the response of the superconductive detector is another key ingredient for the success of the mission. We present our modelling of the detector response and a framework to study non-linearity effects due to thermal and optical loading fluctuations.

Lastly, we present results of detector characterization using a test-bed under development that will be used to further our understanding of the interaction between various telescope sub-systems.

Contents

Appendices

List of Figures

List of Abbreviations

CMB	Cosmic Microwave Background
FRW	Friedman-Robertson-Walker
LSS	Last Scattering Surface
CDM	Cold Dark Matter
ΛCDM	Lambda Cold Dark Matter
COBE	Cosmic Background Explorer
WMAP	Wilkinson Microwave Anisotropy Probe
LiteBIRD	Lite (Light) satellite for the studies of B-mode polarization and Inflation from cosmic background Radiation Detection
BOOMERanG	Balloon Observations Of Millimetric Extragalactic Radiation ANd Geophysics
ACT	Atacama Cosmology Telescope
BICEP	Background Imaging of Cosmic Extragalactic Polarization
SPT	South Pole Telescope
ABS	Atacama B-Mode Search
EBEX	E and B Experiment
MAXIMA	Millimeter Anisotropy eXperiment IMaging Array
SO	Simons Observatory
CMB-S4	CMB Stage 4
SKA	Square Kilometre Array
ALMA	Atacama Large Millimeter/submillimeter Array
FWHM	Full Width Half Maximum
HWP	Half Wave Plate
SMB	Superconductive Magnetic Bearing
YBCO	Yttrium Barium Carbon Monoxide
PMU	Polarization Modulation Unit

SQUID	Superconductive QUantum Interference Device
TES	Transition Edge Sensor
ADC	Analog-to-Digital Converter
PSD	Polarization Sensitive Detector
CAMB	Code for Anisotropies in the Microwave Background
TOD	Time-Ordered Data
TOI	Time-Ordered Information

1

Cosmic Microwave Background

1.1 Introduction

The Cosmic Microwave Background (CMB) is the dominant extra-galactic source at radio and mm-wave frequencies. The CMB signal is remarkably homogeneous and isotropic across the sky, as established soon after its discovery in 1965 [6, 7]. During the first few decades after its discovery, most experiments focused on measuring the CMB spectrum across a wide frequency range. All these measurements have confirmed with high accuracy that the spectrum is very well described by a black body function with temperature $T_0 = 2.72548 \pm 0.00057$ K [8]. All these observed properties are at the basis of the hot Big Bang model which is at the foundation of the *Standard Model of Cosmology*. In this paradigm our Universe is homogeneous and isotropic on large scales, and it is expanding from a denser and hotter state. The space-time is well described by the Friedman-Robertson-Walker (FRW) metric, which defines the evolution of the CMB temperature with respect to the redshift z as $T(z) = T_0(1 + z)$.

Although small deviations from a perfect black body spectrum (known as spectral distortions) are expected from the theory, none have been observed, and only upper limits from the COBE satellite are available to date [9]. Since the COBE experiment, CMB spectral distortions have received little experimental attention from the scientific community, however in recent years a renewed interest has been growing, driven by technology advancement that may enable a successful detection. At present a few experiments are being designed to improve the COBE data; the interested reader can look at [10, 11] for a review of the theoretical background, predictions and future observation plans.

While we acknowledge the importance of spectral distortions to improve and consolidate our understanding of the early history of our Universe, in this thesis we will focus on a different but complementary aspect: CMB angular anisotropies [12–14]. In the last two decades this subject has been the main area of research for all major CMB experiments. Variations of the temperature of the CMB of the order 10^{-5} across the sky were firstly observed by the COBE satellite at low resolution ($\theta \sim 10^\circ$) [15]. After the success of COBE, new experiments have improved both the angular resolution and sensitivity to gather more accurate information at smaller angular scales. For about a decade a lot of effort was put into improving the results of COBE from the ground and the upper atmosphere; of all the experiments, MAXIMA and BOOMERanG balloon-borne missions require a special mention for being the first experiments to observe the first acoustic peak of the temperature angular power spectrum [16–19]. All these efforts culminated with the WMAP satellite in the early 2000s [20–24]. This experiment significantly improved the accuracy of the data, solidifying the observational evidence that is at the basis of the *Standard Model of Cosmology*.

After the success in measuring temperature anisotropies, the interest begun shifting from temperature to polarization anisotropies, which are around one order of magnitude fainter than the former. Polarization anisotropies have been the main goal of the third generation CMB satellite Planck [25–27] as well as current and future ground-based experiments like BICEP [28], POLARBEAR [29], ACT [30], SPT [31], Simons Observatory [32] and CMB-Stage 4 [33] (just to mention a few). These experiments are either trying to push forward the resolution capabilities or improving the sensitivity of low resolution measurements (or both), with the ultimate goal of improving the constraints on cosmological parameters, specifically the tensor-to-scalar ratio parameter r. An accurate measurement of r is needed to test inflation, one of the main open questions of the *Standard Model of Cosmology*.

The quest to measure the tensor-to-scalar ratio parameter through observations of the polarized CMB signal is the subject of this thesis, specifically in the context of next generation experiments like LiteBIRD [5, 34, 35], a recently selected JAXA satellite mission to be launched at the end of the 2020s.

1.2 CMB anisotropies

As mentioned in Section 1.1, CMB observations have determined the level of temperature anisotropies to be of the order 10^{-5}, while polarization anisotropies are at least 1 order of magnitude fainter (10^{-6}).

CMB temperature maps $T(\theta, \phi)$ can be conveniently decomposed in a series of multipole terms through a spherical harmonic expansion [36–41]:

$$T(\theta, \phi) = \sum_{\ell m} a_{\ell m} Y_{\ell m}(\theta, \phi), \tag{1.1}$$

where $Y_{\ell m}(\theta, \phi)$ are the ℓ-order spherical harmonics and $a_{\ell m}$ are the expansion coefficients.

In a similar way, polarization maps defined using the Stokes Q and U parameters can be expanded using spin-2 spherical harmonics (${}_{\pm 2}Y_{\ell m}(\theta, \phi)$):

$$[Q \pm iU](\theta, \phi) = \sum_{\ell m} {}_{\mp 2}a_{\ell m} {}_{\mp 2}Y_{\ell m}(\theta, \phi). \tag{1.2}$$

Monopole: With this framework in place, the CMB average temperature $T_0 = 2.72548 \pm 0.00057$ K can be seen as the monopole (a_{00}) term.

Dipole: The dipole term ($\ell = 1$) presents the largest amplitude: 3.36208 ± 0.00099 mK [27]. However, most of the signal is not of cosmological origin; it is due to doppler effect caused by the solar system motion with respect to the Last Scattering Surface (LSS) where the CMB originates. The intrinsic amplitude is expected to be at least ~ 2 orders of magnitude lower and therefore hard to separate.

From the latest Planck release [27] the velocity of the Sun with respect to the CMB has been determined to be 369.82 ± 0.11 km s^{-1} towards Galactic coordinates $(\ell,\ b) = (264.021° \pm 0.011°,\ 48.253° \pm 0.005°)$.

Due to its apparent nature, the dipole signal is usually removed during the cosmological analysis. However, given that it is bright, accurately known and can be rapidly modulated with an appropriate scanning strategy, the dipole signal is used as the main photometric calibrator for balloon and space-based mapping experiments.

$\ell > 1$ **anisotropies:** Current theories tell us that anisotropies at higher multipoles are due to small perturbations in the early Universe. The tight interaction between photons and baryonic matter in the early Universe imprints a signature of these perturbations in the radiation at the time of matter recombination at redshift $z \sim 1100$. At recombination, the expanding Universe cools the primordial plasma allowing protons and electrons to recombine and form neutral atoms, and photons to decouple from baryonic matter and free-stream through the Universe [42]. Therefore by studying CMB anisotropies we can learn about the physical conditions of the early Universe and the perturbations in the primordial plasma. These perturbations are the same that cause the formation of structures in the Universe at later stages.

Under the assumption of isotropy and of Gaussian statistics (no correlations between different modes) there is no preferred direction in the Universe, therefore the statistics of the power distribution across the sky depends only on the angular separation between two points. In this limit, the anisotropies can be fully characterized by the 2-point correlation function or angular power spectrum, defined as the variance of the spherical harmonic coefficients: $C_\ell = \langle |a_{\ell m}|^2 \rangle$. Since for each multipole ℓ there are $2\ell + 1$ m-modes, the power spectrum at a given ℓ value can be estimated as the average over all modes:

$$C_\ell = \frac{1}{2\ell + 1} \sum_{\ell=-m}^{m} \langle |a_{\ell m}|^2 \rangle. \tag{1.3}$$

Theoretical models can be tested by comparing model predictions for the power spectra and measured data.

However, there are some unavoidable limitations to the achievable accuracy. The observed sky is a single realization, which sets a fundamental limit to the accuracy commonly referred to as *cosmic variance*, which is particularly relevant at large angular scales (low ℓ): $\sigma_{C_\ell} \propto \sqrt{2/(2\ell+1)}$. This limit is boosted for observations of portions of the sky by a factor $1/\sqrt{f_{sky}}$, where f_{sky} is the observed sky fraction.

The multipole range that can be covered by an experiment has two important limits. The first one is due to the angular extension of the observed sky fraction and sets a limit on the low-end of the ℓ-range. The second limits the high-end of the ℓ-range, and it is fixed by the telescope resolution. If the angular size of the observed sky fraction is α (radians), the lowest observable multipole is defined in first approximation as $\ell \sim \pi/\alpha$. On the other hand, if we define β as the FWHM (Full Width Half Maximum) of the telescope beam in radians, the experiment sensitivity in ℓ-space decreases with the beam window function $e^{-\ell(\ell+1)(\beta/2.355)^2}$[1].

1.2.1 The physics of anisotropies

As mentioned in the previous section, the basis of the *Standard Model of Cosmology* is the Big Bang theory and its mathematical framework relies on the FRW metric, which describes a nearly isotropic and homogeneous Universe on large scales. The *standard* Big Bang scenario has been proven extremely successful thanks to the experimental confirmation of the accuracy of its theoretical predictions, e.g. the presence of the CMB. However, some of the predicted and observed major characteristics of this framework, namely the observed large-scale isotropy and homogeneity as well as the nearly zero curvature, are difficult to explain without assuming unrealistic fine-tuned initial conditions (horizon and flatness problems).

Inflation has been proposed as a solution to these problems. By introducing an initial exponential expansion of the Universe the initial conditions do not require fine tuning to obtain the current observed conditions.

In the inflationary paradigm the perturbations in the primordial plasma are generated by quantum fluctuations and their magnitude is set by the energy of

---

[1] Here we assume a gaussian beam approximation. In this limit the FWHM β is related to the standard deviation σ of the gaussian beam as $\beta = 2\sqrt{2\ln 2} \sim 2.355\sigma$

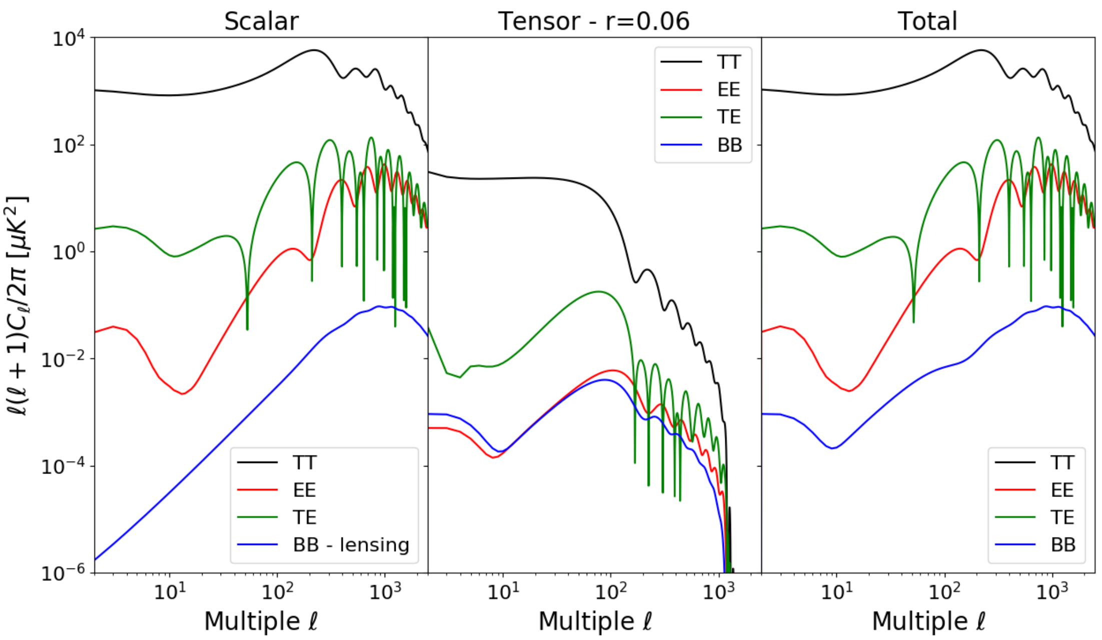

Figure 1.1: Spectra generated with CAMB [43, 44] from Planck best fits cosmological parameters and $r = 0.06$ (current upper limit).

the inflationary field and the slope of the potential. The details of inflation vary depending on the theoretical model and a detailed discussion is beyond the scope of this thesis, but a common characteristic is the generation of both scalar (density perturbations) and tensor modes (gravitational waves). The presence of these perturbations in the primordial plasma imprints the temperature and polarization anisotropy pattern in the CMB photons at last scattering through Thomson scattering. We usually distinguish between two polarized components: E-modes and B-modes, which are defined through a coordinate transformation of the usual Stokes Q and U parameters to obtain quantities that are rotationally invariant. From Equation 1.2 we can rewrite the harmonic coefficients to define the E-mode and B-mode power spectra in analogy to 1.3:

$$a^E_{\ell m} = -\frac{{}_2a_{\ell m} + {}_{-2}a_{\ell m}}{2} \tag{1.4}$$

$$a^B_{\ell m} = -i\frac{{}_2a_{\ell m} - {}_{-2}a_{\ell m}}{2}. \tag{1.5}$$

Scalar modes are mostly responsible for temperature and polarized E-mode anisotropies (tensor modes can also create them but the contribution is several order of magnitude lower). However, primordial polarized B-modes are solely generated by tensor modes. Therefore, measurements of all three anisotropy fields, and their angular power spectra, are necessary to fully constrain the physics of inflation.

1.2.2 Cosmological parameters

The effective shape of the angular power spectra in Figure 1.1 (generated with CAMB[2]) depends on the details of the matter and energy content and evolution of our Universe. These details can be captured by defining a number of cosmological parameters that fully describe the Universe and its evolution. By measuring the angular power spectra we can constrain the cosmological parameters and the physics of the current and early Universe.

Scalar perturbation. Density perturbations are expected to be nearly scale invariant for most inflationary models. Therefore, the power spectrum of scalar (or curvature) fluctuations is defined as:

$$P_s(k) = A_s \left(\frac{k}{k_0}\right)^{n_s-1}, \tag{1.6}$$

where k is the wavenumber and k_0 is a pivot scale (usually $k_0 = 0.05\ \mathrm{Mpc}^{-1}$) that defines the amplitude A_s. Since we expect a nearly scale-invariant spectrum, the spectral index $n_s \sim 1$.

Tensor perturbation. Similarly to scalar perturbations, the power spectrum of tensor perturbations (gravitational wave) can be defined by the amplitude A_t and slope n_t as:

$$P_t(k) = A_t \left(\frac{k}{k_0}\right)^{n_t}, \tag{1.7}$$

The effective value of these four parameters depends on the energy of inflation and the slope of the potential of the inflationary field.

Commonly these initial condition parameters are reduced to three: A_s, n_s and the tensor-to-scalar ratio r. The tensor-to-scalar ratio measures the relative

---

[2] `https://camb.info/`

amplitude of tensor modes to scalar modes at some pivot scale (usually 0.002 Mpc^{-1})[3], and it strongly depends on the energy of inflation: for higher energy a stronger gravitational wave background is expected, and therefore a higher r value.

While current and past experiments have been able to determine the amplitude and slope of the density perturbations through measurements of the temperature and E-mode power spectra, a direct measurement of r is still to be obtained through a direct measurement of the primordial B-mode spectrum.

Reionization. After recombination, the Universe became neutral. However, soon after the first stars ignited at low redshift, hydrogen became partially ionized again and the CMB photons were again efficiently scattered by free electrons. The integrated Thomson scattering optical depth at reionization (τ) can be constrained through features imprinted in the angular power spectra at low-ℓ (large angular scales).

Universe expansion rate. As the Universe is expanding a key parameter defines the expansion rate at the present time: H_0, often called Hubble constant.[4]

Matter and energy density. The content of the Universe is expressed in terms of the critical density: $\rho_{crit} = 3H_0^2/8\pi G$ (G is the gravitational constant). With this definition the contribution to the total density of a species i can be parameterize as $\Omega_i = \rho_i/\rho_{crit}$. The most relevant are the matter density (including both baryonic and cold dark matter) Ω_m, the dark energy density Ω_Λ and the contribution of curvature, which is commonly defined as $\Omega_K = 1 - \Omega_{tot}$, where Ω_{tot} includes all species. The contribution of radiation is subdominant compared to the one already listed, and can be determined directly from the CMB temperature.

More parameters can be added to explain fine feature of the power spectra and account for new physics, e.g. the density of massive neutrinos (Ω_ν). These additional parameters will play an increasingly important role in the future, as

---

[3] BICEP/Keck collaboration often reports result for 0.05 Mpc^{-1}.

[4] Often the dimensionless parameter h is reported. It is defined through the relation $H_0 = 100h$ km s^{-1}Mpc^{-1}.

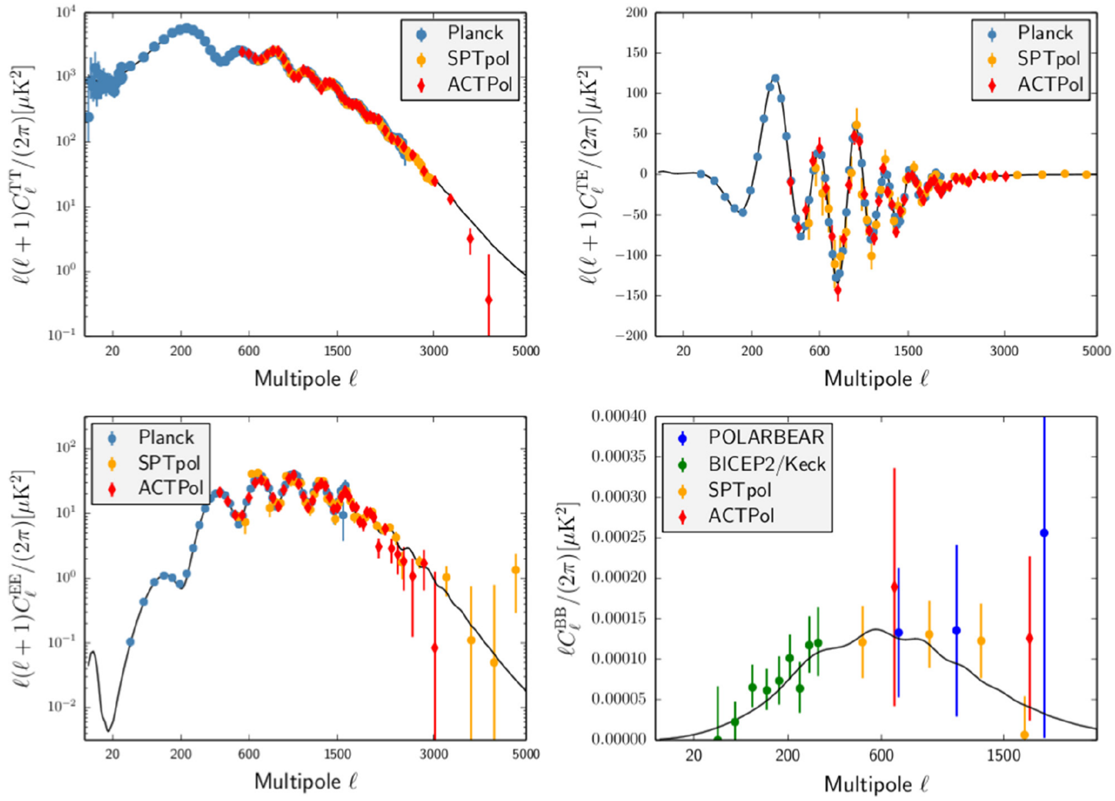

Figure 1.2: Summary of the most recent relevant results from 5 major CMB experiments: Planck [45], SPT [31], ACT [30], POLARBEAR [29] and BICEP [28]. Image from [46].

experiments become more sensitive. However a detailed description is beyond the scope of this thesis.

1.3 Current results

A number of experiments have been active in recent years (see Figure 1.2 for a summary of recent data from some of the major experiments)[5]. With the amount of data produced, very tight constraints have been placed on the temperature anisotropy angular power spectrum C_ℓ^{TT} from $\ell = 2$ to $\ell \sim 3000$. The same can be said for the E-mode angular power spectrum C_ℓ^{EE} for a slightly smaller ℓ range ($50 \lesssim \ell \lesssim 2000$)[6], and the cross correlation spectrum C_ℓ^{TE}. Non-zero correlation is expected for temperature and E-mode anisotropies, due to the fact that both

---

[5] Recently both POLARBEAR and ACT collaborations reported new data not shown in Figure 1.2 [47, 48].

[6] Data have been published up to $\ell \sim 5000$, however the precision at these scales can be greatly improved (see Figure 1.2).

originate from the same primordial density perturbations (the tensor contribution to both is expected to be several orders of magnitude lower).

The results of C_ℓ^{TT}, C_ℓ^{TE} and C_ℓ^{EE} are consistent with an expanding, isotropic, homogeneous and nearly flat universe currently dominated by the negative-pressure component Λ (cosmological constant) that is causing the expansion to accelerate; while most of the matter content is in the form of cold dark matter (CDM). Given the importance of the cosmological constant, the *Standard Model of Cosmology* is also known as ΛCDM.

$\Omega_b h^2$	0.02233 ± 0.00015
$\Omega_{cdm} h^2$	0.1198 ± 0.0012
$100\theta_*$	1.04108 ± 0.00031
τ	0.0540 ± 0.0074
$\ln 10^{10} A_s$	3.043 ± 0.014
n_s	0.9652 ± 0.0042
H_0 [km s^{-1}Mpc^{-1}]	67.37 ± 0.54

Table 1.1: Best fit ΛCDM cosmology parameters from the Planck collaboration [45]. The first 6 parameters are the minimum parameters needed to fully describe the model, the Hubble constant H_0 is reported for clarity. As described in the text, h is the dimensionless Hubble constant, Ω_b is the baryon density, Ω_{cdm} is the cold dark matter density, θ_* is the angular scale of the sound horizon, τ is the optical depth at reionization, A_s and n_s are the amplitude and spectral index of scalar perturbations.

The Planck Collaboration is currently reporting 6 minimum cosmological parameters required to fully describe the model: $\Omega_b h^2$ (Ω_b is the baryon density and h is the dimensionless Hubble constant as defined in 1.2.2), $\Omega_{cdm} h^2$ (Ω_{cdm} is the cold dark matter density), θ_* (angular scale of the sound horizon), τ, A_s and n_s. All other parameters can be derived from these basic 6 parameters. In Table 1.1 we report the best fit results from [45] for reference; we also included H_0 for clarity.

Even though these remarkable results have helped constrain several cosmological parameters and define the *Standard Model of Cosmology*, more can be done to push even further our understanding of the Universe. As an example, a higher accuracy on data at large angular scales can tighten the constraints on τ, and shed new light on the reionization history of the Universe. At the same multipole range, both WMAP and Planck have observed small anomalies in the C_ℓ^{TT} spectrum which can be an indication of non-Gaussianity or new physics beyond the standard model. However, more data are needed to have a final say on these issues.

The same can be said in the context of the B-mode angular power spectrum (C_ℓ^{BB}). The primordial signal is expected to be at least one order of magnitude smaller than the E-mode signal (from current upper limits), therefore very challenging for current technologies, especially given the presence of Galactic contamination and systematic effects. A detection of the primordial B-mode signal will allow us to directly measure the tensor-to-scalar ratio r and constrain the energy of inflation.

In recent years, a few ground-based experiments have pushed forward the search for the B-mode signal. POLARBEAR, ACT and SPT have focused on small angular scales, where the primordial B-mode signal is dominated by the lensing signal (E-modes partially converted to B-modes through gravitational lensing along the line-of-sight), and all collaborations have published B-mode polarization data [49–51]. A lot of effort is being put on obtaining more accurate data at these scales. In combination with new data available in the future about the matter distribution in the Universe, experiments will be able to remove this secondary anisotropy and unveil the underlying primordial signature.

At the other end of the spectrum, at low-ℓ, the primordial B-mode signal should be larger than the lensing signal for $r \gtrsim 0.01$ at $\ell \lesssim 200$ (including both the reionization and recombination peaks), and for $r \gtrsim 0.001$ at $\ell \lesssim 20$. Therefore, in this ranges, the primordial B-mode signature can be directly measured. This has been the aim of the BICEP/Keck experiment based at the South Pole. In 2014 the BICEP/Keck collaboration claimed a detection suggesting a tensor-to-scalar ratio value $r \sim 0.2$, however further analysis combined with the data from the Planck satellite revealed that the observed signal was consistent with residuals from Galactic emission [52]. Since then more data and further analysis of the combined data sets have helped defining an upper limit $r \leq 0.06$ [53][7].

---

[7] BICEP and Planck combined data.

1.4 Future observations

An accurate characterization of the B-mode signal is at the core of the CMB research in the next decade. New data will be available from the ground with upgrades of current experiments, and larger experiments becoming operative soon, from the stratosphere with balloon experiments and space.

Each environment presents some advantages and some challenges. Ground-based experiments are certainly the less expensive and present lower risks, given the possibility of "fixing" the telescope system as needed. On top of these advantages we can also add the virtually unlimited experiment size and duration. However the presence of an unstable atmosphere and the limited sky availability pose limits on the ability to access the largest scales, as well as frequencies above ~ 300 GHz.

Even though the BICEP collaboration has shown the possibility of accessing the low-ℓ range down to $\ell \sim 20 - 30$, larger scales may ultimately require a space mission. Space offers the advantages of unlimited frequency range, increased stability due to the absence of the atmosphere and availability of the whole sky on short time scales, therefore removing some of the constraints on the accessibility of the largest scales. On the other hand, space missions are expensive and longer to be laid out, and present higher risks. Both the size and observation time are subject to tighter constraints.

In between these two extremes, balloon missions are a compromise, even though the observation time is generally very limited compared to both ground and space experiments. However, the lower cost and similar observation conditions make them a perfect laboratory for new technology and observation strategies for space missions.

Ultimately, given the extent of the challenge to finally characterize the primordial B-mode signal, a single experiment (be it on the ground, on a stratospheric balloon or in space) is certainly not sufficient to fully achieve the goal and exploit what the CMB has to offer, but a synergy between experiments, in terms of research and development of new and more mature technology, as well as data analysis is necessary.

In the following two sections we will highlight some of the major challenges faced by all experiments.

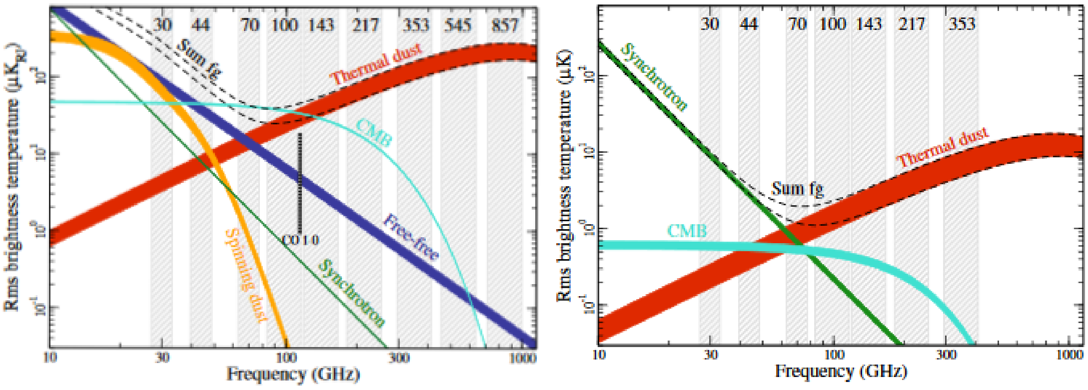

Figure 1.3: CMB and Galactic components brightness as a function of frequency from Planck (2015). Total intensity in the *left* figure and polarized emission on the *right*. Image from [54].

1.4.1 Foregrounds

One of the major challenges faced by CMB experiments is represented by Galactic foregrounds. In Figure 1.3 from [54], we show the major Galactic emissions considered by the Planck collaboration in units of μK_{RJ} as a function of frequency. It can be clearly seen that there is only a small range of frequencies where the CMB signal is dominant over the Galactic foregrounds across the whole sky. At low frequency ($\nu \lesssim 100$ GHz) the dominant components are free-free, spinning dust (total intensity only) and synchrotron (both total intensity and polarized emissions), while at higher frequencies thermal dust emission becomes the dominant source.

In Figure 1.4, we show the total intensity and polarization maps from Plank LFI 30 GHz channel [55] and Plank HFI 100 and 353 GHz channels [56] in Galactic coordinates. The dominant Galactic foregrounds contribution can be seen in the lowest and highest frequency channels. Even at 100 GHz (where the CMB signal is expected to be more dominant) the Galaxy emission is clearly visible along the Galactic plane, while the CMB signal is dominant in total intensity and polarization at higher and lower latitudes. However, for what concerns the B-mode signal alone the contribution of Galactic foregrounds can not be neglected at any frequency and any position on the sky, as the experience of BICEP has made clear.

For this reason, the approach for most future experiments has shifted from targeting small "foreground-clean" sky regions and frequency channels, to more ex-

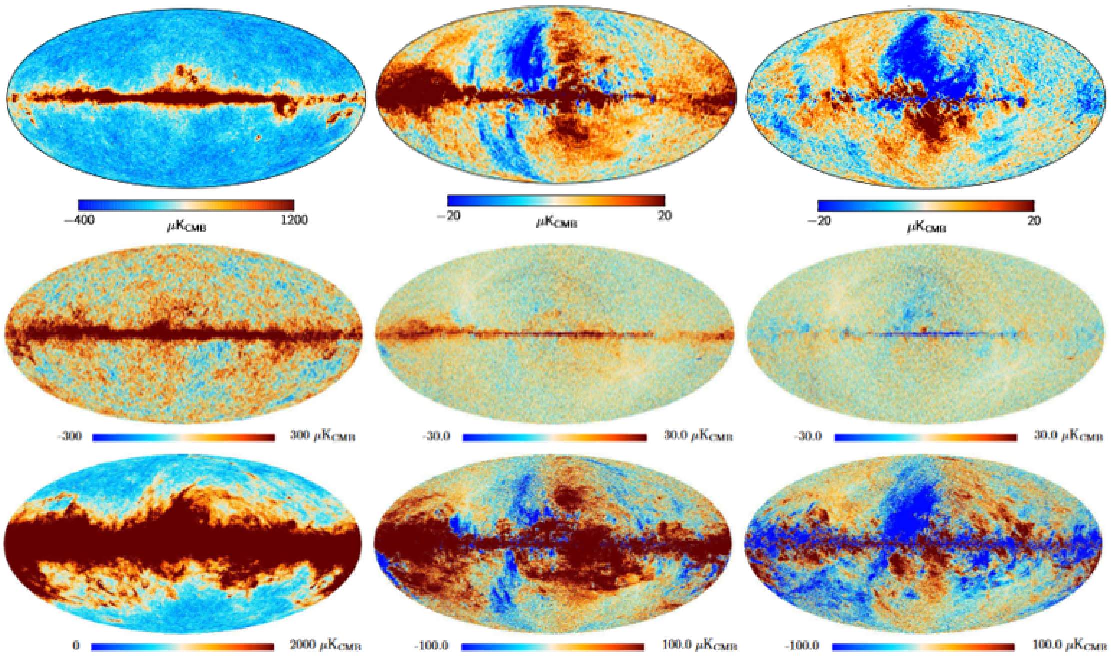

Figure 1.4: *Top:* Planck LFI 30 GHz I, Q and U maps from Planck 2015. *Middle:* Planck HFI 100 GHz I, Q and U maps from Planck 2015. *Bottom:* Planck HFI 353 GHz I, Q and U maps from Planck 2015. We can clearly see the presence of the dominant synchrotron emission at low frequency and the thermal dust at high frequency. From [55] and [56].

tended observations at multiple frequencies with the aim of precisely characterize the Galactic emission to clean the maps and unveil the underlying cosmological signal.

One of the ways to separate the Galactic components is to parameterize their frequency response and constrain the free parameter from multi-frequency data. We report here the model used in this thesis for the brightness temperature (in Rayleigh-Jeans units) of synchrotron and thermal dust. In this thesis we focused on future polarization data, therefore we did not consider the other unpolarized components (with the exception of Carbon Monoxide).

Synchrotron. Synchrotron emission (in Rayleigh-Jeans units – see Appendix A for details about units conversion) is described as a power low with spectral index β_s:

$$S_s(\nu) = A_s(\nu_0)\left(\frac{\nu}{\nu_0}\right)^{\beta_s}, \tag{1.8}$$

where S can take the form of one of the three Stokes parameters I, Q or U and A_s is the amplitude at some arbitrary pivot frequency ν_0 [57]. The Planck collaboration has determined a value $\beta_s = -3.1 \pm 0.5$. However, recent data have revealed that the spectral index might not be constant across frequencies, but *steeper* at lower frequencies. To take this effect into account next generation experiments are introducing a *curvature* factor [58, 59].

Thermal dust. Thermal dust emission (in Rayleigh-Jeans units) is described as a modified black-body (grey-body) with spectral index β_d and temperature T_d:

$$S_d(\nu) = A_d(\nu_0)\left(\frac{\nu}{\nu_0}\right)^{\beta_d+1} \frac{e^{h\nu_0/k_B T_d} - 1}{e^{h\nu/k_B T_d} - 1}, \tag{1.9}$$

where A_d is the amplitude at some arbitrary pivot frequency ν_0 [57]. The Planck collaboration has determined a value $\beta_d = 1.55 \pm 0.1$ for total intensity data, $\beta_d = 1.6 \pm 0.1$ for polarized data and $T_d = 19.5 \pm 3$ K for both cases.

New data suggest that the spectral indices may not be spatially constant, as well as the presence of multiple dust populations along the line of sight. Therefore, we acknowledge the need for considering an increased sky complexity in future data analysis, but this goes beyond the scope of this thesis.

Carbon monoxide (CO). One of the open question for next generation space missions is to determine the best strategy to avoid contamination from CO emission, given the impact observed on Planck data particularly at 100 GHz. Carbon monoxide molecules emit radiation at quantized frequencies due to the molecule rotational transition energies. The most abundant specimen ^{12}CO emits at 3 frequencies relevant for CMB observations: 115 (CO $J = 1 \rightarrow 0$), 230 (CO $J = 2 \rightarrow 1$) and 345 GHz (CO $J = 3 \rightarrow 2$) with decreasing brightness (the second most abundant specimen ^{13}CO also emits at slightly shifted frequencies: 110, 220, 330 GHz). In Figure 1.5, we report one of the results from [60] for the total intensity emission of CO $J = 1 \rightarrow 0$. The Planck collaboration estimated an upper limit on intrinsic polarization of CO $\leq 1\%$.

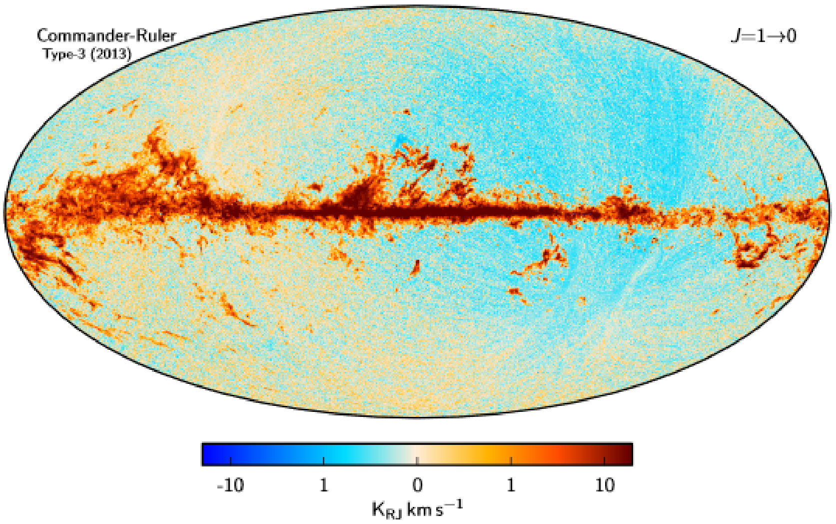

Figure 1.5: (CO J$= 1 \rightarrow 0$) as seen by Planck. Most of the signal lies along the Galactic plane. From [60].

1.4.2 Instrumental systematic effects

Controlling instrumental systematic effects is the second big challenge for future B-mode experiments. In Figure 1.6 we show a result reported in [56], where the Planck team addresses the contribution of each known systematic effect with respect to the E-mode power spectrum. The first thing we can observe is that in most polarized channels the dominant source of uncertainty is the non-linearity of the Analog-to-Digital Converter (ADC). This effect is limiting particularly for the large scale signal (low-ℓ), where its contribution becomes comparable to the expected cosmological signal for all channels analyzed.

Figure 1.6 shows many interesting features that could be discussed at length, here we want to point out two that are interesting for the scope of this thesis: band-pass and calibration mismatch. Both effects increase in importance with increasing frequency because of the increasing brightness of dust. Due to Planck HFI design and observation strategy, band-pass mismatch between orthogonal polarization sensitive detectors causes total-intensity to polarization leakage, which becomes increasingly stronger with the brightness of the Galactic foregrounds. At the same time calibration accuracy worsen at high frequency because of the calibrator (CMB dipole signal) becoming relatively less bright compared to the thermal dust signal.

This effect couples to the baseline calibration time, which is set by the dipole modulation period. Therefore, a scanning strategy that allows a short modulation period should increase the calibration accuracy [61].

Two more important lessons can be learnt from Figure 1.6. First, the level of systematics observed in Planck is low enough to allow the detection of the E-mode signal. However, for the current r upper limit, the expected primordial B-mode signal is completely dominated by at least 3 systematic sources in all HFI polarization sensitive channels. Second, most effects appear to have a larger contribution at low-ℓ, therefore we can conclude that in general instrumental systematics will be one of the main limiting factors for a correct observation of the primordial B-mode signal. Thus great effort should be put into developing strategies to mitigate them,

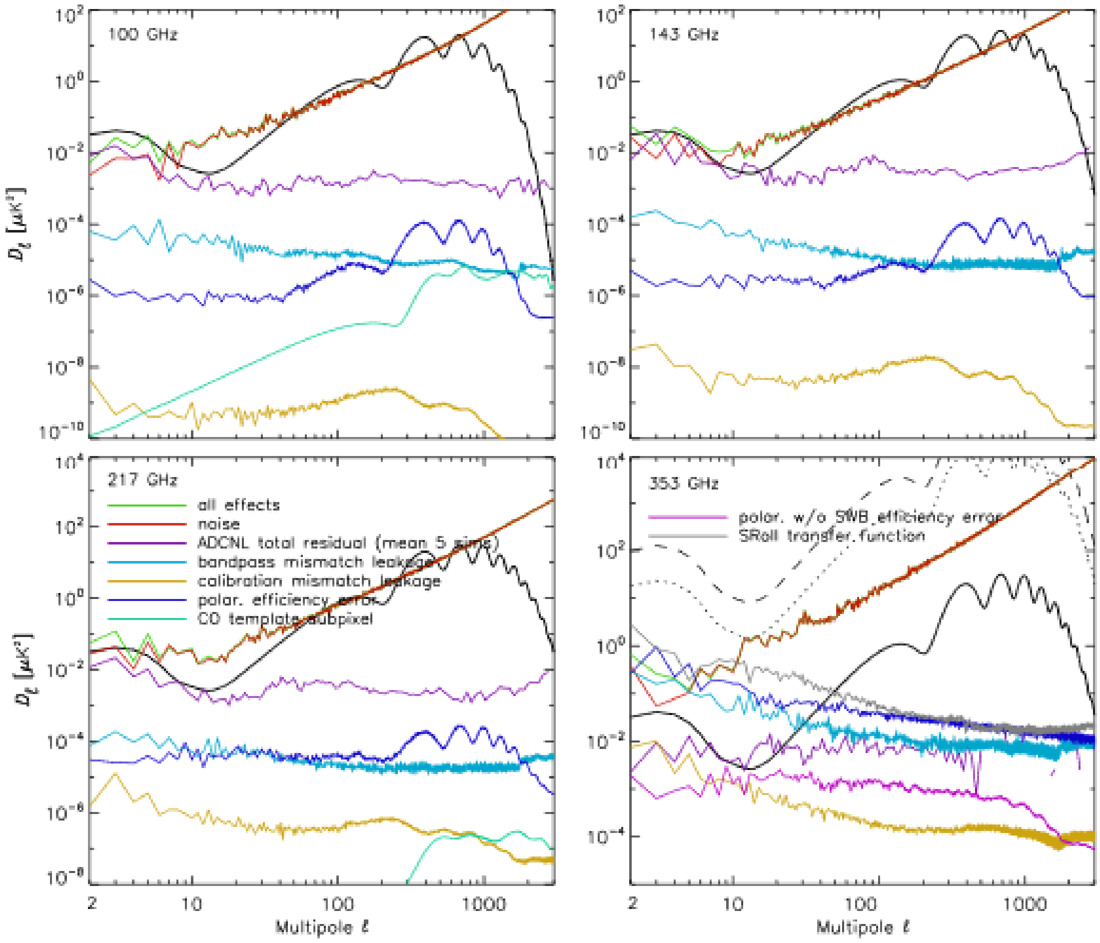

Figure 1.6: A summary of the contribution of each instrumental systematic analyzed by the Planck HFI team. Image from [56].

as well as study and characterize them carefully.

Some of the instrumental systematics can also couple to the presence of Galactic foregrounds (e.g. band-pass mismatch), it is therefore important to take them into account when addressing these effects.

In this thesis we analyze some of the systematic effects in the context of the recently selected LiteBIRD satellite mission. Together with the mathematical description of these effects, for some of them, we simulate and address their impact on the data. We also try to directly connect the systematic effect to the instrument characteristics to define calibration requirements to minimize the impact on the data.

The reminder of this thesis is organized as follows. In Chapter 2 we review some of the key technological advancements that will make LiteBIRD possible, and we briefly give an overview of the LiteBIRD experiment. In Chapter 3 we define the data model for a LiteBIRD-like detector and we discuss the origin of systematic effects, focusing in particular on bandpass related effects. We point out here that although we employed a parametric component separation method in part of the analysis presented in this Chapter in order to quantify the impact of some instrumental systematics, we do not address the complex details of the component separation problem in this thesis, such as the methodology (Internal Linear Combination, parametric fitting, template fitting, blind approach, etc.) the spatial variability of the spectral parameters, the actual number of galactic and extra-galactic components that we need to account for, the possible impact of the uncertainty in the absolute value of the frequency maps mean value ($\ell = 0$) on higher ℓ-modes, and many other. In Chapter 4 we model the TES bolometer response and noise properties, and we analyze non-linearity effects and their possible origin. In Chapter 5 we describe the cryogenic test-bed we are developing at Kavli IPMU to study the detector response when interacting with other telescope sub-systems (e.g. the polarization modulator) that may disrupt the normal operation. We also present preliminary results from the test-bed using TES bolometers inherited from ground-based experiments.

2

Next Generation Experiment: LiteBIRD

In principle, as discussed in [62], a 5σ detection of $r = 0.07$ (already excluded by new data at the time of this thesis but equal to the upper-limit at the time of this study), would require mapping 1% of the polarized sky with map depth $\sigma_p = 7$ μK·arcmin (map noise in CMB units). In [63], the authors argue that for ideal conditions, this result could be achieved by a single noiseless detector[1] in ~ 1 month of observation. This is clear assuming a noise equivalent temperature (NET) dominated by the CMB contribution $NET_{cmb} = 10$ $\mu\mathrm{K}\sqrt{\mathrm{s}}$, from:

$$t = 2\Big(\frac{NET_{cmb}}{\sigma_p}\Big)^2 \frac{A_{sky}}{\eta}, \tag{2.1}$$

where t is the observation time required to achieve the map sensitivity σ_p on a sky area A_{sky}[2] for a given noise NET_{cmb} and efficiency η (assumed to be unity in the calculation).

However, such a low noise level has never been demonstrated, neither on the ground which suffers from the presence of the atmosphere (best results obtained at $\nu \sim 150$ GHz are of the order of $NET \sim 200$ $\mu\mathrm{K}\sqrt{\mathrm{s}}$), nor in space, where Planck HFI recorded best values as low as ~ 50 $\mu\mathrm{K}\sqrt{\mathrm{s}}$ [64].

---

[1] For noiseless detector we assume an ideal situation where the only noise source are the photons received from the CMB.

[2] A_{sky} is in units of [arcmin^2]. The whole sky is equivalent to $4\pi(10800/\pi)^2$ arcmin^2 $\sim 1.5 \times 10^8$ arcmin^2.

On top of this, it is fundamentally impossible to achieve perfect efficiency. Typically $\eta \sim 0.3 - 0.5$, due to bad weather conditions (on the ground), calibration operation, fridge recycling and other routine operations that reduce the effective amount of time dedicated to observation[3].

All these factors tremendously increase the observation time needed to achieve high sensitivity. One way of overcoming this problem is to employ arrays of detectors. If the noise is uncorrelated between detectors the equivalent NET for an array of N detectors scales as the square-root of the number of detectors: $\sqrt{N}$. Therefore, the observation time to obtain the same map sensitivity σ_p can be reduced by a factor N[4].

For this reason, over the last two decades, experiments have been increasing the number of detectors. As an example, bolometeric focal planes of ground-based experiments went from $\sim 10 - 100$ detectors in the early 2000s (BICEP1 - [28]) to ~ 1000 (POLARBEAR - [29]) in the 2010s and ~ 10000 (SO and BICEP array - [32, 65]) in the 2020s. The next step, with CMB-S4, will increase the number of detectors by one order of magnitude to ~ 100000 [33]. Unfortunately, space-based missions are unable to increase the number of detectors at the same rate as the ground due to several constraints: cost, mass, preparation time, power consumption, technology readiness etc. Hence, the LiteBIRD collaboration is designing an instrument that can allocate a total of ~ 4000 detectors divided into three focal planes and 15 frequency bands [5]. PICO, a follow-up space mission that is being planned for the 2030s, will increase the detector count even further to ~ 10000 [66].

One of the technology advancements that facilitates the increase in detector count is the development of multi-chroic detectors [67–73]. By using broad-band antennas it is possible to use on-chip filters to split the power collected from the sky in sub-bands that can be processed separately by different detectors. This has the advantage of increasing the number of detectors and the total throughput of the telescope without having to increase the size of the focal plane. In recent years, POLARBEAR and SPT (SPT-3G) have implemented respectively di-chroic and tri-chroic pixels (2 and 3 colours per antenna). LiteBIRD will employ tri-chroic

---

[3] Optical efficiency of the telescope optics also contributes to a reduction of sensitivity.

[4] In the approximation of white uncorrelated noise between detectors.

pixels with the exception of 3 of the 15 total bands. In Section 2.1 we will review the details and status of multi-chroic technologies.

As mentioned above, the reason for using arrays of detectors is that assuming perfectly uncorrelated white noise between detectors, we can improve the sensitivity by a factor $\sqrt{N}$ (number of detectors). However, this is not always true, and the presence of noise correlations and $1/f$ noise due to atmospheric instability (on the ground) and thermal fluctuations of the focal plane or the optical elements of the telescope is well known and documented. To mitigate the presence of $1/f$ noise, several experiments have been implementing polarization modulators to shift the signal of interested to higher frequencies where the noise is uncontaminated by the $1/f$ component [74, 75][5]. In Section 2.2 we will review the current technologies with particular focus to the candidate technology to be used in the Low Frequency Telescope of LiteBIRD.

We will conclude this chapter with an overview of the LiteBIRD experiment in Section 2.3.

2.1 Multi-chroic detectors

As already mentioned, in the last decade several research groups (led by Berkeley/LBNL and NIST) have developed multi-chroic detectors for CMB observations. This technology is particularly important for a space mission because it allows more detectors to be packed into a fixed focal-plane size compared to single-colour detectors. LiteBIRD [5] will employ two types of multi-chroic pixels: lenslet-coupled dual-polarized sinuous antennas and circular corrugated feed-horn antennas. The former are a heritage of the POLARBEAR and SPT collaborations, while the latter have been employed by the ACT collaboration.

For both architectures an antenna couples the signal to TES detectors through a microstrip transmission line. In Figure 2.1 the basic building blocks of the lenslet-coupled sinuous antenna design are shown. A hemispherical silicon lenslet increases

---

[5] GroundBIRD is taking a different approach, implementing a fast continuously rotating telescope [76].

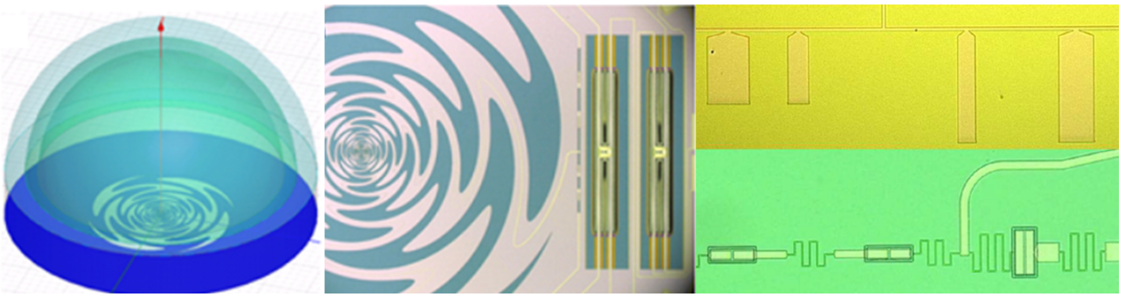

Figure 2.1: Silicon lenslet-coupled sinuous antenna. From left to right: a HFSS simulation of the hemispherical silicon lenslet with a dual-polarized sinuous antenna. The broadband sinuous antenna collect the light from the sky and through a microstrip transmission line couples it to TES detectors. The broadband signal is split in narrower bands (∼30% bandwidth) thanks to a diplexer made either with distributed elements (stubs) or lumped elements. The LiteBIRD detectors will use triplexers. Figures from [68, 77].

the gain of the broadband dual-polarization sinuous antenna. Due to the high dielectric constant of silicon ($\epsilon \sim 11.7$), the lenslet requires an anti-reflection (AR) coating to maintain high optical efficiency. Depending on the specific frequency range needed, single or multiple epoxy (or loaded epoxy) layers of AR coating have been developed to achieve efficiency close to unity.

The dual polarization signal is collected by the planar sinuous antenna and separated into the 2 polarized components on separate transmission lines. Each polarization is further divided in narrower bands by two (diplexer) or three (triplexer) on-chip lumped-elements filters. After the band definition the signal is fed to a TES detector suspended on an *island* over the silicon wafer using four silicon nitride legs for thermal isolation. Details of the detector's principle of operation, stability and noise will be discussed in detail in Chapter 4.

In Figure 2.2 we show also the building blocks of the second architecture that will be used for LiteBIRD, specifically for the high frequency channels. In this case the beam-former is a circular corrugated feed-horn antenna made with thin gold-plated silicon platelets. The two linear polarizations are extracted by a planar OMT (Orthomode Transducer) and coupled to TES detectors after defining narrow bands via distributed-element (stubs) filters. Detailed descriptions of the two architectures can be found in [63, 67–72, 77].

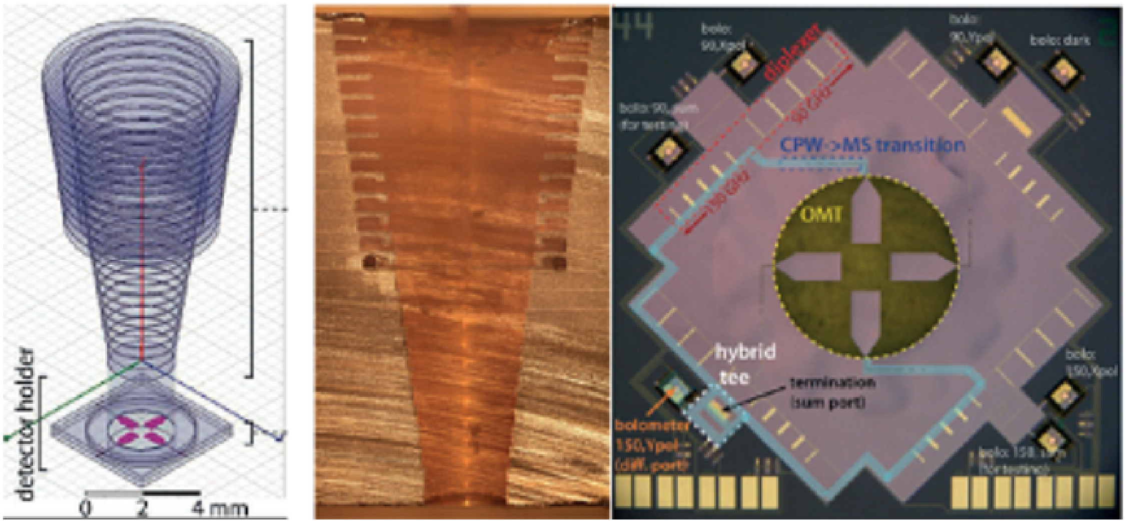

Figure 2.2: Feed-horn antenna. From left to right: HFSS simulation of a corrugated horn antenna with a planar OMT that splits the two orthogonal linear polarizations. A cross-section of the horn antenna fabricated with a gold-plated stack of silicon platelets. Each polarization is channeled through a microstrip transmission line to a diplexer that splits the broadband signal into narrower bands each fed to different TES detectors to be detected. Figures from [77].

2.2 Polarization modulator

As mentioned in the introduction to this chapter, the presence of $1/f$ noise and other systematic effects is a major concern for CMB polarization experiments because of the high sensitivity required to achieve the goal of successfully characterizing the B-mode polarization signal. In order to mitigate both effects several experiments, starting with the MAXIPOL [78] balloon experiment, have implemented polarization modulation units.

The presence of atmospheric fluctuations and long-timescale thermal instability of the telescope structure when observing from the ground introduce a dominant $1/f$ noise component in the detector response. A polarization modulator unit shifts the signal of interest to higher frequency where the noise is purely white. For balloon-borne or space observation the atmosphere is not a concern, however thermal instability can be increased by the effect of cosmic ray showers.

A second advantage of a well-calibrated polarization modulator is a better rejection of instrumental systematics. Signals that are produced in the optical path after the polarization modulating stage are received by the detectors without being modulated, therefore allowing their rejection during data analysis. The rotation of the polarized signal caused by a polarization modulator also allows each sky pixel to be scanned with a more evenly distributed range of angles, therefore improving the cross-linking which helps to reduce the impact of certain systematics (e.g. I to P leakage). This will be discussed in Chapter 3.

At present several different implementations of polarization modulator units (PMU) exist for CMB observation. Most of the existing configurations have been reviewed in [75]. LiteBIRD will employ two of these existing technologies: a multi-layer sapphire HWP and two metamaterial HWPs. We will describe and review the former technology highlighting the design process and challenges.

Rapid signal modulation is often used in radio astronomy [79] to minimize the impact of detector instabilities. Linear polarization modulation has been proven to be promising in rejecting systematic effects for the search of CMB B-modes [80, 81]. A birefringent plate can be used to rotate the incoming polarized signal. By knowing the material properties and tuning the thickness of the plate (t), we can obtain a Half-Wave Plate that introduces a phase shift of 180° ($\delta = \pi$) between two orthogonal polarizations:

$$\delta = 2\pi \frac{|n_o - n_e|}{\lambda} t, \tag{2.2}$$

where n_o and n_e are the refractive index of the ordinary and extraordinary axis of the birefringent plate, and λ is the wavelength of the incoming signal (c/ν). By continuously rotating the HWP at frequency f_{hwp}, the incoming polarized signal

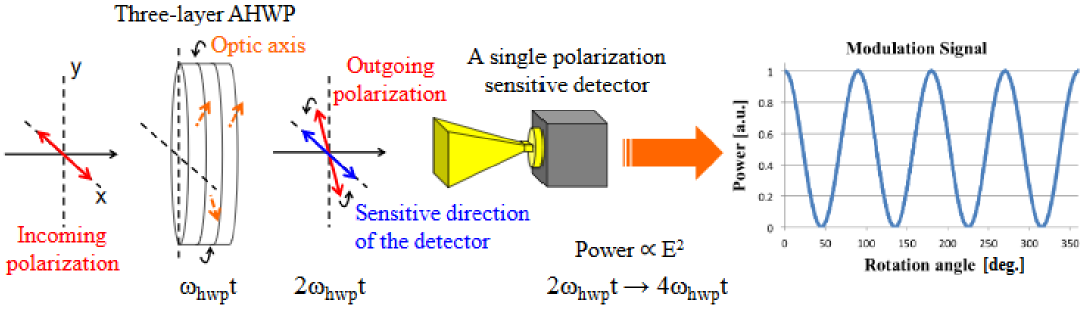

Figure 2.3: Polarization modulation using a continuously rotating HWP. Figure from [4].

is modulated at a rate $4f_{hwp}$, as shown in Figure 2.3 from [4].

As defined in [80], the signal modulated by the HWP seen by a polarization sensitive detector can be written, in terms of the usual Stokes quantities (I, Q and U) as:

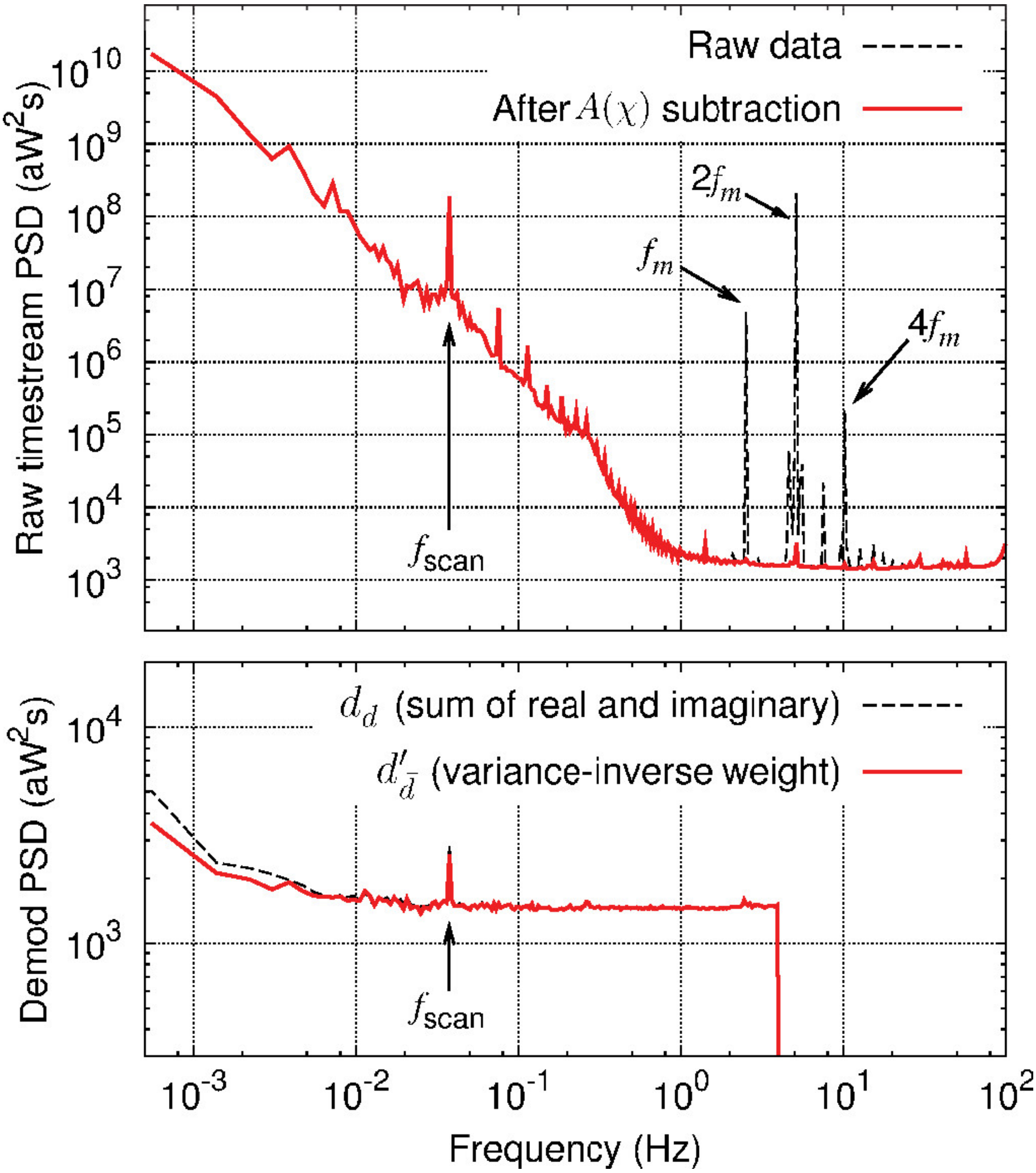

Figure 2.4: Power spectra of the modulated and demodulated data from Atacama B-mode Search (ABS). We can notice that most of the $1/f$ component due to atmospheric fluctuations is suppressed after demodulation. Figure from [80]. In the plot f_{scan} is the telescope scan frequency and f_m is the HWP rotation frequency. In the top panel the authors have highlighted the $2f_m$ and $4f_m$ components. For an ideal HWP the polarized signal would appear uncontaminated at $4f_m$.

$$d = I + \epsilon \mathrm{Re}\{(Q + iU)e^{-i4\rho}\}, \tag{2.3}$$

where ρ is the angle between the incident polarization plane and the reference (ordinary) optical axis of the HWP, and ϵ is the efficiency of the HWP at modulating the polarized signal (modulation efficiency).

If, during the observation of the sky, we keep track of the HWP rotation information, we can demodulate the signal by multiplying the data vector d in Equation 2.3 by the conjugate of the modulating function $m(\rho) = e^{-i4\rho}$. As shown in Figure 2.4 from [80], the dominant $1/f$ component is largely suppressed with this modulation technique. For more details see [80, 81].

In addition, a rotating HWP allows one to use a single polarization sensitive detector (PSD) to simultaneously measure the Q and U parameters, contrary to the commonly used technique of differentiating the signal from two orthogonal polarization sensitive detectors. This offers the advantage of preserving the sensitivity, and a higher level of immunity from certain systematic effects arising from differential response of the two orthogonal detectors (see for example the effect of bandpass mismatch in [82]).

2.2.1 Multi-layer Pancharatnam HWP

As shown in Equation 2.3, one of the important parameters in the design of a polarization modulator based on a HWP is the polarization modulation efficiency ϵ. A single birefringent layer of a given material (e.g. sapphire) with refractive indices n_o (ordinary axis) and n_e (extraordinary axis) can be tuned, by adjusting the thickness, to be used as a HWP polarization modulator with unit-level efficiency at a given frequency ν from Equation 2.2. However, most current and future experiments will deploy multi-chroic focal planes spanning several octaves in frequency. As an example, LiteBIRD Low Frequency Telescope (LFT) is designed to cover the frequency range from 34 to 161 GHz with 9 overlapping bands with $\sim$ 30% bandwidth.

In the current design, LFT will implement a single HWP that needs to achieve an efficiency reasonably close to unity across the whole bandwidth in order not

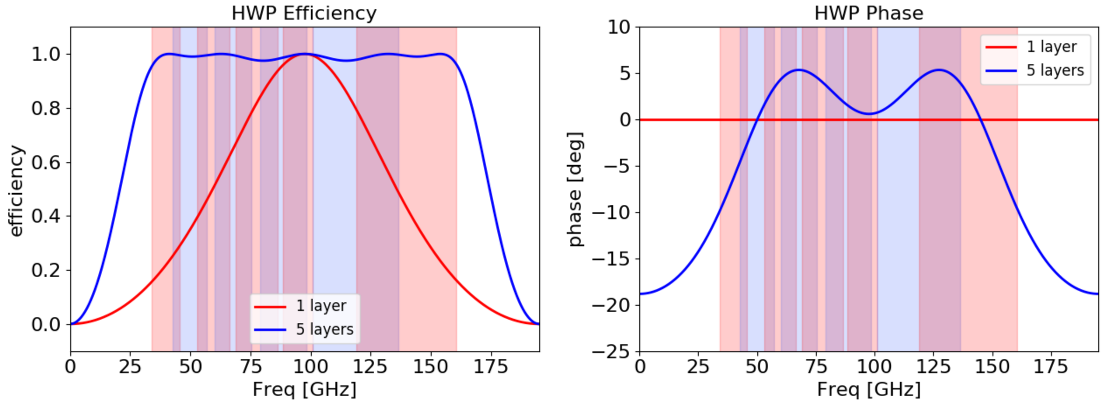

Figure 2.5: Predicted modulation efficiency (left) and phase (right) of 1-layer and a 5-layer Pancharatnam sapphire HWPs. LiteBIRD LFT bands are shown with shaded red and blue areas. The 5-layer design has been optimized following [4] targeting an integrated efficiency $> 98\%$ for each LFT band. Each sapphire layer is assumed to be 4.89 mm thick. Angle distribution for the 5 layers is: $81.1°$, $58.9°$, $0°$, $58.9°$, $81.1°$; the central layer is used as the reference. A disclaimer: this is not the configuration considered for the LFT HWP, but it is used by the author purely to demonstrate the design procedure.

to lose sensitivity to the polarized signal. A technique used to achieve a broader frequency coverage (Achromatic HWP - AHWP) was developed by S. Pancharatnam in [83, 84], and consists in stacking several single layer HWP with different optical axis orientations.

The HWP of LFT will apply this technique using multiple sapphire layers. For the sake of discussion, we implemented the design procedure described in [4] to find a possible layer stack configuration to obtain an AHWP that can cover the whole LFT frequency range. As a design target we require that the integrated modulation efficiency is $> 98\%$ for all 9 bands of LFT. We need to stress that the results shown here are not the design values that will be used by the real instrument, and this exercise was conducted purely for the sake of illustrating the design procedure.

From [4], the effect of a AHWP on an incident wave described in terms of the Stokes parameter can be defined by its Mueller matrix[6] written in the most

---

[6] According to Mueller formalism an optical element can be represented as a 4×4 matrix that acts on a Stokes vector (I, Q, U, V) representing the incident electromagnetic wave.

generic way as:

$$\Gamma_{AHWP} = \begin{pmatrix} m_{ii} & m_{iq} & m_{iu} & m_{iv} \\ m_{qi} & m_{qq} & m_{qu} & m_{qv} \\ m_{ui} & m_{uq} & m_{uu} & m_{uv} \\ m_{vi} & m_{vq} & m_{vu} & m_{vv} \end{pmatrix}. \tag{2.4}$$

Knowing the orientation ρ_i (angle) of each birefringent layer with respect to an origin (e.g. the ordinary optical axis of one of the birefringent layers), the AHWP Muller matrix can be expressed as: $\Gamma_{AHWP} = \prod_i^n R(-\rho_i)\Gamma_i R(\rho_i)$. Here Γ_i is the Muller matrix of a birefringent plate of retardance δ_i and $R(\rho)$ is the generic rotation matrix:

$$\Gamma_i = \begin{pmatrix} 1 & 0 & 0 & 0 \\ 0 & 1 & 0 & 0 \\ 0 & 0 & \cos\delta_i & -\sin\delta_i \\ 0 & 0 & \sin\delta_i & \cos\delta_i \end{pmatrix} \quad R(\rho_i) = \begin{pmatrix} 1 & 0 & 0 & 0 \\ 0 & \cos 2\rho_i & -\sin 2\rho_i & 0 \\ 0 & \sin 2\rho_i & \cos 2\rho_i & 0 \\ 0 & 0 & 0 & 1 \end{pmatrix}. \tag{2.5}$$

Following [4], the efficiency and phase can be found as:

$$\epsilon = \frac{\frac{1}{4}\sqrt{(m_{qq} - m_{uu})^2 + (m_{qu} - m_{uu})^2}\sqrt{Q_{in}^2 + U_{in}^2}}{\frac{1}{2}m_{ii}I_{in} + \frac{1}{4}(m_{qq} + m_{uu})Q_{in} + \frac{1}{4}(m_{qu} + m_{uq})U_{in}} \tag{2.6}$$

$$\phi = \frac{1}{4}\arctan\frac{m_{qu} + m_{uq}}{m_{qq} - m_{uu}}. \tag{2.7}$$

Assuming a sapphire layer with $n_o = 3.047$ and $n_e = 3.361$ we find that a thickness $t \sim 4.89$ mm results in a retardance $\delta = \pi$ (HWP) at the central frequency of the full LFT bandwidth $\nu_c \sim 97.5$ GHz. The simulated performance of a single-layer HWP with these parameters is shown in red in Figure 2.5. We can observe that a single layer HWP meets the design requirement ($\epsilon > 0.98$) only in a narrow band centered around 97.5 GHz.

In Figure 2.5 we show in *blue* also a design using 5 layers with the same thickness ($t \sim 4.89$ mm) optimized in order to meet the modulation efficiency requirement. The angle orientation for the 5 layers is: 81.1°, 58.9°, 0°, 58.9°, 81.1°; where the central layer defines the reference orientation. We obtained these values using a *python* script (see Appendix E for details) that implements the procedure explained above and keeps looping the algorithm sampling randomly the angle distribution until it finds a combination that satisfies the modulation efficiency requirement. The configuration described here is not the one under consideration for the LFT

HWP, it is part of an exercise used by the author for the sake of describing and demonstrating the design procedure.

While the optimization process takes into account only a modulation efficiency threshold, more requirements are under study at present and the final design may have to take into account more parameters to be optimized. As an example in Chapter 3 we will briefly discuss the effect of the HWP phase on the data. An example of the HWP phase is shown in Figure 2.5 for the design described above.

Anti-Reflection Coating. The optimization procedure described above, does not take into account the effect of the discontinuity seen by the incident wave at the boundary between free-space and the sapphire HWP. If not taken care of, in this basic configuration about half of the incident light is reflected (one quarter of the power)[7]. In order to avoid this, several Anti-Reflection Coating (ARC) approaches have been studied and applied in various experiments to different optical elements including HWPs, lenses, and infrared filters [77]. Some examples include multi-layer loaded epoxy coating [85], plastic sheet coating [86], saw diced sub-wavelength structures [87, 88] and laser machined sub-wavelength structures [89, 90]. The baseline for LFT HWP is to use the last technique [91, 92]. The details of the technique are still under further investigation, but conceptually the technique consists in smoothing the transition between free-space and the sapphire plate by machining sub-wavelength (pyramidal) structures to obtain a transition layer where the effective refractive index slowly changes from the one of vacuum (~ 1) to the value of sapphire (~ 3).

2.3 LiteBIRD

LiteBIRD (Lite satellite for the studies of B-mode polarization and Inflation from cosmic background Radiation Detection) has been recently selected (May 2019) by the JAXA Institute of Space and Astronautical Science (ISAS) as a strategic large class mission. At present, JAXA is targeting a launch by the end of Japanese

---

[7] Reflectivity: $R = \left|\frac{n_1 - n_2}{n_1 + n_2}\right|^2$.

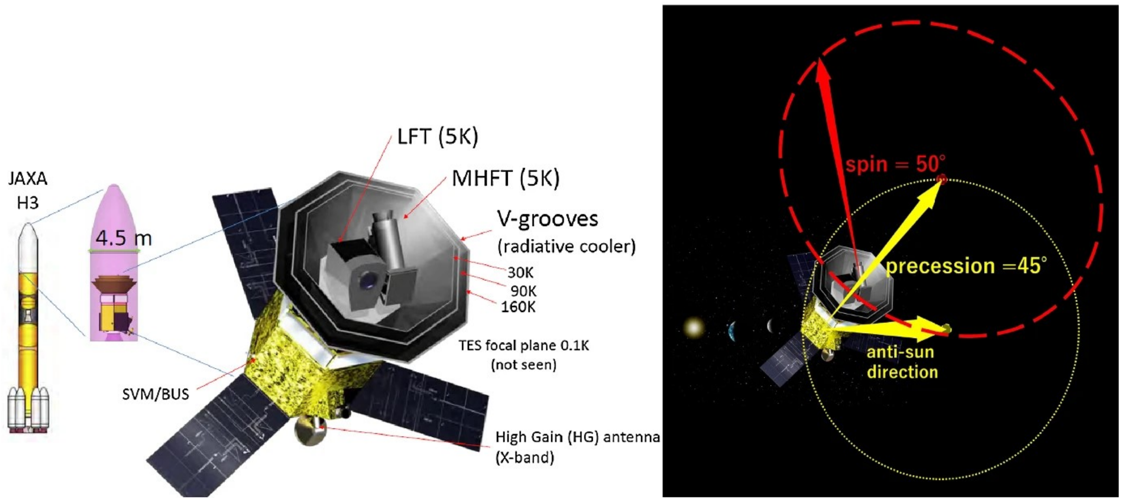

Figure 2.6: *Left:* LitBIRD satellite artistic sketch showing LFT and MHFT structures as well as the passive cooler structure. *Right:* A sketch illustrating LiteBIRD scanning strategy. The scan pattern is defined by the combined effect of the spacecraft precession around the anti-Sun direction and spin around an axis that forms a 45° angle with the anti-Sun direction. The boresight of the telescopes forms a 50° angle witht the spin axis. As it is visible in the skecth the LFT and MHFT boresights are symmetrical with respect to the spin axis. Figure from [5].

Fiscal Year 2027 (early 2028) using a JAXA H3 rocket. This puts LiteBIRD in the position of being in the most advanced phase among all proposed future satellites for CMB observation.

The developments in TES detector technology, specifically the use of multichroic pixels, and polarization modulators for ground-based experiments make these technologies mature enough for their application in a compact satellite like LiteBIRD covering the frequency range 34-448 GHz.

In the current baseline design $\sim$ 4000 TES bolometers will be divided between 3 telescopes: Low Frequency Telescope (LFT, 34–161 GHz), Mid Frequency Telescope (MFT, 89–224 GHz) and High Frequency Telescope (HFT, 166–448 GHz).

LFT and MFT will deploy multichroic lenslet-coupled sinuous antenna pixels, while HFT will use horn-OMT coupled pixels. Most of the pixels used in LFT and MFT will be trichroic with the exception of the *light grey* pixels in Figure 2.7 which will be dichroic, while HFT will use dichroic pixels with the exception of the highest frequency band (402 GHz) which will be assigned to monochromatic pixels. In Figure 2.7 we report the telescope details from [5]. In *red* the trichroic pixels

Expected launch	2028 (JFY 2027)
Observation time	3 years
Target multipole range	$2 \leq \ell \leq 200$
Orbit	Lissajous at 2^{nd} Sun-Earth Lagrangian point (L2)
Precession angle	45°
Precession rate	0.001-0.01 rpm
Spin angle	50°
Spin rate	0.05-0.1 rpm
Cooling	Combination of passive radiative (V-grooves) and mechanical (Striling and JT) & Multiple ADRs for continuous sub-K cooling of the focal plane
Detectors	4676 TES detectors in multichroic pixels
Observing frequencies	15 bands between 34 and 448 GHz
Polarization modulator	3 rotating HWPs
Pointing requirements	$\lesssim 2.1$ arcmin
Target combined sensitivity	2 μK arcmin
Target r sensitivity	$\lesssim 1 \times 10^{-3}$

Table 2.1: Parameters for the current baseline design of LiteBIRD [5]. In the analysis presented in Chapter 3 we assumed 0.05 rpm for the spin rate and ∼ 0.005 rpm for the precession rate.

covering 40, 60, 78 GHz frequency bands, in *yellow* the trichroic pixels covering 50, 68, 89 GHz, in *green* the trichroic pixels covering 68, 89, 119 GHz and finally in *light blue* the trichroic pixels covering 78, 100, 140 GHz. *Bottom center:* MFT focal plane. In *dark grey* the trichroic pixels covering 100, 140, 195 GHz frequency bands and in *light grey* the dichroic pixels covering 119, 166 GHz. *Bottom right:* HFT focal plane. In *pink* the dichroic pixels covering 195, 280 GHz frequency bands, in *green* the dichroic pixels covering 235, 337 GHz and lastly in *blue* the monochromatic pixels covering 402 GHz.

Each telescope will have a Polarization Modulation Unit (PMU) using a Superconductive Magnetic Bearing (SMB) to uniformly rotate a broadband HWP. The SMB consists of a fixed ring (attached to the telescope structure) made of YBCO (Yttrium Barium Carbon Monoxide – superconductive below ∼ 93 K) and permanent magnets (SmCo – samarium-cobalt) embedded in the HWP support ring. When the telescope is cooled below the YBCO critical temperature, the

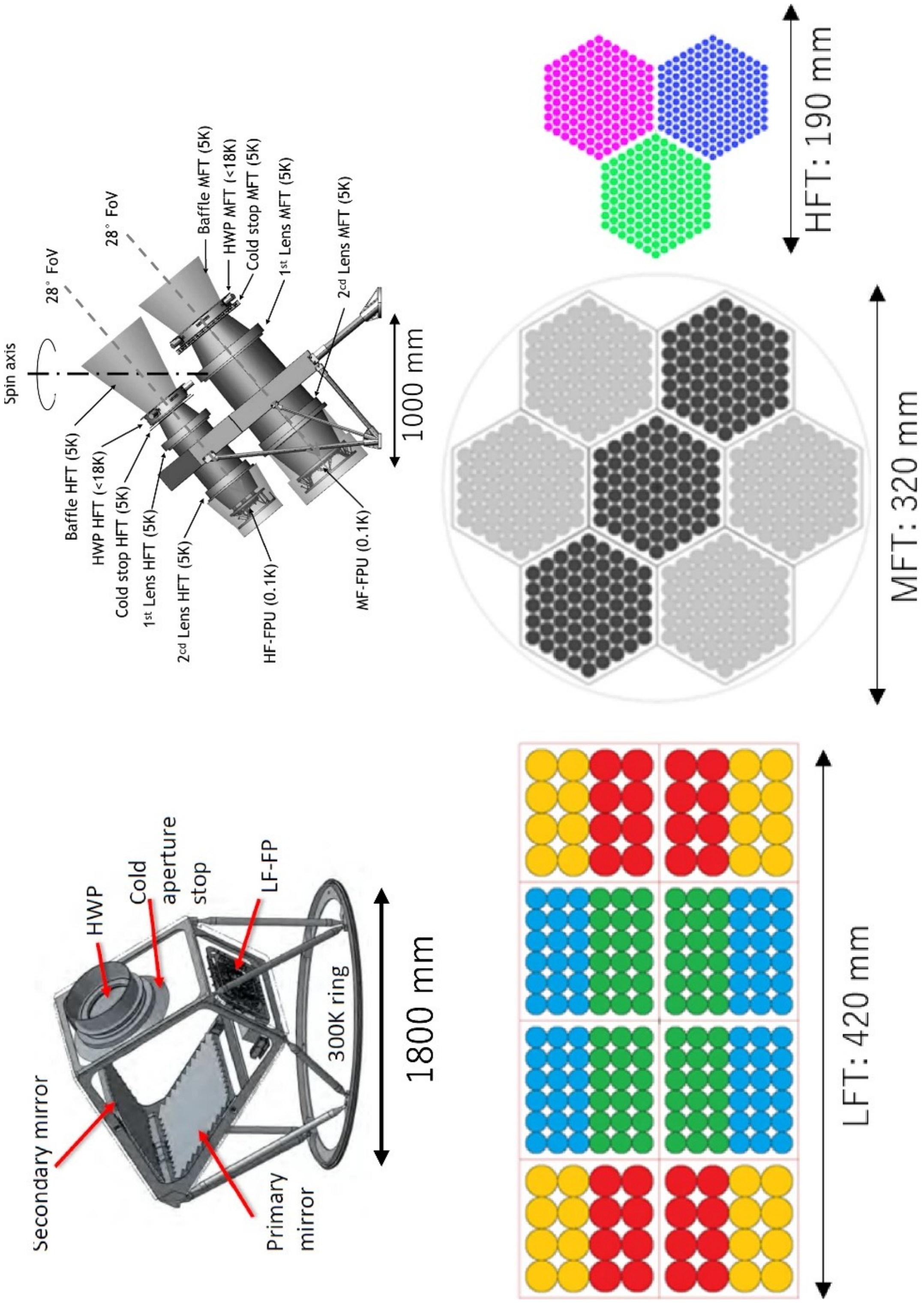

Figure 2.7: *Top left:* Reflective cross-Dragone design of LFT. *Top right:* Refractive design of MFT and HFT. Figure from [5].

Telescope	LFT	MFT	HFT
Configuration	Reflective	Refractive	Refractive
Frequency (GHz)	34-161	89-224	166-448
FOV	20° × 10°	28°	28°
Aperture diameter (mm)	400	300	200
Resolution (arcmin)	70-24	38-28	29-18
HWP rot. rate (rpm)	46-83	39-70	61-110
# Detectors	1248	2074	1354

Table 2.2: LiteBIRD telescopes design parameters [5]. In the analysis presented in Chapter 3 we assumed a single value of 46 rpm for the HWP rotation.

HWP levitates and a magnetic motor allows a stable contactless rotation which minimizes friction and heat dissipation [91]. In the current baseline LFT will employ a Pancharatnam (multi-layer) sapphire HWP with laser machined SWS AR coating, as explained in the previous section. On the other hand, MFT and HFT will employ 2 metamaterial refractive HWPs [75, 93]. As described in the previous section, polarization modulation allows for the suppression of the $1/f$ noise component as well as a better control of systematic effects.

In the current configuration, the detector critical temperature is $\sim$ 170 mK. This requires the focal planes to be cooled to 100 mK for noise optimization (see Chapter 4 for details). To achieve this temperature the spacecraft will employ a multi-stage cryogenic chain. A passive cryogen-free system consisting of radiative V-grooves (see Figure 2.6) will cool the payload to $\sim 5K$. This allows the whole telescope structure to be stable at $\sim$ 5 K during operation, suppressing thermal noise and spillovers. To further reduce the temperature on the intermediate stages, two mechanical coolers (Sterling and Joule-Thomson) will be employed. Finally, a series of multi-stage ADRs (Adiabatic Demagnetisation Refrigerators) will guarantee stable and continuous sub-K cooling of the 3 focal planes [94].

The baseline operation is guaranteed for 3.5 years, therefore allowing for 6 months margin on the proposed 3 years of observations for calibration operations and the time spent by the spacecraft to reach the second Earth-Sun Lagrange point (L2), where it will be kept in orbit (Lissajous) for the duration of the mission. The choice of this particular location is standard for every space mission that

Telescope	ν_c (GHz)	Bandwidth (GHz)	# Detectors	Pol. sensitivity (μK arcmin)
LFT	40	12 (30%)	64	39.76
LFT	50	15 (30%)	64	25.76
LFT	60	14 (23%)	64	20.69
LFT	68	16 (23%)	208	12.72
LFT	78	18 (23%)	208	10.39
LFT	89	20 (23%)	208	8.95
LFT/MFT	100	23 (23%)	530	6.43
LFT/MFT	119	36 (30%)	632	4.30
LFT/MFT	140	42 (30%)	530	4.43
MFT	166	50 (30%)	488	4.86
MFT/HFT	195	59 (30%)	640	5.44
HFT	235	71 (30%)	254	9.72
HFT	280	84 (30%)	254	12.91
HFT	337	101 (30%)	254	19.07
HFT	402	92 (23%)	338	43.53

Table 2.3: A possible configuration for the CMB satellite mission LiteBIRD [3, 5]. Central frequency, number of detectors and sensitivity to polarization forecast in unit of temperature per arc-minute are given for all frequency bands. These are the values assumed in the various analyses presented in this thesis.

requires good control of the thermal environment to minimize extra loading and noise from nearby objects, namely the Sun, the Earth and the Moon. In fact, from this location all three objects are always lying in the same direction, and so they can be easily avoided choosing an appropriate scanning pattern. However, the environment is far from benign in space, the absence of atmosphere does not offer any shielding against the constant bombardment by Galactic cosmic rays as well as solar cosmic ray showers, which can dramatically affect the bolometers, as observed in Planck HFI data [64]. Therefore, understanding the impact of cosmic rays on LiteBIRD detectors and developing mitigation techniques is of vital importance for the LiteBIRD space mission [95].

As shown in Figure 2.6 and in Table 2.1, the scanning strategy of LiteBIRD is defined by the combination of the spacecraft precession around the anti-Sun direction and its spin around an axis that forms a 45 degree angle with the anti-Sun direction (together this guarantees that the main beam never falls on the Sun,Earth or Moon). The constant precession period will be $\sim$ few hours, and the constant spin rate will be $\sim$ 0.05–0.1 rpm [8]. The bore-sight axes of the three telescopes are tilted at 50 degrees with respect to the spin axis. This configuration offers a uniform coverage of most of the sky [82], and good cross-linked scan throughout the mission. The cross-linking improves even further thanks to the HWP rotation, as will be shown in Chapter 3 and Appendix D.

Table 2.2 shows the design parameters for the 3 telescopes, including the angular resolution. The shallow angular resolution (degree-level) is due to the fact that LiteBIRD has been designed with the goal of characterizing the largest angular scales (multipole range $2 \leq \ell \leq 200$). Therefore, a close synergy between LiteBIRD and next-generation ground-based experiments (more sensitive on small scales) can greatly benefit both.

In Table 2.3, we summarize the sensitivity to polarization assumed in the analysis discussed in Chapter 3. The details of the sensitivity calculation are discussed in Appendix B.

In the following chapters we use the design parameters presented in this section in various analyses of systematic effects in order to further define some of the instrument requirements that are necessary to meet the science goals and to keep the systematic uncertainty under control.

---

[8] The precise numbers are still being investigated, however in Chapter 3 we assume $\sim$ 3.2 hours for the precession period and 0.05 rpm for the spin rate as a case study

3

Systematic Effects

In this chapter we focus on some of the known systematic effects concerning CMB experiments. Specifically, we focus on band-pass related effects. We use LiteBIRD as a case study and analyze in detail some of the issues observed by in the Planck experiment, starting from the work presented in [82]. As discussed in Chapter 1, Figure 1.6 shows the effect of systematic effects on Planck HFI data.

By using a continuously rotating HWP, LiteBIRD will be able to produce polarization maps from single detectors, therefore mitigating one of the systematic sources observed in Planck: band-pass mismatch. However, poor band-pass knowledge can still introduce uncertainties in the data. This issue is analysed in detail in Section 3.2, where we assume an ideal HWP with frequency-independent modulation efficiency and phase. In Section 3.4 we briefly introduce a mathematical formalism to extend the analysis of Section 3.2 including a non-ideal HWP response.

Another source of systematics observed in Planck, related to band-pass response, is due to the presence of CO emission lines. Total intensity-to-polarization leakage has been particularly detrimental in the Planck experience. The origin of this effect has been identified, for HFI 100 GHz channel, in the CO $J1 \rightarrow 0$ line falling at the edge of the band where the difference in transmission among detectors can be large. Therefore causing a leakage of CO total intensity in the difference of two orthogonal detectors. One of the proposed techniques to avoid the same issue in

LiteBIRD consists of introducing notch filters (band-stop) in the on-chip filters. In Section 3.3 we analyse this effect in the context of LiteBIRD to determine whether the use of notch filters is required and/or beneficial.

Finally, we briefly discuss other major systematic effects that will need special attention for the success of the LiteBIRD mission.

3.1 Data model

For a single polarization-sensitive detector observing the sky through a rotating HWP that modulates the linearly polarized signal, we can write the data vector (time-ordered data or TOD) as:

$$\begin{aligned} d(t) = \frac{S(t)}{2} \int d\nu \, \frac{\lambda^2}{\Omega_b} G(\nu) \int d\Omega \; B(\nu,\Omega) \Big\{ I(t,\nu) \, + \\ + \; \epsilon(\nu) \Big[Q(t,\nu) \cos(4\rho(t) - 2\psi(t) + 4\phi(\nu)) \, + \\ + \; U(t,\nu) \sin(4\rho(t) - 2\psi(t) + 4\phi(\nu)) \Big] \Big\} + n(t), \end{aligned} \tag{3.1}$$

where:

- $S(t)$ is the detector-readout combined sensitivity in units of [V/W] (see Chapter 4).
- λ^2/Ω_b is the telescope effective area A_e. λ is the wavelength of the incoming signal, while $\Omega_b = \int_{4\pi} B(\nu,\Omega) \; d\Omega$ is the solid angle of the telescope beam $B(\nu,\Omega)$[1].
- $G(\nu)$ is the band-pass response of the detector (including the effect of the optical system).
- $\epsilon(\nu)$ is the modulation efficiency of the HWP as defined in Chapter 2.
- I, Q and U are the Stokes components of the incoming signal in units of spectral radiance [$\mathrm{Wm^{-2}sr^{-1}Hz^{-1}}$]. See Appendix A for details about units conversion.

---

[1] $A_e = \lambda^2/\Omega_b$ for single mode antennas.

- $\rho(t)$ is the HWP rotation angle and depends on the rotational frequency of the HWP ω_{hwp}.
- $\psi(t)$ is the polarization-sensitive detector projection on the sky.
- $\phi(\nu)$ is the frequency-dependent phase response of the HWP as defined in Chapter 2.
- Lastly, $n(t)$ is the noise term. See Chapter 2 for LiteBIRD sensitivity, Chapter 4 for the definition of TES detector and readout noise properties and Appendix B for the details of the sensitivity calculation.

Poor knowledge or imperfect modelling of any of the above items result in an imperfect reconstruction of the sky signal.

3.2 Photometric and bandpass response calibration

This Section is partially based on the paper [3] recently submitted to JCAP (not accepted yet at the time of the sumbission of this thesis).

Although the author is not directly involved in the fabrication of on-chip bandpass filters for LiteBIRD detectors, in Appendix C we report the procedure and results of prototype bandpass filters fabricated for the SKA band 5 receiver by the author. The author has followed a procedure similar to the one used to fabricate the bandpass filters for LiteBIRD and other CMB experiments.

As already discussed in Chapter 2, the LiteBIRD mission [5, 34, 35] is under design with the goal of measuring the primordial B-mode signal with a sensitivity (in terms of tensor-to-scalar ratio) $\sigma_r \leq 0.001$. Observations will cover a wide frequency range from 34 to 448 GHz, divided into 15 frequency bands. This is justified by the requirement to carefully survey the Galactic foregrounds in order to be able to characterize them with high accuracy and separate them from the underlying cosmological signal. Having many frequency bands requires accurate inter-frequency calibration. An imperfect photometric calibration or poor band-pass knowledge may cause leakage of foreground signals into the estimated CMB maps. These effects have been the subject of other studies such as the study presented in [96], where the authors focused on future ground-based experiments. In this Section we apply a similar approach to study these effects in the context of next generation satellite missions, using LiteBIRD as a case study.

In order to set photometric calibration and band-pass resolution requirements, we have performed simulations of component separation in the map (pixel) domain. Propagating the effect of an imperfect calibration (photometric or band-pass resolution) to the maps, we estimate the impact on the reconstruction of the tensor-to-scalar ratio. We can then set requirements to minimize the bias on the recovered cosmological parameter. With this procedure, we can test the combined effect of instrumental systematics and contamination from Galactic sources (synchrotron and dust) at different frequencies, to find which bands are more sensitive to miscalibration and hence define the calibration requirements. Assuming the CMB dipole as the main photometric calibrator, we can also define the band-pass resolution necessary to minimize the effect of an imperfect colour correction due to the presence of the Galactic foregrounds. This study is particularly important because it can guide the experiment to select the most appropriate observation strategy to suppress photometric calibration uncertainty, and drive the design of the ground calibration system (most likely a Fourier Transform Spectrometer) used to characterize the band-pass response of the telescope in order to achieve the required resolution.

3.2.1 Formalism

Here we describe the formalism used in this study: the instrumental model (which has been simplified from Equation 3.1 to take into account only a non-ideal bandpass response), the sky modelling assumptions and how we define the effect of band-pass response on the data.

3.2.1.1 Instrumental model

We assume all parameters in Equation 3.1 to be ideal, static, frequency-independent and perfectly known, with the exception of the band-pass response. We emphasize that this is an approximation in order to focus on the photometric and band-pass calibration accuracy. With this approximation we can write the instrumental model for a single detector on the focal plane of a CMB polarimeter as:

$$d = \int d\nu \; G(\nu) \Big\{ I(\nu, \hat{n}) + \Big[Q(\nu, \hat{n}) \cos 2\psi + U(\nu, \hat{n}) \sin 2\psi \Big] \Big\} + n^{2}, \tag{3.2}$$

where $G(\nu)$ is the band-pass response, $I(\nu, \hat{n})$, $Q(\nu, \hat{n})$ and $U(\nu, \hat{n})$ represent the total intensity and polarized intensity of the sky, n is the detector noise and ψ represents the orientation of the polarization-sensitive detector on the sky. As defined in Equation 3.1, when the polarimeter employs a polarization modulator such as a rotating HWP, we can rewrite ψ in Equation 3.2 as $2\rho - \psi$ where ρ is the HWP angle.

Traditionally experiments like Planck reconstruct the polarization pattern (Q and U) by differencing orthogonal detector pairs. This approach is simple but susceptible to mismatches such as differences in the band-pass responses. A mismatch in the band-pass response between the two orthogonal detectors leads to total intensity leakage into the final Q and U maps [82, 97]. A more detailed description of this effect is described in the next Section in the context of carbon monoxide (CO) contamination.

This effect is mitigated using a polarization modulator as the first optical element of the telescope, as in the ABS experiment [80, 98]. The modulation of the polarized signal allows to use a single detector to measure both the Q and U parameters simultaneously. Therefore this approach is immune to mismatch between orthogonal detectors. Thus, the main contribution to the uncertainty in the data comes from the finite knowledge of the band-pass response, as it will be clear in the following sections.

---

[2] Since we assume a perfectly known beam function $B(\nu, \Omega)$, we omit the antenna effective area $A_e = \lambda^2/\Omega_b$ ($\Omega_b = \int d\Omega B(\nu, \Omega)$), and the integration over the solid angle $\int d\Omega$. A term ν^{-2} due to the telescope effective collective area A_e is left implicit, however it is taken into account when performing the calculation.

A thorough discussion of the I to P leakage in the absence of a polarization modulator can be found in [82, 97].

3.2.1.2 Sky model

We model the sky emission at frequency ν and position $\hat{n}$ as a sum of the CMB signal and Galactic foregrounds described in Chapter 1 [82]:

$$I(\nu,\hat{n}) = I_0(\nu) + \left.\frac{\partial B(\nu,T)}{\partial T}\right|_{T_0} \Delta T_{cmb}(\hat{n}) + \sum_f I_f(\nu,\hat{n}) \tag{3.3}$$

$$Q(\nu,\hat{n}) = \left.\frac{\partial B(\nu,T)}{\partial T}\right|_{T_0} \Delta Q_{cmb}(\hat{n}) + \sum_f Q_f(\nu,\hat{n}) \tag{3.4}$$

$$U(\nu,\hat{n}) = \left.\frac{\partial B(\nu,T)}{\partial T}\right|_{T_0} \Delta U_{cmb}(\hat{n}) + \sum_f U_f(\nu,\hat{n}) \tag{3.5}$$

where I_0 represents the CMB monopole with temperature $T_0 \sim 2.7$ K, and the second term on the right hand side of Equation 3.3 is the anisotropy of the CMB, $B(\nu,T)$[3] is the black body spectrum and $\Delta T_{cmb}(\hat{n})$ is the temperature fluctuation around T_0. The last term is the sum of every other relevant sky component f (i.e. thermal dust, synchrotron, etc). In the same way, in Equations 3.4 and 3.5 we define the two Stokes parameters for polarization.

As mentioned in Chapter 1, we take into account two Galactic foreground emissions: thermal dust and synchrotron. The model assumed is defined in Equations 1.8 and 1.9 (with constant spectral parameters across the sky).

In this study we do not take into account contributions from free-free emission, spinning dust and carbon monoxide (CO) transition lines. Previous experiments have shown negligible polarization levels for these components ($\lesssim 1\%$, see [59, 99–101]).

3.2.1.3 Systematic effect due the band-pass uncertainty

In [82, 97] the effect of total intensity to polarization leakage due to both the scanning strategy and band-pass uncertainty has been discussed extensively, especially in the case of a polarimeter that does not employ a rotating HWP. The authors showed

---

[3] In equation 3.2 we have already implicitly multiplied by the antenna effective area $A_b = \lambda^2/\Omega_b$ and computed the integral over the solid angle and the, therefore in this scenario the black body function is in units of W/Hz.

that this effect becomes negligible when using an ideal polarization modulator, thanks to the absence of pair-differencing between orthogonal detectors, as well as a more uniform scanning-angle (ψ in Equation 3.2) distribution that helps reducing the deviation of the cross-linking matrix from its ideal case (see the next section for more details).

We discuss another effect arising from a limited knowledge of the band-pass response that has the same impact for both polarimeter architectures in first approximation, with or without a polarization modulator (it is expected to be dominated by the I-to-P when a HWP is not employed). As explained in the following, the band-pass knowledge is closely related to the photometric calibration accuracy of the data, therefore we developed a framework to include both effects.

A poor photometric calibration accuracy of the data can cause an imperfect estimation of the foreground signals, and lead to a leakage of these into the recovered CMB maps. Because of the brightness of polarized dust and synchrotron with respect to the CMB B-mode signal at all frequencies, this leakage could have a dramatic impact on the ability of an experiment to achieve the accuracy required for a successful measurement of the primordial B-mode signal.

In order to derive calibration requirements for a future CMB satellite mission, like LiteBIRD, we developed a simple top-down framework to generate sky maps that take into account the presence of foregrounds, photometric calibration and band-pass response uncertainties. If we integrate Equation 3.2 and write explicitly each component in our sky model of Equations 1.9, 1.8 we obtain:

$$\begin{aligned} d = {} & g(I_{cmb}(\nu_0) + \gamma_d I_d(\nu_0) + \gamma_s I_s(\nu_0)) + \\ & + g(Q_{cmb}(\nu_0) + \gamma_d Q_d(\nu_0) + \gamma_s Q_s(\nu_0)) \cos 2\psi + \\ & + g(U_{cmb}(\nu_0) + \gamma_d U_d(\nu_0) + \gamma_s U_s(\nu_0)) \sin 2\psi + n, \end{aligned} \tag{3.6}$$

where the subscript d refers to the thermal dust component and the subscript s refers to the synchrotron component. Assuming the CMB dipole [102, 103] as the natural photometric calibrator for a satellite mission, we define g as the photometric calibration factor and $\gamma_{d,s}$ as the colour correction factors. The colour-correction accounts for the different spectral shape of dust and synchrotron compared to the calibrator (CMB dipole). In Equation 3.6, ν_0 is the effective central frequency of the given frequency band. If there is no effect other than the band-pass response to take into account, the calibration factor g (if the CMB dipole is the calibrator) is determined from the data. Therefore, it does not depend explicitly on the band-pass response knowledge.

If the photometric calibration uncertainty (defined here as δ_g) is negligible, the dominant contribution to take into account is the colour correction effect (in CMB units – see Appendix A):

$$\gamma_{d,s} = \left(\frac{\int d\nu \; G(\nu) \frac{I_{d,s}(\nu)}{I_{d,s}(\nu_0)}}{\int d\nu \; G(\nu) \frac{\partial B(\nu,T)}{\partial T}\Big|_{T_0}} \right) \frac{\partial B(\nu_0,T)}{\partial T}\Big|_{T_0}, {}^{4} \tag{3.7}$$

which depends on the prior knowledge of the band-pass response $G(\nu)$. A limited or poor characterization of the band-pass response can result in systematic leakage of foreground signal into the final CMB maps because of an improper calibration of the Galactic signal. We can define the uncertainty on the colour correction factor γ estimation as:

$$\delta_{\gamma}^{(d,s)} = \frac{\gamma^{'}_{d,s} - \gamma^{0}_{d,s}}{\gamma^{0}_{d,s}}, \tag{3.8}$$

where $\gamma^{0}_{d,s}$ is the colour correction factor for an ideal infinite precision (sample spacing $\Delta\nu \to 0$) on the knowledge of the band-pass response, and $\gamma^{'}_{d,s}$ is the colour correction factor for a realistic finite band-pass resolution.

We ultimately write the maps for a single detector j as:

$$\begin{pmatrix} I_j \\ Q_j \\ U_j \end{pmatrix} = g \left[\begin{pmatrix} I_{cmb} \\ Q_{cmb} \\ U_{cmb} \end{pmatrix} + \gamma_d \begin{pmatrix} I_d \\ Q_d \\ U_d \end{pmatrix} + \gamma_s \begin{pmatrix} I_s \\ Q_s \\ U_s \end{pmatrix} \right] + n_j, \tag{3.9}$$

and use this to propagate the calibration uncertainty directly at the map level, without the need to generate computationally expensive time-ordered data.

---

[4] As already mentioned, in both integrals a term ν^{-2} due to the telescope effective collective area A_e is left implicit, however it is taken into account when performing the calculation. See Appendix A.

3.2.1.4 Propagation of the uncertainty at map level

We can combine the single detector maps in Equation 3.9 to obtain I, Q and U maps for each frequency band, and study the global effect of photometric calibration or band-pass accuracy. If the detectors in the frequency band i are uncorrelated (noise and uncertainties), and the calibration accuracy per detector (either the photometric calibration factor g or the colour correction factor γ) is known with a precision $\delta_{g,i}$ ($\delta_{\gamma,i}$ for colour correction), we can easily propagate the uncertainty to the final (full mission) frequency maps as:

$$\Delta_{[g,\gamma],i} = \frac{\delta_{[g,\gamma],i}}{\sqrt{m_i}} \tag{3.10}$$

where m_i is the number of detectors in the frequency band i. Using this factor we propagate the calibration or colour correction error into the maps following Equation 3.9, where:

$$[g,\gamma]_i = 1 + \Delta_{[g,\gamma],i}. \tag{3.11}$$

With this definition contaminated sky maps can be analytically generated by multiplying the ideal sky map at frequency i (including CMB, thermal dust and synchrotron) by the factor g_i (or γ_i for colour correction).

3.2.2 Analysis procedure

In Figure 3.1 we show a flow chart of the analysis procedure. After artificially propagating the calibration uncertainty to the frequency maps using the g_i (γ_i) factors, as defined in Section 3.2.1, we apply a parametric foreground cleaning method [104–106][5] to define the impact of the calibration uncertainty on the recovered CMB maps. After estimating the B-mode angular power spectrum we find the level of contamination in terms of bias on the tensor-to-scalar ratio.

We explicitly describe the procedure for the photometric calibration analysis. For the procedure for the colour correction analysis we simply substitute Δ_g with Δ_γ.

---

[5] `https://github.com/fgbuster/fgbuster`

3.2.2.1 Map preparation

We generate full mission sky maps using the *PySM* package (see [107][6][7] for details) for all frequency bands in Table 2.3 including the sky components mentioned in Section 3.2.1.2. We adopt the cosmological parameters reported by the Planck experiment in [45]. Since the goal of LiteBIRD is to target a total uncertainty $\sigma_r \leq 0.001$ for $r = 0$, we adopt $r = 0$ as input to generate the CMB maps.

The sky maps are perturbed as described in Section 3.2.1.4. Specifically making use of Equation 3.9 to simulate the effect of an imperfect calibration. As mentioned in 3.2.1.2 we do not account for spatial variations of the spectral parameters in this analysis. A white and isotropic noise component is added according to the sensitivity values in Table 2.3. We assume LiteBIRD baseline parameters as reported in [5]. This procedure can potentially be applied to other instrument configurations by changing the instrumental parameters according to a specific design.

Following the formalism introduced in [96], for each frequency band i the calibration factor g_i with uncertainty $\Delta_{g,i}$ is:

$$g_i = 1 + \mathcal{N}(0, \Delta_{g,i}), \tag{3.12}$$

where $\mathcal{N}(\mu, \sigma)$ is a random number generated with a Gaussian distribution with mean value $\mu = 0$ and standard deviation $\sigma = \Delta_{g,i}$.

3.2.2.2 Analysis steps

A similar analysis was presented for the Simons Observatory case in [96]. However, the authors do not make an explicit distinction between frequency bands. We decided to proceed in the following way to determine which bands are more sensitive to calibration uncertainties (see also Figure 3.1 for a flow chart of the analysis procedure):

1. We choose a few representative values for $\Delta_{g,i}$ between 10^{-6} and 10^{-2}. To verify the relation (see Section 3.2.3.1 for details) between the calibration

---

[6] https://github.com/bthorne93/PySM_public

[7] https://pypi.org/project/pysm3/

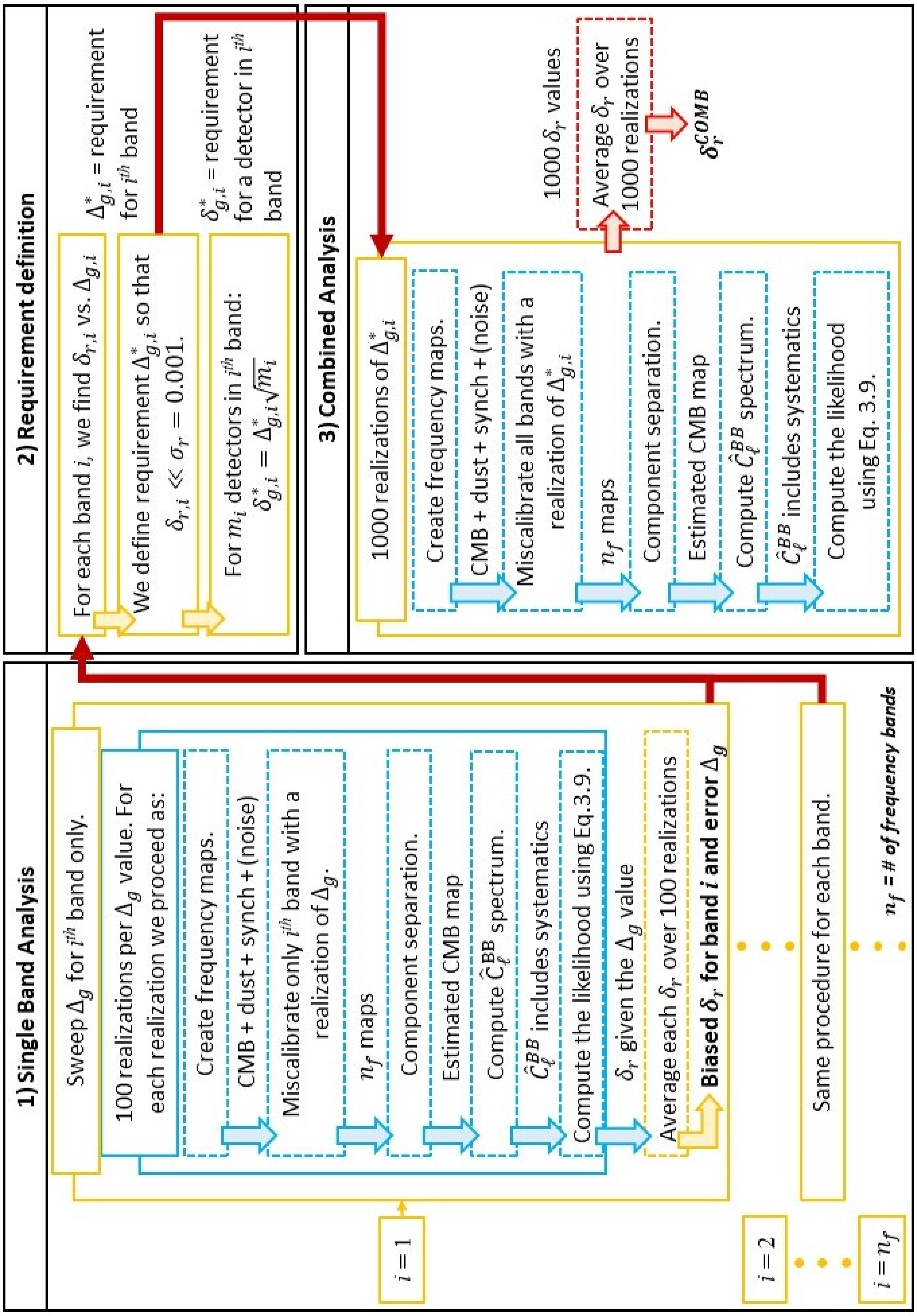

Figure 3.1: Flow chart of the analysis method followed in this work to study the effect of calibration uncertainty in presence of foreground contamination. The analysis is divided in 3 main steps: single frequency band analysis, requirement determination for each frequency band, and finally requirement validation.

accuracy of each frequency band ($\Delta_{g,i}$) and the induced bias to the tensor-to-scalar ratio (δ_r), we perform 15 separate analysis (one for each frequency band). For each analysis step, we propagate the uncertainty only in one frequency band using the factors from Equation 3.12. After the component separation step, we can relate the uncertainty value directly to the computed δ_r from the excess in the component separation residuals.

2. Once we find the relation between $\Delta_{g,i}$ and δ_r for each frequency band i, we define requirements for each band ($\Delta^*_{g,i}$) that reduce the bias below the target sensitivity: $\delta_r \ll \sigma_r \leq 0.001$. We adopt the requirement: $\delta_r \leq 5.7 \times 10^{-6}$. This value corresponds to $\lesssim 1\%$ of the target σ_r of the experiment.[8] The results can be easily re-scaled by the reader for any given requirement.

3. We perform a final simulation propagating the calibration uncertainty in all frequency bands simultaneously using the $\Delta^*_{g,i}$ values found from the previous step. Since there are 15 frequency bands and the uncertainties are uncorrelated, we expect to find a total bias to the tensor-to-scalar ratio (δ_r^{COMB}) roughly $\sqrt{15}$ times higher than the threshold value mentioned at the previous point ($\delta_r \leq 5.7 \times 10^{-6}$). However, because the single frequency requirement $\delta_r \leq 5.7 \times 10^{-6} \ll \sigma_r$, we expect this to be true for the total tensor-to-scalar ratio bias: $\delta_r^{\mathrm{COMB}} \ll \sigma_r$.

This procedure has the advantage of reducing the complexity of a 15 free parameters analysis.

---

[8] We assume that the total uncertainty can be divided in σ_{fg} due to the component separation residuals and σ_{sys} due to systematic effects. By requiring that these two terms have the same value, including a margin term σ_m and combining them in quadrature to obtain the total uncertainty, we define the uncertainty value allocated to each term: $\sigma_i \sim 5.7 \times 10^{-4}$. Since we expect the experiment to suffer from multiple systematic effects, we assign to each effect 1% of the total systematic budget.

3.2.2.3 Component separation

To perform the component separation we employ the *FgBuster*[9] code, which is a *python* implementation of the parametric maximum likelihood foreground estimation algorithm described in [104].

The sky, observed in multiple frequency bands, is modeled at map level, pixel-by-pixel as:

$$d_p = A_p s_p + n_p \tag{3.13}$$

where p denotes a single sky pixel, d_p is the observed signal vector (including $n_s = 3$ Stokes parameters for n_f frequency bands), s_p is the real sky signal vector (n_s Stokes parameters for n_c number of components), n_p is the noise vector and $A_p \equiv A_p(\beta_i)$ is the mixing matrix of the form $(n_f \cdot n_s) \times (n_c \cdot n_s)$. The mixing matrix is parameterized by the free parameters β_i describing the spectrum of each sky component (see Section 3.2.1.2). As mentioned, in this analysis we consider 3 components: CMB, synchrotron and thermal dust, therefore we have 3 unknown spatially-uniform parameters β_s, β_d and T_d. For p pixels we can remove the subscript and re-write:

$$\boldsymbol{d} = \boldsymbol{A}\boldsymbol{s} + \boldsymbol{n}. \tag{3.14}$$

Defining the symmetric block diagonal noise matrix $\boldsymbol{N}$ we write the likelihood function as

$$-2\ln\mathcal{L}(\boldsymbol{s},\boldsymbol{\beta}) = \mathrm{const} + (\boldsymbol{d}-\boldsymbol{A}\boldsymbol{s})^t\boldsymbol{N}^{-1}(\boldsymbol{d}-\boldsymbol{A}\boldsymbol{s}). \tag{3.15}$$

The full data likelihood is found as the sum of the likelihood for each single pixel and is maximized when

$$\boldsymbol{s} = (\boldsymbol{A}^t\boldsymbol{N}^{-1}\boldsymbol{A})^{-1}\boldsymbol{A}^t\boldsymbol{N}^{-1}\boldsymbol{d}. \tag{3.16}$$

Then, substituting Eq. 3.16 in Eq. 3.15 we find:

$$-2\ln\mathcal{L}(\boldsymbol{s},\boldsymbol{\beta}) = \mathrm{const} + (\boldsymbol{A}^t\boldsymbol{N}^{-1}\boldsymbol{d})^t(\boldsymbol{A}^t\boldsymbol{N}^{-1}\boldsymbol{A})^{-1}(\boldsymbol{A}^t\boldsymbol{N}^{-1}\boldsymbol{d}). \tag{3.17}$$

The algorithm finds the set of parameters $\{\boldsymbol{\beta}_i\}$ that maximize the likelihood function. For more details see [104].

---

[9] `https://github.com/fgbuster/fgbuster`

3.2.2.4 Tensor-to-scalar ratio bias

After component separation, we obtain an estimated CMB map that is the sum of the input CMB map m_{cmb}^{true}, and residuals due to noise m_n and residual foreground signal from the component separation method itself m_{fg}. Understanding how to improve the component separation efficiency is the subject of other studies [108]. Here we investigate the role that instrumental systematic effects have in boosting the amplitude of the component separation residuals m_{fg}.

In order to isolate the residuals due to the calibration uncertainty, we perform a parallel analysis for every value of Δ_g and noise realization. With the same components and noise maps we run two separate simulations, one with an ideal instrument unaffected by calibration uncertainty ($\Delta_g = 0$) and the other propagating the uncertainty Δ_g into the maps.

The recovered CMB maps from these two parallel analyses, m_{cmb}^0 ($\Delta_g = 0$) and m_{cmb} ($\Delta_g \neq 0$) respectively, can be differenced to obtain the residuals map. This is then analyzed to compute the B-mode power spectrum due induced by the calibration uncertainty:

$$\Delta m = m_{cmb} - m_{cmb}^0 \Rightarrow \hat{C}_{\ell,\sigma}^{BB}[10]. \tag{3.18}$$

Finally, to define the tensor-to-scalar ratio bias, we apply the probability distribution function for a measured B-mode power spectrum $\hat{C}_\ell^{BB}$ and a given value of r [109, 110]:

$$-2\ln\mathcal{L}(\hat{C}_\ell^{BB}|r) = \frac{2\ell+1}{2} f_{sky}\left[\frac{\hat{C}_\ell^{BB}}{C_\ell^{BB}} + \ln C_\ell^{BB} - \frac{2\ell-1}{2\ell+1}\ln\hat{C}_\ell^{BB}\right]. \tag{3.19}$$

The measured signal $\hat{C}_\ell^{BB}$ is here equal to the residual BB power spectrum in Equation 3.18, while $C_\ell^{BB} = rC_\ell^{GW} + C_\ell^L + N_\ell^{BB} + C_{\ell,fg}^{BB}$ is the expected spectrum, where C_ℓ^{GW} is the primordial B-mode spectrum (computed for $r = 1$), C_ℓ^L is the lensing B-mode spectrum, N_ℓ^{BB} is the noise spectrum after component separation

---

[10] We mask the galactic plane during the analysis with Planck inherited 70% sky mask.

and $C_{\ell,fg}^{BB}$ is the residuals spectrum due to foreground components. The tensor-to-scalar ratio bias is found as the peak of:

$$\ln \mathcal{L}(r) = \sum_{\ell=2}^{\ell_{max}} \ln \mathcal{L}(\hat{C}_\ell^{BB}|r), \tag{3.20}$$

where $\ell_{max} = 200$ (assuming this as LiteBIRD ℓ-range). The tensor-to-scalar ratio bias value is defined as the r value corresponding to the maximum of the likelihood function. We can define a relation between the calibration uncertainty and the bias value on the recovered tensor-to-scalar ratio, δ_r vs. Δ_g (or Δ_γ).

3.2.3 Results

We divide the results into 3 subsections, following the steps described in Section 3.2.2.1.

3.2.3.1 Single frequency band analysis

As explained above, in this first part of the analysis, we propagate the photometric calibration error one frequency band per time and study the impact on the data after component separation. In Figure 3.2 we give an example of the analysis. In

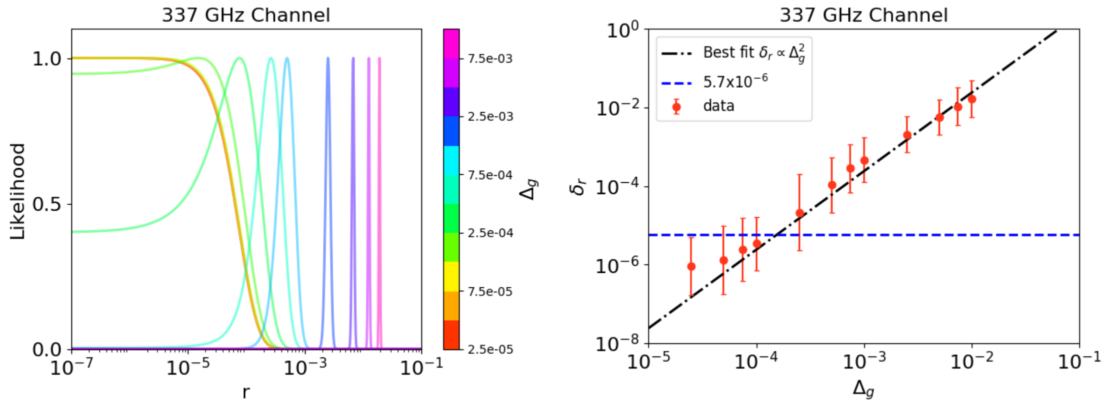

Figure 3.2: *Left:* Likelihood functions for different values of the Δ_g factor for one frequency band (337 GHz). *Right:* For each value of Δ_g we performed 100 simulations with different noise realizations, computed the tensor-to-scalar ratio likelihood for all of them, and calculated the mean δ_r values. Results are shown for 337 GHz band. We find that the mean δ_r scales with the square of Δ_g, as expected. The small departure from square-law for small Δ_g values is due to the finite grid step of the likelihood function calculation.

the *left* panel we show the likelihood functions from the residuals map as explained in Equation 3.19, for different values of Δ_g for the 337 GHz band.

For each band and for a given value of Δ_g, we perform 100 simulations varying the noise seed randomly and the effective Δ_g with a Gaussian distribution with mean value 0 and standard deviation equal to Δ_g, as explained in Section 3.2.2.1. We define the bias to the tensor-to-scalar ratio (δ_r) due to the calibration error as the r value corresponding to the peak of the likelihood function. For clarity we plot in the *left* panel of Figure 3.2 only one representative curve for each Δ_g value.

In the *right* panel of Figure 3.2, for the same frequency band, we computed the mean value of δ_r over all 100 realizations for each Δ_g value. We can easily observe a square-law relation between the computed δ_r and the input Δ_g value. This relation is due to the fact that Δ_g acts as a multiplicative factor on the polarization map. Therefore we expect the miscalibration to propagate to the

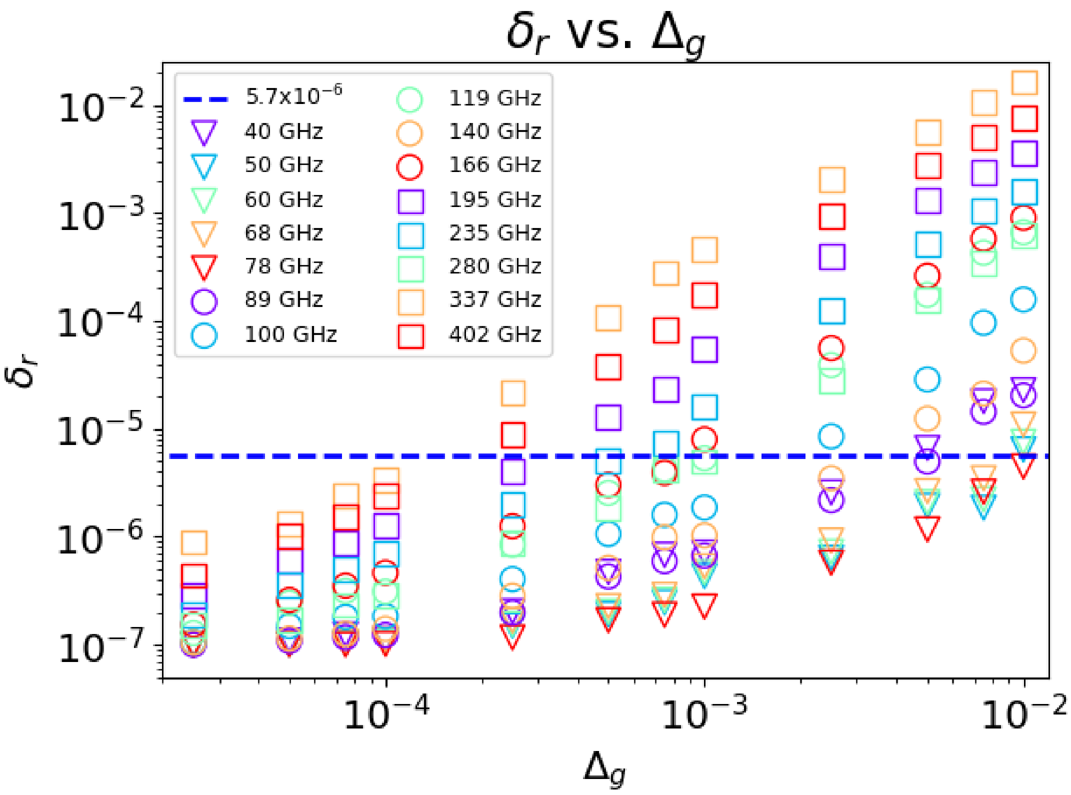

Figure 3.3: A summary of the first step of the analysis showing the δ_r vs. Δ_g relation for every LiteBIRD frequency band.

residual polarization map as:

$$[Q \pm iU](\theta, \phi) \propto \Delta_g \sum_{\ell,m} {}_{\pm 2}a_{\ell,m\pm 2}Y_{\ell,m}(\theta, \phi). \tag{3.21}$$

We can propagate to the spherical harmonic expansion coefficients of the residual B-mode map

$$a_{B,\ell m} \propto \Delta_g \frac{i}{2}({}_2a_{\ell,m} - {}_{-2}a_{\ell,m}), \tag{3.22}$$

and thus to the angular power spectrum is proportional to Δ_g^2:

$$C_\ell^{BB} \propto \sum_m a_{B,\ell m} a^*_{B,\ell m} \propto \Delta_g^2. \tag{3.23}$$

In Figure 3.3, we show a summary of the results of the analysis for every frequency band in Table 2.3. The relation $\delta_r \propto \Delta_g^2$ holds for every frequency band[11]. For a given Δ_g value, δ_r decreases going from low frequencies towards central frequencies and then it increases at higher frequencies. Our interpretation is that this is due to the relative amplitude of the Galactic foregrounds compared

Band (GHz)	$\Delta_{g,\gamma}$	$\delta_{g,\gamma}$
40	2.5×10^{-3}	2.0×10^{-2}
50	7.5×10^{-3}	6.0×10^{-2}
60	7.5×10^{-3}	6.0×10^{-2}
68	7.5×10^{-3}	10.8×10^{-2}
78	1.0×10^{-2}	14.4×10^{-2}
89	5.0×10^{-3}	7.2×10^{-2}
100	1.0×10^{-3}	2.3×10^{-2}
119	1.0×10^{-3}	2.5×10^{-2}
140	2.5×10^{-3}	5.7×10^{-2}
166	7.5×10^{-4}	1.6×10^{-2}
195	2.5×10^{-4}	0.6×10^{-2}
235	5.0×10^{-4}	0.8×10^{-2}
280	1.0×10^{-3}	1.6×10^{-2}
337	1.0×10^{-4}	0.16×10^{-2}
402	1.0×10^{-4}	0.18×10^{-2}

Table 3.1: A summary of the requirements in terms of the overall frequency bands ($\Delta_{g,\gamma}$), and per detector ($\delta_{g,\gamma}$) assuming the number of detectors in Table 2.3.

---

[11] The small deviation visible for small Δ_g values for some of the frequency channels is due to the finite resolution used in the likelihood calculation: $\Delta r = 10^{-7}$.

to CMB (Figure 1.3), which leads to higher residuals in the CMB map. We point specifically to the two highest frequency bands, 337 and 402 GHz, which clearly appear to drive the requirements.

3.2.3.2 Requirements

The goal of LiteBIRD, as for most next generation CMB experiments, is to measure the tensor-to-scalar ratio with high accuracy. In this work we assume $r = 0$, and a total target uncertainty $\sigma_r \leq 0.001$. In order to be successful the cumulative bias of all systematic effects has to be negligibly small.

Because it is reasonable to expect several systematic effects in a single experiment, we decide a threshold value $\delta_r \lesssim 5.7 \times 10^{-6}$ which is negligible compared to the target sensitivity. This value is marked with a blue dashed line in both Figure 3.2 and Figure 3.3. From the analysis summarized in Figure 3.3 we can define a requirement $\Delta^*_{g,i}$ for each frequency band that satisfies the condition we have defined above: $\delta_r(\Delta^*_{g,i}) \lesssim 5.7 \times 10^{-6}$. A summary of the requirements is given in Table 3.1. Using the number of detectors per band in Table 2.3 we also derive the requirement per detector $\delta^*_{g,i}$ from Equation 3.10. It is important to keep in mind that the detector requirements summarized in Table 3.1 are valid if the detector noise and calibration uncertainties are uncorrelated.

3.2.3.3 Combined analysis

In the final step of the analysis, we propagate the calibration errors in all 15 bands at the same time from the $\Delta^*_{g,i}$ values of Table 3.1. For a perfectly linear procedure and uncorrelated errors we would expect the cumulative mean bias to be equal to $\sqrt{15} \times 5.7 \times 10^{-6}$.

We perform 1000 simulations varying the random noise seed and the $\Delta^*_{g,i}$ realizations. A summary of the results is shown in Figure 3.4. The total tensor-to-scalar ratio bias $\delta_r^{\mathrm{COMB}} = 4.8 \times 10^{-5}$ (mean value over 1000 realizations in Figure 3.4) is higher than the threshold value defined in Section 3.2.3.2, but slightly in excess than the expected value for a perfect linear system. However, the parametric component separation step is a non-linear process.

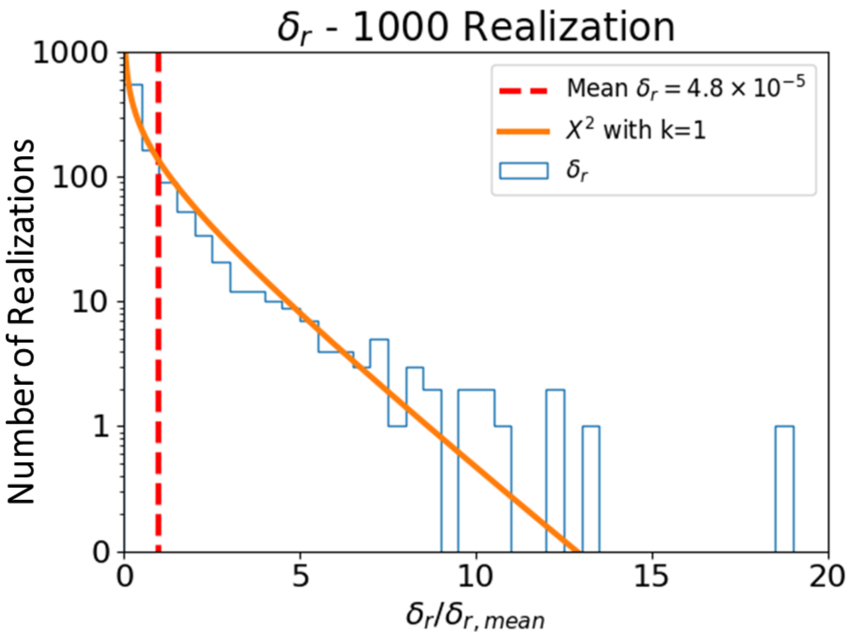

Figure 3.4: Summary of the 1000 simulations where we propagate the calibration error in all frequency bands at the same time using the values in Table 3.1. We compute the bias to the tensor-to-scalar ratio (as the r value corresponding to the peak of the likelihood function) for each of the 1000 simulations, and we plot the distribution in units of the mean value $\delta_{r,mean}$. The mean value (corresponding to 1 in these units) is shown as a vertical dashed *red* line. A χ^2-distribution with $k = 1$ degree of freedom is shown for comparison (the residuals amplitude).

In Figure 3.4, we show the distribution of the computed tensor-to-scalar ratio values for all 1000 simulations. The calibration factors are randomly selected from a normal distributions with standard deviations $\Delta^*_{g,i}$. For a perfectly linear component separation process, we would expect the amplitude of the residual maps to follow a normal distribution. Figure 3.5 shows the distributions of the 1000 g-factors used in the simulation and the distribution of the amplitude of the residuals in the CMB maps. Thus, from Equations 3.21, 3.22 and 3.23, we find that the δ_r distribution should follow a χ^2-distribution with 1 degree of freedom (the residuals amplitude). In Figure 3.4 we can observe a fairly good agreement between the data and the χ^2-distribution, apart for a small excess in the tail which is responsible for the excess in the computed mean value δ_r^{COMB}.

Table 3.1 summarize the calibration requirements for each frequency band. We carried out the same analysis for the colour correction factor $\gamma_{[s,d]}$. We found the

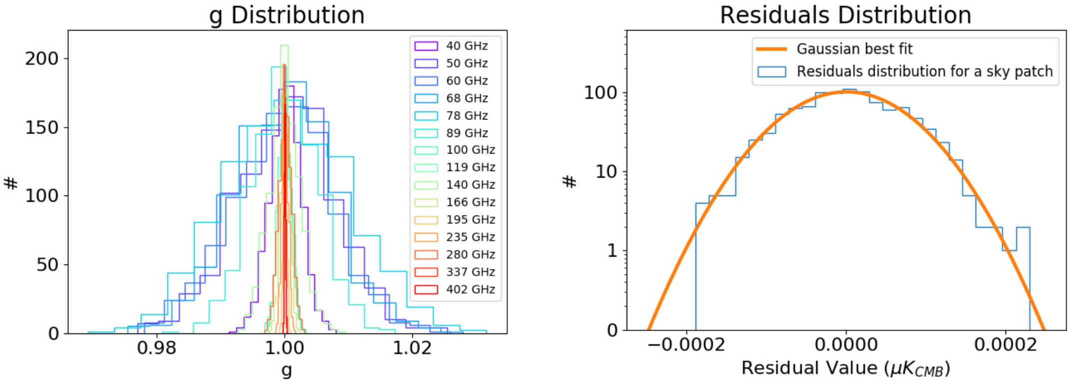

Figure 3.5: *Left:* Distribution of the g-factors used in the final steps of the analysis presented in this section. *Right:* Distribution of the mean Q residual value (similar distribution for U) over 1000 simulations in a sky patch. We perform a Gaussian fit of the data.

same requirements as for the photometric calibration factor g in Table 3.1, and thus we avoid reporting them separately.

3.2.4 Discussion of the results

From this analysis we find that the most sensitive band to calibration errors is 337 GHz. Therefore, we adopt the value at this frequency as the overall experiment requirement. In this way, the contribution from the other bands becomes negligible and we can achieve a total bias $\delta_r^{\mathrm{COMB}} \sim 5.7 \times 10^{-6}$.

It is worth mentioning that an increase of the number of detectors at high frequency allows to reduce the requirement on a single detector. However, this solution might be impractical due to cost issues, especially in the case of a space mission.

3.2.4.1 Band-pass

We use the results reported above to address the colour correction effect and define the required band-pass response resolution.

In Equation 3.7 we defined the colour correction factor for each Galactic foreground signals, and in Equation 3.8 we defined the error for the colour correction factor for a finite band-pass resolution. For a given finite resolution $\Delta\nu$ of the

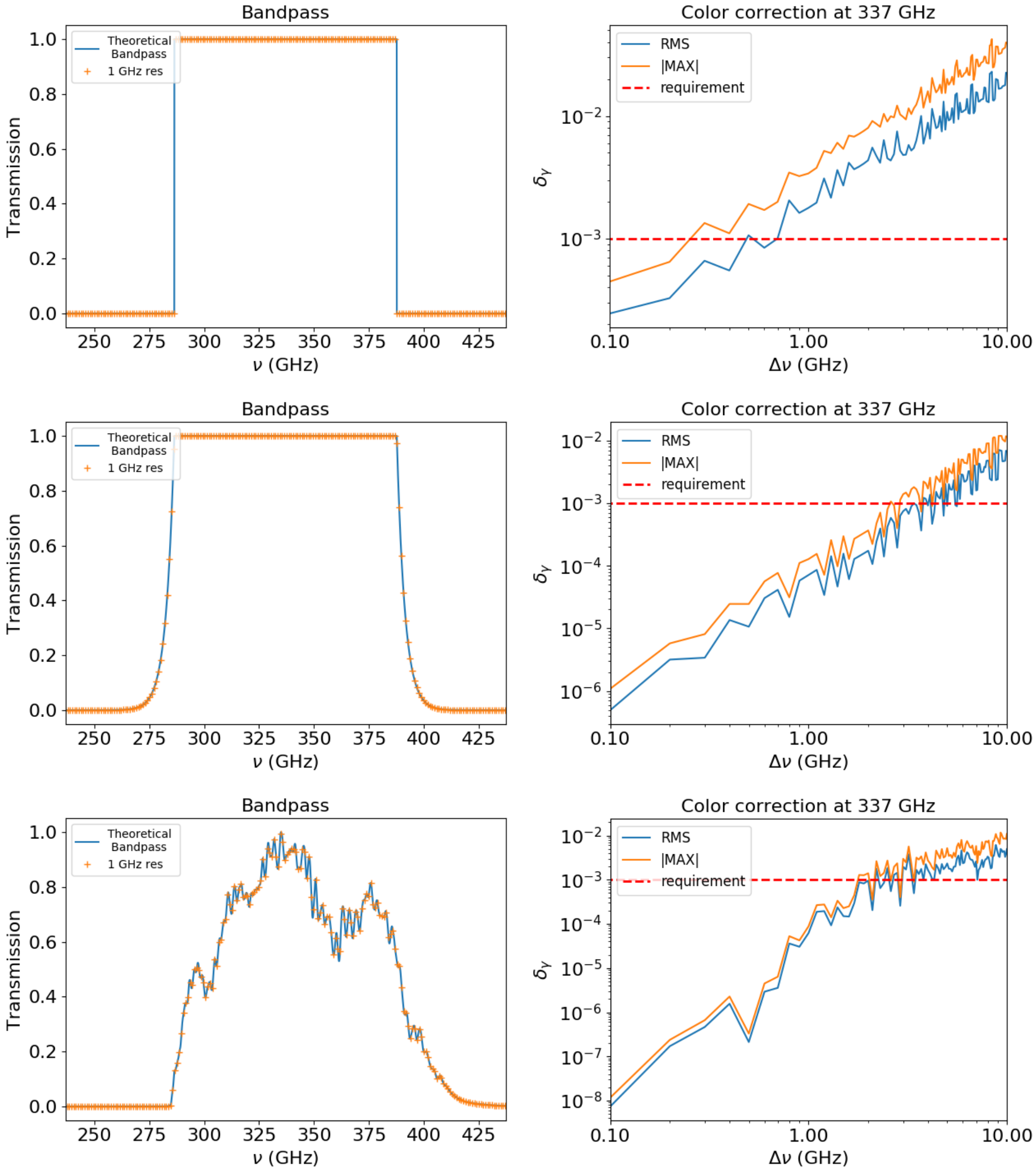

Figure 3.6: *Left:* In *blue* solid line examples of three theoretical band-pass responses at 337 GHz with 30% bandwidth are shown. From *top* to *bottom*, we show a perfect top-hat ideal band-pass response, a top-hat with a more realistic transitions at the edges, and finally, using publicly available Planck data we re-scaled one of the Planck 353 GHz band-pass responses to 337 GHz. A re-sampling process with 1 GHz resolution is also shown as a scattered plot. *Right:* Calculation of the colour correction error for dust (δ_γ^d) as a function of decreasing resolution for the band-pass response on the left. The *blue* solid line represents the *rms* value for 100 realizations of the re-sampling process with a given resolution, while the *orange* solid line represents the maximum value between 100 realizations. The requirement shown by the *red* dashed line.

band-pass response $G(\nu)$, Equation 3.7 can be re-written as:

$$\gamma_{d,s} = \left(\frac{\sum_i \Delta\nu G(\nu_i) \frac{I_{d,s}(\nu_i)}{I_{d,s}(\nu_0)}}{\sum_i \Delta\nu G(\nu_i) \frac{\partial B(\nu_i, T)}{\partial T}\Big|_{T_0}} \right) \frac{\partial B(\nu_0, T)}{\partial T}\Big|_{T_0}. \tag{3.24}$$

As already mentioned, similarly to what we have presented in Section 3.2.3 for the calibration factor g, we performed the analysis for the colour correction factors γ. We avoid reporting the full analysis here because the requirements found on γ are consistent with those reported for g above. This correspondence between the two results can be explained by noticing that the combined Galactic foreground components dominate the CMB B-mode signal at all frequencies. Therefore, since the cosmological signal is negligible compared to the foreground signal, the effect of g and γ becomes indistinguishable in Equation 3.9. From the δ_g (δ_γ) values reported in Table 3.1 we find the necessary band-pass resolution that minimizes the colour correction uncertainty and thus the recovered tensor-to-scalar ratio bias.

To better illustrate the procedure, we analyze band 337 GHz, which was found to be the most sensitive to calibration error in the previous sections. At this frequency the dominant sky component is thermal dust, therefore we limit the analysis to it. Comprehensive results for all bands and both Galactic emissions can be found at the end of the section (Figures 3.8, 3.9, 3.10, 3.11, 3.12 and 3.13). The required calibration accuracy for a single detector at 337 GHz is 0.16×10^{-2} (see Table 3.1), therefore we need to find a band-pass resolution ($\Delta\nu$) that satisfies this requirement.

In Figure 3.6, we test three situations to show how the shape of the band-pass response can influence the calculation of δ_γ. We create the three band-pass responses with very fine resolution ($\Delta\nu = 0.1$ MHz)[12]. We proceed by re-sampling the ideal response with lower resolution and calculate δ_γ for each new resolution step from Equation 3.8. In Figure 3.6 *top-left*, *center-left* and *bottom-left* the three ideal band-pass responses are plotted in *blue* solid line. To illustrate the process, one re-sampling (for each case) with 1 GHz resolution is shown in *orange* as an example .

---

[12] Current and past experiments have reported measuring the band-pass response with ~ 1 GHz resolution [111], and therefore a 0.1 MHz resolution is a good approximation for a nearly infinite resolution.

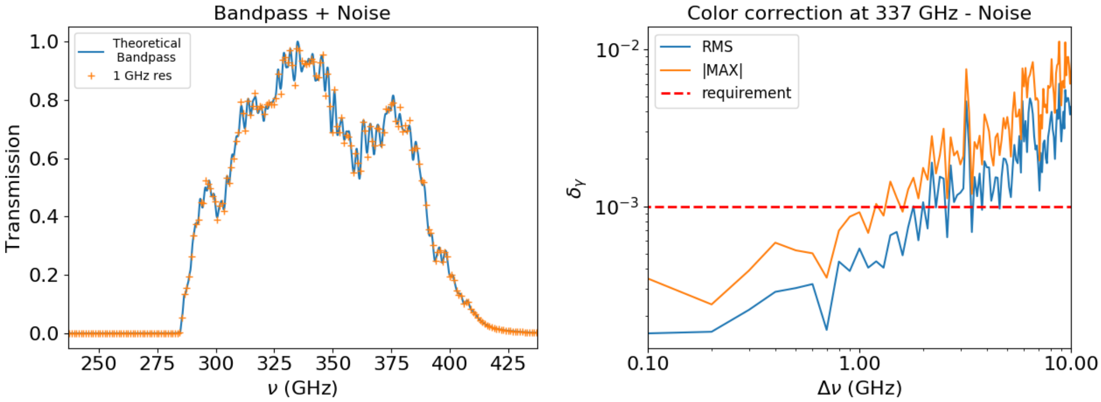

Figure 3.7: *Left:* In *blue* solid line a theoretical band-pass responses at 337 GHz with 30% bandwidth, simulated using publicly available Planck data is shown. We re-scaled one of the Planck 353 GHz band-pass responses to 337 GHz. A re-sampling process with 1 GHz resolution is also shown as a scattered plot. A white noise measurement component is simulated during the re-sampling process *Right:* Calculation of the colour correction error for dust (δ^d_γ) as a function of decreasing resolution for the band-pass response. The *blue* solid line represents the *rms* value for 100 realizations of the re-sampling process with a given resolution, while the *orange* solid line represents the maximum value between 100 realizations. The requirement is shown by the *red* dashed line. The statistical uncertainty boosts δ_γ especially for high resolution.

In the *top-left* panel of Figure 3.6 we show a top-hat band-pass. This case is characterized by a perfectly flat in-band response with sharp transitions at the edges of the in-band frequency range. This ideal band shape is never obtained in reality. Nevertheless, in the *top-right* panel of Figure 3.6 we show our calculation of the colour correction uncertainty for this case, to highlight that the sharp transitions at the edges of the band-pass response impact negatively the colour correction factor. A very fine resolution would be required to reduce the uncertainty.

A more realistic case is shown in Figure 3.6 *center-left*. We still have the flat response in-band, however we introduce smoother edge transitions to mimic a more realistic case. The choice of the steepness of the transitions is completely arbitrary and this example has been included to purely show the effect of smoother transitions compared to the ideal top-hat case. The *center-right* panel of Figure 3.6 clearly shows that the smoother transition helps reducing the uncertainty of the γ factor.

Lastly, we create a more realistic band-pass response from publicly available

Planck data at 353 GHz[13,14]. We shift and re-scale the data to match the 337 GHz central frequency expected for LiteBIRD, as shown in the *bottom-left* panel of Figure 3.6. As for the other two cases, Figure 3.6 *bottom-right* shows δ_γ as a function of the resolution. The original resolution of the data is ~ 2 GHz, therefore we have to perform an interpolation to simulate a fine resolution. Because of the original resolution there is a lack of information for resolutions finer than ~ 2 GHz. This is clear in Figure 3.6 *bottom*. The computed δ_γ shows a different behaviour below ~ 2 GHz, where it drops faster. From the top-hat result and this last case (Planck filter) we can determine that a resolution $0.2 \text{ GHz} \lesssim \Delta\nu \lesssim 2 \text{ GHz}$ is required to achieve an error lower than the threshold value, depending on the effective shape of the band-pass function.

This procedure can be followed for every other frequency band and for other Galactic foreground emission, as shown in Figures 3.8, 3.9, 3.10, 3.11, 3.12 and 3.13 at the end of this Section.

Band-pass resolution. As shown, the calculation of the colour correction depends on the effective shape of the band-pass response. Usually, the zeroth-order approximation for a band-pass response is a top-hat function at the nominal central frequency. This shape has a dramatic impact on the uncertainty of the colour correction factor, because of the steep edge transitions. A shallower transition helps reducing the error as shown in the second case of Figure 3.6. Another source of error can be fast fringes in the response, caused by standing waves (common in most measurement set-ups) between the optical elements of the telescope. Therefore, we recommend future experiments to carefully and realistically simulate the the spectral response of the system to fully understand the impact that this might have on calibration and the following observations.

So far we have not included statistical uncertainty and systematic effects within the set-up to measure the band-pass response. The first, depending on the noise level, can limit the high-resolution end of Figure 3.6 *right*. Therefore, for a given

---

[13] `https://wiki.cosmos.esa.int/planck-legacy-archive/`

[14] `https://pla.esac.esa.int/`

noise level we expect that increasing the resolution above a certain point will not help reducing the colour correction uncertainty as shown in Figure 3.7. Systematic effects in the set-up can create artificial features in the measured band-pass response.

In Figure 3.7 *left*, we report a case similar to 3.6 *bottom-left*, with the addition of a 2% white noise component to the data. This value is in line with the results reported by the POLARBEAR collaboration in [111]. In [111] a signal-to-noise ratio $S/N \sim 20$ has been reported, which would correspond to $\sim 5\%$ noise level. However, the authors break down the uncertainty into a statistical component and systematic component, and they identify the former to be $\sim 2\%$ in the worst case reported. Since we consider here only a statistical component we decided to use the $\sim 2\%$ value. By comparing Figures 3.6 *bottom-right* and 3.7 *right*, we clearly see a deterioration of the colour correction factor uncertainty in the fine resolution region in presence of statistical uncertainty.

Calibration. We have assumed that a space mission will make use of the dipole signal as the primary photometric calibrator for every frequency band. The dipole is the most accurate known photometric calibrator for a CMB space-borne mission because it is well-characterized. Other possible calibrators, like planets (or an artificial calibrator, see [112]), present higher uncertainties and therefore the calibration accuracy might suffer from such a choice. In addition, when using non-extended sources, like planets, the calibration is more sensitive to beam uncertainties (far-side lobes, etc.).

If a different calibrator will be used for some of the analysis, Equation 3.6 needs to be adapted to the calibrator spectrum, which may be different compared to the CMB and dipole signals (planets are "dusty" sources, therefore a grey-body spectrum has to be assumed). In this situation a different colour correction scheme has to be taken into account.

Sky model. We have assumed a fairly simple sky model with only two Galactic components, with uniform spectral parameters. A more complex sky is likely going to induce higher residuals due to the sky complexity, making more complicated to distinguish between the residuals intrinsic to the component separation method, and those due to the systematic effect under study [108]. At present we can not exclude that assuming a more complex sky model (e.g. with multiple dust populations) with more free parameters, might have the effect of absorbing more efficiently the calibration errors, resulting in a relaxation of the requirements.

Uncorrelated noise. We have assumed uncorrelated uncertainties among detectors. The assumption of uncorrelated detector noise is justified by the fact that if we consider correlations among detectors, the sensitivity per band in Table 2.3 needs to be recomputed according to the level of correlation expected. In which case this analysis has to be repeated for the new sensitivity details. Some techniques have been developed in the past to mitigate the presence of correlated noise [113, 114]. Even in the presence of correlated noise among detectors, we do not have evidence at present of the possible presence of correlations in the bandpass uncertainty which justify the use of Equation 3.10 to re-scale the uncertainty. This assumption has to be reconsidered if and when we will have evidence of the contrary.

1/f noise. 1/f noise is certainly one of the challenges for LiteBIRD or any other next-generation CMB surveys (especially for low ℓ measurements). A HWP rotating at ~ 1 Hz shifts the polarized cosmological signal to a higher frequency ~ 4 Hz, where the noise level is expected to be uncontaminated by the 1/f component. Details of the 1/f mitigation using a continuously rotating HWP has been discussed in Chapter 2. LiteBIRD will make use of a rotating HWP to mitigate the 1/f component, therefore for now we have not considered the effected of 1/f noise. However, in future we will carefully study the origin and magnitude of the 1/f component and its possible impact on the data. The work reported in Chapter 4 can be useful in this context.

3.2.4.2 Conclusion of this work

The method presented can be used to address the impact of photometric calibration uncertainty in the presence of Galactic foregrounds. We applied this method to derive requirements for the calibration accuracy to minimize the effect on the data. From plausible instrument parameters (baseline design of the LiteBIRD satellite), we have simulated the effect of an imperfect calibration, and showed that for the configuration in Table 2.3 the requirements per frequency band are $\Delta_{g,\gamma} \sim 10^{-4} - 2.5 \times 10^{-3}$. These translate to single-detector requirements as: $\delta_{g,\gamma} \sim 0.18 \times 10^{-2} - 2.0 \times 10^{-2}$. We have found that the high-frequency bands (specifically 337 and 402 GHz) are the most sensitive to calibration uncertainty (δ_g). After modelling the effect of a finite band-pass resolution, we have derived resolution requirements that minimize the effect of a limited band-pass knowledge. From representative examples of the band-pass response we found $\Delta\nu \sim 0.2 - 2$ GHz, depending on the band-pass shape assumed. Although the Planck-like band-pass is the most representative of a real scenario, the derived requirement of $\Delta\nu \sim 2$ GHz might suffer from the resolution of the original data. However, given the unrealistic edge transitions sharpness of the top-hat case, we can assume the 0.2 GHz resolution requirement as a conservative worst-case scenario.

For completeness, in Figures 3.8, 3.9, 3.10, 3.11, 3.12 and 3.13 we show the results for all frequency bands for the 3 bandpass template shown in Figure 3.6 for noiseless measurement and 2% noise level. In each plot we show the requirement coming from band 337 GHz and the relevant band as per Table 3.1.

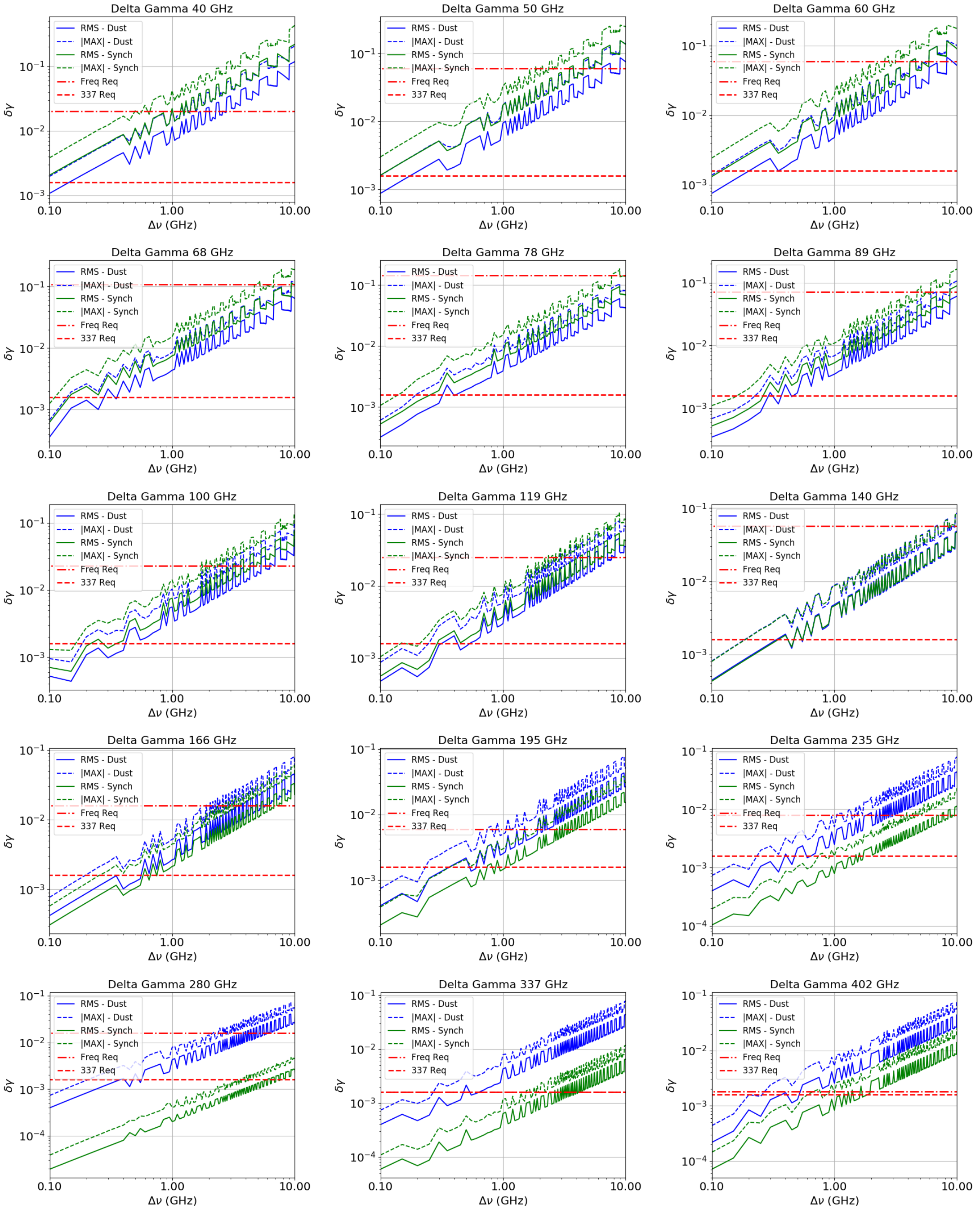

Figure 3.8: $\delta\gamma$ vs. sampling for all bands assuming a top-hat bandpass and noiseless data for dust in blue and synchrotron in green.

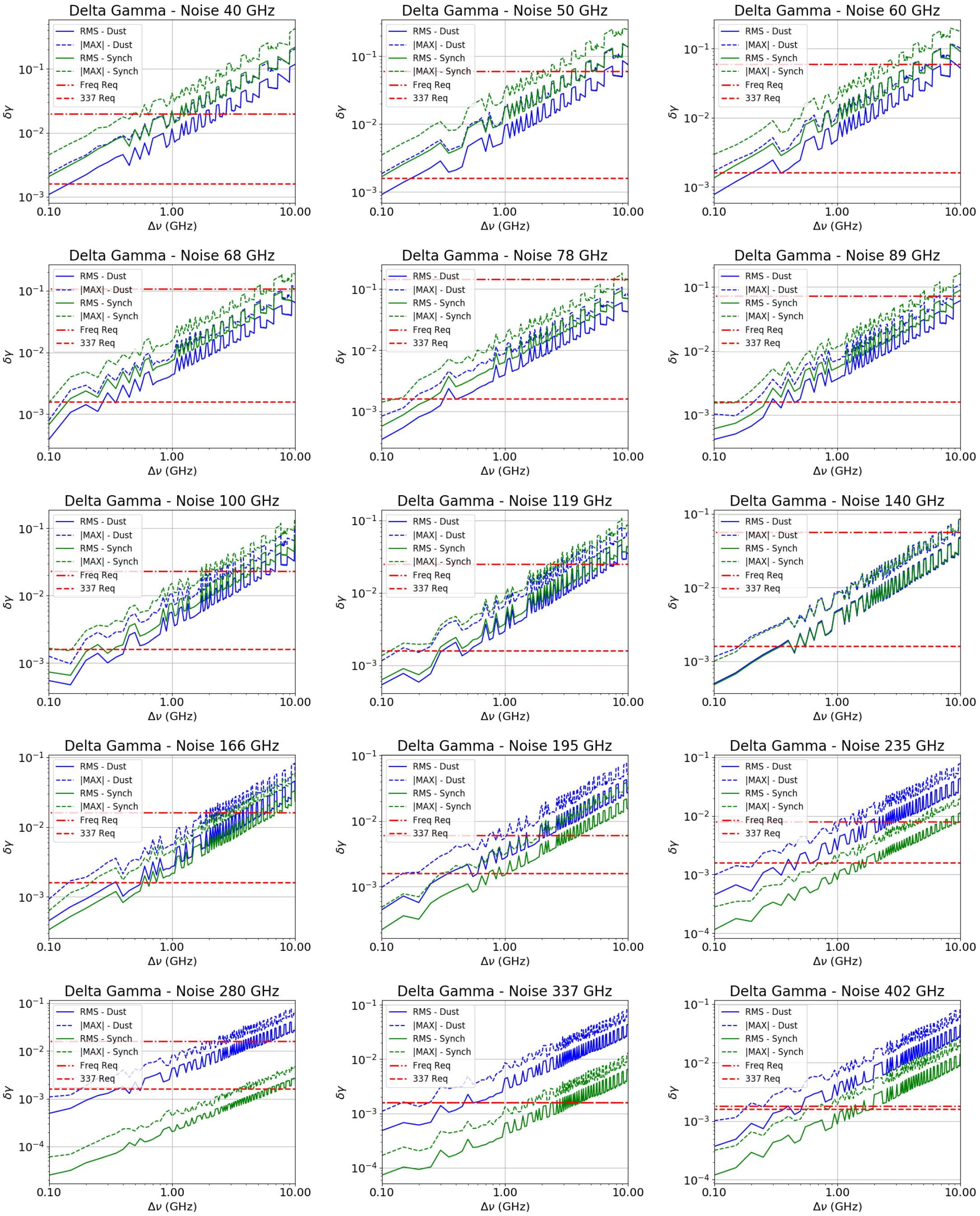

Figure 3.9: $\delta\gamma$ vs. sampling for all bands assuming a top-hat bandpass including 2% noise for dust in blue and synchrotron in green.

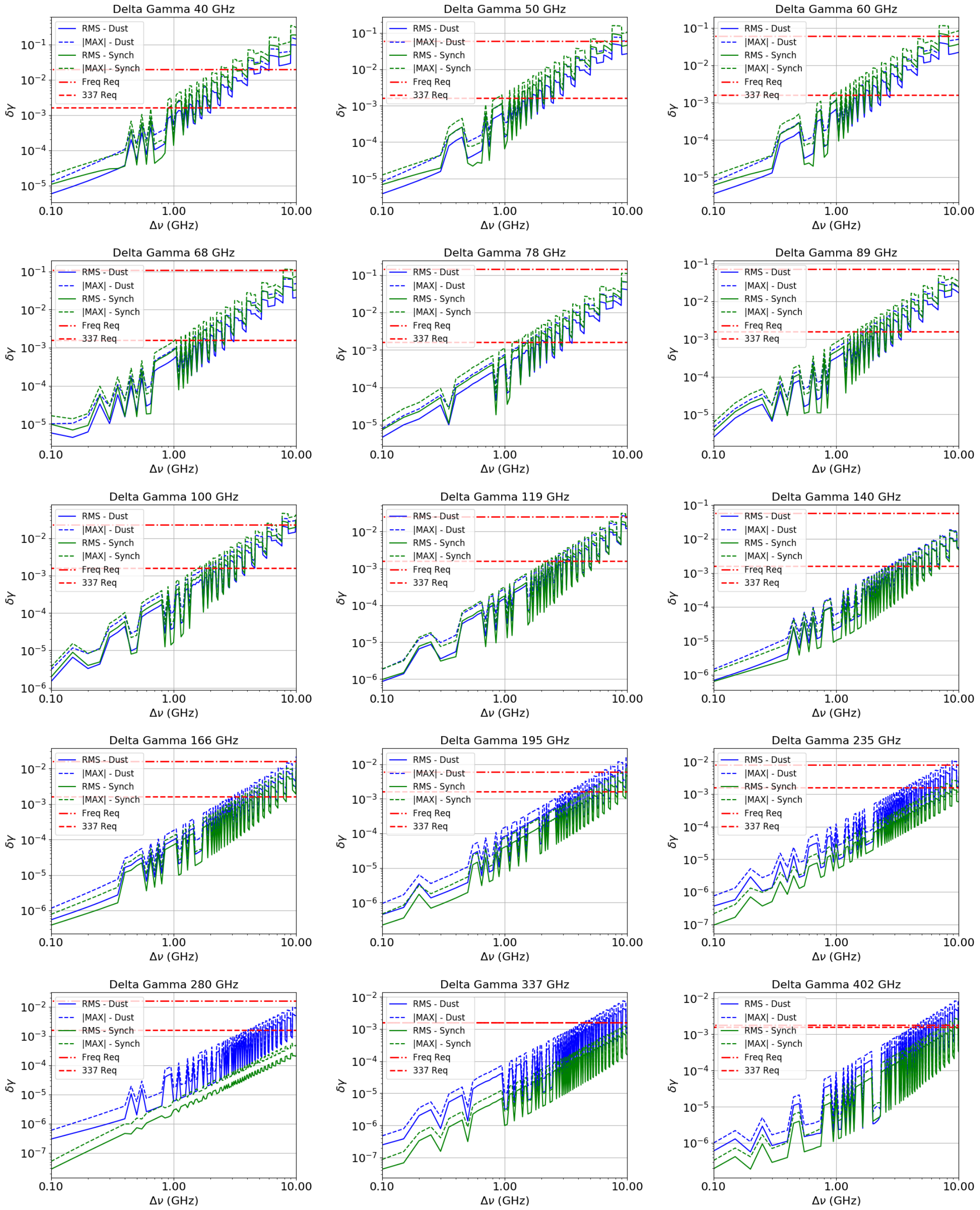

Figure 3.10: $\delta\gamma$ vs. sampling for all bands assuming a top-hat bandpass with smoothed transitions and noiseless data for dust in blue and synchrotron in green.

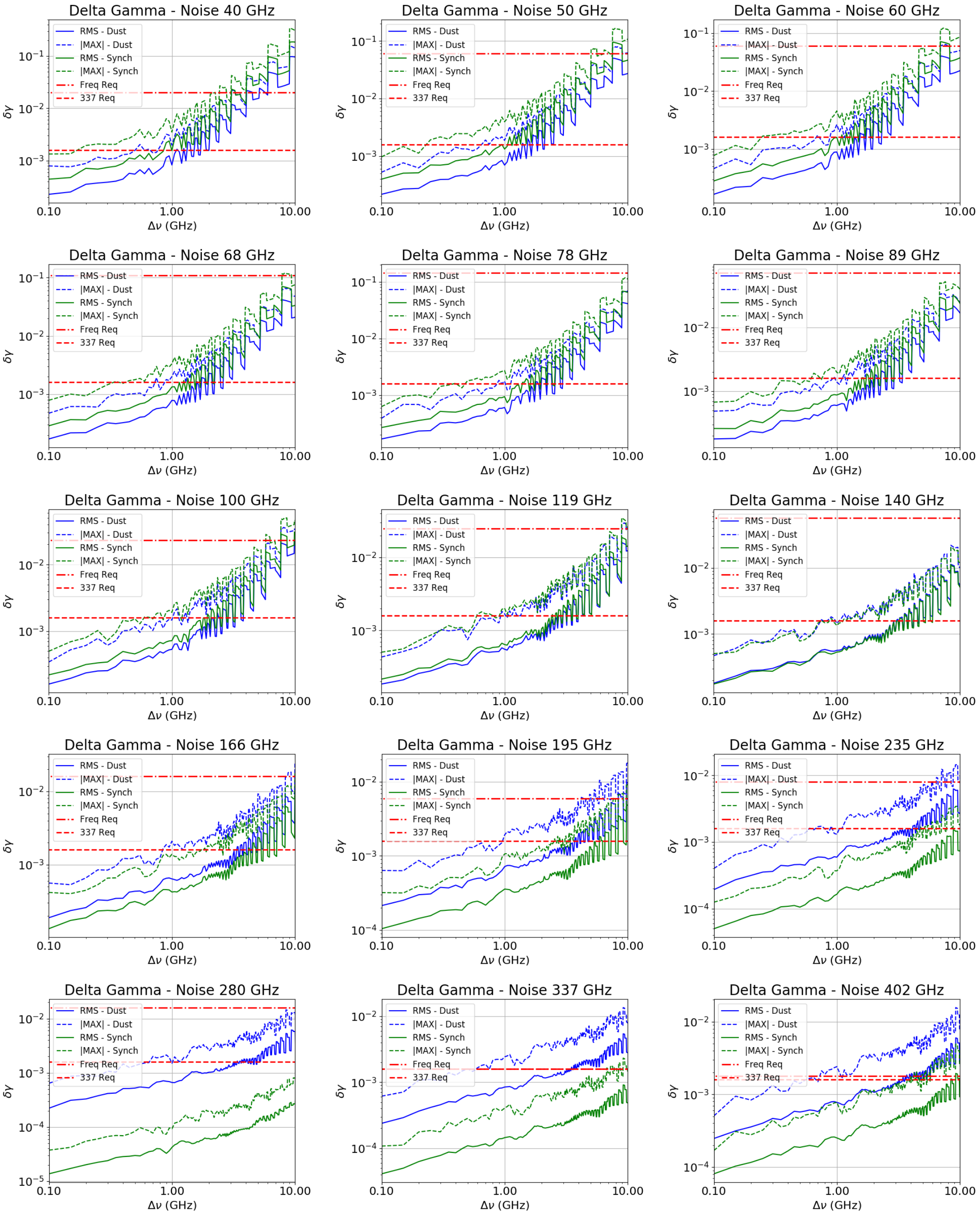

Figure 3.11: $\delta\gamma$ vs. sampling for all bands assuming a top-hat bandpass with smoothed transitions including 2% noise for dust in blue and synchrotron in green.

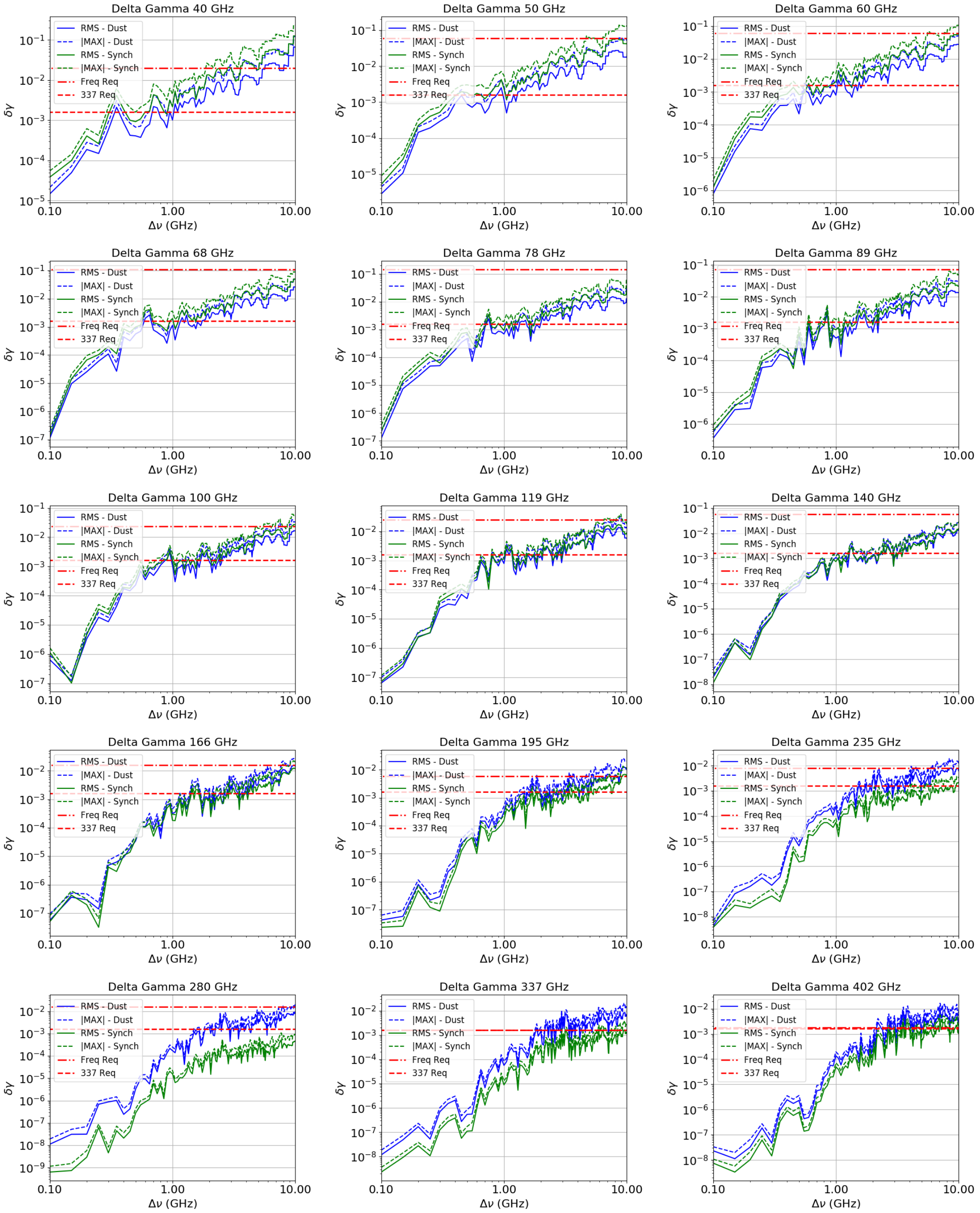

Figure 3.12: $\delta\gamma$ vs. sampling for all bands assuming the rescaled Planck bandpass and noiseless data for dust in blue and synchrotron in green.

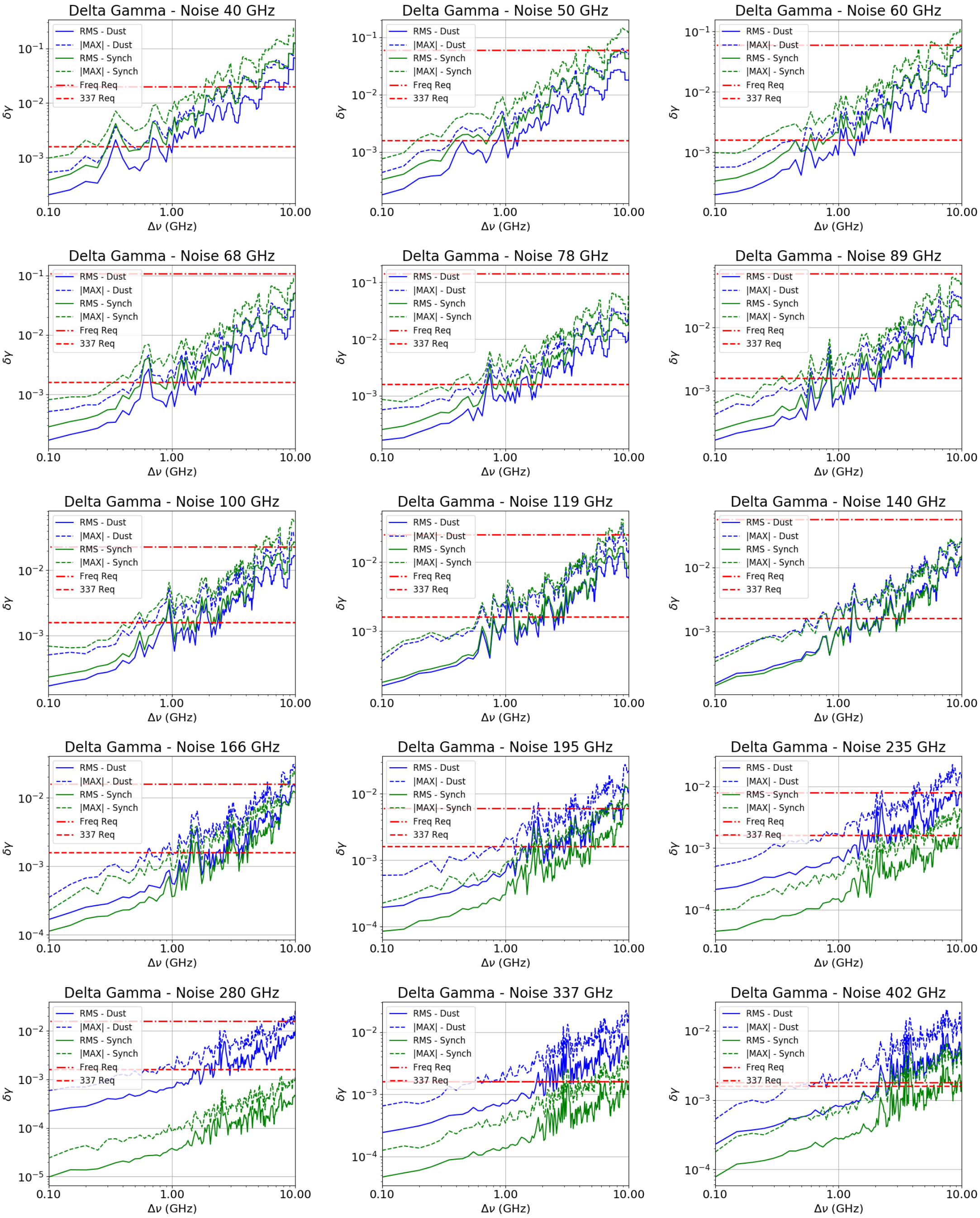

Figure 3.13: $\delta\gamma$ vs. sampling for all bands assuming the rescaled Planck bandpass including 2% noise for dust in blue and synchrotron in green.

3.3 Carbon monoxide emission lines

In this section we analyse the effect of carbon monoxide (CO) line emission on CMB data. Especially we focus on studying the need for notch filters to remove contaminated frequencies from the data. We analyse the most common CO species ^{12}CO, which in the LiteBIRD case presents 3 relevant emission lines [115]: CO J 1 $\rightarrow$ 0 at $\sim$ 115 GHz, CO J 2 $\rightarrow$ 1 at $\sim$ 230 GHz and CO J 3 $\rightarrow$ 2 at $\sim$ 345 GHz. However, a second less abundant species ^{13}CO can show relatively strong emission at $\sim$ 110, $\sim$ 220, $\sim$ 330 GHz. Given the line positions, the frequency bands impacted will be 119, 235 and 337 GHz. However, due to possible blue or red leakage in neighbouring bands, we also analyze the impact on 100, 140, 195, 280, 402 GHz bands.

3.3.1 Formalism

We adopted the formalism described in [82] to create total intensity to polarization leakage maps, adapting it to the case of CO intrinsic polarization as well. CO total intensity templates are taken from the Planck products (see Figure 1.5), while intrinsic polarization maps have been generated by Giuseppe Puglisi according to [101], assuming a 1% upper level limit on the intrinsic polarization compared to total intensity. The analysis procedure follows the procedure described in the

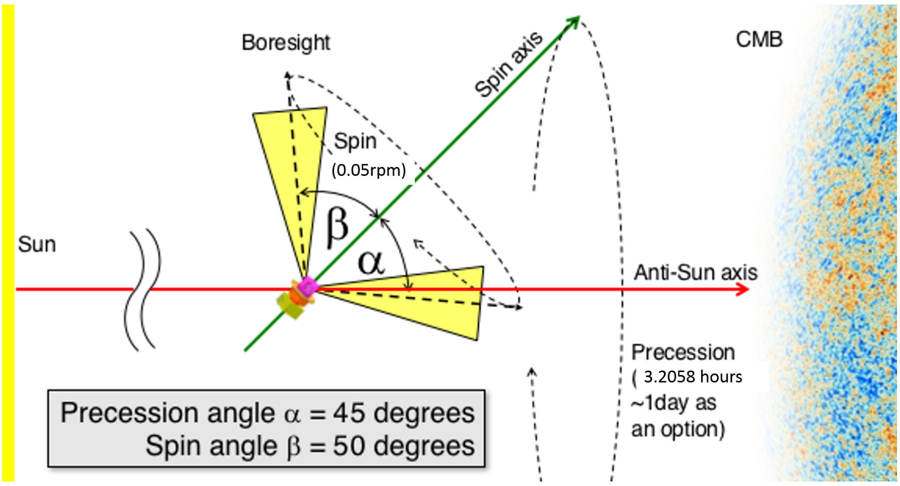

Figure 3.14: LiteBIRD observation strategy. For the HWP rotation we assumed only LFT revolution rate = 46 rpm for simplicity.

previous section. After simulating sky maps including CMB, dust, synchrotron and varying level of leakage of CO total intensity (or contamination from CO intrinsic polarization) we pass them through a component separation procedure (*FgBuster*) and finally compute the estimated bias on r due to the presence of residual CO signal. As in the previous Section, we model the sky as the sum of CMB, dust and synchrotron. We expect that the excess due to the presence of unaccounted CO signal will result in boosted residuals after component separation.

The first step of the analysis consists in creating the cross-linking maps from the scanning strategy parameters to analytically simulate the CO contamination. Although LiteBIRD will employ a rotating HWP to modulate the signal, we study also the case without rotating HWP in case the observation strategy will change or to account for the failure of the polarization modulator unit. In Table 3.2 we give a summary of the cases we have studied. Details about the hit map and cross-linking maps generation are in Appendix D.

Ultimately we aim at determining whether the use of notch-filters to remove CO-contaminated frequencies is necessary and/or beneficial to the LiteBIRD mission.

3.3.1.1 Map making without HWP

In the absence of a polarization modulator, the most common procedure to reconstruct the polarized signal consists in computing the difference between two orthogonal polarization-sensitive detectors. For each detector pair (detectors a and b) we can write the single sky pixel signal averaged ($\langle ... \rangle$) over the full duration of the observation as:

$$\begin{aligned} d_a &= I + Q\langle \cos 2\psi_a \rangle + U\langle \sin 2\psi_a \rangle && (3.25) \\ d_b &= I + Q\langle \cos 2\psi_b \rangle + U\langle \sin 2\psi_b \rangle, && (3.26) \end{aligned}$$

where ψ is the orientation of the polarization-sensitive detector projected on the sky as usual. Since the two detectors are orthogonal $\psi_a = \psi_b + \pi/2$, and we can write:

$$\Delta d = \frac{1}{2}(d_a - d_b) = Q\langle \cos 2\psi_a \rangle + U\langle \sin 2\psi_a \rangle + S, \qquad (3.27)$$

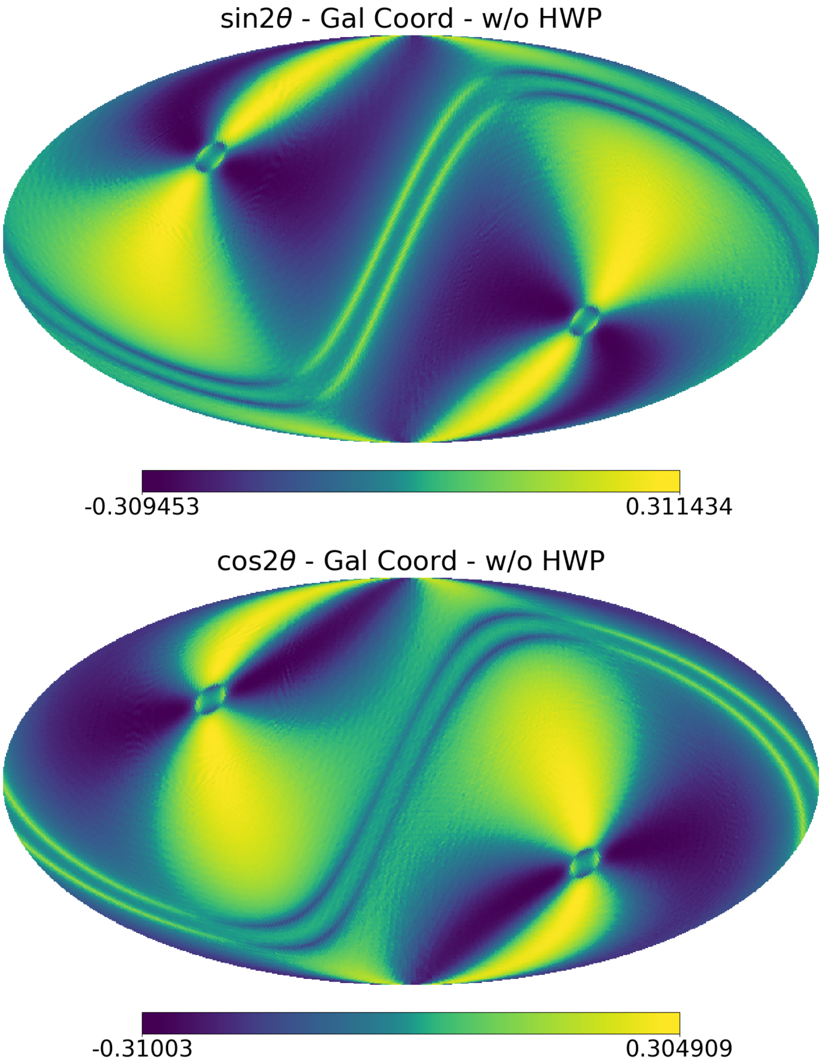

Figure 3.15: Cross link $\sin 2\psi$ (*top*) and $\cos 2\psi$ (*bottom*) maps in Galactic coordinates for 3 years of observation for a boresight detector without HWP. Details about the map generation can be found in Appendix D.

where S represents a possible mismatch between the 2 detectors. If the noise covariance matrix is diagonal, the sky signal can be reconstructed as:

$$\begin{pmatrix} S \\ Q \\ U \end{pmatrix} = \begin{pmatrix} 1 & \langle \cos 2\psi \rangle & \langle \sin 2\psi \rangle \\ \langle \cos 2\psi \rangle & \langle \cos^2 2\psi \rangle & \langle \sin 2\psi \rangle \langle \cos 2\psi \rangle \\ \langle \sin 2\psi \rangle & \langle \sin 2\psi \rangle \langle \cos 2\psi \rangle & \langle \sin^2 2\psi \rangle \end{pmatrix}^{-1} \begin{pmatrix} \Delta d \\ \Delta d \langle \cos 2\psi \rangle \\ \Delta d \langle \sin 2\psi \rangle \end{pmatrix} \quad (3.28)$$

We make use of Equation 3.28 to simulate the reconstructed Q and U maps, including the effect of the scanning strategy by generating template maps of the cross-linking parameters that appear in the matrix on the right hand side of the equation from the scanning parameters in Figure 3.14.

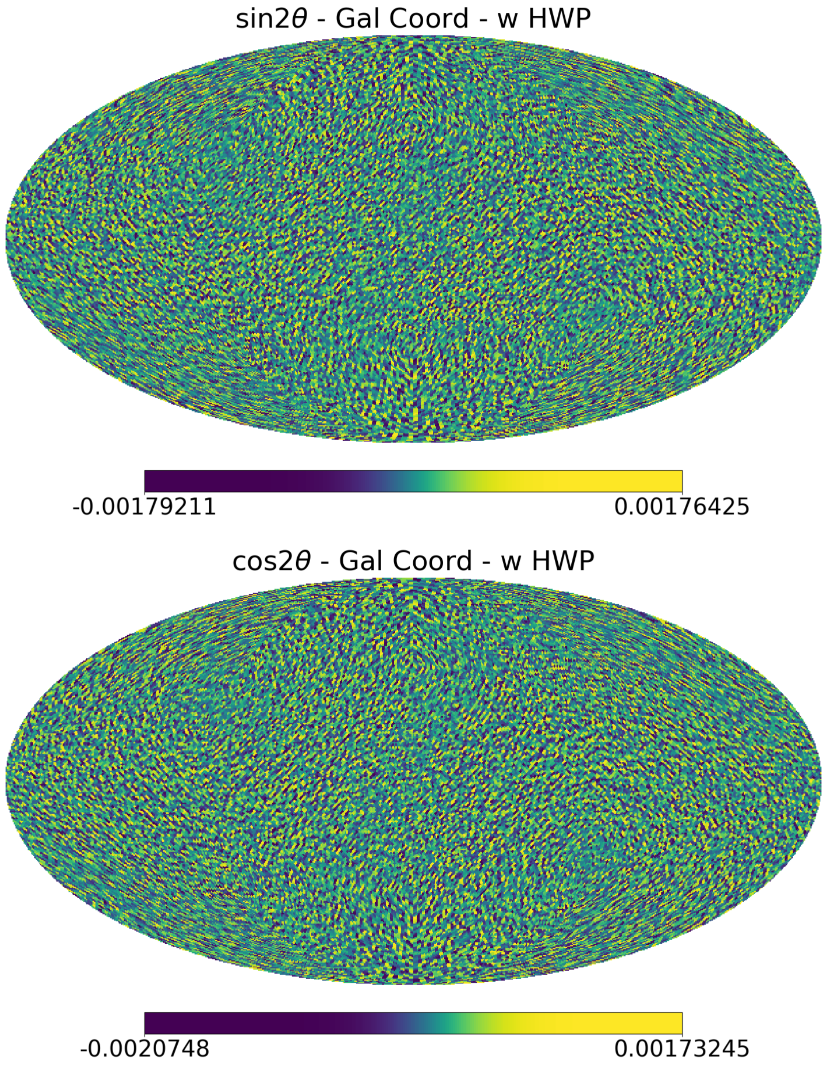

Figure 3.16: Cross link $\sin(4\rho - 2\psi)$ (*top*) and $\cos(4\rho - 2\psi)$ (*bottom*) maps in Galactic coordinates for 3 years of observation for a boresight detector with rotating HWP. Details about the map generation can be found in Appendix D.

In Figure 3.15 we show the $\cos 2\psi$ and $\sin 2\psi$ maps averaged over three years of observations for the LiteBIRD scan parameters in Figure 3.14.

3.3.1.2 Map making with HWP

For each detector we can write a single sky pixel signal averaged ($\langle ... \rangle$) over the full mission as:

$$d = I + Q\langle\cos(4\rho - 2\psi)\rangle + U\langle\sin(4\rho - 2\psi)\rangle, \tag{3.29}$$

where ψ is the orientation of the polarization-sensitive detector projected on the sky

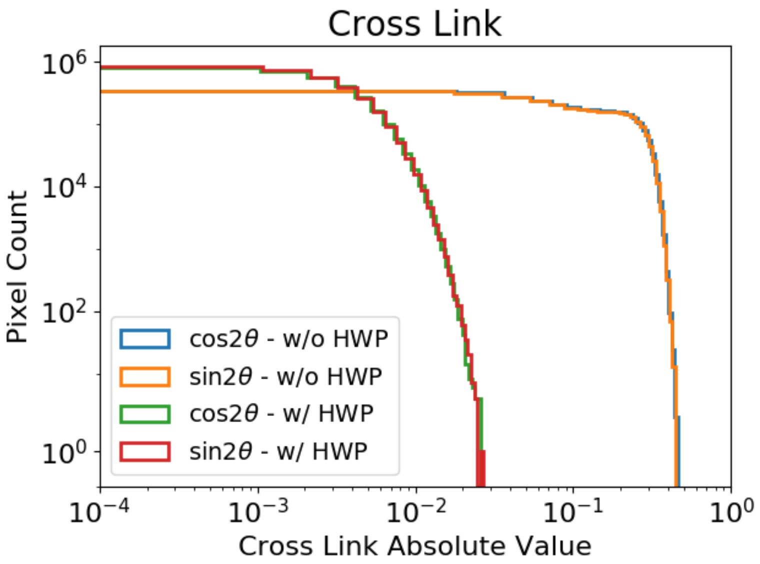

Figure 3.17: Histogram plot of the spin-2 cross-linking value (absolute) from Figures 3.15 and 3.16 for a nside=512 map.

and ρ is the HWP angle.[15] The polarized signal is modulated by the rotation of the HWP, and we can demodulate the signal as (for compactness we redefine $\theta = 2\rho - \psi$):

$$\begin{cases} d = I + Q\langle\cos 2\theta\rangle + U\langle\sin 2\theta\rangle \\ d\langle\cos 2\theta\rangle = I\langle\cos 2\theta\rangle + Q\langle\cos^2 2\theta\rangle + U\langle\sin 2\theta\rangle\langle\cos 2\theta\rangle \\ d\langle\sin 2\theta\rangle = I\langle\sin 2\theta\rangle + Q\langle\sin 2\theta\rangle\langle\cos 2\theta\rangle + U\langle\sin^2 2\theta\rangle \end{cases} \tag{3.30}$$

If the noise covariance matrix is diagonal, the sky signal can be reconstructed as:

$$\begin{pmatrix} I \\ Q \\ U \end{pmatrix} = \begin{pmatrix} 1 & \langle\cos 2\theta\rangle & \langle\sin 2\theta\rangle \\ \langle\cos 2\theta\rangle & \langle\cos^2 2\theta\rangle & \langle\sin 2\theta\rangle\langle\cos 2\theta\rangle \\ \langle\sin 2\theta\rangle & \langle\sin 2\theta\rangle\langle\cos 2\theta\rangle & \langle\sin^2 2\theta\rangle \end{pmatrix}^{-1} \begin{pmatrix} d \\ d\langle\cos 2\theta\rangle \\ d\langle\sin 2\theta\rangle \end{pmatrix} \tag{3.31}$$

In both cases for an optimized scanning strategy we expect the cross-linking matrix to reduce to:

$$\begin{pmatrix} 1 & 0 & 0 \\ 0 & 1/2 & 0 \\ 0 & 0 & 1/2 \end{pmatrix}^{-1} . \tag{3.32}$$

However, we expect residuals from the non-diagonal terms as can be seen from Figure 3.15 for the LiteBIRD scanning strategy without HWP and Figure 3.16 for

---

[15] We assume an ideal frequency-independent HWP phase ϕ.

CO	w/o HWP	w/ HWP
I	I to P caused by band-pass mismatch and cross-linking.	No band-pass mismatch, and improved cross-linking.
P	Same effect in first approximation in both cases.	

Table 3.2: Summary of the three cases studied in this Section. We aim at determining the level of contamination due to CO after foreground cleaning when CO is not modelled in the cleaning procedure. Although LiteBIRD will employ rotating HWPs, we study also a case where we assume the same scanning strategy but no rotating HWP to compare the effect. Total intensity can leak to polarization maps due to band-pass mismatch when a HWP is not employed. A rotating HWP mitigates this effect in two ways: by removing the detector pair differencing and improving the cross-linking.

the LiteBIRD scanning strategy with HWP. From Equations 3.28 and 3.31, we find that the components $\langle\cos 2\theta\rangle$ and $\langle\sin 2\theta\rangle$ drive the total intensity to polarization leakage. In the case of observation without a rotating HWP, bandpass mismatch couples to the I to P leakage because of the detector pair-differencing.

3.3.2 Total Intensity to Polarization Leakage

When we do not make use of a rotating HWP, if the bandpass response of the two orthogonal detectors is perfectly matched, the total intensity to polarization leakage vanishes. However, if the bandpass response $G(\nu)$ of the two detectors presents different transmission levels at frequency ν_{CO} (frequency of the CO emission line), Equation 3.27 can be rewritten as:

$$\Delta d = Q\langle\cos 2\theta\rangle + U\langle\sin 2\theta\rangle + \frac{1}{2}I_{CO}\delta, \tag{3.33}$$

where $\delta = G_a(\nu_{CO}) - G_b(\nu_{CO})$. The CO total intensity to polarization leakage becomes:

$$\begin{pmatrix} Q \\ U \end{pmatrix}_{CO-leak} = I_{CO}\delta \begin{pmatrix} \langle\cos 2\theta\rangle \\ \langle\sin 2\theta\rangle \end{pmatrix}. \tag{3.34}$$

In a similar way we can define the case employing a rotating HWP, where now we have to replace the mismatch δ with the bandpass transmission at the CO line frequency $G(\nu_{CO})$.

To simulate the overall leakage per band we assume that the bandpass transmissions are randomly distributed around a mean value. Therefore the total leakage

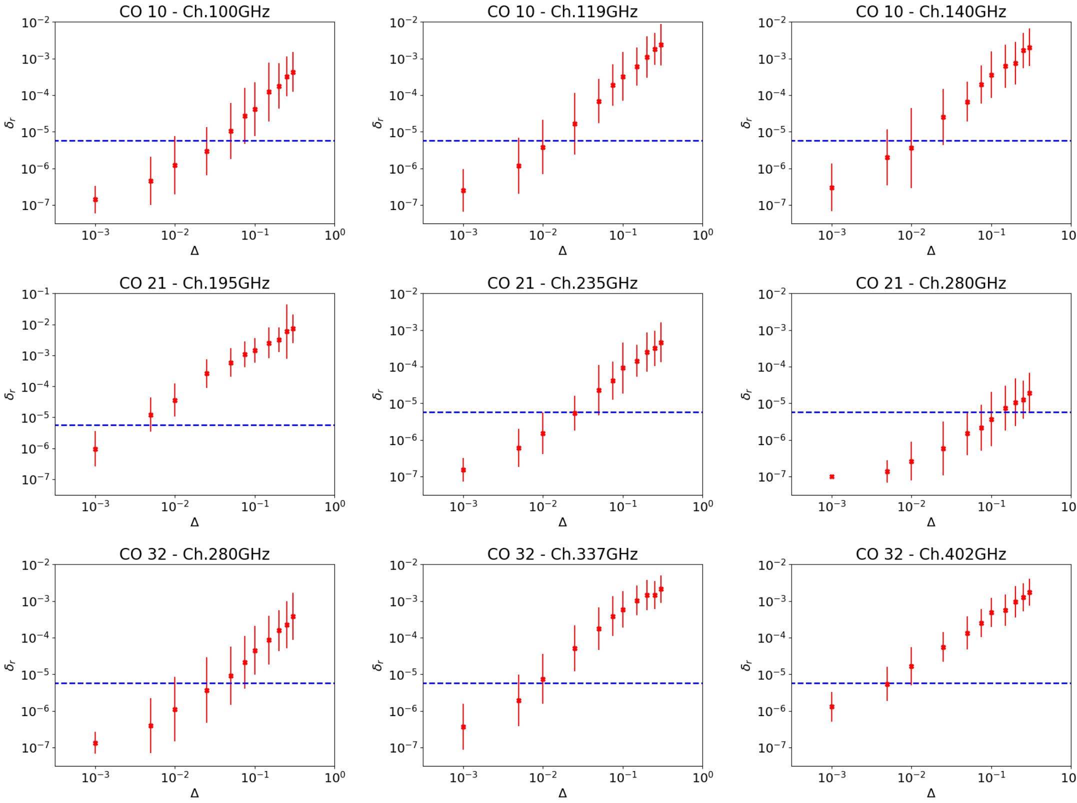

Figure 3.18: CO total intensity to polarization leakage in the case of observation without a rotating HWP.

can be computed from the total number of detectors N in the given band:

$$\Delta = \frac{\delta}{\sqrt{N}}. \tag{3.35}$$

In order to study the impact of CO leakage on the data, we generate polarization sky maps including CMB, dust, synchrotron and noise (as in the previous Section) plus CO I to P leakage using Equations 3.34 and 3.27 (for Δ values between 0.1% and 25%). As in the previous Section we determine the residual after component separation and compute the tensor-to-scalar ratio for each Δ value.

3.3.2.1 Case 1: I to P leakage without HWP

Figure 3.18 shows all bands studied assuming the LiteBIRD scanning strategy without rotating HWP. We can see that for most cases the tolerable leakage uncertainty per band is $\lesssim 1\%$ to obtain a tensor-to-scalar bias lower than the requirement ($\delta_r \leq 5.7 \times 10^{-6}$) as assumed in the previous Section.

From the number of detector per band N, we can convert to the tolerable leakage per detector by multiplying by $\sqrt{N}$. Of all bands considered the lowest number of detectors are in bands 280 and 337 GHz, each with 254 detectors. The conversion factor for these bands is $\sqrt{254} \sim 15$. Therefore, an uncertainty in the transmission level of $\sim 15\%$ can be tolerated if the uncertainty is not correlated between detectors.

3.3.2.2 Case 2: I to P leakage with HWP

Figure 3.19 shows all bands studied for LiteBIRD scanning strategy with a rotating HWP. We can see that for all cases the leakage (up to 100%) does not cause any detectable bias to the tensor-to-scalar ratio.

This part of the study highlights that an ideal HWP mitigates efficiently the I to P leakage effect. Similar results have been shown in [82] considering dust leakage.

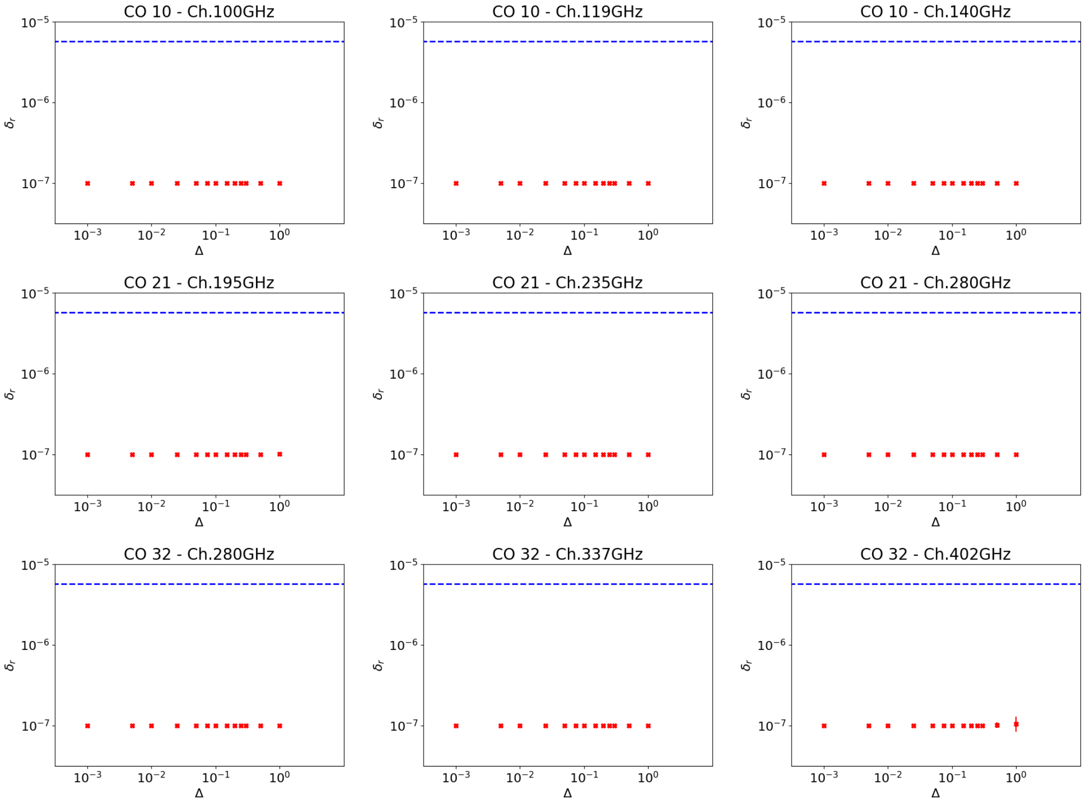

Figure 3.19: CO total intensity to polarization leakage in the case of observation with a rotating HWP.

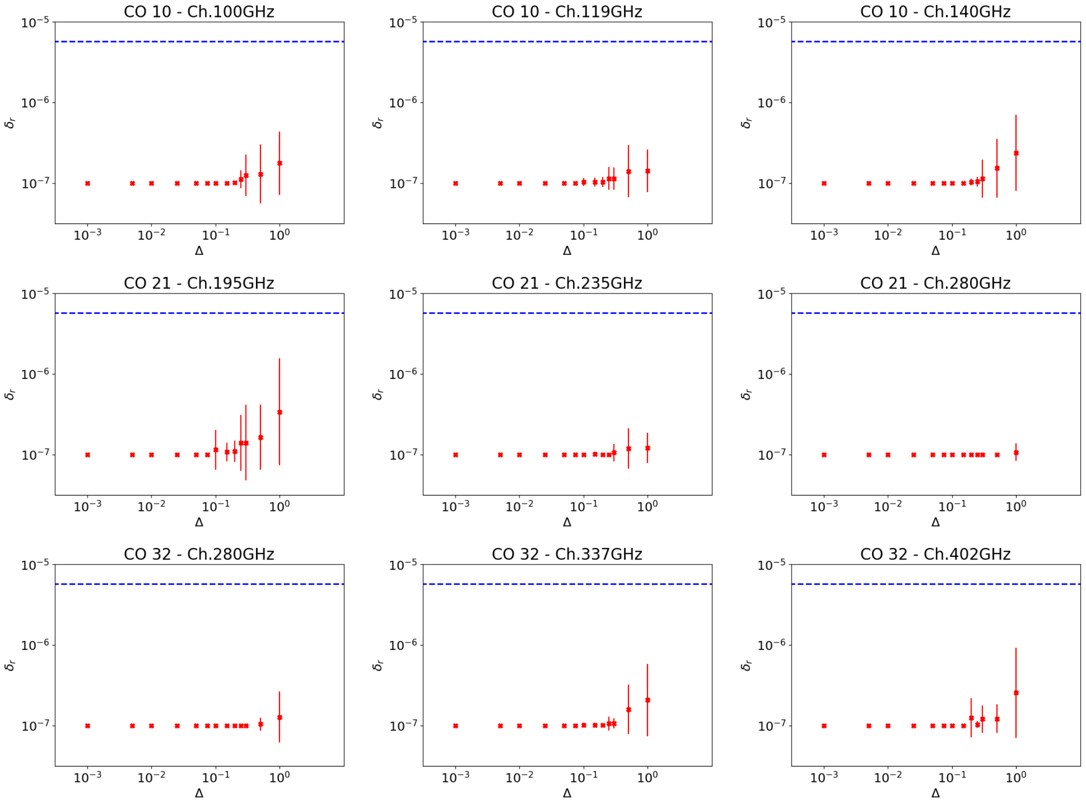

Figure 3.20: CO intrinsic polarization impact assuming a $\sim 1\%$ upper limit on the level of polarized emission.

3.3.3 Intrinsic Polarization

The case of CO intrinsic polarization can be treated in first approximation in the same way for both observation strategies:

$$\begin{pmatrix} Q \\ U \end{pmatrix}_{CO-pol} = G(\nu_{CO}) \begin{pmatrix} Q_{CO} \\ U_{CO} \end{pmatrix} . \tag{3.36}$$

Therefore the effect will be the same in the two cases considered.

The results in Figure 3.20 show that for both observation strategies the CO intrinsic polarization will not impact the tensor-to-scalar ratio measurement.

3.3.4 Bandpass and notch filters

One of the proposed strategies to mitigate the contamination from CO emission lines on the data is to include notch (bandstop) filters as part of the on chip filter to block contaminated frequencies from reaching the detectors. Practically, notch

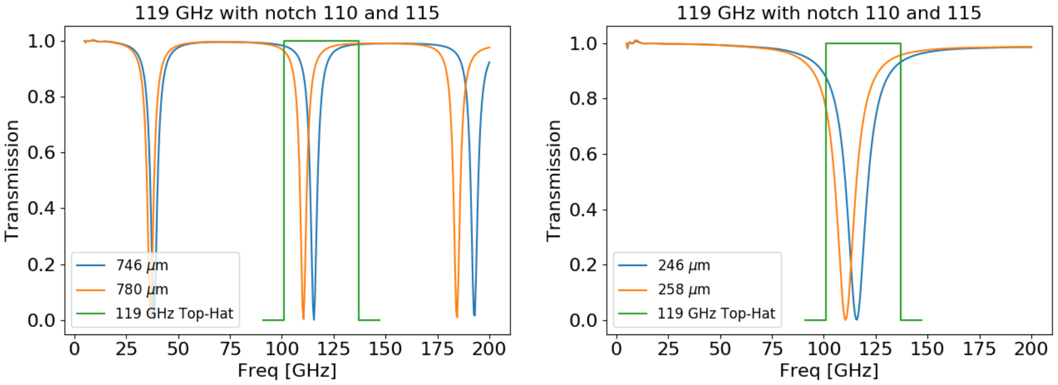

Figure 3.21: Two designs of notch filters for the CO J $1 \rightarrow 0$ lines (notching both ^{12}CO and ^{13}CO). We plot a top-hat bandpass for band 119 GHz for reference (courtesy of Aritoki Suzuki).

filters are implemented by adding a resonant stub on the transmission line to remove the signal at frequency ν_{CO}. Examples of notch filter response to remove both ^{12}CO and ^{13}CO J1 → 0 lines are shown in Figure 3.21 (courtesy of Aritoki Suzuki). A top-hat bandpass at 119 GHz is shown for comparison.

Of all cases studied the only one that might justify the use of notch filters is CO total intensity to polarization leakage if the experiment does not employ a rotating HWP. However we list a number of reasons for not using notch filters even in this case:

Number of detectors: Given the large number of detectors ($>$ 250 for all relevant bands – Table 2.3), the bandpass transmission accuracy per detector is relatively relaxed, therefore *normal* bandpass can probably meet the requirement without the need for notch filters. The introduction of notch filters may even be detrimental due to the steep narrow transition that could maximise differences in the response between detectors, unless extremely efficient control of the manufacturing process is not achieved.

Low TRL of notch filters: The low technology readiness level of notch filters without a thorough hardware-oriented study may cause higher uncertainty than *normal* bandpass filters. This risk is amplified by the absence of any prior experience in implementing this hardware solution for other experiments. This may put extremely tight requirements on detector fabrication and calibration.

Reduced in-band sensitivity: The presence of notch filters "cutting away" part of the photons reduces the sensitivity. Assuming a top-hat bandpass responses and a single narrow notch filter design provided by Aritoki Suzuki (Figure 3.21 *left*), we found a reduction in raw sensitivity $\sim 5-10\%$[16], that will result in a degradation of the achievable σ_r. The reduction of sensitivity is even higher if two notch filters are included to remove both ^{12}CO and ^{13}CO lines. A wider notch filter, like the one in Figure 3.21 *right*, is potentially a better choice to relax resolution requirements, however it will reduce the sensitivity even further.

3.4 Half-wave plate phase response

We can generalize the γ parameter analysis discussed in Section 3.2 to include both the effect of band-pass response $G(\nu)$, HWP modulation efficiency $\epsilon(\nu)$ and frequency-dependent phase response $\phi(\nu)$ as defined in Chapter 2. In this Section we present the formalism, the analysis is left to future work.

The noiseless data (dropping the time dependence for compactness) can be written as:

$$d = \int d\nu\ G(\nu)\Big\{I(\nu) + \epsilon(\nu)\Big[Q(\nu)\cos(4\rho - 2\psi + 4\phi(\nu)) + \\ + U(\nu)\sin(4\rho - 2\psi + 4\phi(\nu))\Big]\Big\}. \tag{3.37}$$

Using the following trigonometric functions we can rewrite the data vector to separate the frequency-independent $4\rho - 2\psi$ part from the frequency-dependent $4\phi(\nu)$ part:

$$\cos(x+y) = \cos x \cos y - \sin x \sin y \tag{3.38}$$

$$\sin(x+y) = \sin x \cos y + \cos x \sin y \tag{3.39}$$

We can separate the CMB from the foreground components (we account only for dust and synchrotron in the present analysis). Following the procedure used in the

---

[16] Assuming a rescaling factor $g_{notch} = \frac{\int G_{notch}(\nu)d\nu}{\int G_{normal}(\nu)d\nu}$.

previous section, assuming the CMB dipole as the calibration source, we can write:

$$
\begin{aligned}
d(\nu_0) =& I_{cmb}(\nu_0) + \gamma_d I_d(\nu_0) + \gamma_s I_s(\nu_0) + \\
&+ \gamma_{cmb}^{\mathrm{cos}} Q_{cmb}(\nu_0)\cos(4\rho - 2\psi) - \gamma_{cmb}^{\mathrm{sin}} Q_{cmb}(\nu_0)\sin(4\rho - 2\psi) + \\
&+ \gamma_{d}^{\mathrm{cos}} Q_{d}(\nu_0)\cos(4\rho - 2\psi) - \gamma_{d}^{\mathrm{sin}} Q_{d}(\nu_0)\sin(4\rho - 2\psi) + \\
&+ \gamma_{s}^{\mathrm{cos}} Q_{s}(\nu_0)\cos(4\rho - 2\psi) - \gamma_{s}^{\mathrm{sin}} Q_{s}(\nu_0)\sin(4\rho - 2\psi) + \\
&+ \gamma_{cmb}^{\mathrm{cos}} U_{cmb}(\nu_0)\sin(4\rho - 2\psi) + \gamma_{cmb}^{\mathrm{sin}} U_{cmb}(\nu_0)\cos(4\rho - 2\psi) + \\
&+ \gamma_{d}^{\mathrm{cos}} U_{d}(\nu_0)\sin(4\rho - 2\psi) + \gamma_{d}^{\mathrm{sin}} U_{d}(\nu_0)\cos(4\rho - 2\psi) + \\
&+ \gamma_{s}^{\mathrm{cos}} U_{s}(\nu_0)\sin(4\rho - 2\psi) + \gamma_{s}^{\mathrm{sin}} U_{s}(\nu_0)\cos(4\rho - 2\psi),
\end{aligned}
\tag{3.40}
$$

where, as in the previous section we have defined the colour correction factors γ as:

$$
\gamma_{[d,s]} = \left(\frac{\int d\nu \; G(\nu)\frac{I_{d,s}(\nu)}{I_{d,s}(\nu_0)}}{\int d\nu \; G(\nu)\frac{\partial B(\nu,T)}{\partial T}\Big|_{T_0}} \right) \frac{\partial B(\nu_0,T)}{\partial T}\Big|_{T_0} \tag{3.41}
$$

$$
\gamma_{[cmb,d,s]}^{cos} = \left(\frac{\int d\nu G(\nu)\epsilon(\nu)\frac{P_{d,s}(\nu)}{P_{d,s}(\nu_0)}\cos 4\phi(\nu)}{\int d\nu \; G(\nu)\frac{\partial B(\nu,T)}{\partial T}\Big|_{T_0}} \right) \frac{\partial B(\nu_0,T)}{\partial T}\Big|_{T_0}, \tag{3.42}
$$

$$
\gamma_{[cmb,d,s]}^{sin} = \left(\frac{\int d\nu G(\nu)\epsilon(\nu)\frac{P_{d,s}(\nu)}{P_{d,s}(\nu_0)}\sin 4\phi(\nu)}{\int d\nu \; G(\nu)\frac{\partial B(\nu,T)}{\partial T}\Big|_{T_0}} \right) \frac{\partial B(\nu_0,T)}{\partial T}\Big|_{T_0}. \tag{3.43}
$$

In this generalized version the polarized component P (either Q or U) is weighted by the product of the modulation efficiency and the *cosine* (or *sine*) function of the frequency-dependent phase response of the HWP. For an ideal HWP with *flat* (frequency-independent) phase response in the limit of perfect modulation efficiency ($\epsilon(\nu) = 1$) $\gamma_{d,s}^{cos} = 1$ and $\gamma_{d,s}^{sin} = 0$. However, this is not always the case, as shown in Chapter 2.

We can rearrange the terms in Equation 3.40 by isolating $\cos(4\rho - 2\psi)$ and $\sin(4\rho - 2\psi)$:

$$
\begin{aligned}
d(\nu_0) =& I_{cmb}(\nu_0) + \gamma_d I_d(\nu_0) + \gamma_s I_s(\nu_0) + \\
&+ \Big[\gamma_{cmb}^{cos} Q_{cmb}(\nu_0) + \gamma_d^{cos} Q_d(\nu_0) + \gamma_s^{cos} Q_s(\nu_0) + \\
&+ \gamma_{cmb}^{sin} U_{cmb}(\nu_0) + \gamma_d^{sin} U_d(\nu_0) + \gamma_s^{sin} U_s(\nu_0) \Big] \cos(4\rho - 2\psi) + \\
&+ \Big[\gamma_{cmb}^{cos} U_{cmb}(\nu_0) + \gamma_d^{cos} U_d(\nu_0) + \gamma_s^{cos} U_s(\nu_0) + \\
&- \gamma_{cmb}^{sin} Q_{cmb}(\nu_0) - \gamma_d^{sin} Q_d(\nu_0) - \gamma_s^{sin} Q_s(\nu_0) \Big] \sin(4\rho - 2\psi).
\end{aligned}
\tag{3.44}
$$

Form Equation 3.44, it is clear that if the HWP phase response is not accounted for properly, it can cause Q-U mixing. After N_{hit} observation of a sky pixel $\hat{n}$ we can re-write using the mean value $\langle ... \rangle$:

$$\begin{aligned} d(\nu_0, \hat{n}) = I'(\nu_0, \hat{n}) &+ Q'(\nu_0, \hat{n}) \langle \cos(4\rho - 2\psi) \rangle + \\ &+ U'(\nu_0, \hat{n}) \langle \sin(4\rho - 2\psi) \rangle , \end{aligned} \tag{3.45}$$

where the *primed* quantities (I', Q' and U') are:

$$\begin{aligned} I' =& I_{cmb}(\nu_0) + \gamma_d I_d(\nu_0) + \gamma_s I_s(\nu_0), \\ Q' =& \gamma_{cmb}^{cos} Q_{cmb}(\nu_0) + \gamma_d^{cos} Q_d(\nu_0) + \gamma_s^{cos} Q_s(\nu_0) + \\ &+ \gamma_{cmb}^{sin} U_{cmb}(\nu_0) + \gamma_d^{sin} U_d(\nu_0) + \gamma_s^{sin} U_s(\nu_0), \\ U' =& \gamma_{cmb}^{cos} U_{cmb}(\nu_0) + \gamma_d^{cos} U_d(\nu_0) + \gamma_s^{cos} U_s(\nu_0) + \\ &- \gamma_{cmb}^{sin} Q_{cmb}(\nu_0) - \gamma_d^{sin} Q_d(\nu_0) - \gamma_s^{sin} Q_s(\nu_0). \end{aligned} \tag{3.46}$$

We can demodulate as in the previous section to reconstruct the signal at pixel $\hat{n}$ and central frequency ν_0 in the uncorrelated noise limit (we rewrite $4\rho - 2\psi = 2\varrho$ and drop ν_0 and $\hat{n}$ for compactness):

$$\begin{pmatrix} \hat{I} \\ \hat{Q} \\ \hat{U} \end{pmatrix} = \begin{pmatrix} 1 & \langle \cos 2\varrho \rangle & \langle \sin 2\varrho \rangle \\ \langle \cos 2\varrho \rangle & \langle \cos^2 2\varrho \rangle & \langle \cos 2\varrho \sin 2\varrho \rangle \\ \langle \sin 2\varrho \rangle & \langle \cos 2\varrho \sin 2\varrho \rangle & \langle \sin^2 2\varrho \rangle \end{pmatrix}^{-1} \begin{pmatrix} d \\ d\langle \cos 2\varrho \rangle \\ d\langle \sin 2\varrho \rangle \end{pmatrix} . \tag{3.47}$$

The cross-linking matrix (first term on the right-hand side) is the same as in the previous section. We can analytically simulate $d(\nu_0, \hat{n})$ and combine the maps to obtain contaminated maps including both the effect of the band-pass and the frequency-dependent HWP modulation efficiency and phase.

In this section we have presented the mathematical formalism. We leave the analysis to future work.

3.5 Other major systematic effects

Other major known systematic effects are due to the telescope beam ($B(\nu, \Omega)$ in Equation 3.1), the polarization angle reconstruction, and detector (and read-out) response (including cosmic ray glitches). This last one is analyzed in detail in Chapter 4.

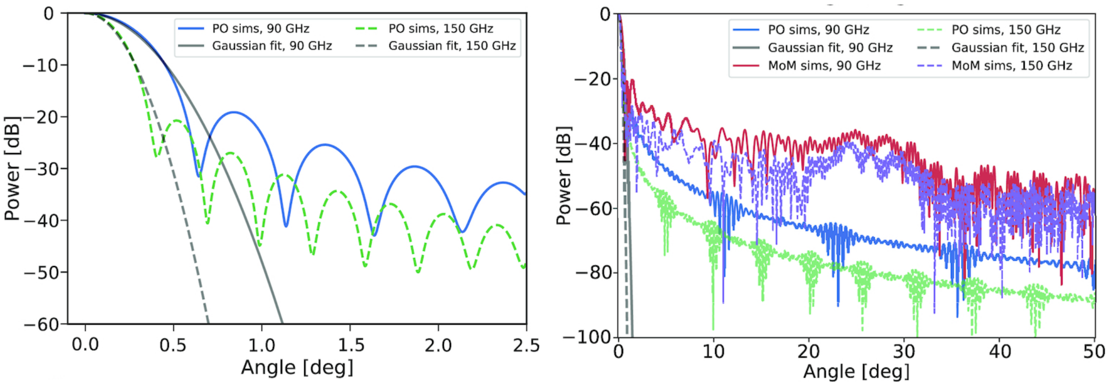

Figure 3.22: Simulated beams for a LiteBIRD like telescope at 90 and 150 GHz from [116]. On the left the area close to the main beam is shown from a PO (physical optics) simulation along with the main beam Gaussian fit. On the right the extended beams up to ∼ 50° are shown both from a PO simulation and a MoM (Method of Moments).

Beam. For what concern the telescope beam, it is common to quote the size of the beam in terms of FWHM which defines the solid angle around the boresight of the telescope where the power response is half of the response at the peak. In Figure 3.22 from [116], the FWHM can be identified as the width of the main beam at -3 dB. Although most of the power is collected in the main beam, there are extended structures away from the telescope boresight that can pick up signal in regions distant from the area that is being scanned. If not accounted properly in the data model, these side lobes can have a negative impact on the data, particularly in the presence of strong Galactic foregrounds.

The telescope beam depends also on the frequency and focal plane position. These two effects need to be properly accounted for during calibration to build a correct instrument model. In particular, for pixels far from the center of the focal plane the beam tends to become more and more elliptical [116]. An elliptical beam causes a higher efficiency along one polarization direction, resulting in an incorrect estimation of the polarized signal. This effect has been studied in detail in the context of CMB polarization measurements in [117].

Polarization angle. All current and future CMB experiments employ polarization-sensitive detectors. A correct calibration of the detector orientation is critical for the success of these experiments. Several components need to be correctly modelled and tested in this context. In [71, 118], the authors showed that the polarization direction of sinuous antenna is frequency-dependent. This effect is know as *wobble* and it influences the angle ψ in Equation 3.1. A correct estimation of the effect is required to properly reconstruct the polarization angle of the incoming signal.

In the same way, the orientation of the optical axis of the HWP ρ as well as the frequency-dependent phase ϕ are necessary to determine the polarization angle. The first will be tracked during observation using an optical encoder that reads the position of the HWP in real time. The second effect has been studied to some degree in [119, 120] in the context of the EBEX balloon-borne mission; a detailed modelling of this effect has been discussed in this Chapter in Section 3.4 expanding the formalism described in Section 3.2. It will be further examined in the future to determine the appropriate HWP design and calibration requirements to mitigate its impact on the data.

4

Detector modelling and systematics

CMB experiments have historically employed both major categories of detectors: coherent and incoherent (or direct). Coherent detectors preserve both amplitude and phase of the incoming signal, while incoherent devices do not preserve the phase.

While coherent detection techniques are mostly in use in radio astronomy, direct detection is employed in optical astronomy. This distinction comes from the photon occupation number in Bose-statistics: $n(\nu, T) = (\exp h\nu/k_B T - 1)^{-1}$. Radio astronomy operates mainly in Rayleigh-Jeans regime ($h\nu \ll k_B T$) where the occupation number is $n \gg 1$, while in the Wien regime ($h\nu \gg k_B T$), where optical astronomy operates, the occupation number becomes $n \ll 1$. In the case of CMB astronomy the signal is dominated by a black-body with temperature $T \sim 2.725$ K (the spectrum peaks at $\nu \sim 160$ GHz), therefore for typical observation frequencies around ~ 100 GHz the photon occupation number is close to unity ($n \sim 1$). This fact justifies the historical use of both technologies for CMB observations.

As demonstrated in [67, 121], coherent detection is penalised compared to direct detection above ~ 100 GHz when the incoming signal is dominated by the CMB black-body:

$$\frac{NEP_{coherent}}{NEP_{direct}} = \sqrt{\frac{\eta n(\nu, T) + 1}{\eta n(\nu, T)}}. \tag{4.1}$$

In Equation 4.1 the ratio of the photon contribution to the Noise Equivalent Power (NEP) for the two technologies is expressed in terms of occupation number and detector efficiency η. We can observe that in the coherent detection case the NEP does not vanish even for a dark detector. This is commonly referred to as quantum noise limit, and its presence becomes non-negligible for $n \ll 1$.

In principle coherent detection is still a competitive and viable option for space observation at low frequency. However, with the Galactic foreground minimum around $\sim 80 - 100$ GHz and the need to constrain the foreground signal both at lower and higher frequencies, direct detection has become more suitable.

The most common direct detection devices used in CMB observations are bolometers. Thanks to a well-known temperature-resistance relation, a bolometer measures the power of the incoming radiation by observing the change in resistance caused by the heating due to photon absorption [122]. In recent years Kinetic Inductance Detectors (KIDs) are also becoming increasingly competitive, and they will certainly play a bigger role in the future [123, 124]. However, they are probably not-technologically mature enough yet for a space mission, because of high susceptibility to $1/f$ noise and existing technological challenges in fabricating them for low frequency ($\lesssim$ 100 GHz).

We can roughly distinguish between two types of bolometers used extensively and successfully for CMB observations: semiconductor-based (e.g. Neutron Transmutation Doping-Germanium – NTD-Ge) and superconductive (e.g. Transition Edge Sensors – TES). The working principles are very similar, and the major distinction is the temperature-resistance relation. In the following we will describe the working principles valid for both types of bolometer. However, we will focus on TES bolometers (specifically in the context of LiteBIRD) highlighting some of the reasons that made experiments shift from the use of semiconductor technology in the 1990s to superconductive technology in recent years.

A major achievement in the last decade, and one of the advantages of TES over NTD-Ge bolometers, has been the ability to fabricate detectors in large arrays. This advancement offers the possibility to dramatically increase the experiment sensitivity, at the cost of increasing the complexity of the read-out technology. Experiments had to abandon a simple single detector read-out scheme and develop multiplexing systems that can read multiple detectors within a single channel. At present several read-out schemes exist, although a comprehensive description of all existing schemes is beyond the scope of this thesis. Here we will focus on the scheme that will be employed in the LiteBIRD mission called Digital frequency Multiplexing or DfMux.

After describing the detector technology, we will focus on the main subject of this chapter: TES detector non-linearity effects. By modelling the electrical and thermal response of the detector to external signals, we can address the sources of non-linearity in the detector response. We analyze some of them to forecast calibration requirements in the context of the LiteBIRD mission.

Keeping in mind that Planck HFI was based on a different technology, non linear response (ADC non-linearity) has been found to be the main limiting factor to HFI sensitivity in most frequency channels, as it is clearly visible in Figure 1.6. More recently, both POLARBEAR [81] and EBEX [125] (both experiments based on TES technology) have observed detector non-linear response due to an unexpected excess in the optical signal seen by the bolometers. In [125], the authors argue that this loading excess is associated with HWP non-idealities, and it results in total intensity contamination of the reconstructed polarized signal. Since LiteBIRD will employ a similar detector technology and HWP configuration, it is vital to address the possible presence of detector non-linearity and its impact on the data.

4.1 Bolometers

As already mentioned, a bolometer is a device that measures the power of the incoming radiation by absorbing the incoming photons. The photon absorption process heats up the detector and causes a change in its electrical resistance. By knowing the temperature-resistance relation of the detector it is possible to measure the power deposited from the incoming radiation.

A bolometer is made of an absorber, characterized by a heat capacity C, connected to a thermal bath at stable temperature T_b through a weak thermal link

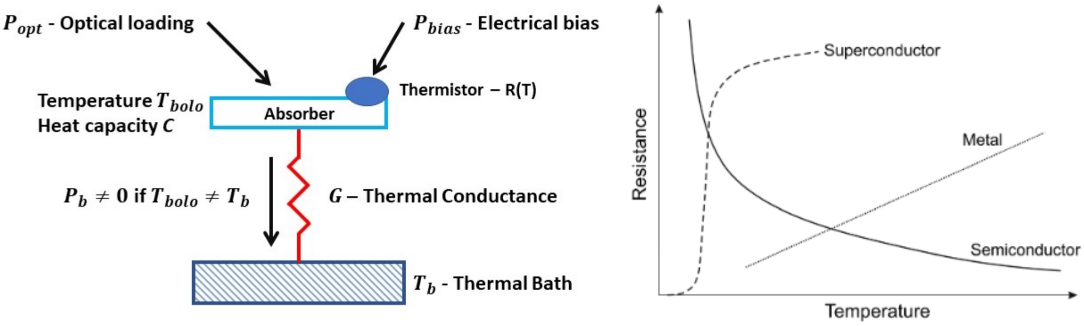

Figure 4.1: *Left:* A simple sketch of the working principle of a bolometer. The bolometer temperature T_{bolo} is kept slightly higher than the thermal bath temperature thanks to a combination of optical loading power P_{opt} and the thermal power dissipated by the electrical bias P_{bias}. This power imbalance creates a power flow P_b between the absorber and the bath through the weak link G. The time evolution of this system is defined by the heat capacity value C and the thermal conductance of the weak link G as $\tau = C/G$. *Right:* The temperature-resistance relation for normal metal, semiconductor-based or superconductive thermistors.

of thermal conductance G. In Figure 4.1 we show a simplified sketch illustrating the working principles of a bolometer. For an external power falling on the bolometer we expect the temperature of the absorbing element to increase from the temperature of the thermal reservoir T_b to a new value T_{bolo} ($T_{bolo} > T_b$). If the power falling on the bolometer is a combination of optical loading P_{opt} and thermal dissipation due to an electrical bias (P_{bias}), the total incident power compensates P_b, the power flowing out of the bolometer through the weak thermal link to the bath: $P_b = P_{opt} + P_{bias}$. We can compute the temperature evolution in time of the bolometer through the thermal differential equation (neglecting noise contributions):

$$C\frac{dT}{dt} = -P_b + P_{opt} + P_{bias}. \tag{4.2}$$

While this is true for every type of bolometer, the evolution of the current flowing through the bolometer depends on the effective temperature-resistance relation of the specific bolometer. In general we want the bolometer to have a non-constant resistance around the operation point, but a well determined dependence from the temperature: $R(T)$. In this way a change in temperature due to a varying incident power is converted to a change in the bolometer resistance that can be read out.

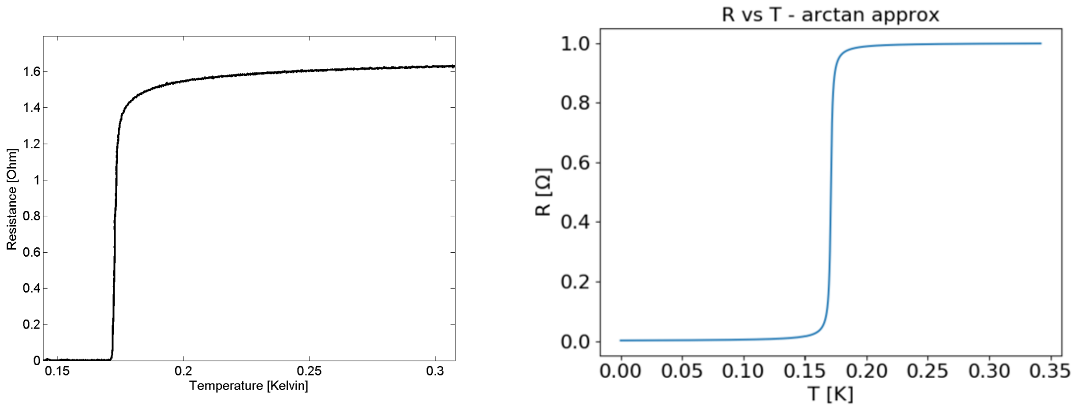

Figure 4.2: Temperature-resistance relation for a TES detector with superconductive transition at critical temperature $T_c \sim 0.17$ K (LiteBIRD like). *Left:* data from a test detector courtesy of Aritoki Suzuki at LBNL. *Right:* An analytical model for the expected LiteBIRD-specific detectors with $R_n = 1\ \Omega$.

The main difference between classical semiconductor-based bolometers and superconductive TES sensors is that the former are characterized by a high resistance (~ 1 MΩ) and relatively small negative value of the logarithmic derivative ($-10 \lesssim \alpha \lesssim -5$):

$$\alpha = \frac{d \log R}{d \log T}, \tag{4.3}$$

while the latter are characterized by a much smaller value of resistance ($\sim 1\ \Omega$ or lower) and a positive value of α ($\gtrsim 100$). Due to these characteristics, semiconductor bolometers are usually operated in current-bias mode ($P_{bias} = I^2_{bias} R(T)$), while TESes are operated in voltage-bias mode ($P_{bias} = V^2_{bias}/R(T)$) to obtain a stable operation thanks to the Electro-Thermal Feedback (ETF) effect. In fact in both cases, for a stable electrical bias, an increase in temperature due to an increase in optical loading causes the joule heating power P_{bias} to decrease, therefore keeping the bolometer operation point stable.[1]

Semiconductor bolometers have two main disadvantages. Firstly, the high impedance can easily amplify microphonic excitation that can contaminate the

---

[1] In the semiconductor case, the temperature increase causes a decrease in resistance which lower the value of P_{bias}. On the other hand, in the superconductive case, an increase in temperature causes the resistance to increase. When the detector is voltage biased the value of P_{bias} decreases.

data. Secondly, a larger absolute value of α produces a stronger Electro-Thermal Feedback effect that allows TES sensors to achieve a more stable operation.

In Equation 4.2, the power P_b flowing through the thermal link between the bolometer island at temperature T and the thermal bath at temperature T_b , is classically modelled as:

$$P_b = \frac{G}{nT^{n-1}}(T^n - T_b^n), \tag{4.4}$$

where $n = \beta + 1$ and the value of β depends on the primary thermal carriers. For electrons $\beta = 1$, while in the case of phonons $\beta = 3$. In the following we will assume phonons to be the primary thermal carriers in the case of TES bolometers, therefore $n = 4$.

4.1.1 Transition Edge Sensors

Two representative temperature-resistance relations are shown in 4.2. On the *left* we report the measured relation (courtesy of Aritoki Suzuki) for a test detector with critical temperature $T_c \sim 0.17$ K. The target normal resistance (Ohmic branch for $T > T_c$) for LiteBIRD detectors is $R_n \sim 1\ \Omega$, therefore on the *right* we also show an analytical model using a arctan approximation to mimic the behaviour of the superconductive transition. The analytical model is created with the assumption that the width of the transition is 10 mK, defined as the temperature window where $0.25\ \Omega < R < 0.75\ \Omega$. With this assumption we obtain a value of $\alpha \sim 100$ at the center of the transition (R 0.5 Ω).

In Figure 4.3 we show the computed value of the logarithmic sensitivity α for the two cases in Figure 4.2. The arctan approximation is a fairly good assumption for $R \gtrsim 0.5 R_n$. Typically TESes are operated at $R \sim 0.7 R_n$.

As mentioned previously, to make use of the ETF effect, TESes are operated in voltage-bias mode. In Figure 4.4 we show a basic DC circuit to voltage-bias and read-out a TES detector. On the *right* side we also show the Thevenin equivalent circuit. A biasing current is split between a shunt resistor R_s and the TES (R_{TES}) in series with an inductor L. If $R_s \ll R_{TES}$ the Thevenin equivalent circuit voltage

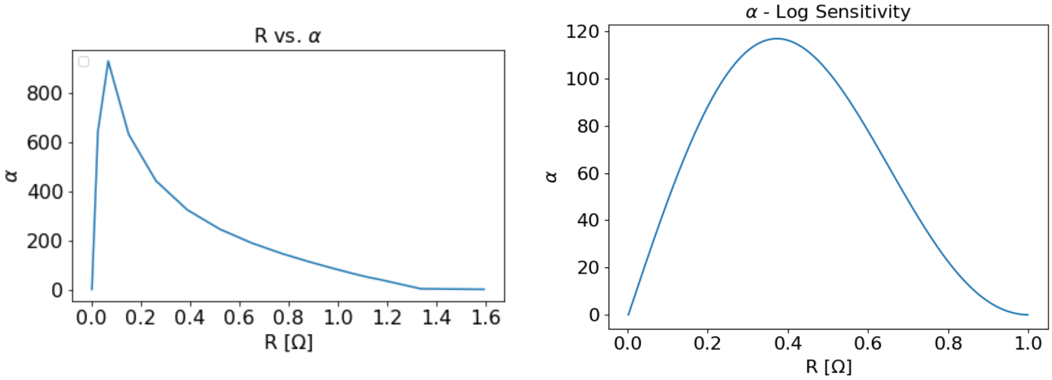

Figure 4.3: *Left:* R vs. α for the curve in the *left* image of Figure 4.2. *Right:* R vs. α for the analytical curve in the *right* image of Figure 4.2.

is constant $V \sim I_{bias}R_s$. Typical values of the shunt resistor are of the order 1 m$\Omega \lesssim R_s \lesssim 10$ mΩ. To avoid the effect of parasitic resistance TES detectors are operated at $R \sim 0.7R_n$, however smaller values can be used if parasitic effects are well under control with the advantage of obtaining stronger ETF effect and higher detector stability, as we will show in the next sections.

For the simple read-out scheme in Figure 4.4 we can write the time evolution of the current flowing through the detector as:

$$L\frac{dI}{dt} = V - R_{TES}I - R_sI, \tag{4.5}$$

where L is the inductor that couples the TES detector to the SQUID amplifier, and defines the electrical time-response $\tau_{el} \sim L/R_{TES}$. A thorough analysis of the stability criteria for the system is beyond the scope of this thesis and can be found in [122]. However, We report here some of the relevant parameters for the continuation of this thesis, the loop gain:

$$\mathcal{L} = \frac{\alpha P_{bias}}{GT} \tag{4.6}$$

which defines the strength of the ETF effect and the stability of the detector response, the thermal time constant sped-up by the loop gain:

$$\tau = \frac{C}{G}\frac{1}{\mathcal{L}+1} \quad [s], \tag{4.7}$$

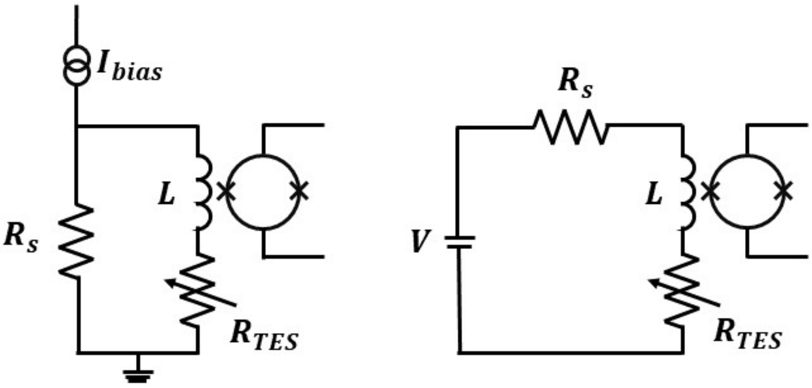

Figure 4.4: *Left:* A simple DC circuit to voltage-bias the TES. If the shunt resistor $R_s \ll R_{TES}$ the TES is bias by a constant voltage $V \sim I_{bias} R_s$. *Right:* The equivalent Thevenin circuit. The TES is paired to a SQUID amplifier through an input inductor L.

and lastly the current responsivity (gain) of the detector to an external signal of angular frequency ω:

$$S_I = -\frac{1}{V}\frac{\mathcal{L}}{\mathcal{L}+1}\frac{1}{1+i\omega\tau} \qquad [A/W]. \tag{4.8}$$

For an external signal varying slowly compared to the time response of the system, and $\mathcal{L} \gg 1$ the detector gain becomes stable and independent of the operation point of the detector $S_I \sim -1/V$.

The electrical time constant τ_{el} sets a fundamental limit to the speed of the detector: $\tau > (\mathcal{L}-1)\tau_{el}$, a faster response becomes quickly unstable. Therefore an appropriate inductor needs to be used depending on the target detector response speed.

By solving the two coupled differential equations 4.2 and 4.5 we can simulate the detector response in time to external inputs like the power across the sky, thermal instabilities of the thermal bath, instability of the bias and varying magnetic fields. Each of these will be discussed in the next sections.

4.1.2 Noise

The high sensitivity achievable by bolometers is undoubtedly the reason for their success and widespread use in CMB experiments nowadays. The detection of CMB B-modes requires very high sensitivity (of the order of tens of nK); bolometers, compared to coherent detectors, can be packed together in large arrays and are not intrinsically noise limited. Since the early 2000s various research groups have fabricated and tested background-limited bolometers, both for ground and space environment [126].

Background limited performances (BLIP) requires that the main source of uncertainty is due to the statistical uncertainty in the arrival of photons from the source (photon noise), hence the detector is not limited by intrinsic noise sources. Therefore, if we can define each noise source j in terms of its Noise Equivalent Power (NEP)[2], background limited performance is obtained for $NEP_{j,tot} < NEP_{\gamma}$, where NEP_{γ} is the photon NEP, and $NEP_{j,tot}$ is the combined NEP of every other noise source ($NEP_{j,tot} = \sqrt{\sum_j NEP_j}$).

4.1.2.1 Photon noise

The photon noise can be calculated from the optical spectral power $P_{\nu,opt}$[3] falling on the detector [121]:

$$NEP_{\gamma}^2 = \int_0^{\infty} 2h\nu P_{\nu,opt} d\nu + \int_0^{\infty} P_{\nu,opt}^2 d\nu, \tag{4.9}$$

where the first integral represents the Poisson term (or shot-noise), while the second integral is the bunching term (the bunching term contribution becomes increasingly negligible with increasing frequency)[4]. For space-based observations where the dominant photon source is the CMB, assuming polarization sensitive observation bands between ~ 10 and ~ 500 GHz with $\sim 30\%$ bandwidth and optical efficiency ~ 0.5, typical value of optical power loading is of the order $\sim 0.1 - 1$ pW (including the contribution from the optical elements of the telescope). With these assumptions we find $NEP_{\gamma} \sim 10^{-17}$ W/$\sqrt{\text{Hz}}$[5].

---

[2] The Noise Equivalent Power is defined as the input power that results in a S/N (signal-to-noise ratio) of 1 for 0.5 s of integration time.

[3] If the photon source can be approximated with a black-body with temperature T, P_{opt} for a polarization sensitive bolometer can be calculated as $P_{opt} = \frac{1}{2}\int_0^{\infty} B(\nu,T)G(\nu)\Omega A_e d\nu$, where B is the Planck function, G is the bandpass response and ΩA_e is the detector throughput. In the Rayleigh-Jeans limit for a top-hat bandpass response and diffraction limited observation ($\Omega A_e \sim \lambda^2$), P_{opt} reduces to $k_B T \eta \Delta\nu$, where η is the optical efficiency in band.

[4] For a narrow bandpass response $\Delta\nu$ around ν_0 where $P_{\nu,opt}$ can be assumed to be constant, we can approximate $NEP_{\gamma}^2 = 2h\nu_0 P_{opt} + P_{opt}^2/\Delta\nu$. Where P_{opt} is the integrated power received in the frequency band $\Delta\nu$, and for a narrow bandwidth we defined $P_{\nu,opt} = P_{opt}/\Delta\nu$.

[5] The CMB only contribution is $NEP_{\gamma} \sim 9 \times 10^{-18}$ W/$\sqrt{\text{Hz}}$ around the peak of the spectrum $\nu \sim 160$ GHz.

4.1.2.2 Bolometer noise

The bolometer intrinsic noise is dominated by two main sources: thermal carrier (phonons) fluctuations in the link connecting the bolometer island and the thermal bath (phonon noise – NEP_G), and thermal noise due to the electrical carriers in the thermistor (Johnson noise – NEP_J) [127, 128]. Both of them are related to the temperature of operation of the bolometer, therefore low temperature operation results in lower intrinsic noise.

The total intrinsic noise of the bolometer can be expressed as: $NEP_{bolo}^2 = NEP_J^2 + NEP_G^2$.

Johnson noise. The contribution of Johnson noise to the total NEP can be computed knowing the temperature T and electrical resistance R of the thermistor as:

$$NEP_J^2 = \frac{4k_BT}{R}\frac{1}{S_I^2}, \tag{4.10}$$

where S_I is the detector responsivity as defined in Equation 4.8.

Phonon noise. The thermal link between the bolometer island at temperature T and the thermal bath at temperature T_b is out of thermal equilibrium. From [127] we can compute NEP_G from:

$$NEP_G^2 = 4k_BT^2\gamma g \quad \text{with} \quad \gamma = \frac{\beta+1}{2\beta+3}\frac{1-\left(\frac{T_b}{T}\right)^{2\beta+3}}{1-\left(\frac{T_b}{T}\right)^{\beta+1}}, \tag{4.11}$$

where for phonons $\beta = 3$, $g = \partial P_{sat}/\partial T$ is the dynamic thermal conductance and P_{sat} is the saturation power that defines the dynamical range of operation of the bolometer. Assuming that the bolometer island is suspended over the thermal bath thanks to N *legs* (thermal link) of length ℓ, cross section A and thermal conductivity of the form k_0T^β, the saturation power can be tuned through the relation:

$$P_{sat} = N\frac{A}{\ell}\int_{T_b}^{T} k_0T^\beta = N\frac{A}{\ell}\frac{k_0}{\beta+1}(T^{\beta+1} - T_b^{\beta+1}). \tag{4.12}$$

We can compute the dynamical thermal conductance as:

$$g = N\frac{A}{\ell}k_0 T^{\beta}. \tag{4.13}$$

Typically the phonon noise contribution is approximated with the thermal equilibrium case: $NEP_G^2 \sim 4k_B T^2 G$. However, for a given P_{sat} value, from Equation 4.11 it is possible to find the optimal operation temperature that minimizes the phonon noise contribution: $T \sim 1.71 \times T_b$ [71]. In the case of LiteBIRD, the baseline bath temperature is $T_b = 0.100$ K, therefore the TES bolometers are designed to be operated at $T \sim 0.17$ K. This value corresponds to the target transition temperature T_c.

The saturation power P_{sat} is an extremely important parameter in the detector design process. The total power on the detector is the sum of the optical power from the sky P_{opt} (and some loading due to the telescope structure) and the electrical power due to the electrical biasing of the thermistor P_{bias}. For stable operation $P_{bias} \sim P_{opt}$, therefore the total power on the detector is $P_{tot} \sim 2 \times P_{opt}$. However, in order to allow for some margin, a typical design solution is to tune $P_{sat} \sim 2.5 \times P_{opt}$. A higher value would increase the dynamical range of the detector at the cost of increased phonon noise ($NEP_G^2 \propto P_{sat}$). Combining Equations 4.11, 4.12 and 4.13 we can rewrite the phonon NEP as:

$$NEP_G^2 = 4P_{sat}k_B T_b \frac{(\beta+1)^2}{2\beta+3}\frac{(T/T_b)^{2\beta+3}-1}{[(T/T_b)^{\beta+1}-1]^2}. \tag{4.14}$$

Secondly, once P_{sat} and the target thermal time constant $\tau = C/G$ are defined we can derive the required value of G, by substituting P_b in Equation 4.4 with P_{sat}, and C to meet these targets. As an example, in the simulations and analysis in the next sections, by assuming a representative loading $P_{opt} = 0.5$ pW we can assign $G \sim 30 \times 10^{-12}$ W/K to obtain a saturation power $\sim 2.5 \times P_{opt}$. The target *normal* thermal time constant for LiteBIRD detectors is $\tau \sim 33$ ms; we can use this to fix the value of $C \sim 1 \times 10^{-12}$ J/K. Note that the thermal time constant is sped-up by the loop-gain, therefore for a target $\mathcal{L} \sim 10$ (common target for most CMB experiments employing TES bolometers), following Equation 4.7, the thermal time constant becomes $\tau \sim 3$ ms.

From Equation 4.10 and the NEP_G thermal equilibrium approximation we can compute their expected typical values for a LiteBIRD detector. In the limit of high loop-gain ($\mathcal{L} \gg 1$) the responsivity $S_I \sim -1/V$, therefore NEP_J^2 can be rewritten as $NEP_J^2 = 4k_B T P_{bias}$. If $P_{bias} \sim P_{opt} \sim 0.5$ pW, the Johnson noise contribution to the total NEP is $\sim 2 \times 10^{-18}$ W/$\sqrt{\text{Hz}}$ ($< NEP_\gamma$). And, for the value of G obtained in the previous paragraph, $NEP_G \sim 7 \times 10^{-18}$ W/$\sqrt{\text{Hz}}$ ($< NEP_\gamma$). As highlighted in [127], assuming the thermal equilibrium approximation, the phonon noise is overestimated by up to 30%. This is clearly visible in Figure 4.5.

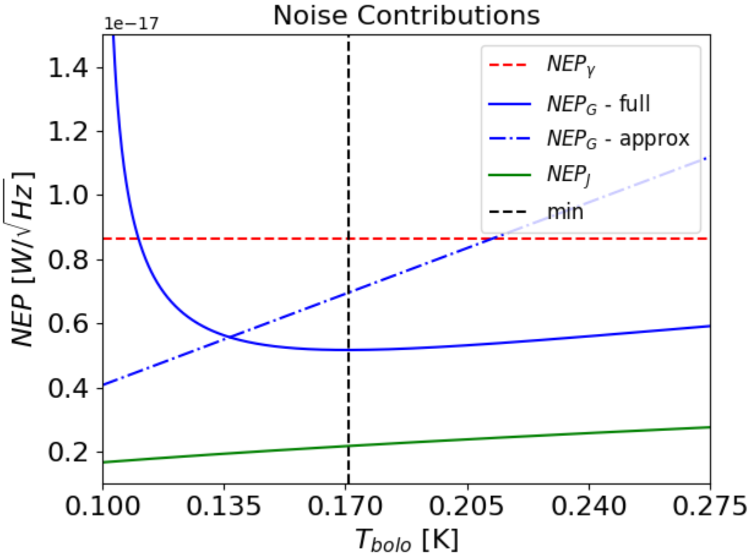

Figure 4.5: Representative noise levels expressed as NEP for LiteBIRD detectors, assuming an optical power $P_{opt} = 0.5$ pW constant across a narrow 30% bandwidth at 100 GHz (this is an approximation). The photon noise level does not depend on the bolometer operation temperature as it is clear from the *red dashed* line. The optimal phonon noise is found from [127] at $T_{bolo} \sim 1.7 \times T_b$ as shown by the *blue solid* line and highlighted by the *black dashed* line that indicates the minimum. As mentioned, the thermal equilibrium approximated formula slightly overestimates the phonon noise level at the operation point (*blue dot-dashed* line). Finally, the Johnson noise contribution is shown as a *green solid* line.

4.1.3 SQUID

Superconductive QUantum Interference Devices (SQUIDs) are ubiquitous in CMB experiments using TES bolometers, independently of the experiment specific readout configuration, thanks to their intrinsic low noise performance. A full discussion of the noise properties of SQUIDs is beyond the scope of this thesis, the interested reader can find useful information in the context of CMB and TES bolometers in [129, 130], as well as [131, 132] for details about the SQUIDs and electronics used for the work presented here. Note that these are commercial SQUIDs and are employed only for lab tests, not for the real instrument.

For the sake of the discussion we will report briefly the working principle of a DC SQUID. A DC SQUID is a superconductive loop connecting two Josephson junctions (Superconductive-Insulator-Superconductive – SIS) as seen in the sketch in Figure 4.6 (AC SQUID requires a single junction). When the biasing current I_b

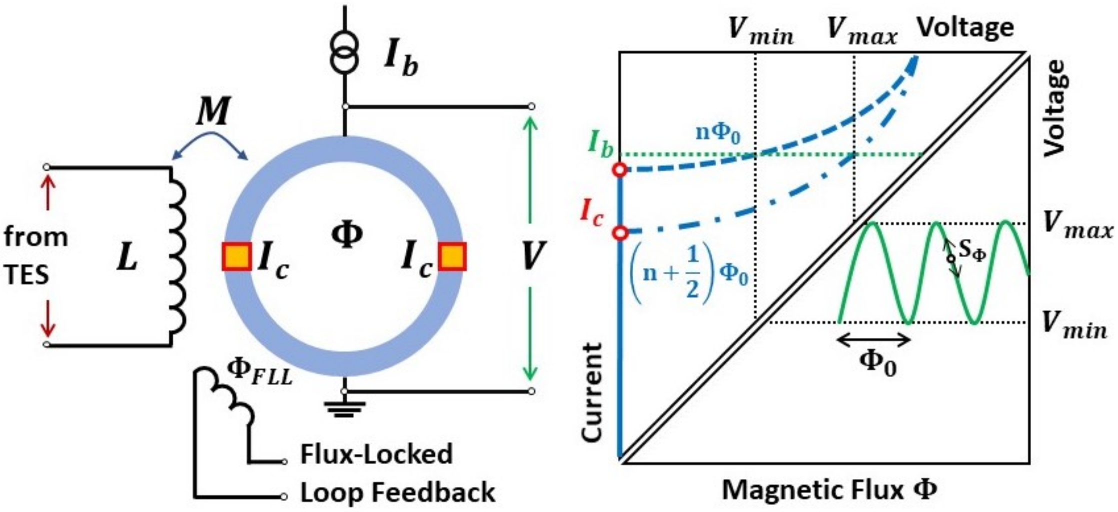

Figure 4.6: A simplified sketch of a SQUID. The superconductive ring in *blue* is interrupted by two thin insulating layers (in *red*) that creates two Josephson junctions. When the bias current is larger than the critical current of the Josephson junction ($I_b > I_c$) a voltage V appears across the junction. At the same time the superconductive ring reacts to a magnetic flux Φ generated by the inductor in series with the TES detector, by creating a current that tries to null the net flux through the ring. This current changes direction every $\frac{1}{2}\Phi_0$ as seen from the *green* $\Phi - V$ curve. Since the response is periodic, a feedback circuit is used to keep the SQUID at a stable fixed working point (FLL) with constant gain $S_\Phi = \partial V/\partial\Phi$. The overall sensitivity of the system is defined by the SQUID gain S_Φ and the mutual inductance M between the SQUID and the input inductor.

exceeds the critical current I_c of the junction, the current carriers (Cooper pairs) in the superconductor can quantum tunnel through the insulating barrier, and a voltage appears across the junction, as described by the $I - V$ curve in Figure 4.6.

The allowed magnetic flux through the superconductive ring is quantized: $\Phi_0 = h/2e = 2.07 \times 10^{-15}$ Tm^2. When the applied flux $\Phi \neq n\Phi_0$ (where n is an integer number), the SQUID reacts by creating a screening current to bring the net flux to $n\Phi_0$. The screening current changes sign (flowing direction in the superconductive loop) every $\frac{1}{2}\Phi_0$. This results in the periodic behavior seen in the *green* $V - \Phi$ curve of Figure 4.6. Typical noise values for state-of-the-art SQUIDs are of the order $\sim 10^{-6}\ \Phi_0/\sqrt{\mathrm{Hz}}$ (see [129, 132, 133]).

Since the response is periodic, in order to use the SQUID as an amplifier, a feedback circuit is required to lock the SQUID at a fixed operation point that maximizes and stabilizes the responsivity $S_\Phi = \partial V/\partial\Phi$ at a constant value. This type of operation is called Flux-Locked Loop (FLL) and can be achieved with a second inductor that supplies the feedback flux Φ_{FLL}. Details of hardware implementation solutions can be found in [130].

Ultimately the responsivity of the input inductor-SQUID system is defined by the flux sensitivity S_Φ of the SQUID and the mutual inductance M of the system:

$$S_V = M\frac{\partial V}{\partial \Phi} \qquad [V/A]. \tag{4.15}$$

Note that, for real applications, SQUID amplifiers are made of arrays of tens of SQUIDs in series (see [132]).

4.2 TES response simulator

With the definitions given up to now, the data time stream from the detector and read-out can be written in the following way (in units of voltage V or ADU):

$$d = [S_I(s + n_\gamma) + n_J + n_G + n_X + n_R]S_V + d_{off}, \tag{4.16}$$

where S_I ([A/W]) and S_V ([V/A] or [ADU/A]) are respectively the bolometer and SQUID responsivity. The term s represents the observed sky signal in units of power ([W]) after integration over the band and the beam, and n_γ is the photon noise contribution ([W]). The other noise terms are referred to the SQUID input and therefore are expressed in units of current ([A]). The terms n_J, n_G and n_R are respectively the Johnson noise and phonon noise of the bolometer, and the read-out noise. We included two extra terms n_X and d_{off} that represent possible additional noise due to the hardware (e.g. microphonic effects) or external sources (e.g. cosmic rays) and a non-zero offset of the read-out.

In an ideal experiment, the noise contribution is purely *white*, meaning that the Power Spectral Density (PSD) is constant in frequency. Although this is generally true on short time scales ($\sim$ tens of seconds) the noise becomes *pink* ($1/f$) on longer time scales due to environment instabilities (thermal, electrical, optical etc). This can severely limit an experiment capabilities by contaminating the cosmological signal, especially on large angular scales (low-ℓ). Hence, a good understanding of the origin of the noise is required.

Note that this is also one of the reason for the use of polarization modulator in recent CMB experiments; by modulating the polarized signal at a constant frequency f_{mod} ($\sim$ few Hz), the signal of interest is pushed to higher frequencies ($4f_{mod}$) to suppress the impact of the $1/f$ component.

In the following we will analyze some of these terms focusing mostly on the bolometer gain S_I and how it is affected by the environment.

4.2.1 DC simulation

We wrote a simple program in python and C that exploits the Runge-Kutta 4th order method [134] (Appendix F) to integrate Equations 4.2 and 4.5 for $P_{bias} = V^2/R_{TES}$ and P_b as given in Equation 4.4. The temperature-resistance relation for the TES detector R_{TES} can be modelled either analytically (arctan approximation) or from measured data.

```
# TES Simulator based on Irwin & Hilton, 2005
import numpy as np

# TES response model parameters
L = 10.e-8                  # SQUID-input inductor
Rs = 0.02                   # Shunt resistor
```

```python
Ib = 33.e-6             # Bias current 0.5
Tb = 0.1                # Bath temperature
Tc = 1.71*Tb            # TES transition temperature
Rn = 1.                 # TES normal resistance
alpha = 100.            # TES alpha at R = 0.5
n = 4.                  # Thermal carrier +1 (phonon = 3)
P_opt = 0.5e-12         # Expected average optical power
Psat = 2.5*P_opt        # Expected saturation power
K = Psat/(Tc**n-Tbase**n)
G = K*n*Tc**(n-1.)      # TES thermal conductance
tau0 = 33.e-3           # Thermal time constant
C = tau0*G              # TES heat capacity

# TES R vs. T curve - arctan approx
def RT(T):
    A = alpha*np.pi*(Tc**2+1.)*Rn/2./Tc
    return Rn*(np.arctan((T-Tc)*A)+np.pi/2.)/np.pi

# TES T & I evolution
def bolo(IT, Ib, P, Tb):
    I = IT[0]           # Current initial condition
    T = IT[1]           # Temperature initial condition
    R = RT(T)           # TES resistance vs. T
    V = Ib*R*Rs/(R+Rs)  # Voltage bias
    Pb = G*(T**n-Tb**n)/(n*T**(n-1.))   # Power out of the leg
    Pr = V*V/R          # Electrical power
    dITdt = np.array([(V-I*Rs-I*R)/L, (-Pb+Pr+P)/C])  # Differential equations
    return dITdt

# Input
ti = 0.                            # Initial time [s]
tf = 10.                           # Initial time [s]
step = 1000                        # Sampling rate [s-1]
steps = int((tf-ti)*step)          # Steps
t = np.linspace(ti, tf, )          # Time array
Tb = np.ones_like(t)*Tb            # Bath temperature array
P = np.ones_like(t)*P_opt          # Optical power array
Ib = np.ones_like(t)*Ib            # Bias current array

# Initial condition
T0 = Tc                            # Initial bolo temperature
I0 = Ib[0]*Rs/(RT(T0)+Rs)          # Initial bolo current
IT0 = [I0, T0]

# Solve & Update
h=abs(t[1]-t[0])                   # Time step
I = np.zeros(step)                 # I - output array
T = np.zeros(step)                 # T - output array
# Runge-Kutta 4th order solver
for i in range(step):
    k1 = h*bolo(IT0, Ib[i], P[i], Tb[i])
    IT0_tmp = [IT0[0]+0.5*kI1, IT0[1]+0.5*kT1]
    k2 = h*bolo(IT0_tmp, Ib[i], P[i], Tb[i])
    IT0_tmp = [IT0[0]+0.5*kI2, IT0[1]+0.5*kT2]
```

```
        k3 = h*bolo(IT0_tmp, Ib[i], P[i], Tb[i])
        IT0_tmp = [IT0[0]+kI3, IT0[1]+kT3]
        k4 = h*bolo(IT0_tmp, Ib[i], P[i], Tb[i])
        I0 = IT0[0]+(kI1+2*kI2+2*kI3+kI4)/6.
        T0 = IT0[1]+(kT1+2*kT2+2*kT3+kT4)/6.
        IT0 = [I0, T0]
        I[i]=IT0[0]
        T[i]=IT0[1]
```

Listing 4.1: A simplified example of the TES response simulator for a DC biased bolometer. All inputs are set to the ideal operation value and the TES R(T) curve is described with an arctan approximation. The complexity of the system can be increased according to the need of a specific study. The code is publicly available at `https://github.com/tomma90/tessimdc`.

In 4.2.1 we show a simple example of the Python version of the code (the C implementation is more efficient for obvious reason but less compact). Figure 4.7 shows the input and output of the TES simulator when the TES is biased at $R \sim 0.7 \times R_n$ ($R_n = 1\ \Omega$). Assuming an average input power of 0.5 pW the code waits till the operation point is stable (at $t = 0$ s in Figure 4.7). Once the response is stable, we injects a small and slow fluctuation with 1% amplitude on a 10 s time-scale. This condition satisfies $\omega \ll 1/\tau$ as explained in the previous sections. The variation of current flowing through the bolometer and its temperature are shown also in Figure 4.7.

This is a simple example of how this code can be used to simulate the real response of the detector to external input, like the effective power seen by the detector during the observation, or fluctuations of the bath temperature T_b. In the next section we will show some cases studied and their results.

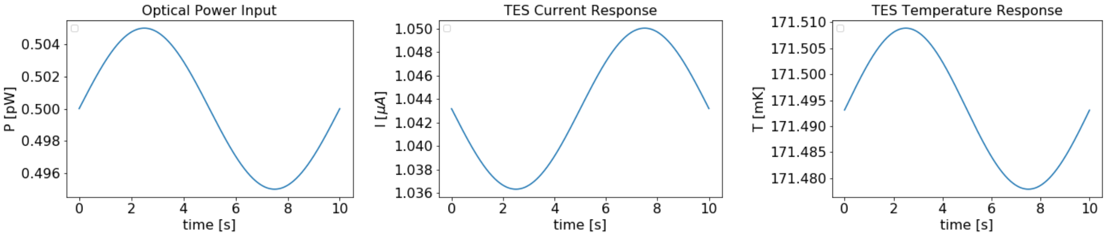

Figure 4.7: TES biased at $R_{TES} \sim 0.7\ \Omega$. *Left:* Input optical power P_{opt}. The default value is 0.5 pW. We add a sinusoidal signal with 1% amplitude to study the detector response. *Center:* TES current response. *Right:* TES temperature response.

A shortcoming of this code is the required simulation resolution. The baseline sampling rate for the LiteBIRD mission will be of the order of a few tens of Hz (after down-link from the spacecraft – the exact value is still under investigation), therefore in principle a Time-Ordered Data (TOD) simulation could be performed at this rate to obtain real representative data. However, due to the expected thermal time constant $\tau \sim 3$ ms during operation, the time resolution for the numerical simulation needs to be higher than the detector response to avoid numerical errors. Hence, a sampling frequency $\gtrsim 1000$ Hz is required.

This can be complicated even further if we want to study the impact of fast events like cosmic ray glitches; a higher resolution may be required.

4.2.2 Multiplexed readout

Before discussing in details the results of the non-linearity studies, we describe briefly the multiplexing readout scheme that will be employed by LiteBIRD: DfMux or Digital-frequency Multiplexing. The same scheme has been used by the Atacama Pathfinder Experiment (APEX), EBEX, SPT and the POLARBEAR collaborations [135]. It is also one of the possible solutions for CMB-S4 [136].

We can divide multiplexed readout technologies into two major categories: Time-Domain Multiplexing (TDM) and Frequency-Domain Multiplexing (FDM) [137]. In the former case (TDM) several detectors are read through the same channel by rapidly (much faster than the response of the single detector) switching between detectors so that at any given time only a single detector in the channel is effectively connected to the read-out. While in the latter case (FDM), detectors in the same read-out channel are biased at different frequencies so that they can be amplified and read-out at the same time. FDM technologies have become more popular with the increase of experiment size because they require less wiring between the coldest stages of telescopes (focal plane) and the warmer stages, therefore reducing thermal loading. DfMux is not the only FDM technology available in the CMB community, but it is currently the more advanced since it has been successfully employed in several experiments with 1000s of deployed detectors. Another scheme that is becoming increasingly popular thanks to its recent partial adoption by the BICEP/Keck collaboration [138] and its selection for future use in Simons Observatory [139], is known as microwave-multiplexing or μMux [140]. Without going into details, the main difference between DfMux and μMux comes from the range of the available total readout bandwidth: $\sim 10-100$ MHz for the DfMux system, and ~ 10 GHz for the μMux system. In principle, if the single detector bandwidth is fixed, this offers a clear advantage to the μMux system because of the much larger total bandwidth. Comprehensive details of the current status of the DfMux system are available in [141, 142]. In Figure 4.8 we show a simplified sketch of the system. The system can be roughly divided into two parts. First, the warm electronics that consists of a FPGA responsible for biasing the detectors as well as reading and storing the output, a warm amplifier and some passive components necessary to set the correct working points. This part of the readout does not require cooling and can be placed outside the cryostat. Second, the cold electronics which consists of the TES detectors on the focal plane (each coupled to a LC filter in series), the SQUID amplifiers, the shunt resistor or inductor. In the current configuration the SQUID amplifier is placed at the same temperature stage as the detectors (100 mK for LiteBIRD). In earlier implementations of the system, the SQUID

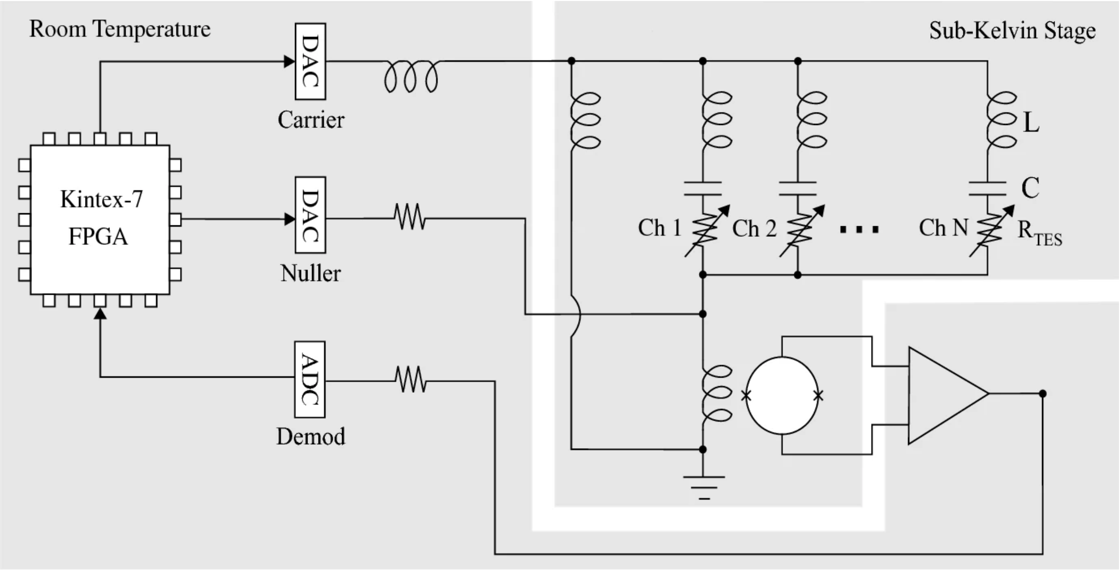

Figure 4.8: The most recent schematic for the DfMux readout system from [142].

amplifier was sitting on a cold intermediate stage. This new solution is projected to reduce the effect of parasitic impedance due to the long wiring needed when detectors and SQUIDs are on different stages.

As visible in Figure 4.8, a SQUID amplifier reads the current from N detectors. The N detectors are AC voltage-biased in parallel, and each detector is connected in series to a LC filter. This solution allows the FPGA to generate a series of N carrier signals at different frequency (tones) on the same bias line. Each LC filter selects only one tone of frequency $\nu_{LC} = 1/2\pi\sqrt{LC}$. The signals are summed again after going through each TES detector and coupled to a single SQUID amplifier. To keep the signal in the SQUID dynamic range a nulling signal of opposite polarity is summed to the signal before coupling it to the SQUID input.

Due to this specific architecture, which AC-biases the detectors (compared to the DC-bias case explained in the previous section) we find that the responsivity of the detector becomes:

$$S_I = -\frac{\sqrt{2}}{V_{rms}}\frac{\mathcal{L}}{\mathcal{L}+1}\frac{1}{1+i\omega\tau} \quad [A/W], \tag{4.17}$$

where V_{rms} is the root mean square value of the AC voltage across the detector (corresponding to $1/2\sqrt{2}$ of the peak-to-peak value for a sinusoidal signal).

By changing the capacitance C_i value of each LC filter N different ν_{LC} tones are obtained in the MHz range. We have modified the simple code presented in 4.2.1 to account for the AC-bias and the presence of the LC filters. However, given the tone frequency range ($\sim 1-10$ MHz), the simulation becomes even more computationally expensive. Therefore, we show in Figure 4.9 only the result of a simple test done to check the code performance, but in the next section we will revert to the DC analysis to test the detector non-linearity. However, with the AC code already implemented, in the future we can develop more extensive studies of the detector response, in particular to address cross-talk effects and correlated noise between detectors. To simulate the AC-biased TES, Equation 4.5 needs to be modified to:

$$(L+L_{LC})\frac{d^2I}{dt^2} = \frac{dV}{dt} - \frac{dI}{dt}(R_{TES}+R_s) - \frac{I}{C_{LC}}, \tag{4.18}$$

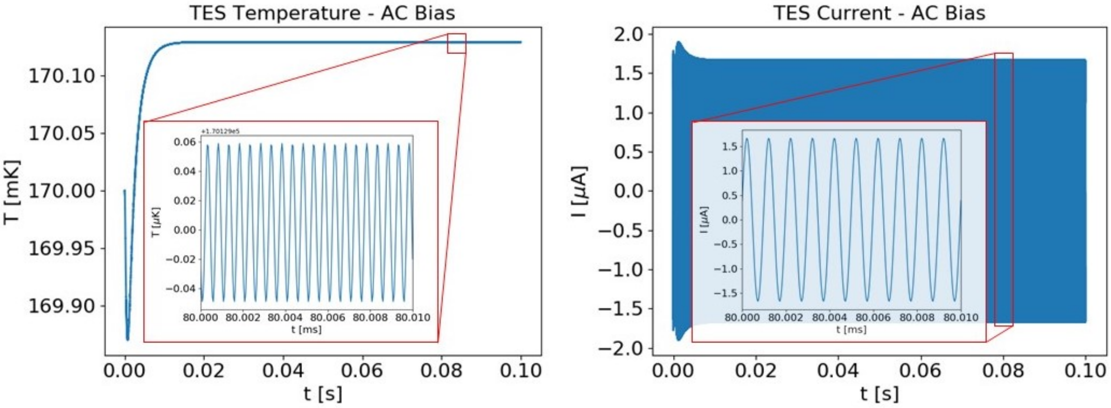

Figure 4.9: AC biased TES response evolution for a stable optical power input of 0.5 pW. The bias is driven at frequency $\nu_{LC} = 1$ MHz for this example. After assigning the initial condition, the detector response stabilizes on a time scale $\sim \tau$.

where L_{LC} and C_{LC} are the inductance and capacitance of the LC filter. For now we assumed a shunt resistance R_s, there is a possibility of using a shunt inductor like in Figure 4.8 that can be also implemented if necessary.

4.3 Non-linearity effects

The response of the detector is fixed by the operation point which is set by the electrical bias and the optical loading power, as well as the temperature of the thermal reservoir. Several external factors can affect the operation point and change the effective responsivity of the detector during observation. In this section we assume the analytical temperature-resistance relation (arctan approximation) in Figure 4.2 (right) to address some of the effects that can cause a non-linear response of the TES detector in the DC-bias case. In first approximation the results presented can be translated to the AC-biased case by computing the amplitude of the equivalent AC voltage required to obtain the same responsivity.

In the following we analyze the effect of variation of the optical loading power P_{opt}, thermal bath T_b and biasing current I_{bias}. A fourth example will be discussed in Chapter 5 when considering external magnetic fields. We study each case for two effective bias points: $R_{TES} \sim 0.7\ \Omega$ and $R_{TES} \sim 0.5\ \Omega$. The first one is justified by the fact that several past and current experiments have used $R_{TES} \sim 0.7 R_n$ as the target for detector operation. However, by moving the operation point deeper into the TES transition, a faster and more stable response can be obtained, as we will see in the following. Therefore, in principle reducing the effective resistance of the detector during operation can be an advantage. Unfortunately, a lower detector resistance can increase the susceptibility of the system to parasitics, hence we need to consider all advantages and disadvantages when defining the optimal operation point. On top of that, the detector speed needs to be limited to avoid instabilities [122]. The recent efforts put into increasing the technological readiness of the DfMux system are pointing in the direction of a reduction of parasitic impedance [142], therefore the choice of $R_{TES} \sim 0.5\ \Omega$ may be justified, although it needs to be experimentally tested.

A summary of the parameters we have taken into account to study detector non-linearity is given in Table 4.1, along with some of the items we have identified that can act as a source of non-linearity associated with each parameter. This list can serve as reference for future studies; at the end of the chapter we present a study of the level of non-linearity expected from the presence of Galactic foregrounds.

Parameter	Source
P_{opt}	Planets
	Galactic plane (foregrounds)
	Excess loading from optical elements
	Cosmic ray direct hits
	HWP differential transmission and emission
T_b	Cosmic ray wafer hits
	Focal plane thermal stability
	Fridge thermal stability
I_{bias}	Parasitics
	"Warm" electronics stability

Table 4.1: Detector non-linearity. In the model presented in this chapter we have identified three parameters that can produce a non-linear response: optical loading P_{opt}, bath temperature T_b and bias current I_{bias}. In this table we list some of the sources that can cause these three parameters to exceed the nominal range and result in non-linear response of the detectors.

4.3.1 Non-linearity for $R_{TES} \sim 0.7\ \Omega$

We use the code described in the previous section to simulate the detector response for an expected optical power $P_{opt} = 0.5$ pW. We fix the bath temperature $T_b = 0.100$ K and we bias the TES at $R_{TES} = 0.7\ \Omega$. Once the response is stable we inject a fluctuation of optical power or bath temperature fluctuations or bias current to study the variation in the detector response. In the following we show a few cases.

4.3.1.1 Optical loading: $P_{opt} = 0.5$ pW ± 1%

In this first case we study the effect of small variations of optical loading power. We inject a sinusoidal signal ($\omega \ll 1/\tau$) with 1% amplitude with respect to the expected value $P_{opt} = 0.5$. For most frequency channels the main signal across the sky (after the CMB monopole and telescope loading) is the CMB dipole which is responsible for variations of the order $\sim \pm 0.1\%$ ($T_{dipole} \sim 3$ mK).

After performing the simulation we compute the relevant detector parameters (α, $\mathcal{L}$, τ and S_I) as a function of the effective loading power, as shown in Figure 4.10. For each parameter we fit the result with a polynomial of order n. We keep increasing the polynomial order till the difference between the simulated data and the fit is $< 0.1\%$. The functional form found through the fitting routine for each parameter is shown in the legend (red dashed line), along with the expected value for stable response value (blue cross).

The rationale of this analysis choice comes from the possibility of using the parameters of the fit to simulate detector non-linearity assuming some well physically motivated variations of loading power, without the need to simulate the detector response at the same time. An example will be given in the last section of this Chapter. Note that this procedure is valid assuming that the variations are slow compared to the thermal response of the detector ($\omega < 1/\tau$). For variations on similar or shorter time scales the detector response needs to be simulated in real-time (e.g. cosmic rays).

The same procedure will be applied to all remaining cases.

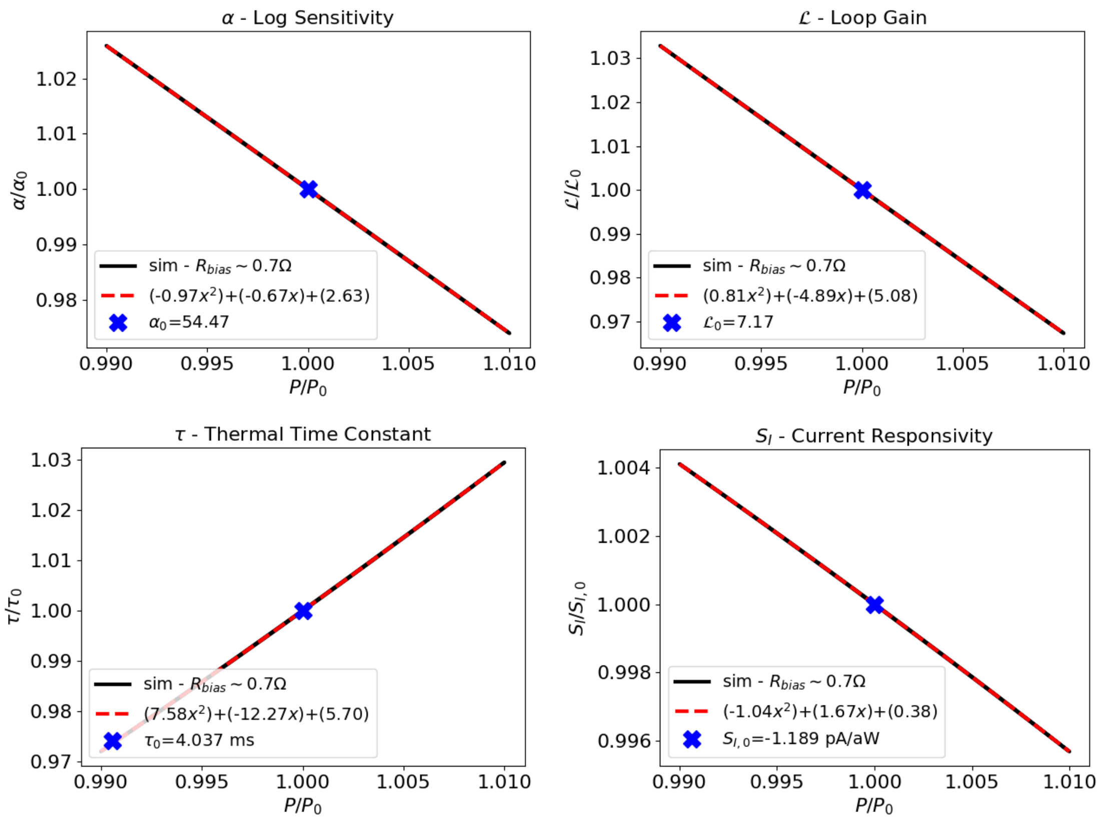

Figure 4.10: TES biased at $R_{TES} \sim 0.7\ \Omega$. We study variation of the logarithmic responsivity α, loop gain $\mathcal{L}$, thermal time constant τ and current responsivity S_I for 1% P_{opt} variation with respect to a default value 0.5 pW. *Top left:* Fractional variation of α as a function of fractional variation of the optical power. *Top right:* Fractional variation of $\mathcal{L}$ as a function of fractional variation of the optical power. *Lower left:* Fractional variation of τ as a function of fractional variation of the optical power. *Lower right:* Fractional variation of S_I as a function of fractional variation of the optical power. The *blue* cross indicates the default value at the bias point for P_{opt} =0.5 pW.

As discussed in [125], differential transmission and emission (along the two orthogonal optical axis of the HWP) of the telescope optical elements can cause "large" optical loading fluctuations and, by coupling to the rotating HWP, create I to P leakage. This effect is clearly visible in the EBEX data presented in [125] when comparing them with Planck data, and should be taken into account carefully when designing LiteBIRD HWP and detectors.

4.3.1.2 Optical loading: $P_{opt} = 0.5$ pW $\pm$ 100%

Although for most frequencies optical variations are expected to be of the order of $\sim 1\%$, thermal dust becomes brighter and dominant along the Galactic plane at high frequency. Therefore, we include a case where the optical power increases up to 100% of the expected value P_{opt}.

From Figure 4.11 we can observe that the detector becomes completely saturated above $\sim$ 60% power increase.

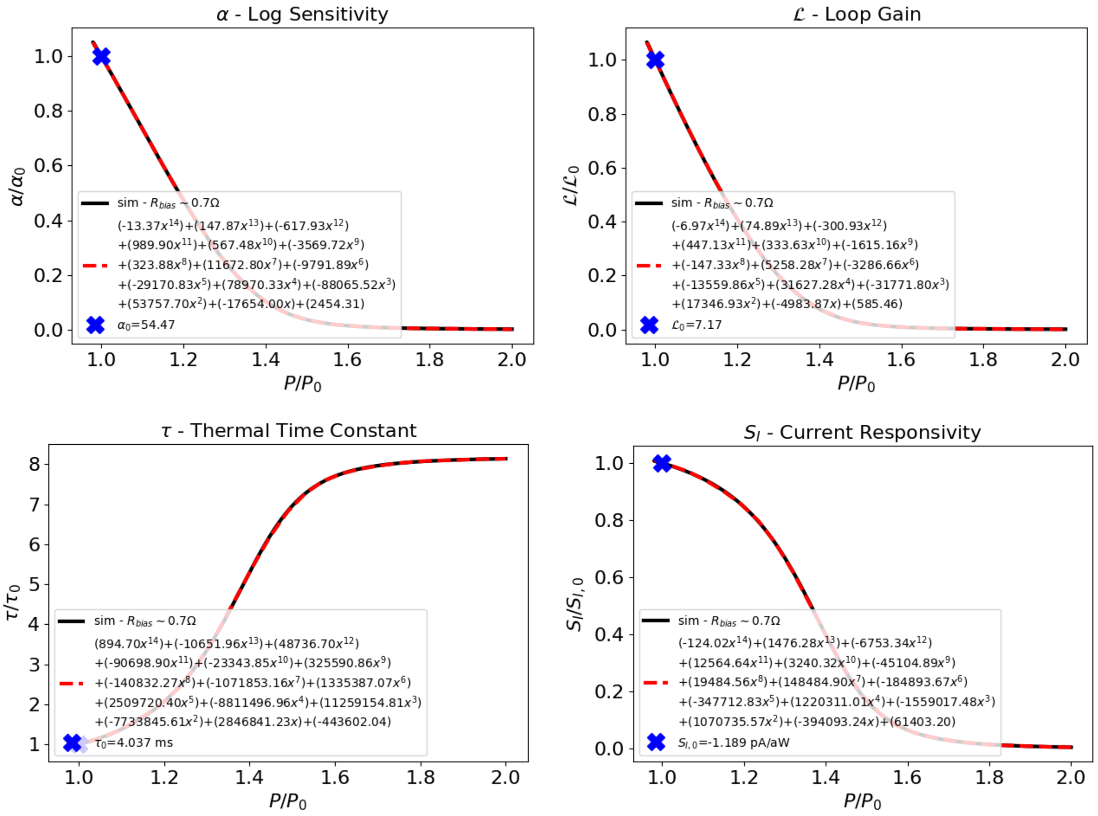

Figure 4.11: TES biased at $R_{TES} \sim 0.7\ \Omega$. We study variation of the logarithmic responsivity α, loop gain $\mathcal{L}$, thermal time constant τ and current responsivity S_I for 100% P_{opt} variation with respect to a default value 0.5 pW. *Top left:* Fractional variation of α as a function of fractional variation of the optical power. *Top right:* Fractional variation of $\mathcal{L}$ as a function of fractional variation of the optical power. *Lower left:* Fractional variation of τ as a function of fractional variation of the optical power. *Lower right:* Fractional variation of S_I as a function of fractional variation of the optical power. The *blue* cross indicates the default value at the bias point for P_{opt} =0.5 pW.

4.3.1.3 Bath temperature: $T_{bath} = 0.100$ K $\pm$ 0.001 K.

Similarly to what we have shown for the optical power we address the effect of varying bath temperature. We limit variations to ±1 mK.

The results are shown in Figure 4.10. This analysis can be revised once the details of thermal fluctuations of the focal plane are well known. This case is of particular interest to study the origin of $1/f$ noise in the detectors.

Under different assumptions this can be used also to simulate the effect of cosmic ray impacts on the focal plane.

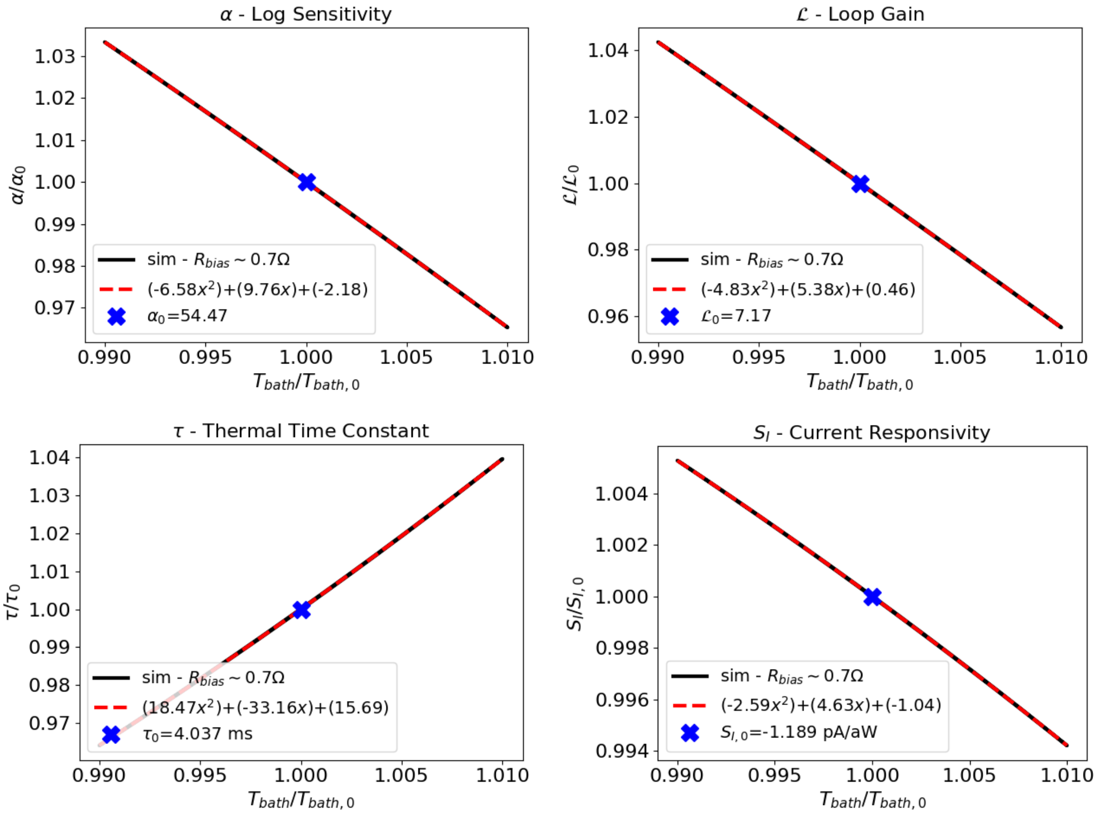

Figure 4.12: TES biased at $R_{TES} \sim 0.7\ \Omega$. We study variation of the logarithmic responsivity α, loop gain $\mathcal{L}$, thermal time constant τ and current responsivity S_I for 0.001 K T_{bath} variations with respect to a default value 0.100 K. *Top left:* Fractional variation of α as a function of fractional variation of T_{bath}. *Top right:* Fractional variation of $\mathcal{L}$ as a function of fractional variation of T_{bath}. *Lower left:* Fractional variation of τ as a function of fractional variation of T_{bath}. *Lower right:* Fractional variation of S_I as a function of fractional variation of T_{bath}. The *blue* cross indicates the default value at the bias point for P_{opt} =0.5 pW and T_{bath} =0.100 K.

4.3.1.4 Bath temperature: $T_{bath} = 0.100$ K $\pm$ 0.01 K.

For the sake of completeness in Figure 4.13 we show the same plots for larger variations of T_{bath}: ±10 mK.

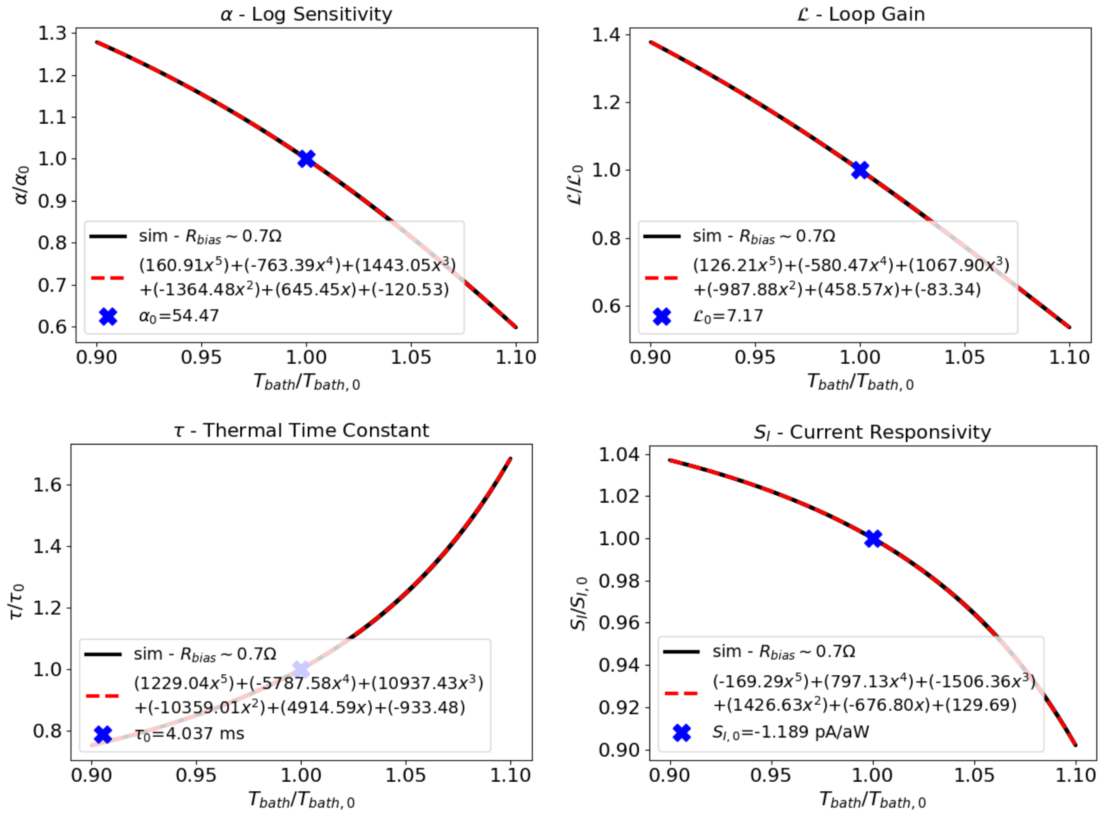

Figure 4.13: TES biased at $R_{TES} \sim 0.7\ \Omega$. We study variation of the logarithmic responsivity α, loop gain $\mathcal{L}$, thermal time constant τ and current responsivity S_I for 0.01 K T_{bath} variations with respect to a default value 0.100 K. *Top left:* Fractional variation of α as a function of fractional variation of T_{bath}. *Top right:* Fractional variation of $\mathcal{L}$ as a function of fractional variation of T_{bath}. *Lower left:* Fractional variation of τ as a function of fractional variation of T_{bath}. *Lower right:* Fractional variation of S_I as a function of fractional variation of T_{bath}. The *blue* cross indicates the default value at the bias point for P_{opt} =0.5 pW and T_{bath} =0.100 K.

4.3.1.5 Bias current: $I_{bias} = 38\ \mu\mathrm{A} \pm 1\ \%$.

Lastly we study non-linearity effects due to varying bias current I_{bias}. We limit variations to ±1%.

Results are shown in Figure 4.14. Variations of the electrical bias might be connected to thermal fluctuations of the warm electronics, although at present a clear physical modelling is missing. These results can serve as a starting point for discussion.

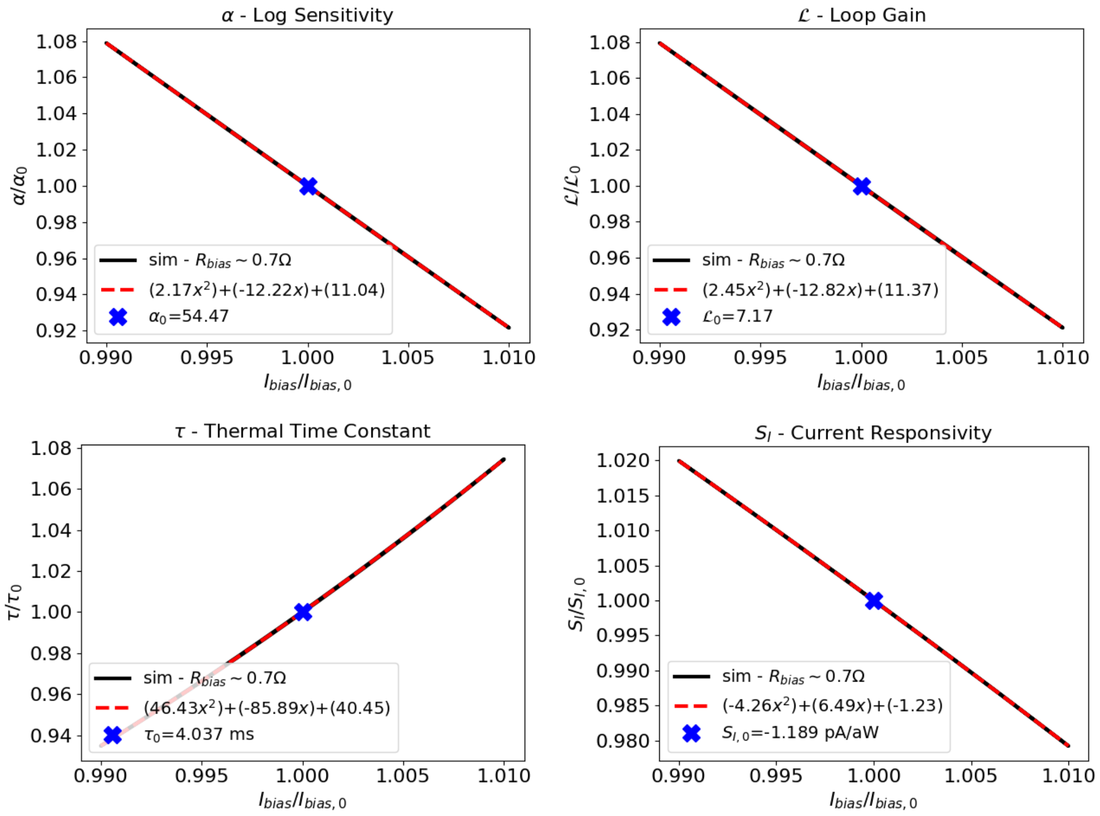

Figure 4.14: TES biased at $R_{TES} \sim 0.7\ \Omega$. We study variation of the logarithmic responsivity α, loop gain $\mathcal{L}$, thermal time constant τ and current responsivity S_I for 1% I_{bias} variations with respect to a default value of 38 μA. *Top left:* Fractional variation of α as a function of fractional variation of I_{bias}. *Top right:* Fractional variation of $\mathcal{L}$ as a function of fractional variation of I_{bias}. *Lower left:* Fractional variation of τ as a function of fractional variation of I_{bias}. *Lower right:* Fractional variation of S_I as a function of fractional variation of I_{bias}. The *blue* cross indicates the default value at the bias point for P_{opt} =0.5 pW and T_{bath} =0.100 K.

4.3.2 Non-linearity for $R_{TES} \sim 0.5\ \Omega$

As already explained, we present the results for a different operation point: $R_{TES} \sim 0.5\ \Omega$. This operation point gives faster and more stable response due to stronger electro-thermal feedback. Therefore, as we can see from the results, non-linearity effects are reduced compared to the $R_{TES} \sim 0.7\ \Omega$ case.

4.3.2.1 Optical loading: $P_{opt} = 0.5$ pW $\pm$ 1%

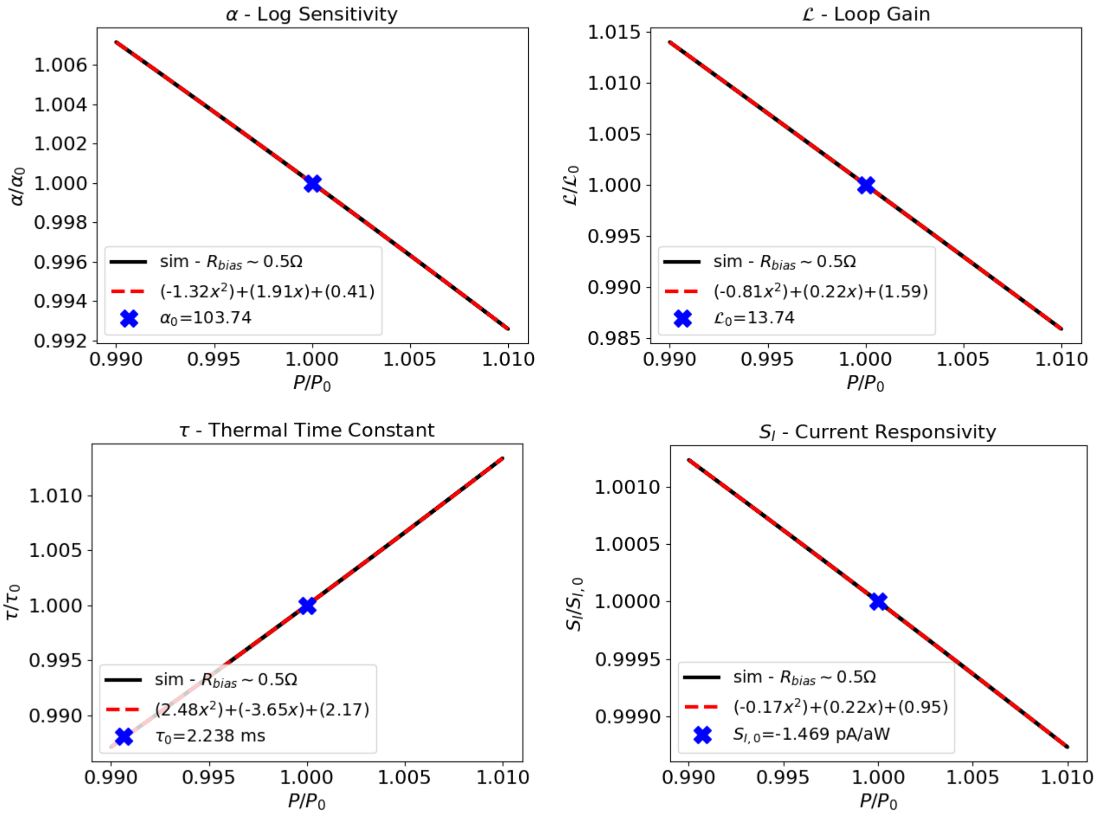

Figure 4.15: TES biased at $R_{TES} \sim 0.5\ \Omega$. We study variation of the logarithmic responsivity α, loop gain $\mathcal{L}$, thermal time constant τ and current responsivity S_I for 1% P_{opt} variation with respect to a default value 0.5 pW. *Top left:* Fractional variation of α as a function of fractional variation of the optical power. *Top right:* Fractional variation of $\mathcal{L}$ as a function of fractional variation of the optical power. *Lower left:* Fractional variation of τ as a function of fractional variation of the optical power. *Lower right:* Fractional variation of S_I as a function of fractional variation of the optical power. The *blue* cross indicates the default value at the bias point for P_{opt} =0.5 pW.

4.3.2.2 Optical loading: P_{opt} = 0.5 pW ± 100%

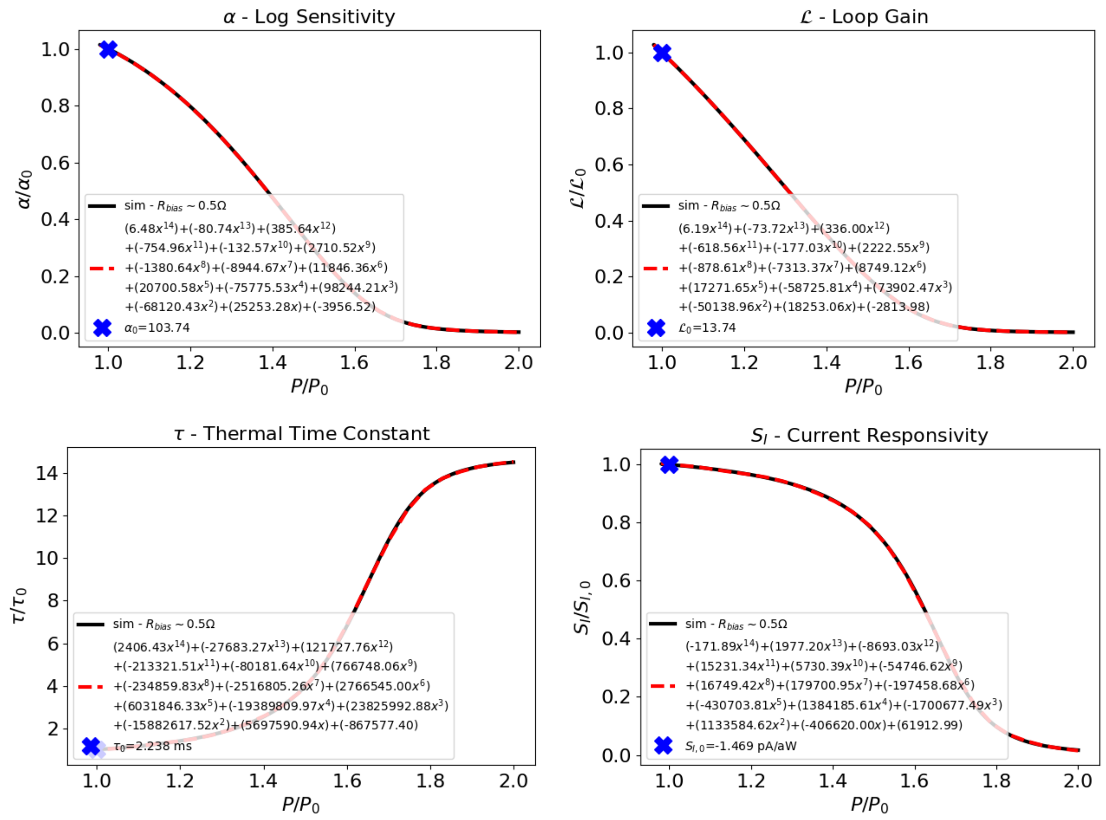

Figure 4.16: TES biased at $R_{TES} \sim 0.5\ \Omega$. We study variation of the logarithmic responsivity α, loop gain $\mathcal{L}$, thermal time constant τ and current responsivity S_I for 100% P_{opt} variation with respect to a default value 0.5 pW. *Top left:* Fractional variation of α as a function of fractional variation of the optical power. *Top right:* Fractional variation of $\mathcal{L}$ as a function of fractional variation of the optical power. *Lower left:* Fractional variation of τ as a function of fractional variation of the optical power. *Lower right:* Fractional variation of S_I as a function of fractional variation of the optical power. The *blue* cross indicates the default value at the bias point for P_{opt} =0.5 pW.

4.3.2.3 Bath temperature: $T_{bath} = 0.100$ K $\pm$ 0.001 K.

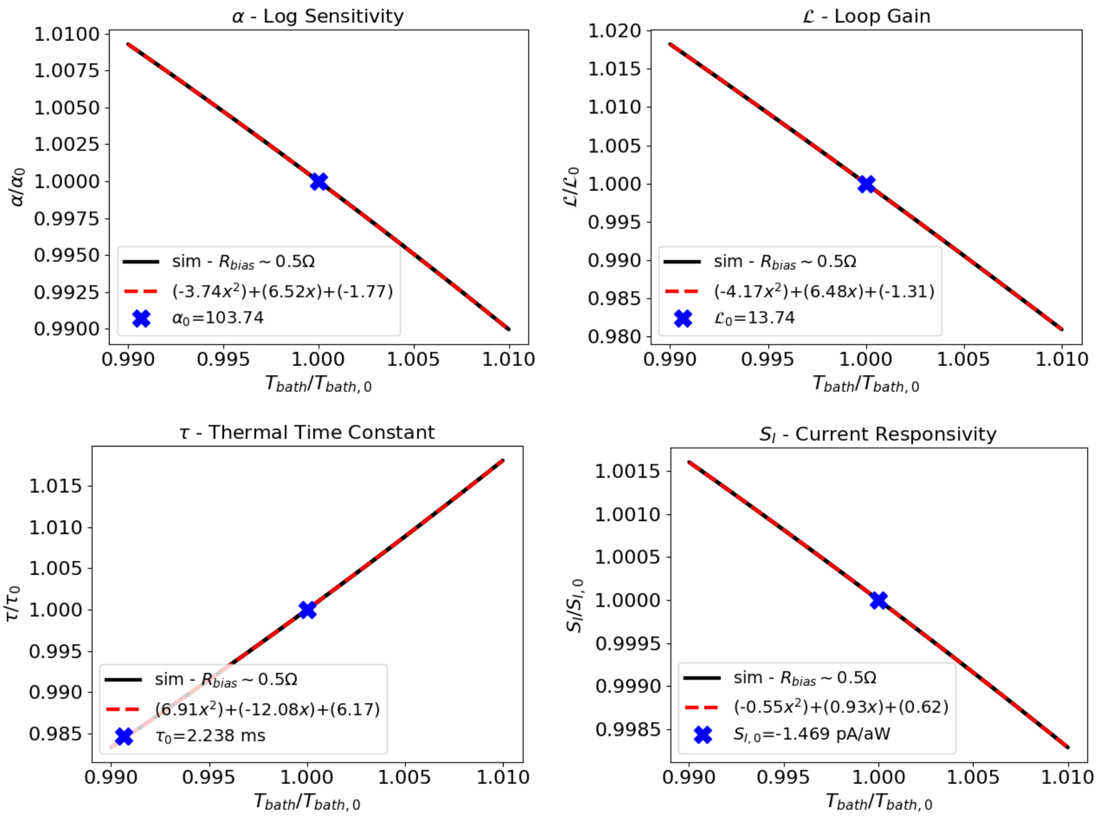

Figure 4.17: TES biased at $R_{TES} \sim 0.5\ \Omega$. We study variation of the logarithmic responsivity α, loop gain $\mathcal{L}$, thermal time constant τ and current responsivity S_I for 0.001 K T_{bath} variations with respect to a default value 0.100 K. *Top left:* Fractional variation of α as a function of fractional variation of T_{bath}. *Top right:* Fractional variation of $\mathcal{L}$ as a function of fractional variation of T_{bath}. *Lower left:* Fractional variation of τ as a function of fractional variation of T_{bath}. *Lower right:* Fractional variation of S_I as a function of fractional variation of T_{bath}. The *blue* cross indicates the default value at the bias point for P_{opt} =0.5 pW and T_{bath} =0.100 K.

4.3.2.4 Bath temperature: T_{bath} = 0.100 K ± 0.01 K.

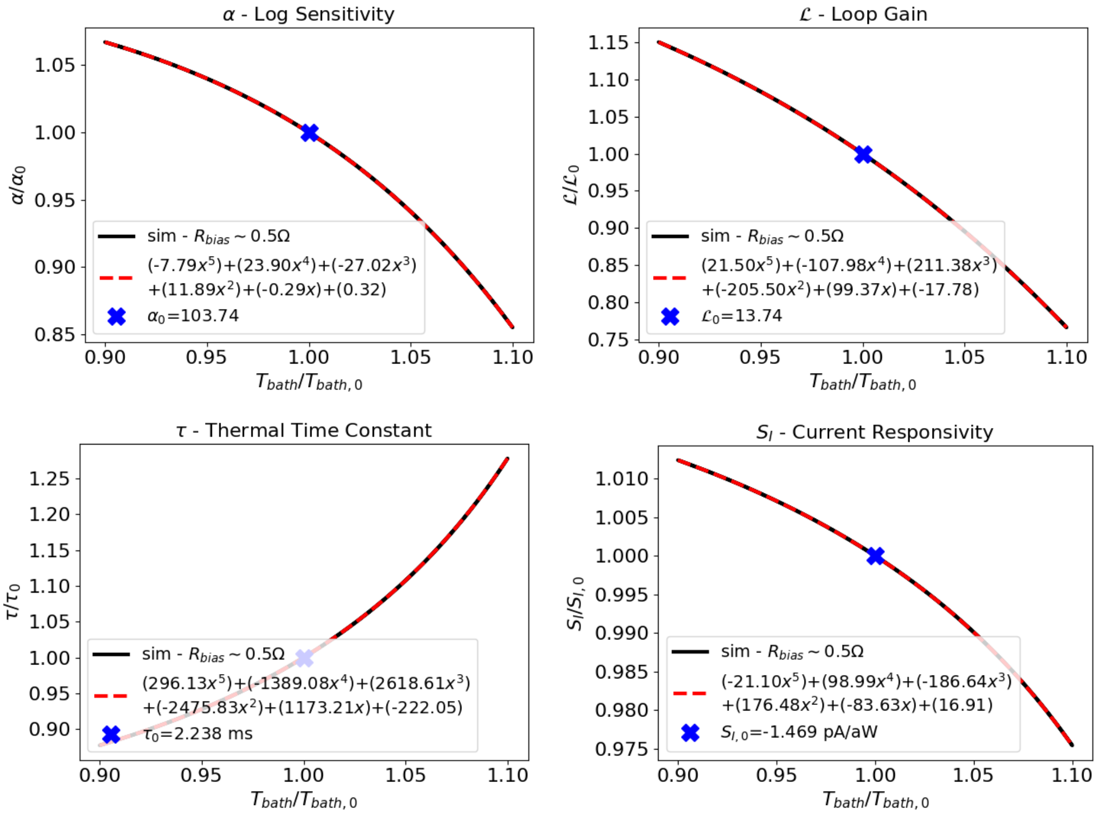

Figure 4.18: TES biased at $R_{TES} \sim 0.5\ \Omega$. We study variation of the logarithmic responsivity α, loop gain $\mathcal{L}$, thermal time constant τ and current responsivity S_I for 0.01 K T_{bath} variations with respect to a default value 0.100 K. *Top left:* Fractional variation of α as a function of fractional variation of T_{bath}. *Top right:* Fractional variation of $\mathcal{L}$ as a function of fractional variation of T_{bath}. *Lower left:* Fractional variation of τ as a function of fractional variation of T_{bath}. *Lower right:* Fractional variation of S_I as a function of fractional variation of T_{bath}. The *blue* cross indicates the default value at the bias point for P_{opt} =0.5 pW and T_{bath} =0.100 K.

4.3.2.5 Bias current: $I_{bias} = 33\ \mu$A $\pm$ 1 %.

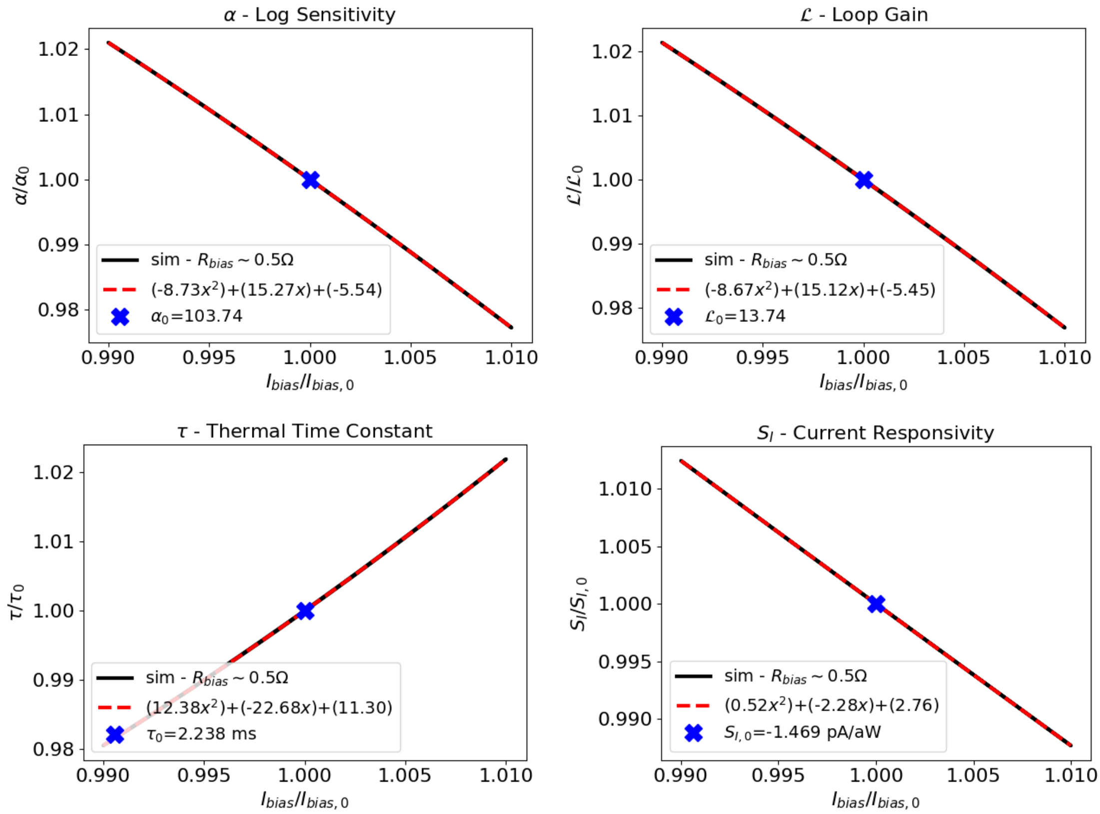

Figure 4.19: TES biased at $R_{TES} \sim 0.5\ \Omega$. We study variation of the logarithmic responsivity α, loop gain $\mathcal{L}$, thermal time constant τ and current responsivity S_I for 1% I_{bias} variations with respect to a default value of 33 μA. *Top left:* Fractional variation of α as a function of fractional variation of I_{bias}. *Top right:* Fractional variation of $\mathcal{L}$ as a function of fractional variation of I_{bias}. *Lower left:* Fractional variation of τ as a function of fractional variation of I_{bias}. *Lower right:* Fractional variation of S_I as a function of fractional variation of I_{bias}. The *blue* cross indicates the default value at the bias point for P_{opt} =0.5 pW and T_{bath} =0.100 K.

4.3.3 Galactic signal

As described in the previous section, varying optical power can drive the detector into non-linear regime and negatively impact the photometric calibration, if not addressed correctly. In Chapter 3 we derived requirements for the photometric calibration accuracy in order to minimize the impact on the recovered tensor-to-scalar ratio parameter. We found a requirement (per detector) $\delta_g \sim 0.16 \times 10^{-2}$ driven by the high frequency channels.

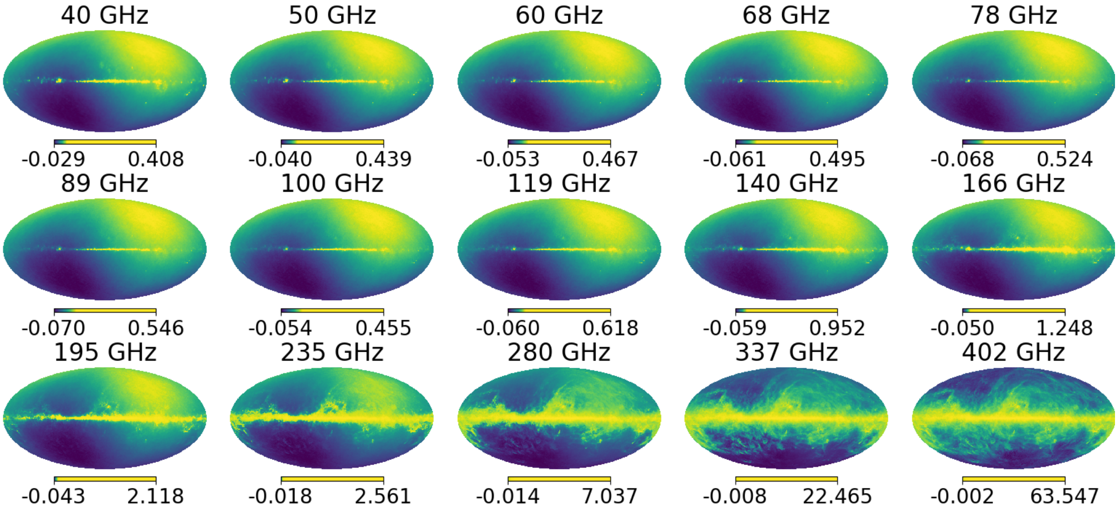

Figure 4.20: Percent variation of optical power with respect to the CMB monopole and telescope loading dominant contributions. As we can see the variations are dominated by the dipole at low frequency, apart for the area close to the galactic plane, while at high frequency the Galaxy becomes more important.

We make use of the P_{opt}-S_I relation found in Figure 4.15 to address the level of non-linearity caused by varying optical power during the observation of the sky. The optical power in space is dominated by the CMB monopole and the loading from the optical elements of the telescope. However, due to CMB temperature anisotropies (including the dipole) and unpolarized foregrounds, the effective power loading the detectors can change from pixel to pixel.

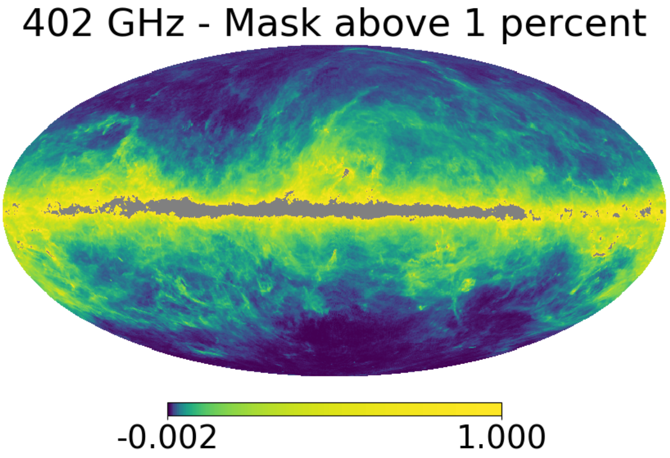

Figure 4.21: Percent variation of optical power with respect to the CMB monopole and telescope loading dominant contributions at 402 GHz. We masked the area corresponding to $\Delta P > 1\%$.

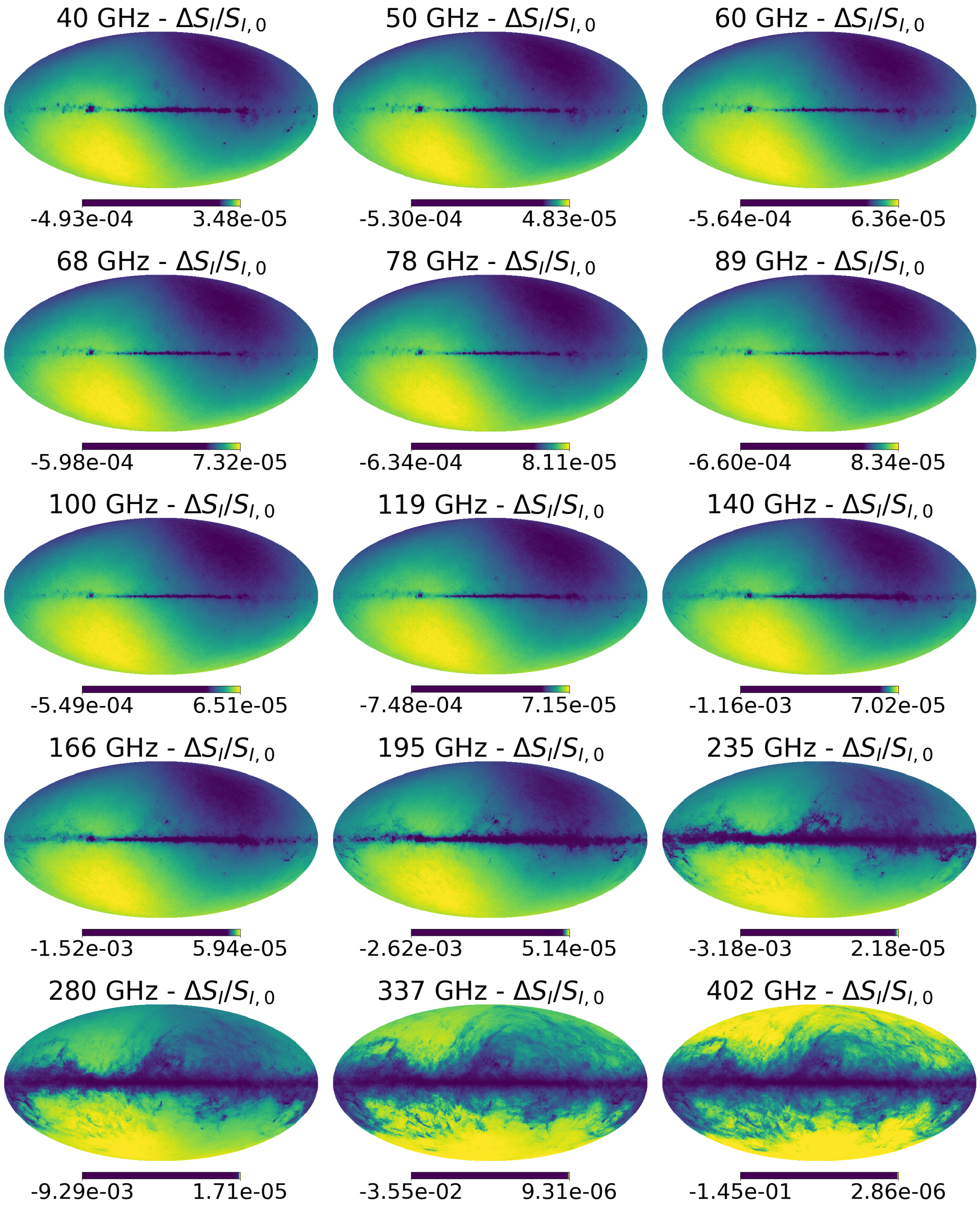

Figure 4.22: Variation of the detector gain due to non-linearity of the TES response due to varying optical power per pixel. The power variation is due to the presence of CMB dipole, anisotropies and Galactic foregrounds and it is computed with respect to the dominant CMB monipole and telescope internal loading.

In Figure 4.20, we created maps per frequency channel including all major components (CMB monopole, telescope loading, dipole, temperature anisotropies, unpolarized dust, synchrotron and free-free) to estimate the varying optical power across the sky. The maps are expressed in percent power variation ΔP with respect to a expected value due to the dominant CMB monopole and telescope loading. We can observe that, at frequencies $\nu \lesssim 150$ GHz, the power remains rather constant with $\Delta P \lesssim 1\%$, while at higher frequencies the thermal dust contribution becomes increasingly dominant along the Galactic plane. However, to show that the effect is limited to an area relatively small and confined to the Galactic plane, typically not used for cosmology, we show in Figure 4.21 the same map at 402 GHz with the area corresponding to $\Delta P > 1\%$ masked.

Using the analysis summarized in Figure 4.15 we can convert the ΔP maps to ΔS_I maps, corresponding to gain fluctuations due to non-linearity of the detector (biased at $R \sim 0.5\ \Omega$ corresponding to $\mathcal{L} \sim 13$):

$$\frac{S_I}{S_{I,0}} = -0.17\left(\frac{P}{P_0}\right)^2 + 0.22\frac{P}{P_0} + 0.95, \tag{4.19}$$

where S_I is the value in each pixel for a power P, while $S_{I,0}$ is the expected value for P_0 (assuming that the signal is dominated by the CMB monopole and the telescope internal loading). In the limit of non-linearity of the system driven solely by varying optical power seen by the detectors, this can be related to the required accuracy of the photometric calibration per detector: $\delta_g = \Delta S_I/S_{I,0}$.

In Figure 4.22 we show the result for all frequency channels. We can notice that for most channels the variation is smaller than the requirement $\delta_g \sim 0.16 \times 10^{-2}$ everywhere across the sky. The only channels where the effect is larger than the requirement are those for $\nu > 195$ GHz. However, even for the worst case channel at 402 GHz, the effect is limited to a small and confined region close to the Galactic center, as we can see in Figure 4.23, where we masked the region where the variation is larger than the requirement value. We can observe that this area is fully contained inside the masked region used in the cosmological analysis in Chapter 3. Therefore we can conclude that in the limit defined at the beginning of this section, this

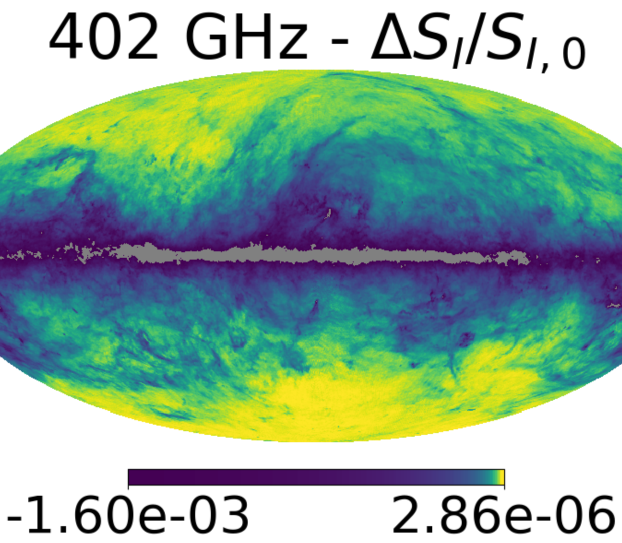

Figure 4.23: Fractional variation of the detector gain due to detector non-linearity caused by varying optical power on the detector at 402 GHz. The area where the variation is larger than the requirement on photometric calibration accuracy as discussed in Chapter 3 is masked (grey colour).

non-linearity effect will have minimal impact on the cosmological analysis. However, it may have a significant impact on Galactic science. In this context we performed a quick test to determine whether the non-linearity can cause a significant bias in the measured polarization level ($P = \sqrt{Q^2 + U^2}$) along the galactic plane, where the

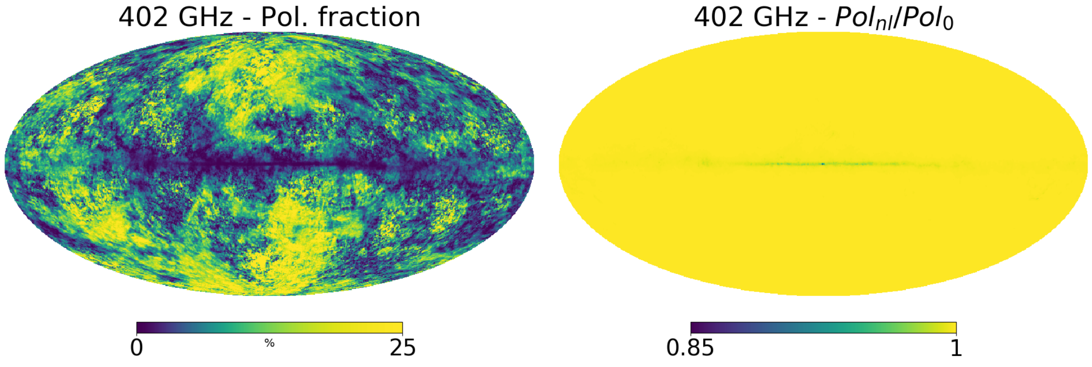

Figure 4.24: *Left:* Dust polarization fraction P/I at 402 GHz. The colorbar shows the percent level. *Right:* Effect of non-linearity on the reconstructed polarized intensity. Fractional difference between input dust map and reconstructed dust map. The effect appears to be significant ($\sim 15\%$) only in the proximity of the galactic center.

non-linearity effect appears to be more dominant. In Figure 4.24 (left) we show the dust polarization fraction (P/I) at 402 GHz as generated with $PySM$ using Planck results. Using these data and the non-linearity maps in Figures 4.22 and 4.23 we created a reconstructed polarized intensity map in presence of detector non-linearity induce by the dust extra loading: $P_{nl} = P_0 + \frac{\Delta S_I}{S_I} P_0$ (where P_0 is the input polarized intensity). In the right panel of Figure 4.24 we show P_{nl}/P_0. The effect appears to be relevant only in the proximity of the galactic center where the polarized intensity is underestimated by $\sim 15\%$. However, a broader analysis of the possible sources of detector non-linearity is required to fully address the scale of this effect.

This and other source of detector non-linearity will be addressed in more details in the future. We hope that this Chapter can serve as a starting point for more comprehensive studies that are needed given the challenging goal of future CMB experiments.

5

Test-Bed Cryostat

In this final chapter, after briefly describing the TES read-out system we implemented and characterized at Kavli IPMU, we present three main topics. In Section 5.1 we describe the TES time-constant model and we show measurements highlighting the dependence from the detector working point. In Section 5.2 we present the design of a test-bed cryostat to test the response of TES detectors in combination with a scaled version of the LFT HWP. Finally in Section 5.3 we discuss the characterization of a customizable castable microwave absorber that could be potentially used to reduce stray-light in optical systems or to fabricate cryogenic calibration targets. The first two sections are partially based on [2], while the third one is based on [1].

Since Kavli IPMU is responsible primarily for the development of the LFT HWP-PMU assembly, we would like to have a test-bed to check that the PMU does not interfere with the detector and read-out system. The first step toward this goal has been to establish a system at Kavli IPMU to learn how to read and test TES detectors. This can be useful to complement tests being done by our American colleagues who are developing these detectors.

In Figure 5.1 we show the set-up at Kavli IPMU. We use a ADR (Adiabatic Demagnetization Refrigerator) from HPD[1], which uses a mechanical refrigerator

---

[1] `https://hpd-online.com/model-106/`

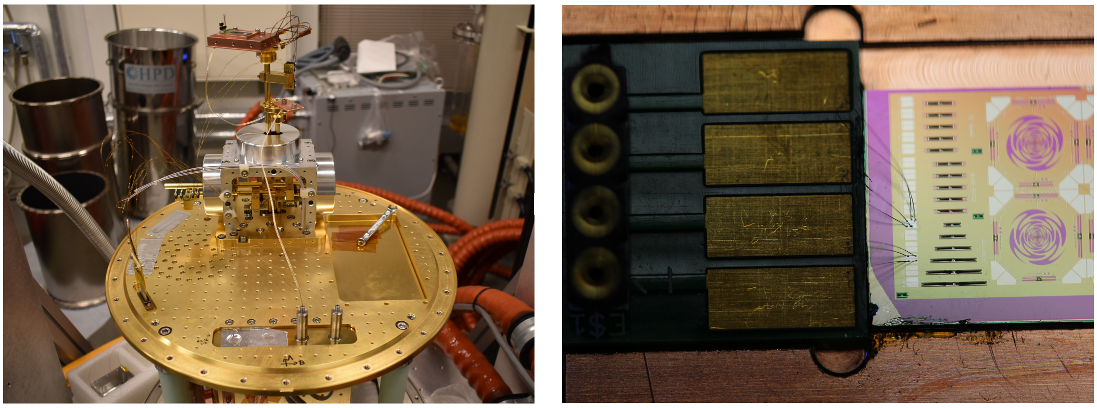

Figure 5.1: *Left:* ADR fridge at Kavli IPMU. The gold-plated plate is cooled by a pulse-tube to 3 K. The ADR has two independent stages: GGG that can be cooled to a base temperature ∼ 500 mK and FAA which can be cooled to a base temperature ∼ 50 mK. A PID system is used to regulate the FAA temperature after cycling the magnet. Two SQUID chips are at the bottom of the picture (not visible because enclosed in Niobium cans for magnetic field shielding). *Right:* A TES test-chip wire-bonded (aluminum wires) to pcb pads ready to be installed on the copper plate attached to the FAA stage of the ADR (top of the picture on the left).

(pulse-tube) to cool two stages to 50 K and 3 K (the 3 K stage is shown in Figure 5.1). The 2-stage ADR fridge sits on the 3 K stage (see Figure 5.1). The two sages use two different paramagnetic salt-pills which set the base temperature of each stage: the GGG (Gadolinium Gallium Garnet) stage can reach 500 mK, while the FAA (Ferric Ammonium Alum) stage can be cooled to ∼ 50 mK. A PID controller can be used to regulate the temperature of the stages after the magnetic cycle. Details about the cooling power of the cryostat can be found in Section 5.2.

We implemented a simple readout scheme with dc-SQUIDs as shown in Figure 5.2. The SQUID chips used are from Magnicon[2] [131, 132]. As discussed in Chapter 4 we use dc-SQUIDs in a FLL (Flux Locked Loop) configuration to linearize the SQUID response (the raw response is periodic as described in Chapter 4 and shown in Figure 5.3). The schematic of the system is shown in Figure 5.2. In this configuration a feedback circuit consisting of a resistor R_{fb} and an inductor coupled to the SQUID with mutual inductance M_{fb} keeps the total magnetic flux through the SQUID constant to obtain a constant gain factor: $\Phi_{in} + \Phi_{fb} =$ const. If we write the magnetic flux through the SQUID as $\Phi = MI$ (where I is the current through

---

[2] http://www.magnicon.com/squid-sensors/squid-series-arrays

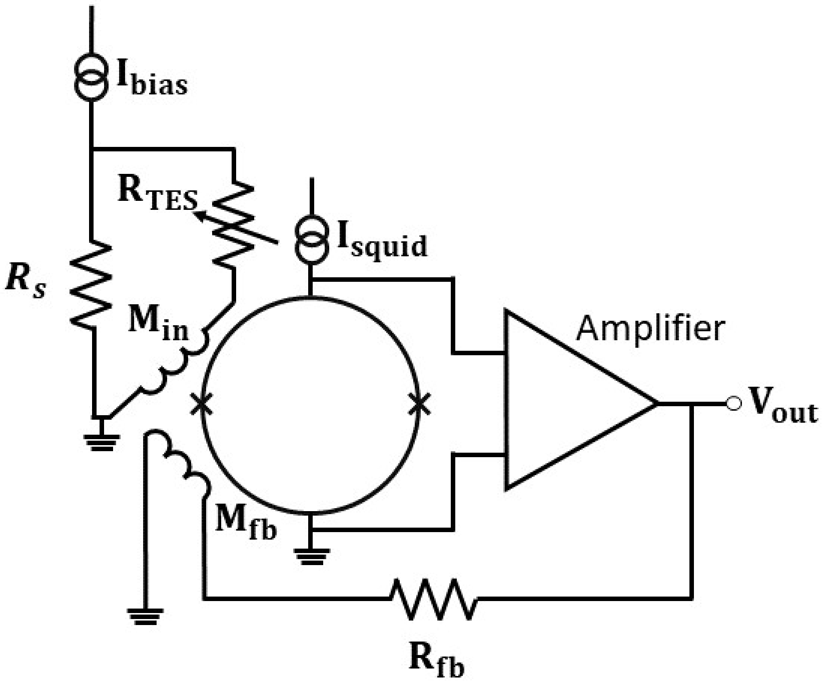

Figure 5.2: Schematic of the TES-SQUID (dc) system implemented in the test-bed cryostat at Kavli IPMU.

a coil and M is the mutual inductance between the coil and the SQUID), in the FLL scheme of Figure 5.2 the output voltage V_{out} can be expressed in terms of the current flowing through the TES I_{TES} as:

$$V_{out} = \frac{R_{fb}}{M_{fb}} M_{in} I_{TES}, \tag{5.1}$$ [3]

where M_{in} is the mutual inductance of the input inductor coupled to the SQUID. In Figure 5.3 we show three plots from the same SQUID showing the periodic response of the SQUID, for the same SQUID bias conditions (adjusted to maximize $\Delta V_{out} = V_{out,max} - V_{out,min}$).

In the left panel we show V_{out} vs. I_{fb}. As expected from the discussion in Chapter 4, we find that one period correspond to a current value equal to the inverse of the feedback coil-SQUID mutual inductance: $1/M_{fb}$. The same plot using the input coil (V_{out} vs. I_{in}) is visible in the central panel, the current value corresponding to one period is equal to $1/M_{in}$. Finally, in the right panel we converted the current values I_{fb} and I_{in} of the previous two panels to the corresponding magnetic

---

[3] M_{fb}, M_{in}, R_{fb} values provided (calibrated) by the manufacturer.

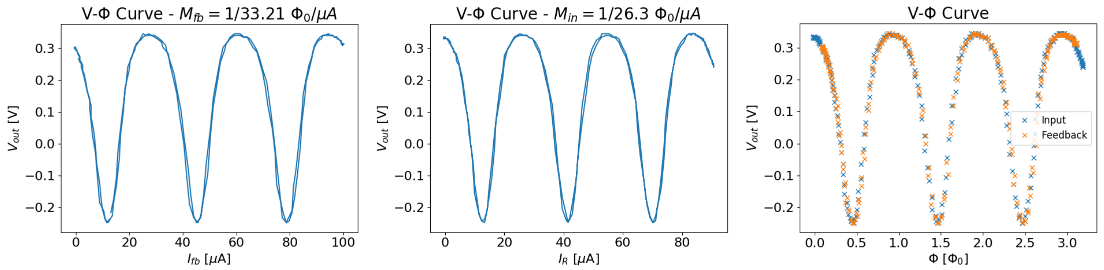

Figure 5.3: SQUID test: $V - \Phi$ curve. The periodic response of the SQUID is shown for optimal bias conditions. *Left:* V_{out} vs. I_{fb}. One period corresponds to a current value $I_{fb} = 1/M_{fb} = 33.21$ μA in this case. *Center:* V_{out} vs. I_{in}. One period corresponds to a current value $I_{in} = 1/M_{in} = 26.3$ μA in this case. *Right:* The previous two plots with the current value converted to magnetic flux in flux quantum units. One period corresponds to one flux quantum.

flux value in units of flux quantum Φ_0. As expected, one period corresponds to one flux quantum Φ_0 in both cases.

When testing the TES detectors we always operate the SQUID in FLL mode to avoid the periodic response of the SQUID. In fact when the total flux through the SQUID is constant, from Equation 5.1 we find that the output voltage value depends only on the constant parameters M_{fb}, M_{in}, R_{fb} (passive components). Thus, the gain is constant and independent from the specific SQUID operating

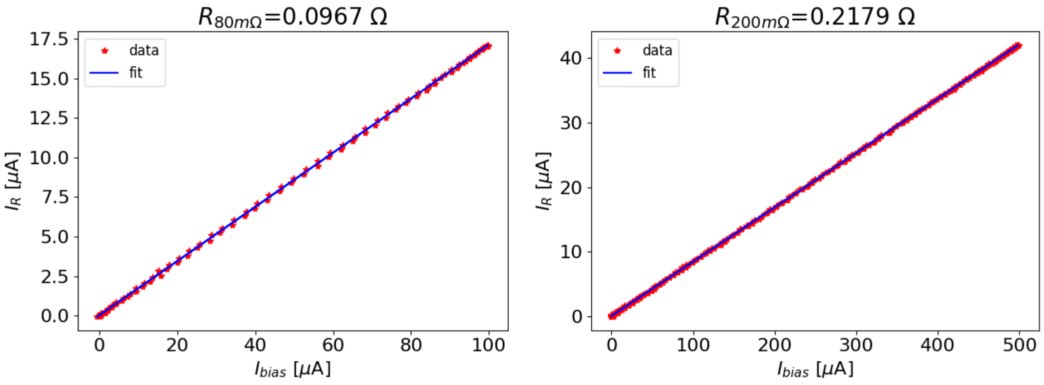

Figure 5.4: SQUID test: measuring resistance of known resistors. *Left:* We replaced the TES with a resistor of known resistance $R = 80$ mΩ at 3 K, and measure it. We obtain the value from a least-square fit $R = 96.7 \pm 0.02$ mΩ. *Right:* Same as *left* with a resistor of known resistance $R = 200$ mΩ at 3 K. We obtain the value from a least-square fit $R = 21.79 \pm 0.01$ mΩ. The excess resistance ~ 0.017 observed in both cases is attributed to the residual resistance of the wiring and soldering material.

point (or the amplifier gain):

$$S_{squid} = \frac{R_{fb}}{M_{fb}} M_{in}. \tag{5.2}$$

In order to measure the absolute resistance of TES detectors, we tested the system with two resistors of known resistance at cryogenic temperature (3 K): 80 and 200 mΩ. The results are shown in Figure 5.4. We vary the input bias current I_{bias} of Figure 5.2 (for $R_s = 0.02\ \ \Omega$) and measure the SQUID voltage output. After converting V_{out} to the input current I_R flowing through the resistor with Equation 5.1, we fit (least-squares) the data with the function:

$$I_R = \frac{R_s}{R_s + R} I_{bias}, \tag{5.3}$$

to obtain the value R. Results for the two resistors are shown in Figure 5.4. We can notice that both results are higher than expected by $\sim$ 17 mΩ. This is likely due to the residual resistance of the pin connectors, soldering material and superconductive niobium-copper wires used to connect the SQUID chip to the resistors (and TES detectors.)

Finally, in Figure 5.5 we show measurements from a TES detector test. In the right panel of Figure 5.1 we show a picture of a TES test chip wire-bonded to a pcb chip ready to be installed on the FAA stage of the ADR cryostat. In the left panel of Figure 5.5 we show measurements of the TES resistance performed

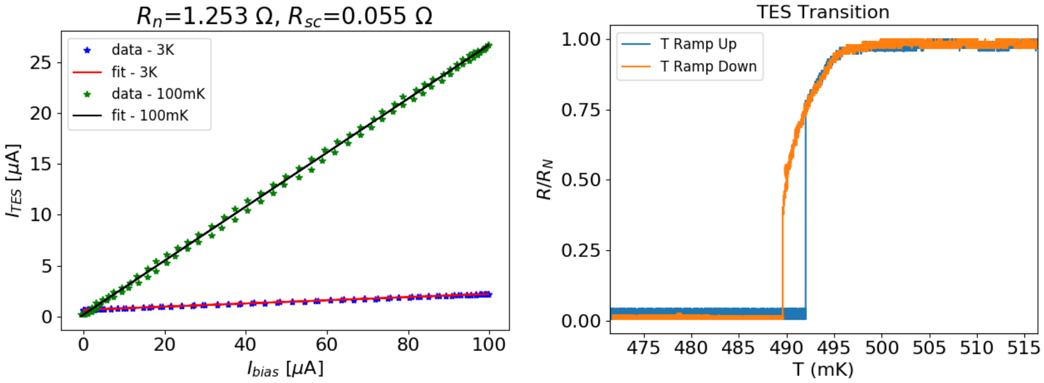

Figure 5.5: *Left:* TES resistance in normal state R_n and superconductive state R_{sc}. *Right:* Transition current (T_c) measurement for a TES detector. The measurement has been performed with both the bath temperature ramping up and down.

following the same procedure as above. To measure the TES normal resistance R_n we regulate the FAA stage temperature to 3 K, while we regulate the FAA stage to 100 mK to measure the superconductive resistance R_{sc}.

The detectors we tested to date are not LiteBIRD-specific, but are old detector implementations designed for ground-based experiments and for 250 mK focal plane temperature. This is clearly visible in the right panel of Figure 5.5, where we can observe a transition temperature of $\sim$ 490 mK. We performed this measurement in two cases: increasing the bath temperature (ramp-up) and decreasing it (ramp-down). We notice a mismatch in the measured R-T curve between the ramp-up and ramp-down cycles. This effect is likely due to the TES normal resistance (for $T_b > T_c$) acting as an extra heat source, therefore keeping the effective temperature of the TES higher than the nominal bath temperature during a ramp-down cycle.

5.1 TES time constant

As shown in [122], the TES response described by Equation 4.2 and 4.5 can be rewritten in the small-signal limit as:

$$\frac{d}{dt}\begin{pmatrix}\delta I\\ \delta T\end{pmatrix} = -\begin{pmatrix}\frac{1}{\tau_{el}} & \frac{\mathcal{L}_I G}{I_0 L}\\ -\frac{I_0 R_{TES}(2+\beta_I)}{C} & \frac{1-\mathcal{L}_I}{\tau}\end{pmatrix}\begin{pmatrix}\delta I\\ \delta T\end{pmatrix} + \begin{pmatrix}\frac{\delta V}{L}\\ \frac{\delta P}{C}\end{pmatrix}. \tag{5.4}$$

Solving the homogeneous form (δV and $\delta P = 0$), the current response can be written as the sum of two exponential functions:

$$\delta I(t) \propto e^{-t/\tau_+} - e^{-t/\tau_-} \tag{5.5}$$

where:

$$\frac{1}{\tau_\pm} = \frac{1}{2\tau_{el}} + \frac{1}{2\tau_I} \pm \frac{1}{2}\sqrt{\left(\frac{1}{\tau_{el}} - \frac{1}{\tau_I}\right)^2 - 4\frac{R_{TES}}{L}\frac{\mathcal{L}_I(2+\beta_I)}{\tau}} \tag{5.6}$$

Here τ_+ and τ_- correspond to τ_1 and τ_2 in Figure 5.7. If the inductance $L \to 0$, the "rise-time" $\tau_+ \to \tau_{el} \sim L/R_{TES}$ (for $R_{shunt} = 0.02\ \Omega \ll R_{TES}$), while the "fall-time" τ_- is the thermal time constant C/G sped-up by the loop gain (Equation 5.7).

We can test the TES time constant using a signal generator in series with the bias line to inject a *small* bias step $\Delta V_b \ll V_b$ (square wave of 4 Hz frequency) and

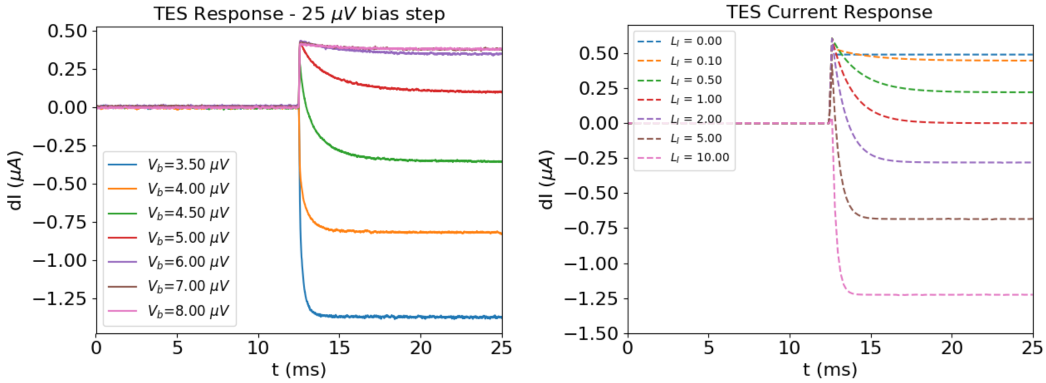

Figure 5.6: *Left:* Detector data from a square wave signal on the bias line for different bias voltages (the bath temperature for these measurement was ∼ 300 mK). *Right:* Simulated response for the same input signal for different loop gain values (bias voltages). The TES steady state output current has been subtracted from the data.

observe the detector response. In Figure 5.6 (left) we show the TES response to a 0.25 μV bias-step. For this test we choose a few bias voltage values (in the range 3.5-8 μV)[4]. We can observe the response becoming faster when going from high bias voltage (loop gain $\mathcal{L} \sim 0$) to low bias voltage ($\mathcal{L} \gg 1$). For reference, and to cross-check our correct understanding of the response of the detector, we modelled the response to a bias step. In Figure 5.6 (right) we show a simulation of the TES response to validate our data. These simulations are performed by numerically solving the linear differential equations governing the thermal and electrical response of a TES to a changing bias voltage (see Chapter 4).

In Figure 5.7, using the data in Figure 5.6 (center), we fit the data to extrapolate the thermal time constant of the detector for each bias voltage value. From the TES response model we expect to find a second time constant ($\sim L/R$) due to the electrical properties of the system. Given an input inductance of 6 nH and the TES resistance $\sim 1\ \Omega$, we expect the value of the electrical time constant to be $\sim 10^{-9}$ s. However, the sampling rate for these measurements is 100 kHz, which limits the possibility to measure such a small value. We find $\tau_1 \sim 10^{-5}$ s, consistent throughout the measurements and consistent with the sampling rate limit. We find values of τ_2, the thermal time constant of the detector, decreasing

---

[4] As explained in Chapter 4 the TES bias voltage is fixed thanks to the shunt resistor $R_s \ll R_{TES}$. This is true only when the TES temperature is $\gtrsim T_c$.

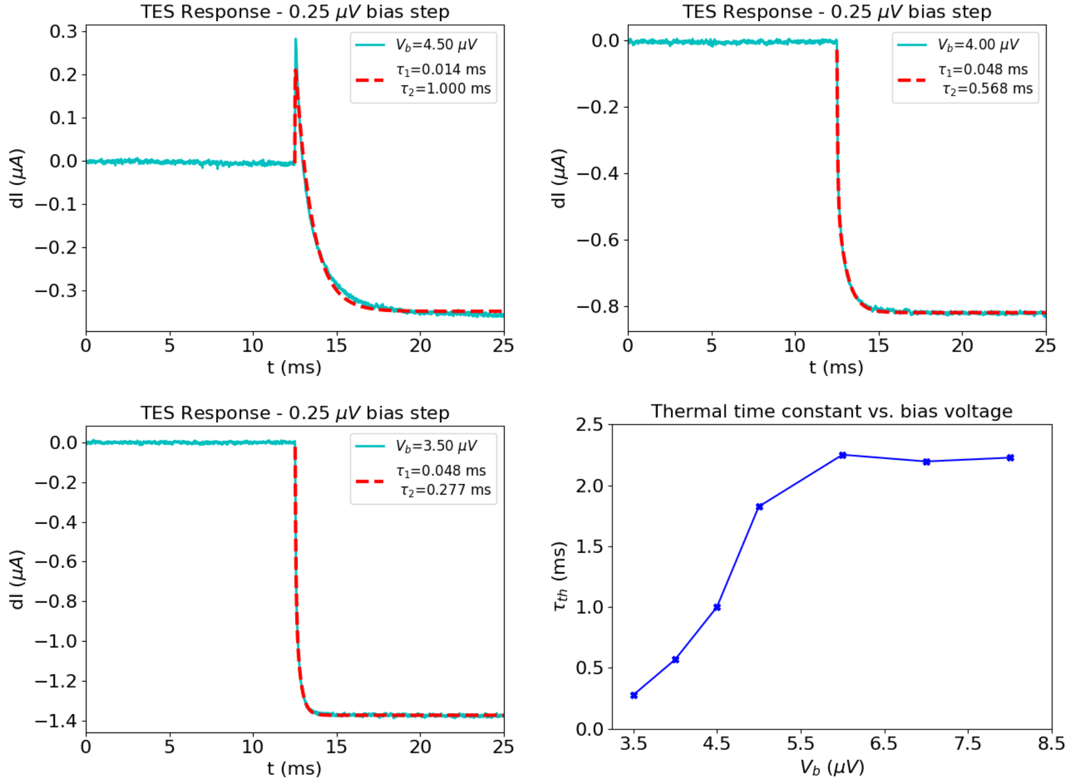

Figure 5.7: Time constant measurement of a TES detector. *Left:* A measurement of the time constant of a TES detector for $\mathcal{L} \sim 1$. The TES steady state output current has been shifted to 0 μA. We can clearly see a fast rise due to the electrical response of the system and a decay due to the thermal response. *Bottom right:* Measured thermal time constant as a function of the bias voltage.

for increasing loop gain as expected:

$$\tau_{th} = \frac{C}{G}\frac{1}{1+\mathcal{L}}. \tag{5.7}$$

As shown in Figure 5.7, the thermal time constant of the detector under test decreases from a value of ~ 2.2 ms to ~ 0.27 ms for the lowest voltage value, which indicates a loop gain value of $\mathcal{L} \sim 10$. In this limit the detector sensitivity S_I can be approximated as $-1/V_b$ as discusse in Chapter 4.

5.2 LFT sub-system testbed

As mentioned, Kavli IPMU is responsible for the development of the LFT Polarization Modulator Unit (PMU) consisting of a continuously-rotating Superconductive

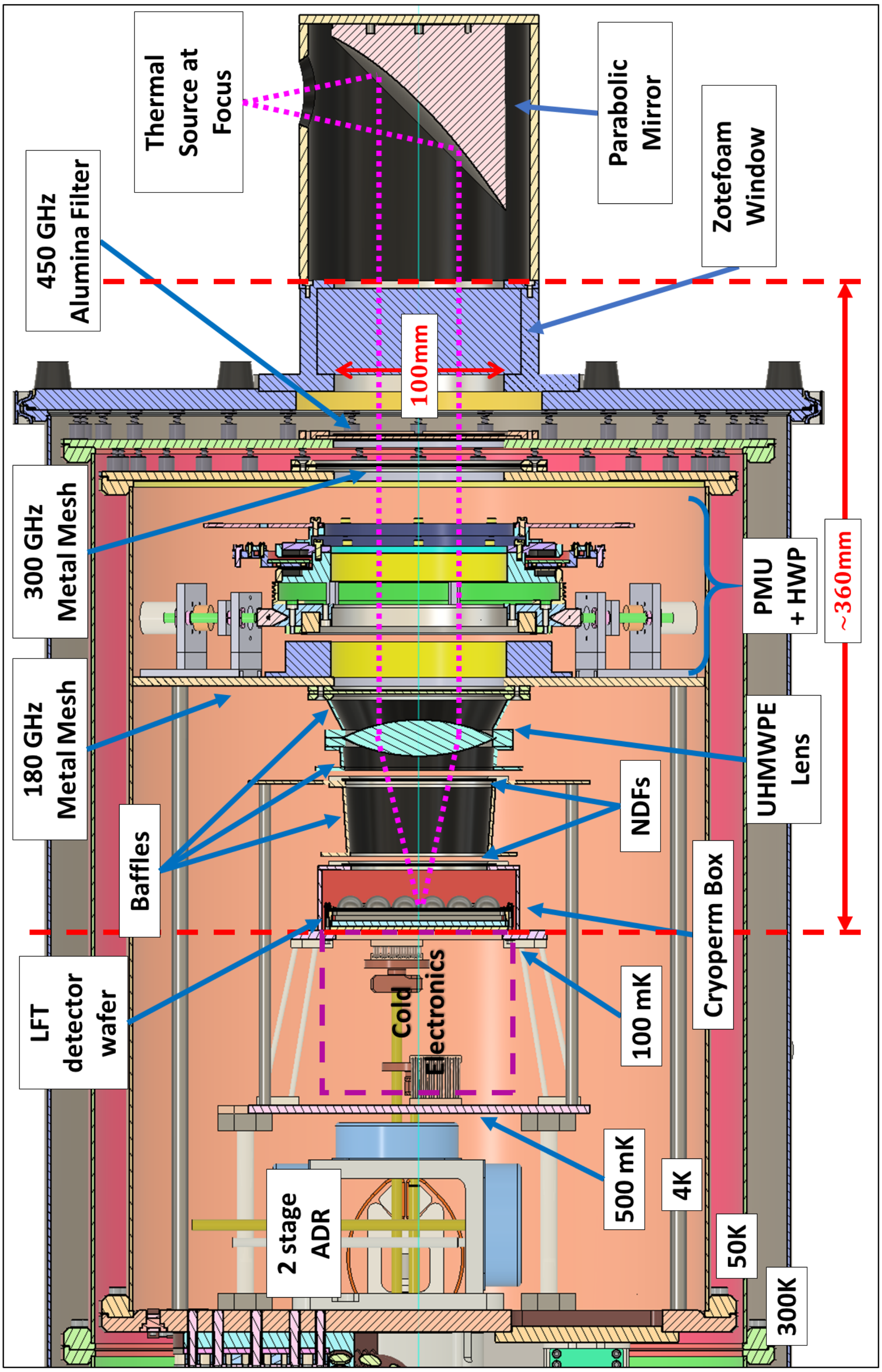

Figure 5.8: 3D model of the cryogenic testbed.

Magnetic Bearing (SMB), a cryogenic holder mechanism, a rotation angle encoder, and a multi-layer sapphire Achromatic Half Wave Plate (AHWP) with the required Anti-Reflection Coating (ARC) made by laser-machining sub-wavelength structures [4, 91, 92]. Before assembling the full telescope, we plan to adapt an existing Adiabatic Demagnetization Refrigerator (ADR) cryostat to host a cryogenic polarimeter to study the detector performance together with the PMU as part of a full telescope system. The two main challenges for such a system are the extremely low saturation power of space optimized bolometers (~ 0.5 pW) and the limited cooling capacity of an ADR cryostat (~ 120 mJ at 0.1 K).

In the following we will describe the testbed design and requirements. The main goal of LiteBIRD is measuring the primordial B-mode signal on large angular scales. However, this is impossible without detailed knowledge of the instrument and its potential systematic effects. In Table 5.1, we identify the items to test with the proposed assembly, the potential issues, and the possible sources. Here we list the potential problems of the detector system when combined with the other components (optical and mechanical) of the telescope.

The LFT focal plane design consists of a modular assembly of 8 detector wafers [5, 143], each 105 × 105 mm, covering a frequency range from 34 GHz to 161

Sources / Tests	Pulse tube	ADR	Lens	Filters	PMU	Environment
White noise	V	M	O	O	V, M, O	O, CR, SL
1/f noise	T, V	T, M	T	T	T, V	T, CR, SL
Correlated noise		M			M, S	CR
Spurious signals		M	SW	SW	S, SW	SL, CR
Time constant		M			S	CR
Gain stability	T	T, M	T, O	T, O	T, O	T, CR, O, SL
Beam			G	G	S, G	SL
Bandpass			SW	SW	SW	
I to P leakage			G	G	S, G	
Pol. Angle					S	

Table 5.1: In this table we summarize the test we want to conduct with the proposed set-up, the possible issues and the sources of these possible systematic effects. *Legend:* V=vibrations, M=magnetic fields, O=optical loading, S=synchronous signals, SL=stray light, SW=standing waves, CR=cosmic rays, T=thermal instability, G=ghosting.

GHz (9 frequency bands) with trichroic pixels. Depending on the frequency range, each wafer has 16 or 36 pixels, arranged in a square pattern. With the proposed system we will be able to test at the same time a sub-set of 9 (for the 16 pixel wafers) or 16 pixels (for the 36 pixel wafers).

The driving requirements for the system in Figure 5.8, other than the already mentioned ADR cooling capacity constraints and detector saturation power, are the need for a collimated beam through the HWP to study its optical properties and a static magnetic field (from the HWP magnetic bearing) < 0.2 G at the focal plane (see Section 5.2.2 for details).

5.2.1 Thermal and optical requirements

For our testbed, we plan to modify the existing 2-stage ADR cryostat with the following thermal specifications: ~ 40 W of cooling power at the nominal 45 K stage, ~ 1.35 W of cooling power at the nominal 4.2 K stage (these first 2 stages are cooled by a pulse tube), 1.2 J of cooling capacity at the GGG stage (nominally at 500 mK) and finally 120 mJ of cooling capacity at the FAA stage (nominally at 100 mK). The limited cooling capacity of the ADR requires a careful thermal design to minimize the thermal loading on the 100 mK focal plane. To do so, we designed a support structure for the 500 mK stage, consisting of four 100 mm Vespel SP1 [144] shafts with 10 mm outer diameter and 9 mm inner diameter, while the 100 mK stage is supported by a octapod structure made with 100 mm Vespel SP22 shafts with a diameter of 3 mm. Radiative loading is the other relevant component in our

Stage	Cooling power / capacity	Radiative loading	Structure loading	Wire loading
50 K	40 W	5 W	1 W	5 W
4 K	1.35 W	0.6 W	0.1 W	0.2 W
500 mK	1.2 J	6 μW	10 μW	0.1 μW
100 mK	120 mJ	25 nW	1 μW	55 nW

Table 5.2: Summary of the cooling power (or capacity) and the thermal loading due to radiation, support structures, and wires, for each stage of our dedicated cryostat. This configuration will allow ~ 10 hours of continuous operation. The ADR recycling time is ~ 5 hours.

thermal budget. To minimize the IR loading we designed a filter stack consisting of a 450 GHz cut-off alumina low-pass filter with a Stycast[5] anti-reflection coating [85] on the 50 K stage, and two metal mesh low-pass filters on the 4 K stage: one with a 300 GHz cut-off before the HWP, and the second after the HWP with a 180 GHz cut-off. A complete summary of our thermal calculation and requirements can be seen in Table 5.2. At the design stage we are not accounting for diffraction effects, we are considering the temperature of all components to be uniform, and the cut-off frequency of the filters to be ideal.

Although this configuration is enough to reduce the radiative loading for thermal purposes, we must also consider the low saturation power of LiteBIRD TES bolometers (~ 0.5 pW). Therefore, we have included in our design two additional filters, one at 500 mK and the second at 100 mK (in front of the focal plane). These two filters could be NDFs (Neutral Density Filters) or absorptive filters made with a slab of Eccosorb [6], to reject $\sim 99\%$ of the incoming radiation and reduce the power at the detector to ~ 0.2 pW (a 100 GHz band with 30% bandwidth has been assumed for the calculation). We are still considering which solution is more suitable, but the absorptive filter solution seems more likely due to the suppression of reflections without having to complicate the geometry by tilting one or more of the optical elements.

5.2.2 Magnetic field requirements

A second important item for the definition of the testbed design is the magnetic field due to the SMB of the HWP rotational mechanism (see Figure 5.10). We derived a < 0.2 G requirement for the magnetic field at the level of the focal plane. External magnetic fields cause the transition temperature of the TES to change [145]. This change increases the phonon noise of the bolometer [71, 127]. The noise equivalent power due to thermal fluctuation in the weak link between

---

[5] `https://www.henkel-adhesives.com/us/en/product/potting-compounds/loctite_stycast_2850ft.html`

[6] `http://www.eccosorb.com/products-eccosorb-cr.htm`

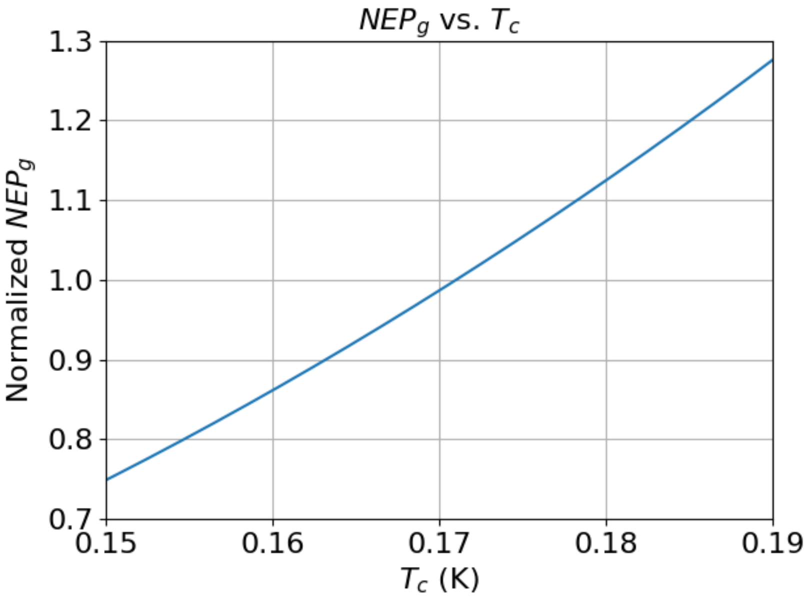

Figure 5.9: Normalized NEP_g vs. T_c. The nominal value is found for $T_c = 0.171K$. An increase of $\sim$ 7 mK degrades the noise by $\sim$ 10%.

temperatures $T_b = 0.1$ K (LiteBIRD focal plane temperature) and T_c can be found by rewriting Equation 4.11 as:

$$NEP_G = \sqrt{4k_B \frac{A}{l} k_0 T_c^{\beta+2} \frac{\beta+1}{2\beta+3} \frac{1-(T_b/T_c)^{2\beta+3}}{1-(T_b/T_c)^{\beta+1}}} \tag{5.8}$$

where A and l are the cross-section and length of the TES legs and $\beta = 3$ for phonons. We compute NEP_G and normalize it to the value at $T_c = 0.171$ (design value for LiteBIRD) to find the relation $NEP_G - T_c$ (see Figure 5.9).

The requirement is found by imposing a $\sim$ 10% limit on the degradation of the phonon noise, and assuming the TES transition temperature sensitivity to an external magnetic field of $\sim$ 4 mK/G. We find that for LiteBIRD detectors, operating at a bath temperature T_b $\sim$100 mK with a nominal transition temperature T_c $\sim$171 mK, the maximum variation of T_c that we can tolerate is $\sim$ 7 mK, which corresponds to an external magnetic field of $\sim$ 2 G. However, since the HWP magnetic bearings are not the only magnetic field source, we assign 10% of the total budget ($\sim$ 2 G) to the magnetic bearings: $\sim$ 0.2 G.

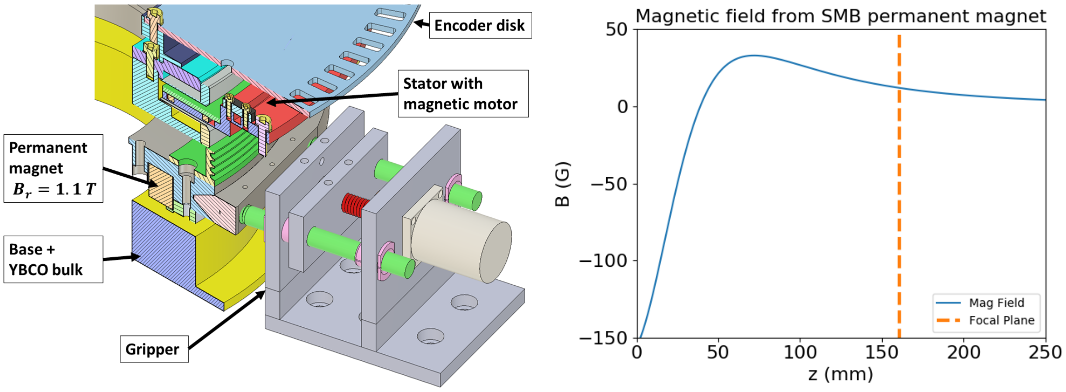

Figure 5.10: *Left:* A cut view of the HWP rotational mechanism, showing the superconductive YBCO bulk and the permanent magnet. *Right:* Calculation of the magnetic field at the focal plane level $\sim$ 160 mm away from the permanent magnet. The calculation shows a magnetic field of $\sim$ 11.8 G.

The permanent magnet of the SMB is a ring with outer and inner radii of 68.5 mm and 58.5 mm (respectively), 12 mm thickness, and presents a remanence magnetization $B_r = 1.1 \times 10^4$ G. We can compute the magnetic field strength at a distance z from the ring magnet from:

$$B(z) = \frac{B_r}{2}\left(\frac{D+z}{\sqrt{R_o^2+(D+z)^2}} - \frac{z}{\sqrt{R_o^2+z^2}} - \frac{D+z}{\sqrt{R_i^2+(D+z)^2}} + \frac{z}{\sqrt{R_i^2+z^2}}\right). \tag{5.9}$$

This geometry results in a magnetic field at the center of the focal plane of $\sim$ 11.8 G (see Figure 5.10), which gives a required shielding factor > 59 for the Cryoperm box surrounding the focal plane. From investigation with commercial partners, this shielding level is easily attainable with existing material and technologies, but we still plan to verify the requirement of the detector magnetic field tolerance, and a proper electromagnetic simulation to study the magnetic field across the focal plane and the best geometry for the magnetic shield.

5.2.3 Optics

Ideally, a scaled version of LiteBIRD LFT telescope would allow us to recreate the same conditions we will have during observation. Unfortunately, a cross-dragone mirror configuration with a rotating HWP will require a very complex supporting structure which is difficult to accommodate due to the limited volume of the existing cryostat; therefore, we intend to simplify the optics using a biconvex UHMWPE (Ultra-high-molecular-weight polyethylene) lens with $f - number = 3$[7] to match the LFT design and the $f - number$ of the beam-formers (hemispherical silicon lenslets). We will place the lens after the HWP, and use a parabolic mirror as the first optical element, to collimate the beam through the HWP in order to be able to study its optical properties under simulated working conditions (Figure 5.8). Using a lens requires an anti-reflection coating [89, 92] which we will develop by mechanical machining sub-wavelength structures on the UHMWPE lens surfaces.

5.3 Customized loaded epoxy for EM-absorbers

Epoxy and epoxy-composites can be used both as anti-reflection layers or as blackening layers to reduce stray-light or as calibration targets. In the following we describe a technique we used to determine the electromagnetic properties of an epoxy-magnetite composite that can be used as a castable EM-absorber and could be useful in the test-bed construction.

Castable electromagnetic wave absorbers are usually composite materials made with a polymer encapsulant matrix and a dielectric or magnetic filler. There are examples of this type of material commercially available. The vendors provide electromagnetic properties (dielectric permittivity, magnetic permeability or loss tangents) up to $\sim 18 - 20$ GHz [8], although, for many applications, values at higher frequencies may be required [146–150].

We have explored the possibility of fabricating a castable absorber using cheap commercially available materials: Stycast 2850 FT[9] as the dielectric encapsulant, and magnetite powder[10] (chemical composition Fe_3O_4) as the magnetic filler. After

---

[7] Focal ratio or $f - number = f/D$ where f is the focal length and D is the lens diameter.

[8] `https://www.laird.com/rfmicrowave-absorbers-dielectrics/molded-machined-casted-coatings/eccosorb-cr/eccosorb-cr`

[9] `https://www.henkel-adhesives.com/us/en\/product/potting-compounds/loctite_stycast_2850ft.html`

[10] `https://www.inoxia.co.uk\/products/chemicals/inorganic-compounds/magnetite-powder`

Sample	Mass-ratio	Δx	$\epsilon_{\rm dc}$
Mag27	27%	2.38 mm	7.57
Mag60	60%	2.31 mm	17.79

Table 5.3: Summary of the samples analysed in this study. Powder-to-epoxy mass-ratio, thickness and permittivity measured with the capacitor are shown for each sample.

fabricating a few samples we measured the properties up to 170 GHz with a vector network analyser (VNA).

We made two samples with different encapsulant-filler mass-ratio, in order to show that it is possible to tune the electromagetic properties to meet the needs of a specific application. The maximum magnetite particle size, as provided by the vendor, is 45 μm and the typical size is 200 nm. Therefore, we do not expect the particle size to have a significant impact, as they are small compared to the wavelengths considered. In fact, we measured transmission and reflection from the samples below 170 GHz, corresponding to wavelengths $\gtrsim$ 1.7 mm. Transmittance and reflectance were measured on a thin ($\sim$ 2 mm) slab of material. An empirical model is employed to extract information about the electromagnetic properties of our samples from transmission data [151–153]. The measurement set-up and one of the measured samples can be seen in Figure 5.11. As a validation of our results, we use the extracted parameters to simulate reflection data and we compare them with measurements.

5.3.1 Characterizing the Absorber

Commonly we assume the complex relative dielectric permittivity and magnetic permeability to be constant, especially if we limit our analysis to a narrow frequency band. But this approximation is not always valid when we extend the analysis to a broader frequency range. If we take into account a direct dependence from the frequency, we can write:

$$\epsilon(\nu) = \epsilon_{\rm r}(\nu) + {\rm i}\epsilon_{\rm i}(\nu), \tag{5.10}$$

$$\mu(\nu) = \mu_r(\nu) + i\mu_i(\nu). \tag{5.11}$$

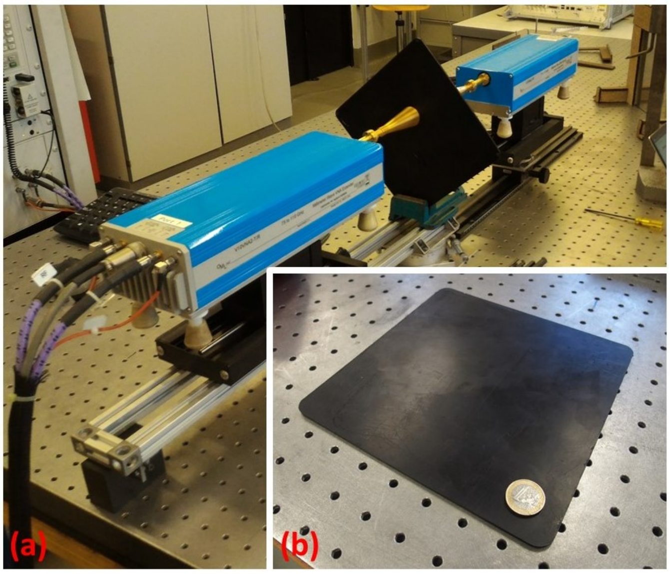

Figure 5.11: a) Measurement set-up. Two horns antenna are facing each other with the thin flat sample on the aperture of one of the antennas. Transmission and reflection data are measured using a VNA. b) One of the measured samples with a 1 euro coin for size reference.

5.3.1.1 Parameter Extraction

Using Equation 5.10 and 5.11, we can write the complex frequency-dependent refractive index as:

$$\hat{\mathrm{n}}(\nu) = \sqrt{\epsilon(\nu)\mu(\nu)} = \mathrm{n}(\nu) + \mathrm{ik}(\nu). \tag{5.12}$$

From Equation 5.12 we define the key parameters to compute reflection and transmission from a layer of thickness Δx [154, 155], the reflection parameter (Equation 5.13) and δ which combine the phase shift and damping factor (Equation 5.14).

$$\mathrm{R} = \left|\frac{\hat{\mathrm{n}}(\nu) - 1}{\hat{\mathrm{n}}(\nu) + 1}\right|^2 \tag{5.13}$$

$$\delta \propto \exp\left(\frac{\mathrm{i}2\pi\hat{\mathrm{n}}(\nu)\nu\Delta\mathrm{x}}{\mathrm{c}}\right) \tag{5.14}$$

Using a Debye relaxation model [156] for the relative permittivity of the medium

$$\epsilon(\nu) = \epsilon_\infty + \frac{\epsilon_{\mathrm{dc}} - \epsilon_\infty}{1 - \mathrm{i}\frac{\nu}{\nu_\epsilon}}, \tag{5.15}$$

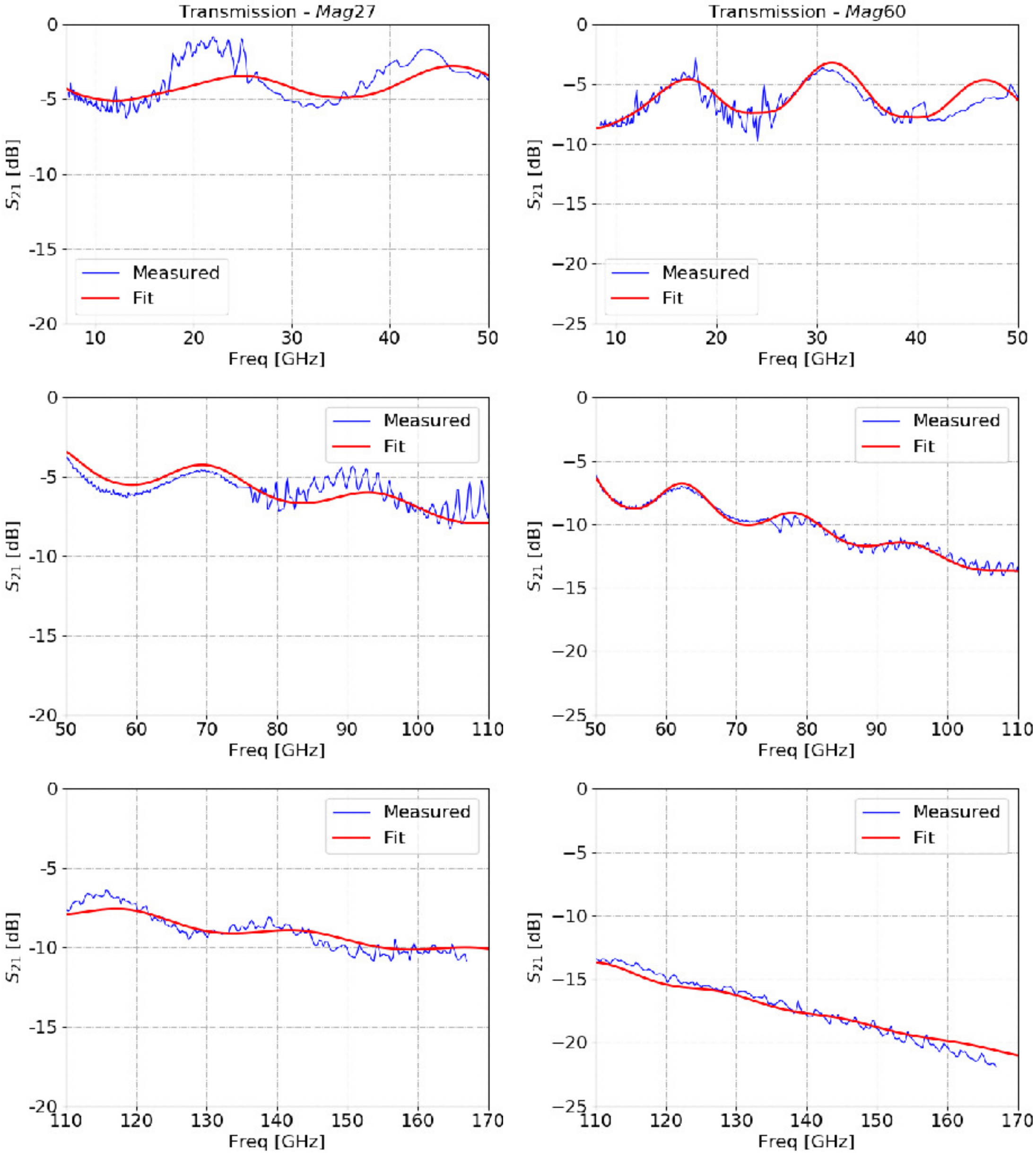

(a) Transmission data and fit for *Mag27*.

(b) Transmission data and fit for *Mag60*.

Figure 5.12: Data and results of the analysis for each sample are split in 3 sub-plots for clarity. *Top row:* X, Ku, K, Ka and Q bands. *Central row:* V and W bands. *Bottom row:* D band.

and a Lorenzian resonant model for the relative permeability

$$\mu(\nu) = 1 + \frac{\mu_{\mathrm{dc}} - 1}{\left(1 - \mathrm{i}\frac{\nu}{\nu_\mu}\right)^2} \tag{5.16}$$

we describe the transmission and reflection from a slab of material of fixed thickness Δx with five free parameters: ϵ_∞ (relative permittivity at high frequency), ϵ_{dc} (static relative permittivity), ν_ϵ (relaxation frequency), μ_{dc} (static relative permeability) and ν_μ (resonant frequency).

5.3.1.2 Sample Fabrication

We fabricated thin (Δx $\sim$ 2 mm) square samples (200 × 200 mm) using a mould consisting of a flat 10-mm aluminium base plate covered with a 1-mm PTFE sheet to facilitate the release of the finished sample. The PTFE sheet is held in place by a second 10-mm aluminum plate with a square aperture (200 × 200 mm) which can be screwed to the base plate to form the moulding structure. In order to obtain the required thickness we used a PTFE lid that can be inserted into the mould aperture. This lid has been fabricated of proper dimensions to obtain a $\sim$ 2 mm thick sample. Once the epoxy-powder mixture is poured into the mould, the lid is inserted into the mould aperture and the excess material can flow out through four holes at the corners of the lid. A release agent was routinely applied inside the mould to prevent the sample from sticking to the aluminum walls.

We show the results of two samples made using Stycast 2850FT (ideal for cryogenic applications), catalyst 24 LV (7% mass ratio) and Fe_3O_4-powder. All samples were prepared by mixing the components (epoxy, catalyst and magnetite powder), outgassing the mixture to remove the air trapped into the epoxy and ensure uniformity, and curing the sample in a oven at 65°C.

The two samples differ in the mass-ratio of magnetic powder and epoxy encapsulant: 27% and 60%. From now on we will refer to the first material as *Mag27* and the second as *Mag60*.

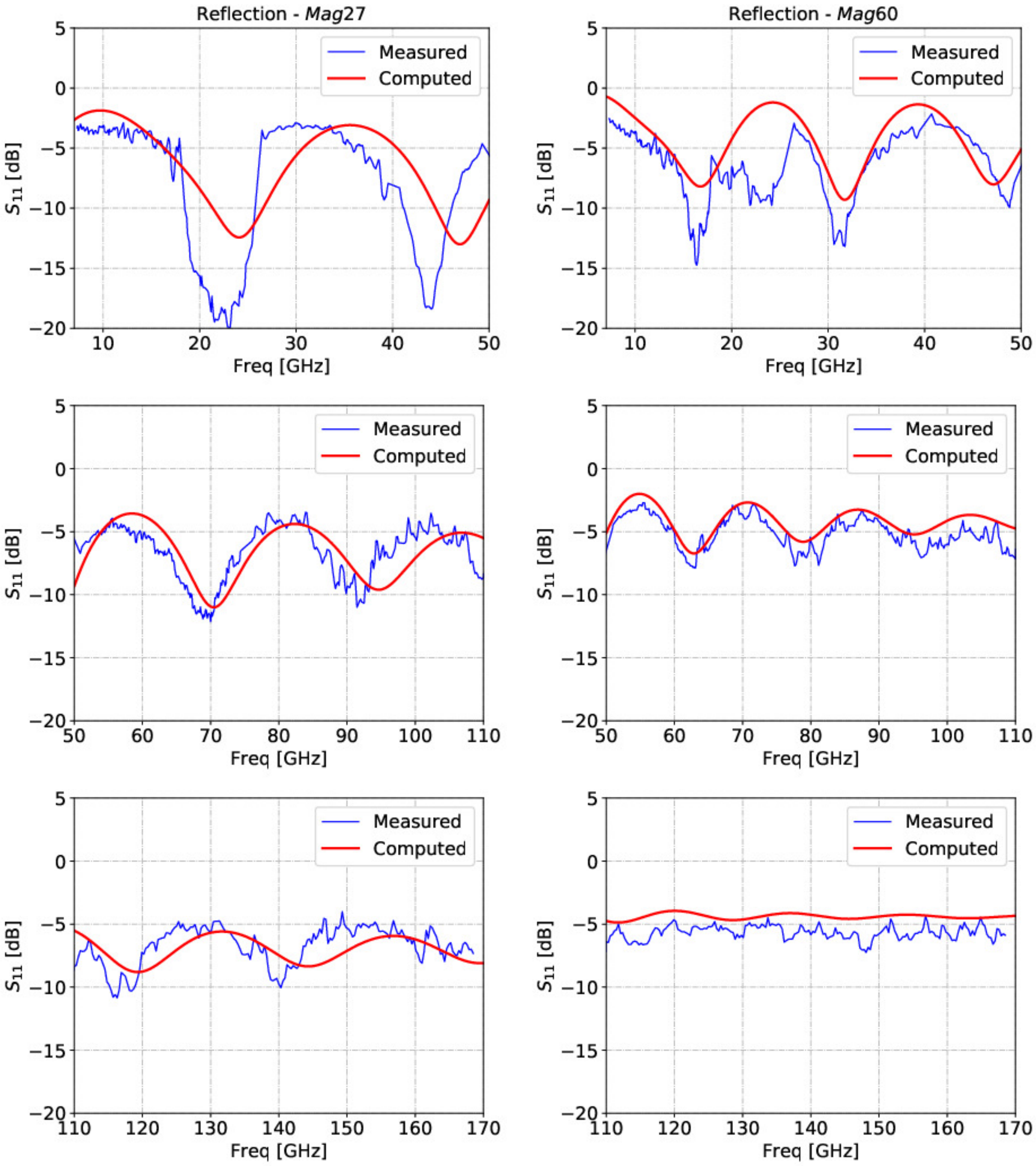

(a) Reflection data and simulated data based on the extracted permittivity and permeability for *Mag27*.

(b) Reflection data and simulated data based on the extracted permittivity and permeability for *Mag60*.

Figure 5.13: Data and results of the analysis for each sample are split in 3 sub-plots for clarity. *Top row:* X, Ku, K, Ka and Q bands. *Central row:* V and W bands. *Bottom row:* D band.

5.3.1.3 Measurement Set-Up

As explained in Sec. 5.3.1.1, our parametric model has five free parameters. To reduce the number of parameters to be determined through the fitting routine of the transmission data, we measure the static permittivity (dc) of the samples independently, using a capacitor made with two planar copper plates of area A:

$$\mathrm{C} = \epsilon_0 \epsilon_{\mathrm{dc}} \frac{\mathrm{A}}{\Delta \mathrm{x}}, \tag{5.17}$$

where C is the capactitance, ϵ_0 is the absolute vacuum permittivity and Δx is the distance between the plates, corresponding to the thickness of the sample. By measuring the capactitance it is possible to compute the static relative permittivity of the sample. Thanks to this step we can reduce the unknown parameters from to four. In Table 5.3, a summary of the results for the static relative permittivity and thickness of the two samples is reported.

Transmission and reflection measurement are carried out using six different pairs of standard rectangular horn antennas, between 7 and 75 GHz, and two pairs of circular corrugated horn antennas, from 75 up to 170 GHz. In total we use eight pairs of antennas to cover the whole frequency range with a vector network analyzer[11]. We place the sample under test on the aperture of the transmitting antenna to record both transmission (S_{21}) and reflection (S_{11}) measurements at the same time. To calibrate the data we measure S_{21} without the sample (free-space), and S_{11} for a perfectly reflective surface (mirror) and for a perfectly absorptive surface (pyramidal foam with $\mathrm{S}_{11} < -50$ dB). The calibrated are computed as:

$$\mathrm{S}_{21,\mathrm{cal}} = \frac{\mathrm{S}_{21,\mathrm{sample}}}{\mathrm{S}_{21,\mathrm{free}}}, \tag{5.18}$$

$$\mathrm{S}_{11,\mathrm{cal}} = \frac{\mathrm{S}_{11,\mathrm{sample}} - \mathrm{S}_{11,\mathrm{foam}}}{\mathrm{S}_{11,\mathrm{mirror}} - \mathrm{S}_{11,\mathrm{foam}}}. \tag{5.19}$$

We perform a fit of $\mathrm{S}_{21,\mathrm{cal}}$ data using the parametric function described in Sec. 5.3.1.1 (least-square method) in two steps:

---

[11] Agilent PNA-X N5245A with N5261A mm-wave test set and related OML extensions: `https://www.keysight.com/en/pdx-x201768-pn-N5245A/`.

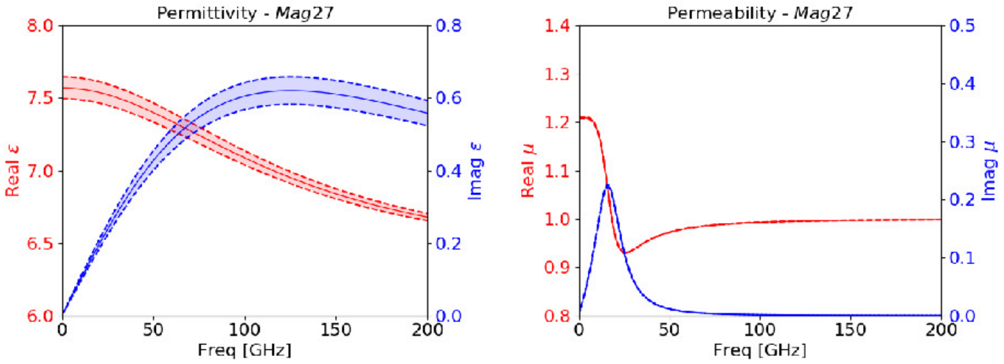

Figure 5.14: Dielectric permittivity and magnetic permeability for *Mag27*, the real parts (*Real* ϵ and *Real* μ) are plotted in *red*, while the imaginary part *Imag* ϵ and *Imag* μ) are plotted in *blue*. The *solid line* represents the best fit, while the *shadowed area* between the *dashed lines* shows the $1-\sigma$ uncertainty after the fitting routine.

- First, we exclude data below 50 GHz. The value of $\epsilon_{\rm dc}$ is fixed by the one obtained with the capacitor measurement described previously (see Table 5.3), and μ is fixed to be constant and equal to unity. This approximation is justified by Equation 5.16 approaching 1 for $\nu \to \infty$. We retrieve ϵ_∞ and ν_ϵ.

- We re-fit $S_{21,\rm cal}$ data. This time we fix the three parameters already extracted in the previous steps, and we include the whole frequency range from 7 to 170 GHz. We retrieve the final two parameters of our model: μ_0 and ν_μ.

Results for the fitting routine are shown in Figure 5.12a for *Mag27* and in Figure 5.12b for *Mag60*. The results have been split in three panels for clarity. The upper panel shows data measured in X, Ku, K, Ka and Q bands, the central panel contains data of the measurements performed in V and W bands, and finally the lower panel shows the data of D band.

5.3.1.4 Parameters Validation

After extracting all the parameters of our model using transmission data, we simulate reflection from a slab of material with the same thickness of our sample, and we compare the computed response to $S_{11,\rm cal}$ data to validate our results. Results can be seen in Figure 5.13a for *Mag27* and in Figure 5.13b for *Mag60*. We can see how the data in the range 18-26 GHz do not agree well with the computed one. This

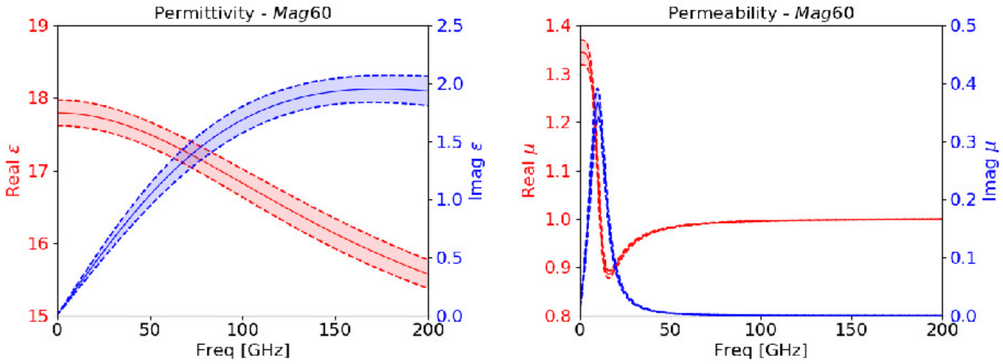

Figure 5.15: Dielectric permittivity and magnetic permeability for *Mag60*, the real parts (*Real* ϵ and *Real* μ) are plotted in *red*, while the imaginary part *Imag* ϵ and *Imag* μ) are plotted in *blue*. The *solid line* represents the best fit, while the *shadowed area* between the *dashed lines* shows the $1-\sigma$ uncertainty after the fitting routine.

is likely due to an imperfect calibration in this band, however this mismatch in reflection data does not have an impact on the result of the fit because we do not use reflection data to constrain the parameters of the model.

With the parameters obtained, we can compute the complex dielectric permittivity and magnetic permeability of the two materials (from Equation 5.15 and Equation 5.16). Results are shown in Figure 5.14 for *Mag27* and in Figure 5.15 for *Mag60*. It can be noted that both values of the real and the imaginary part of both permittivity and permeability increase with the relative amount of magnetite powder in the composite material.

The loss tangent is dominated by magnetic losses at low frequency, while at higher frequency the magnetic loss tangent becomes negligible and the material is dominated by dielectric losses. Loss tangent plots are shown in Figure 5.16.

While Stycast 2850FT has already been employed extensively in similar applications, most applications rely on CIP (carbonyl iron powder) as the filler [157]. Some empirical formulas have been proposed and tested to show the predictability of the behaviour of CIP composites knowing the permittivity and permeability of the filler and the dielectric matrix and their volume ratio [158]. We expect similar formulas to be applicable to magnetite composites, however with only two samples

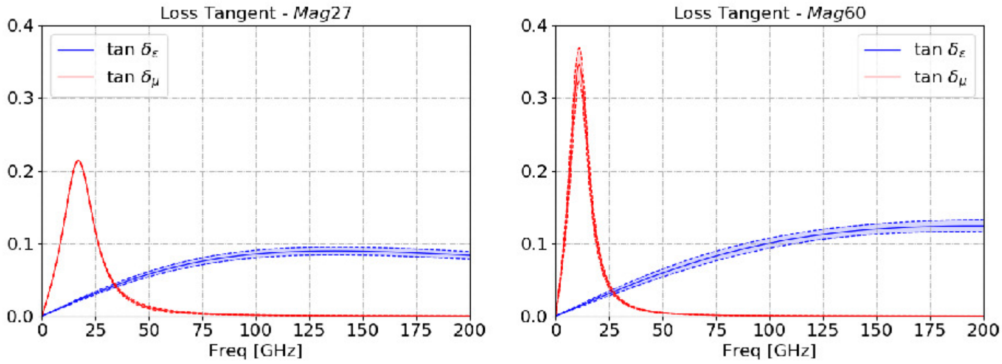

Figure 5.16: Dielectric (*blue*) and magnetic (*red*) loss tangent for *Mag27* and *Mag60*. The *solid line* represents the best fit, while the *shadowed area* between the *dashed lines* shows the $1 - \sigma$ uncertainty after the fitting routine.

with two different ratios, we can not validate at this stage a reliable method to predict the behaviour of Stycast-magnetite composites.

Magnetite has been used in combination with other encapsulants (but not Stycast) [159] and measurements of electromagnetic properties of these composite materials can be found in the literature [160–162]; however most measurements have been performed below $\sim$ 20 GHz.

This work shows that the material can be customized for a specific application and achieve the required permittivity and permeability values by tuning the Fe_3O_4-Stycast 2850FT mass-ratio. However, as can be seen in Figure 5.14, 5.15 and 5.16, the ability to change absorption by increasing the relative fraction of magnetite particles is limited to low frequency ($\leq 20 - 30$ GHz), while at higher frequencies increasing the relative ratio of magnetite does not increase neither magnetic nor dielectric losses significantly. We can notice from Figure 5.16 that the dielectric loss tangent is similar between the two samples despite a different mass-ratio. Magnetite is a ferrimagnetic material, and as such it is characterized by low conductivity, implying that the imaginary part of the permittivity is negligible compared to its real part. This is the reason why the dielectric loss tangent remains stable when we increase the amount of magnetite powder in the material.

The observed greater change in the imaginary part of the permeability compared to its real part can be explained because of the resonant behaviour of magnetite particles dispersed in a dielectric medium. We expect large variations of dc permeability by changing the volume ratio. However, with increasing frequency the real part of the permeability is expected to drop, while around the resonance frequency we expect mainly variation of the imaginary part of the permeability. A limiting factor of this analysis method is the extrapolation of the dc permeability from data at higher frequencies ($\nu > 7$ GHz). For future work we can imagine a set-up to measure this parameter independently similarly to what we have done with the capacitance measurements, to obtain a better constraint of this parameter and reduce even further the number of free parameters to be fitted.

In conclusion, this work shows the possibility of using Stycast 2850FT in combination with magnetite powder to fabricate an RF-absorbing material, and it describes a method to measure complex permittivity and permeability on a broad frequency range with transmission and reflection measurements.

The possibility to tune the loss tangent at low frequency makes this composite material attractive for the LFT as a blackening material to reduce stray light. We could also imagine to use it to fabricate a black-body target for lab measurements. This study can be reapplied to other composite materials to find a combination that can be used at higher frequencies.

6

Conclusion and Future Work

In this thesis we presented the current status and most recent results of CMB cosmology, with a focus on what this field still has to offer in the near future (specifically in the prospect of B-mode measurements), and what are the advantages and disadvantages between ground-based and space-based instruments. Most researchers in the field will agree that despite environmental limitations, a strong synergy between experiments is desirable and necessary in order to maximize scientific production and to achieve a better understanding of the instrument and to minimize systematics.

In Chapter 2 we focused on describing some of the most-significant recent technological developments that most next-generation experiments are going to implement. We focused specifically on those relevant for the LiteBIRD experiment and in particular on those relevant for the Low Frequency Telescope (LFT). We also described the LiteBIRD mission and strategy.

In Chapter 3 we introduced the data model, in order to define some of the most common systematic effects experienced by CMB experiments. We focused in particular on band-pass related effects to define the band-pass calibration requirements for LiteBIRD, and address the issue of CO line contamination. From the latter analysis we found that notch filters to "mask" the CO signal are not necessary for LiteBIRD and possibly harmful. We also presented a mathematical formalism to extend the calibration analysis to include the effect of a non-ideal HWP. In Chapter 4 we described the detector and read-out system and defined the noise properties of TES bolometers. We showed our analysis of detector non-linearity effects due to various environmental factors and we concluded by estimating the level of non-linearity induced by extra loading due to the Galaxy emission at high frequency.

Finally, in Chapter 5 we presented results from tests on single TES bolometers that were performed at Kavli IPMU using a commercial dc-SQUID readout. Although the bolometers tested for this thesis are not LiteBIRD-specific, we showed our ability to test these devices which will be useful once our colleagues will begin production of LiteBIRD detector prototypes. We also showed a preliminary design of a more complex cryogenic test-bed that we plan to implement to perform tests of the detector-readout assembly along with other sub-systems (specifically the LFT PMU) to do a check for possible unwanted behaviours ahead of the integration of the full system. In Chapter 5 we also presented a procedure to fabricate and test epoxy-composites that may be used in the test-bed (or even in the final instrument) as a blackening material or in the fabrication of anti-reflection layers.

In the coming years we will push forward the fabrication of the proposed test-bed, as well as continue to test new prototype detectors. One of the major issues encountered by the Planck satellite, that was not discussed in details in this thesis, is cosmic rays. Therefore, one of the major area of research and development for LiteBIRD, as well as other bolometer-based space missions, consists in developing detectors immune to cosmic rays or develop techniques to mitigate their effect. We are already working on a framework that combines the simulation tool presented in Chapter 4 with COMSOL-based[1] simulations that account for the effect of cosmic ray hits on the focal plane. At the same time we are planning detector irradiation tests using a radioactive source (Americium) to directly probe the detector response to α particles.

---

[1] https://www.comsol.eu/

A combination of measurement and simulation/modelling is a powerful tool to fully understand the impact of cosmic rays and propose new mitigation techniques.

The systematics analysis presented in Chapter 3 and 4 will be the starting point of more complex modelling that will be cross-checked with data from the test-bed. A natural progress of the work presented here will be to compare the detector non-linearity model presented in Chapter 4 with tests. Testing the non-linearity due to temperature and current fluctuation can be done with the present system with minimal modifications, while non-linearity tests due to excess optical loading require the test-bed to be built and will take more time. However, due to POLARBEAR and EBEX experience, determining possible non-linearity due to variable loading produced by the rotating HWP is a necessary analysis for the LiteBIRD mission. At present, one of the strategies for beam-calibration consists in making use of planets. However, it is necessary to define a clear strategy and its feasibility. Planets are point-like sources much brighter than the CMB. It is necessary to define whether the current detector dynamic range is sufficient to allow for the observation of planets without driving the response non-linear or even saturate.

Another possible source of uncertainty is the HWP frequency-dependent phase presented in Section 3.4, which may induce a frequency-dependent and component-dependent polarization angle rotation. New HWP design recipes are being studied to try to minimize in-band phase-differences, and we are developing an extension of the study presented in Section 3.2 to address the effect on the data.

Hopefully, new ground-based experiments coming live soon that are employing rotating HWPs in combination with TES focal planes (POLARBEAR2 and SO) will also offer data to better define our models. A hope for the future is the selection of a balloon experiment[2] employing similar technology to have it tested in a space-like environment before LiteBIRD is launched. On top of the benefit in terms of technology readiness, new data will certainly deliver a better picture of the foreground components nature that will be not only extremely valuable to improve the results on cosmology, but also increase the scientific output of CMB experiments.

---

[2] `https://techport.nasa.gov/view/90920`

Appendices

A

Units Conversion

The black-body spectrum in SI units ([W m^{-2} Hz^{-1} sr^{-1}]) is commonly defined through its spectral radiance function:

$$B(\nu, T) = \frac{2h\nu^3}{c^2} \frac{1}{e^{h\nu/k_B T} - 1}, \tag{A.1}$$

where h ($\sim 6.62607015 \times 10^{-34}$ Js) is the Planck constant, c (~ 299792458 m/s) is the speed of light in vacuum and k_B ($\sim 1.380649 \times 10^{-23}$ J/K) is the Boltzmann constant.

Jansky units: For historical reason the *Jansky* units (Jy) are commonly used in radio astronomy:

$$1 \text{ Jy} = 10^{-26} \text{ Wm}^{-2}\text{Hz}^{-1}, \tag{A.2}$$

therefore $B(\nu, T)$ is usually expressed in Jy/sr.

CMB units: Most CMB experiments are interested in the anisotropy spectrum:

$$B_{anisotropy}(\nu, T + \Delta T) = \left.\frac{\partial B(\nu, T)}{\partial T}\right|_{T_{cmb}} \Delta T, \tag{A.3}$$

therefore CMB temperature units are often used. A generic signal with spectrum $I_x(\nu)$ (in units of spectral radiance) is converted to CMB units by exploiting the factor:

$$b'(\nu) = \left.\frac{\partial B(\nu,T)}{\partial T}\right|_{T_{cmb}} = \left.\frac{2h^2\nu^4}{k_B c^2 T^2}\frac{e^{h\nu/k_BT}}{(e^{h\nu/k_BT}-1)^2}\right|_{T_{cmb}}. \tag{A.4}$$

Following Equations A.3 and A.4 the generic signal x can be expressed in CMB temperature units (K_{cmb}) as:

$$T_{x,cmb} = \frac{I_x(\nu)}{b'(\nu)}. \tag{A.5}$$

In CMB temperature units the CMB spectrum is therefore flat.

Rayleigh-Jeans units: In radio astronomy Rayleigh-Jeans units (K_{RJ}) are defined through the Rayleigh-Jeans approximation of the black-body spectrum ($h\nu \ll k_BT$):

$$B_{RJ}(\nu,T) = \frac{2k_B\nu^2}{c^2}T_{RJ}. \tag{A.6}$$

A generic signal with spectrum $I_x(\nu)$ (in units of spectral radiance) is defined in Rayleigh-Jeans units as:

$$T_{x,RJ} = \frac{c^2}{2k_B\nu^2}I_x(\nu). \tag{A.7}$$

Bandpass integration: We can define the signal hitting a detector from a source with spectrum $I_x(\nu)$ (in spectral radiance units – [W m^{-2} Hz^{-1} sr^{-1}]) as:

$$m_x^W = \mathcal{G}\int_0^\infty d\nu\ A_e G(\nu)\int_{4\pi} d\Omega\ B(\nu,\Omega)I_x(\nu),^{1} \tag{A.8}$$

where $\mathcal{G}$ is the detector specific gain, $G(\nu)$ is the bandpass function, A_e is the effective collecting area of the antenna and $B(\nu,\Omega)$ is the beam function. Under the assumption of single-mode antenna the effective area is $A_e = \lambda^2/\Omega_b$. Therefore, for a beam-filling source we can simplify the Ω_b terms, and a factor $\sim \lambda^2 = c^2/\nu^2$ is left behind. In the following we amalgamate every frequency-independent factor into the gain factor for compactness.

---

[1] For a beam filling source the solid angle integral can be simplified as $\Omega_b = \int_{4\pi} d\Omega\ B(\nu,\Omega)$.

Let's assume that we can observe the CMB only, then we can rewrite in CMB units:

$$\Delta T_{cmb} = \mathcal{G}_{cmb} \int_0^\infty d\nu \ \frac{c^2}{\nu^2} G(\nu) b'(\nu) \Delta T_{cmb}. \tag{A.9}$$

Where $\mathcal{G}_{cmb}$ is a conversion factor from Jy/sr to CMB units. We can simplify and define it as:

$$\mathcal{G}_{cmb} = \frac{1}{\int_0^\infty d\nu \ \frac{c^2}{\nu^2} G(\nu) b'(\nu)}. \tag{A.10}$$

We can use this factor to convert any other signal with a generic spectrum $I_x^{Jy/sr}(\nu)$ to CMB units as (the factor 10^{-26} comes from the conversion from SI units to Jy/sr):

$$m_x^{cmb} = \frac{\int_0^\infty d\nu \ \nu^{-2} G(\nu) I_x^{Jy/sr}(\nu)}{\int_0^\infty d\nu \ \nu^{-2} G(\nu) 10^{-26} b'(\nu)}. \tag{A.11}$$

In the same way we can define the conversion factor from spectral radiance units to Rayleigh-Jeans units as:

$$\mathcal{G}_{RJ} = \frac{1}{\int_0^\infty d\nu \ \frac{c^2}{\nu^2} G(\nu) \frac{2k_B \nu^2}{c^2}}. \tag{A.12}$$

And bandpass-integrate and convert to Rayleigh-Jeans units as:

$$m_x^{RJ} = \frac{\int_0^\infty d\nu \ \nu^{-2} G(\nu) I_x^{Jy/sr}(\nu)}{\int_0^\infty d\nu \ G(\nu) 10^{-26} \ \frac{2k_B}{c^2}}. \tag{A.13}$$

Note: a top-hat bandpass $G(\nu)$ in Equation A.11 has an effective response that follows a ν^{-2} scaling.

B

Sensitivity Calculation

To compute the total power loading a detector due both to the sky signal and the optical elements in the telescope we use the formula:

$$P_{opt} = \int_{\nu_i}^{\nu_f} \left[\sum_{i=0}^{N_{elem}} P_i(T_i, T_{r,i}, \nu) \right] d\nu, \tag{B.1}$$

where the sum runs over all N_{elem} elements in the optical chain and the first element ($i = 0$) is the CMB black-body with temperature $T_i = T_{cmb}$. T_i is the physical temperature of element i and $T_{r,i}$ is the temperature reflected by the element. Here we are approximating the frequency band of central frequency ν_c with a top-hat with edges ν_i and ν_f.

The contribution from the single element i can be calculated for a diffraction-limited aperture as:

$$P_i(T_i, T_{r,i}, \nu) = E_i(\nu) S(T_i, \nu) + R_i(\nu) S(T_{r,i}, \nu), \tag{B.2}$$

where:

$$\begin{aligned}
S(T, \nu) &= \frac{h\nu}{e^{h\nu/k_B T} - 1}, && \text{(B.3)}\\
E_i(\nu) &= \left[\prod_{j=i+1}^{N_{elem}} \eta_j(\nu) \right] \epsilon_i(\nu), && \text{(B.4)}\\
R_i(\nu) &= \left[\prod_{j=i+1}^{N_{elem}} \eta_j(\nu) \right] r_i(\nu). && \text{(B.5)}
\end{aligned}$$

$S(T,\nu)$ is the black-body emitted power seen from a diffraction limited aperture. The quantities $E_i(\nu)$ and $R_i(\nu)$ are the effective emissivity and reflectivity of element i seen by the detector through the optical elements j between element i and the detector. In this framework $\epsilon_i(\nu)$, $\eta_i(\nu)$ and $r_i(\nu)$ are respectively the emissivity, optical efficiency and reflectivity of element i.

Once the expected optical power for a detector in a given band is computed, the photon NEP can be computed from Equation 4.9, while the thermal carrier NEP can be computed from 4.10 and 4.11.

The NEP due to multiple sources i is found by taking the quadrature sum of the single values:

$$NEP_{tot} = \sqrt{\sum_i NEP_i^2}. \tag{B.6}$$

The readout and external (vibrations, magnetic fields, EMI, cosmic rays, etc.) noises are taken into account by assuming that they increase the total NEP by 10% and 15% respectively.

The single detector NEP can be converted to noise equivalent temperature (NET):

$$NET_{det} = \frac{NEP}{\sqrt{2}\, dP/dT_{cmb}}, \tag{B.7}$$

where the factor $\sqrt{2}$ comes from the conversion from $1/\sqrt{\text{Hz}}$ to $\sqrt{\text{sec}}$, and dP/dT_{cmb} is the conversion factor defined for a frequency band with edges ν_i and ν_f, as:

$$\frac{dP}{dT_{cmb}} = \frac{h^2}{k_B T_{cmb}^2} \int_{\nu_i}^{\nu_f} \left\{ \left[\prod_{i=0}^{N_{elem}} \eta_i(\nu) \right] \left(\frac{\nu}{e^{h\nu/k_B T_{cmb}} - 1} \right)^2 e^{h\nu/k_B T_{cmb}} \right\} d\nu. \tag{B.8}$$

The cumulative NET for the whole array of N_f detectors in a frequency band can be computed as:

$$NET_{array} = \frac{NET_{det}}{\sqrt{N_f \times y_d}}, \tag{B.9}$$

where y_d is the detector yield. We assumed for now $y_d \sim 0.8$ (conservative value).

By inverting Equation 2.1:

$$t = 2\left(\frac{NET_{cmb}}{\sigma_p}\right)^2 \frac{A_{sky}}{\eta}, \tag{B.10}$$

we can isolate the sensitivity σ_p. We can substitute NET_{cmb} with the full detector array NET_{array} to forecast the sensitivity to polarization for a given percentage of sky observed f_{sky} (LiteBIRD is a full sky survey therefore we assume $f_{sky} \sim 1$) and observation time t_{obs} (3 years for LiteBIRD):

$$\sigma_p = \sqrt{2\frac{4\pi f_{sky} NET^2_{array}}{\eta t_{obs}}}\left(\frac{10800}{\pi}\right) \quad [\mathrm{K} \cdot \mathrm{arcmin}], \tag{B.11}$$

where we have expressed A_{sky} is in angular units (arcmin^2). The whole sky is equivalent to $4\pi(10800/\pi)^2$ arcmin^2 $\sim 1.5 \times 10^8$ arcmin^2.

C

Bandpass Design

On-chip bandpass filters are microwave filters placed on the detector chip between the antenna and the TES detector to define the frequency band processed by the detector. Although I did not take part in the design of the bandpass filters for LiteBIRD detectors (or prototypes), I developed the filter prototypes for SKA (Square Kilometre Array) bands 5A (4.6-8.5 GHz) and 5B (8.3-15.3 GHz). The design procedure is similar to the one used for LiteBIRD (or other similar experiments) detectors. We report here the design principles and results of our design.

The design procedure of a microwave filter begins with considering the desired insertion loss (IL) in and out of band:

$$\mathrm{IL} = 10\log_{10} P_{LR} \quad [\mathrm{dB}], \tag{C.1}$$

where $P_{LR} = P_{in}/P_{out}$ is the power loss ratio and measures how much of the power available at the input of a circuit is lost before reaching the output. Chebyshev polynomials are often used to optimize the filter design and obtain steep roll-off between in-band and off-band. For a Chebyshev polynomial T_n of order n the power loss ratio is written as:

$$P_{LR} = 1 + k^2 T_n^2\left(\frac{\omega}{\omega_c}\right), \tag{C.2}$$

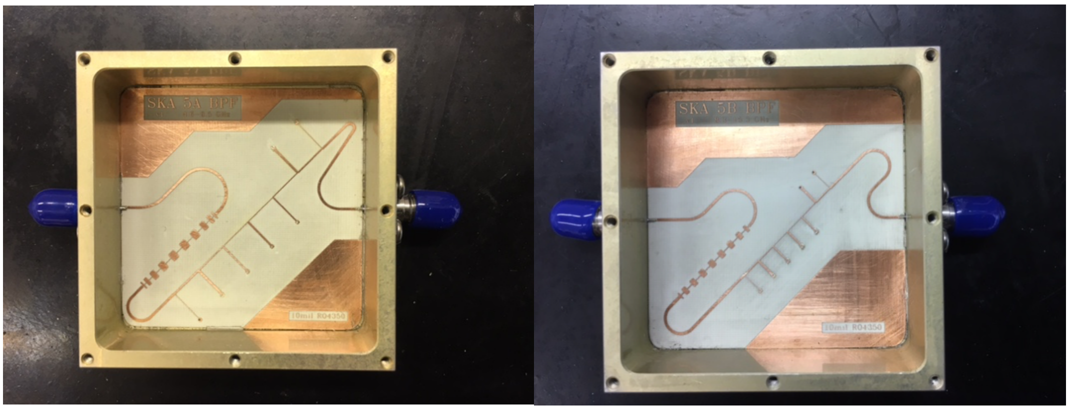

Figure C.1: SKA 5A (left) and 5B (right) band-pass filters.

where ω_c is the cut-off frequency of the filter. The in-band region will not be perfectly flat, but ripples of amplitude $1 + k^2$ are expected. Chebyshev polynomials of any order can be generated using the following formulas:

$$\begin{aligned} T_0(x) &= 1, && \text{(C.3)} \\ T_1(x) &= x, && \text{(C.4)} \\ T_{n+1}(x) &= 2xT_n(x) - T_{n-1}(x). && \text{(C.5)} \end{aligned}$$

A common way of designing filters is to represent them through lumped elements, where the filter is modelled as a combination of ideal resistors, inductors and capacitors connected by perfect conductors. However, for practical reasons, at microwave frequencies the lumped model is then transformed in a combination of distributed elements (transmission line). A practical example of a lumped element filter is the classical LC resonant circuit. For a series LC circuit, the current flowing through the circuit peaks at the resonant frequency $\omega_r = 1/\sqrt{LC}$ (minimum impedance), while for a parallel LC circuit the current reaches a minimum at the same resonant frequency (maximum impedance). The lumped element design can be transformed in the equivalent distributed element design through Richard's transformations and Kuroda identities [163].

In the case of SKA filters we used microstrips to implement the filter design (same as LiteBIRD with different materials). A microstrip is transmission line where the signals travels on a conductor (copper in the case of SKA, niobium in the case

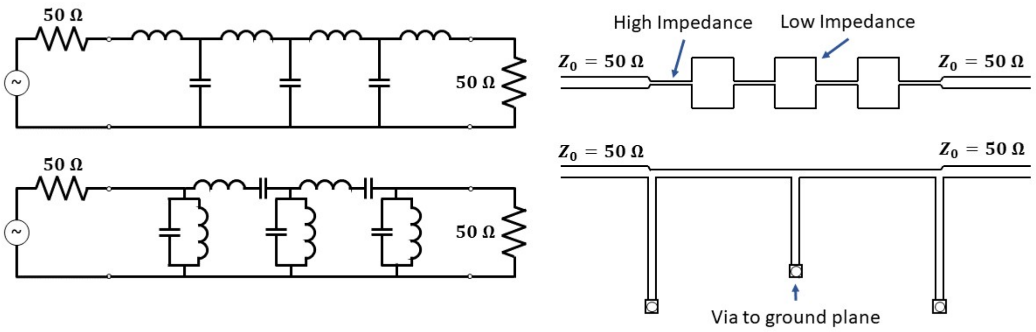

Figure C.2: *Top-left:* Lumped elements model of a low-pass filter. *Top-right:* Distributed element microstrip implementation: stepped-impedance filter. A high frequency signal sees an inductor as a high impedance element, while a capacitor is seen as a low impedance element (short in the limit of infinite frequency). *Bottom-left:* Lumped elements model of a band-pass filter. *Bottom-right:* Distributed element microstrip implementation: closed-stub implementation.

of LiteBIRD) of fixed thickness and width w supported by a dielectric substrate (RO4350 in the case of SKA, crystalline silicon in the case of LiteBIRD) of thickness d and dielectric constant ϵ_r. The impedance of a section of microstrip can be controlled by adjusting its width w.

In the work presented here I designed the two filters as a combination of a low-pass filter implemented following the so-called stepped-impedance design (visible

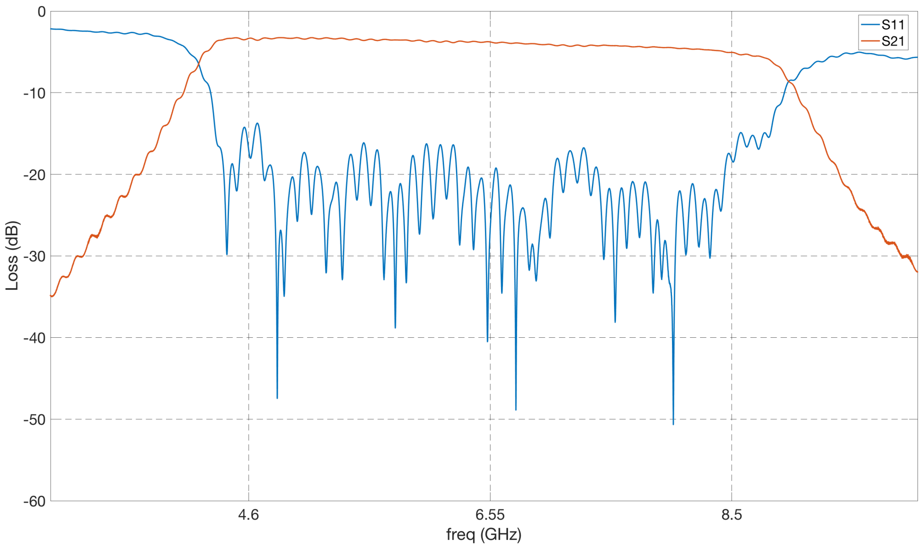

Figure C.3: SKA 5A band-pass filter insertion loss and return loss measured with a VNA.

in both images of Figure C.1 in the first section of the filter), and a band-pass filter implemented following the so-called closed-stub design (visible in both images of Figure C.1 in the second section of the filter). The low-pass filter had to be included to suppress the higher-frequency resonances that appear in distributed stub filters. The stubs are closed by halving their length and adding a via to the ground plane at the end of each stub[1].

Both band-pass filters (Figure C.1) have been developed with standard text book procedures [163] from 17.5 μm-thick copper micro-strips (same thickness of the copper ground plane) on a 0.254 mm-thick substrate of Rogers RO4350 material ($\epsilon_r = 3.66$)[2]. The designs have been optimized using the HFSS Designer software package [3] to produce models of the filters and simulate the response. After validation of the designs the physical filters have been manufactured in the photo-fabrication unit of the Oxford Physics department. The filters shown in Figure C.1 have been assembled inside aluminium boxes (8 × 8 cm) using commercial female SMA connectors to easily connect them to coaxial cables for testing.

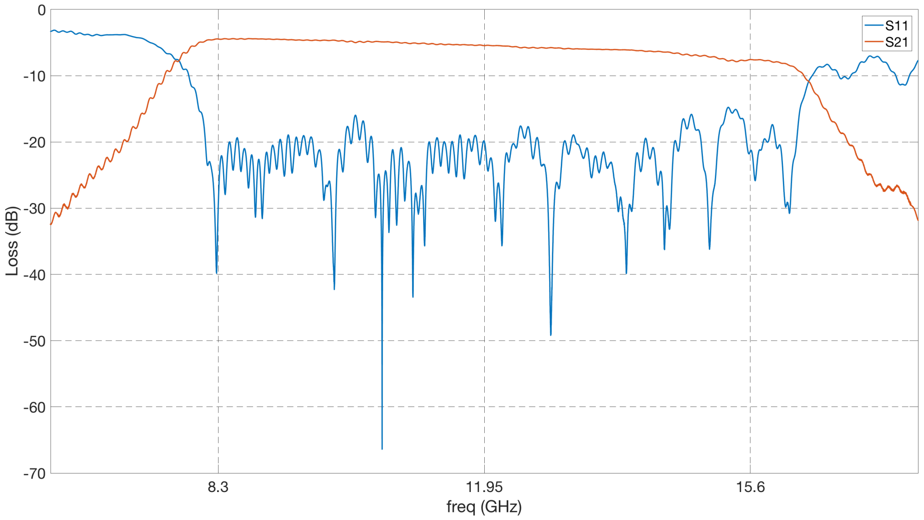

Figure C.4: SKA 5B band-pass filter insertion loss and return loss measured with a VNA.

---

[1] Notch filters are design as a single open resonant stub of $\lambda/4$ length along the microstrip.

[2] https://rogerscorp.com/advanced-connectivity-solutions/ro4000-series-laminates/ro4350b-laminates

[3] https://www.ansys.com/products/electronics/ansys-hfss

Measurements of the S_{21} (inverse of the insertion loss for matched input-output) and S_{11} parameters of the two filters are shown in Figures C.3 and C.4.

D

Telescope Pointing

We can generate the scanning strategy information (pointing, hit maps, detector cross-linking) by simply tracking the motion of the telescope bore-sight axis of Figure D.1 and the orientation of a vector perpendicular to the bore-sight axis that represents the orientation of a polarization sensitive detector with respect to the great circle passing through the ecliptic north pole and the point on the sky-sphere defined by the intersection of the bore-sight axis and the sphere[1].

The simplest and most effective way is to make use of quaternions, which are a 4D-extension of the classical representation of complex numbers in a 2D plane. A quaternion can be written as:

$$q = w + x\mathbf{i} + y\mathbf{j} + z\mathbf{k}, \tag{D.1}$$

where w, x, y, z are real numbers, and $\mathbf{i}$, $\mathbf{j}$, $\mathbf{k}$ can be interpreted as unit vectors each pointing along one of the 3D axes.

A generic 3D vector v can be written as a quaternion p with $w = 0$ and x, y, z equal to the vector components. While a rotation by an angle θ around a unitary 3D vector $u = [u_x, u_y, u_z]$ is defined by the quaternion r:

$$r = \cos(\theta/2) + u_x \sin(\theta/2)\mathbf{i} + u_y \sin(\theta/2)\mathbf{j} + u_z \sin(\theta/2)\mathbf{k}. \tag{D.2}$$

---

[1] See the International Astronomical Union (IAU) polarization convention at `https://lambda.gsfc.nasa.gov/product/about/pol_convention.cfm`.

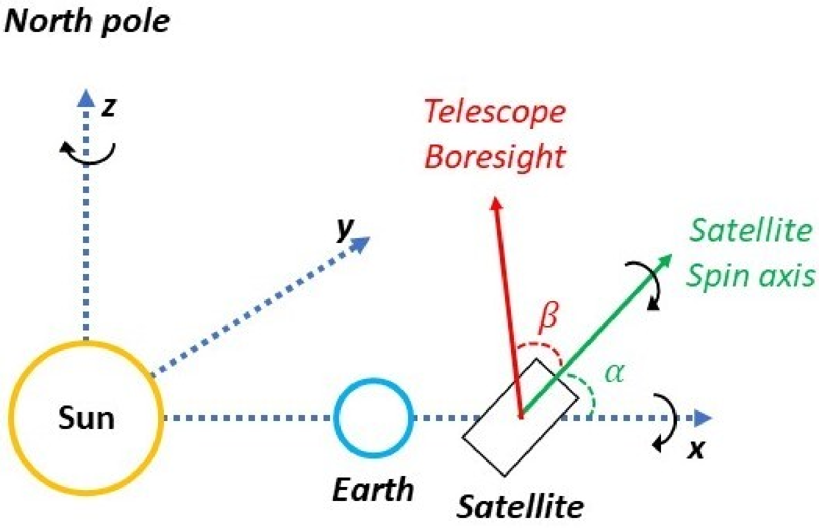

Figure D.1: Scanning strategy sketch. The satellite at L2 revolves around the Sun with the same rotation frequency ν_{sun} of the Earth, completing one revolution every year. The satellite rotates around a spin axis 45°-tilted (α) with respect to the anti-sun direction (aligned with the x-axis in the sketch) at frequency ν_{spin}. The 3 telescopes are oriented along the bore-sight axis tilted 50° (β) with respect to the spin axis. The spin axis rotates around the anti-sun direction with precession frequency ν_{prec}.

The new vector orientation after rotation can be found by applying the double product:

$$p' = r\ p\ r^{-1}, \tag{D.3}$$

where r^{-1} is the conjugate of r, defined as: $r^{-1} = r_w - r_x\mathbf{i} - r_y\mathbf{j} - r_z\mathbf{k}$.

We can combine the 3 rotations described in Figure D.1 to obtain the scanning pattern of the telescope from the bore-sight perspective and project it on to the sky. To track the polarization sensitive detector orientation with respect to the sky, we can define another vector perpendicular to the bore-sight axis.

×	**1**	**i**	**j**	**k**
1	**1**	**i**	**j**	**k**
i	**i**	−**1**	**k**	−**j**
j	**j**	−**k**	−**1**	**i**
k	**k**	**j**	−**i**	−**1**

Table D.1: Multiplication rules for quaternions.

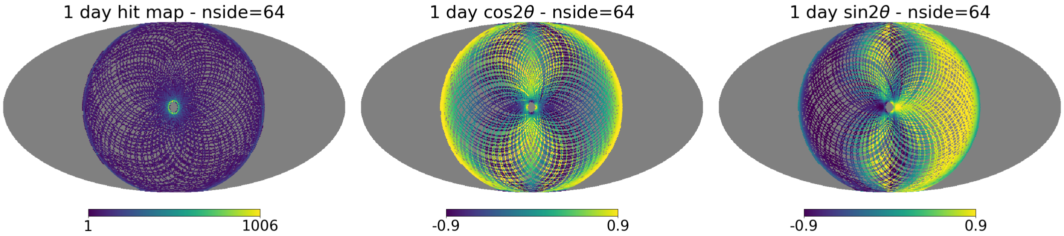

Figure D.2: Hit map (left) and spin-2 cross-linking (center and right) after one day of observation in elliptic coordinates (no HWP). The hit map color bar shows the total number of scans on the pixel, while the cross-linking color bars represent the scan-averaged value of $\cos 2\theta$ (center) and $\sin 2\theta$ (right).

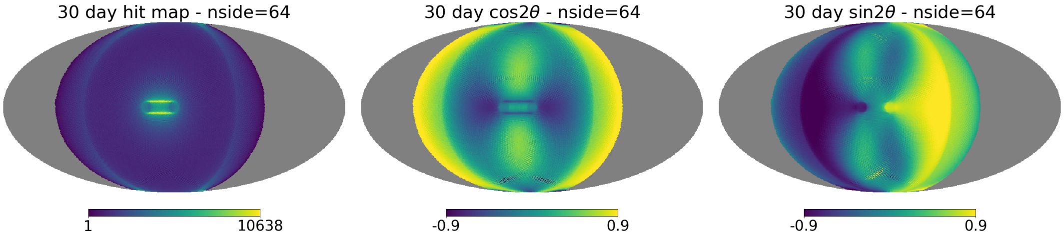

Figure D.3: Hit map (left) and spin-2 cross-linking (center and right) after 30 days of observation in elliptic coordinates (no HWP). The hit map color bar shows the total number of scans on the pixel, while the cross-linking color bars represent the scan-averaged value of $\cos 2\theta$ (center) and $\sin 2\theta$ (right).

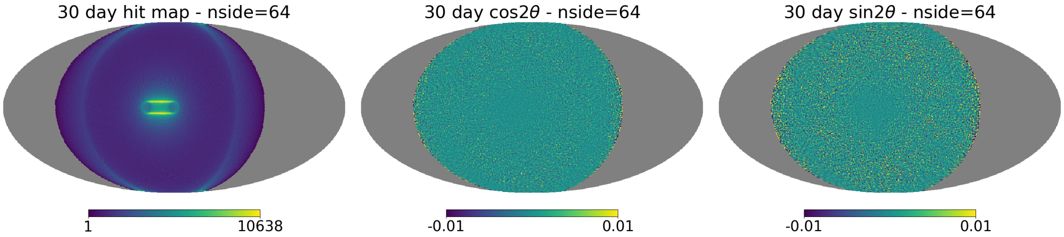

Figure D.4: Hit map (left) and spin-2 cross-linking (center and right) after 30 days of observation in elliptic coordinates. The hit map color bar shows the total number of scans on the pixel, while the cross-linking color bars represent the scan-averaged value of $\cos 2\theta$ (center) and $\sin 2\theta$ (right). We have included the effect of the rotating HWP.

Multiplication between two quaternions can be easily performed by remembering the relations in Table D.1. We initialize it perpendicular to the $y - axis$, and we track its orientation by defining the angle θ with respect to the reference circle coplanar to the yz-plane.

In Figures D.2 and D.3 we show an example of the evolution of the scanning strategy after 1 day from the beginning of the observations, and after 30 days. After 365 days the pattern repeats identically. We also report the spin-2 cross-linking components for both cases. In Figure D.4 we report the case for a spinning HWP to highlight the better cross-linking.

Finally, in Figure D.5 we report the same maps after 3 years of observation, both in the case of no HWP and with a 46 rpm spinning HWP.

For all the maps shown in this section we fixed the precession period around the anti-Sun direction to 3.2058 hours, the spin rate to 0.05 rpm, and the sampling

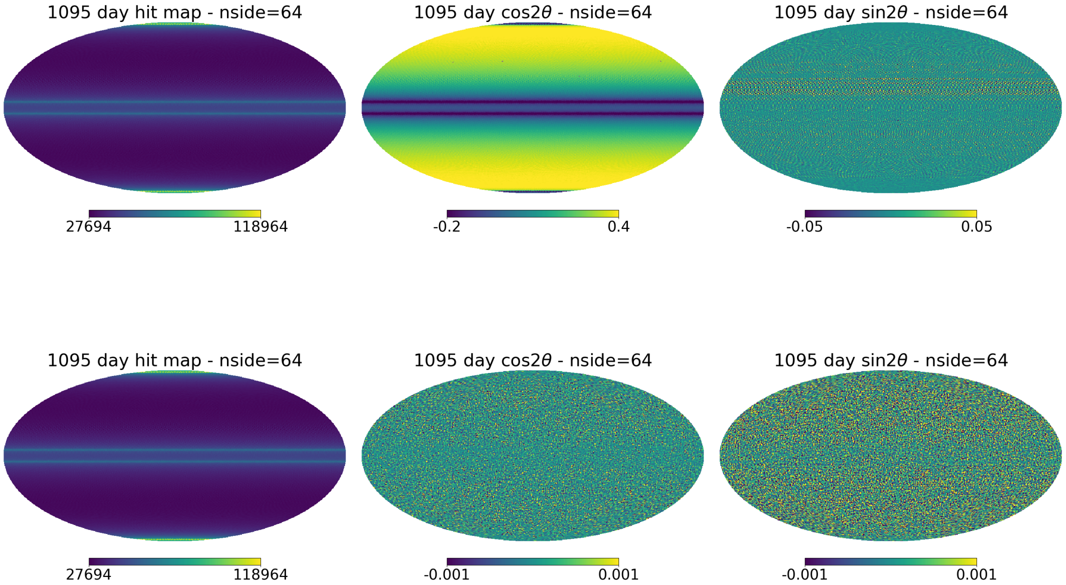

Figure D.5: Hit map (left) and spin-2 cross-linking (center and right) after 3 years of observation in elliptic coordinates. The hit map color bar shows the total number of scans on the pixel, while the cross-linking color bars represent the scan-averaged value of $\cos 2\theta$ (center) and $\sin 2\theta$ (right). *Top row:* no HWP included. *Bottom row:* with rotating HWP included.

rate to 19 Hz. The code used to generate all the maps shown in this appendix is available in the following:

```python
import numpy as np
import healpy as hp
import matplotlib.pyplot as plt
import os
import time
from numba import jit

# Normalize Vector or Quaternion
@jit
def normalize(v):
  size = v.size
  if size == 3:
    lenght = np.sqrt(v[0]*v[0]+v[1]*v[1]+v[2]*v[2])

  if size == 4:
    lenght = np.sqrt(v[0]*v[0]+v[1]*v[1]+v[2]*v[2]+v[3]*v[3])

  return v/lenght

# Quaternion Product
@jit
def q_mult(q1, q2):
  w = q1[0] * q2[0] - q1[1] * q2[1] - q1[2] * q2[2] - q1[3] * q2[3]
  x = q1[0] * q2[1] + q1[1] * q2[0] + q1[2] * q2[3] - q1[3] * q2[2]
  y = q1[0] * q2[2] + q1[2] * q2[0] + q1[3] * q2[1] - q1[1] * q2[3]
  z = q1[0] * q2[3] + q1[3] * q2[0] + q1[1] * q2[2] - q1[2] * q2[1]
  return np.array([w, x, y, z])

# Quaternion Conjugate: q-1
@jit
def q_conjugate(q):
  return np.array([q[0], -q[1], -q[2], -q[3]])

# Rotate a Vector Using a Quaternion: qvq-1
@jit
def rotate_vector(q1, v1):
  q2 = np.concatenate((np.array([0.]),v1))
  return q_mult(q_mult(q1, q2), q_conjugate(q1))[1:]

# Create a Quaternion that defines a rotation by an angle theta (deg)
   around a vector [x,y,z]
@jit
def rotaxis_to_q(v, theta):
  v = normalize(v)
  theta = np.deg2rad(theta)
  w = np.cos(theta/2.)
  x = v[0]*np.sin(theta/2.)
  y = v[1]*np.sin(theta/2.)
  z = v[2]*np.sin(theta/2.)
  return np.array([w, x, y, z])
```

```
# Define rotation around the Sun: 1 deg per day around vector [0,0,1] (z axis)
@jit
def rot_around_sun(v, t):
  nu_around_sun = 1./365./24./60./60.
  z = np.array([0.,0.,1.])
  q = rotaxis_to_q(z, 360.*nu_around_sun*t)
  r = rotate_vector(q, v)
  return r

# Define satellite precession around anti-sun direction:
# initialized with anti-sun direction aligned with x axis [1,0,0]
# precession defined by the period in hour
@jit
def rot_around_antisun_dir(v, precession_hr, t):
  nu_around_antisun_dir = 1./precession_hr/60./60.
  x = np.array([1.,0.,0.])
  q = rotaxis_to_q(x, 360.*nu_around_antisun_dir*t)
  r = rotate_vector(q, v)
  return r

# Define spin around spin-axis tilted by 45 deg with respect to anti-sun direction:
# initialized with spin-axis oriented at 45 deg from x axis in
# the xz plane [1./np.sqrt(2),0.,1./np.sqrt(2)] spin defined by the frequency in rpm
@jit
def rot_around_spin_ax(v, spin_rpm, t):
  nu_around_spin_ax = spin_rpm/60.
  xz45 = np.array([1./np.sqrt(2),0.,1./np.sqrt(2)])
  q = rotaxis_to_q(xz45, 360.*nu_around_spin_ax*t)
  r = rotate_vector(q, v)
  return r

# Define HWP rotation around boresight direction:
# boresight direction defined by the axis variable
# rotation defined by the HWP frequency in rpm
@jit
def rot_HWP(v, hwp_rpm, t, axis):
  nu_around_boresight = hwp_rpm/60.
  q = rotaxis_to_q(axis, 360.*4.*nu_around_boresight*t)
  r = rotate_vector(q, v)
  return r

# Generate scan:
# nside = nside of output maps
# alpha = spin axis precession angle
# precession_hr = precession period in hours
# beta = boresight angle from spin axis
# spin_rpm = spin rate in rpm
# det_gamma = detector orientation in deg
# days = number of days to simulate
# days_out = output map interval in days
# sampling_hz = sampling rate in Hz
# hwp_rpm = HWP rotation rate in rpm (if 0 the HWP is off)
```

```python
def generate_scan(nside, alpha, precession_hr, beta, spin_rpm, det_gamma, days, days_out, sampling_hz, hwp_rpm):

  z = np.array([0.,0.,1.])
  beta = np.deg2rad(beta)
  alpha = np.deg2rad(alpha)
  sec_in_day = 60.*60.*24.
  steps = int(sec_in_day*sampling_hz)

  cos4 = np.zeros(hp.nside2npix(nside))
  sin4 = np.zeros(hp.nside2npix(nside))
  cos2 = np.zeros(hp.nside2npix(nside))
  sin2 = np.zeros(hp.nside2npix(nside))
  nhit = np.zeros(hp.nside2npix(nside))

  # Initialization of the boresight axis in the xz plane at alpha+beta deg from the x axis
  boresight = np.array([np.sin(np.pi/2.-alpha-beta), 0., np.cos(np.pi/2.-alpha-beta)])

  # Quaternion rotation around boresight by angle det_gamma (orientation of the detector in
  # the plane perpendicular to the boresight)
  q_det_gamma = rotaxis_to_q(boresight, det_gamma)

  # Zeroth orientation of the polarization sensitive detector co-planar to the xz plane
  detector_orientation_0 = np.array([-boresight[2], 0., boresight[0]])

  # Rotate the detector to det_gamma angle
  detector_orientation = rotate_vector(q_det_gamma, detector_orientation_0)

  for i in range(int(days+1.)):

    # Save hit map and cross-linking maps
    if i == 1 or i%days_out == 0. or i == 365 or i == 365*2 or i == 365*3 or i == int(days):
      hp.write_map('nhit_day_%d.fits'%i, nhit)
      hp.write_map('cos2_day_%d.fits'%i, cos2)
      hp.write_map('sin2_day_%d.fits'%i, sin2)
      hp.write_map('cos4_day_%d.fits'%i, cos4)
      hp.write_map('sin4_day_%d.fits'%i, sin4)

    # Initial time
    t0 = i * sec_in_day

    for j  in range(int(steps)):

      # Increment time
      t = t0+(j+1.)/sampling_hz

      # Rotate boresight
      v_tmp = rot_around_spin_ax(boresight, spin_rpm, t)
      v_tmp = rot_around_antisun_dir(v_tmp, precession_hr, t)
```

```
        v_new = rot_around_sun(v_tmp, t)

        # Rotate detector vector
        det_tmp = rot_HWP(detector_orientation, hwp_rpm, t, boresight)
        det_tmp = rot_around_spin_ax(det_tmp, spin_rpm, t)
        det_tmp = rot_around_antisun_dir(det_tmp, precession_hr, t)
        det_new = rot_around_sun(det_tmp, t)

        # Great circle plane
        plane_axis = np.cross(v_new, z)

        # Pixel index
        ipix = hp.vec2pix(nside, v_new[0], v_new[1], v_new[2])

        # Detector angle on the sky with respect to the great circle
        angle = np.arcsin(np.dot(det_new, plane_axis)/np.linalg.norm(
    det_new)/np.linalg.norm(plane_axis))
        angle = np.pi/2. - angle

        # Update maps
        cos4[ipix] = cos4[ipix] + np.cos(4.*angle)
        sin4[ipix] = sin4[ipix] + np.sin(4.*angle)
        cos2[ipix] = cos2[ipix] + np.cos(2.*angle)
        sin2[ipix] = sin2[ipix] + np.sin(2.*angle)
        nhit[ipix] = nhit[ipix] + 1.


nside = 64
alpha = 45.
prec_hr = 3.2058
beta = 50.
spin_rpm = 0.05
det_angle = 0.
days = 365. * 3.
days_out = 15.
sampling_hz = 19.
hwp_rpm = 46. # = 0. for no HWP

generate_scan(nside, alpha, prec_hr, beta, spin_rpm, det_angle, days,
    days_out, sampling_hz, hwp_rpm)
```

Listing D.1: A sample of the code used to generate the hit map and cross-linking maps.

E

Multi-Layer HWP Optimization

We report here the code that implements the algorithm described in Chapter 2 to optimize the AHWP configuration.

```
import numpy as np
import scipy
import matplotlib.pylab as plt
import scipy.constants as cost

#Rotation Matrix from Equation \ref{muller_hwp_rot}
def rotation(x):
  return np.array([[1., 0., 0., 0.], [0., np.cos(2.*x), -1.*np.sin(2.*x), 0.], [0., np.sin(2.*x), np.cos(2.*x), 0.], [0., 0., 0., 1.]])

#Birifrangent Matrix from Equation \ref{muller_hwp_rot}
def birefringent(d):
  return np.array([[1., 0., 0., 0.], [0., 1., 0., 0.], [0., 0., np.cos(d), -1.*np.sin(d)], [0., 0., np.sin(d), np.cos(d)]])

#Retardance from Equation \ref{eq:retardance}
def delta(nu, no, ne, t):
  return 2.*np.pi*nu*abs(no-ne)*t/cost.c

df = 0.1 # Frequency step in GHz
f0 = 34. # LFT nu_0 in GHz
f1 = 161. # LFT nu_f in GHz
steps = int((f1-f0)/df+1) # Steps
f = np.linspace(f0, f1, steps)*1.e9 # Frequency range in Hz
fc = f[0]+(f[-1]-f[0])/2 # Central frequency
no = 3.047 # Refractive index ordinary axis
ne = 3.361 # Refractive index extra-ordinary axis
t0 = cost.c/abs(no-ne)/fc/2. # thickness at central frequency for retardance = np.pi
EFF = 0.98 # Target efficiency
```

```
# Define LFT bands lower and upper bounds
i40_i = np.where(f==34.e9)[0][0]
i40_f = np.where(f==46.e9)[0][0]
i50_i = np.where(f==42.5e9)[0][0]
i50_f = np.where(f==57.5e9)[0][0]
i60_i = np.where(f==53.e9)[0][0]
i60_f = np.where(f==67.e9)[0][0]
i68_i = np.where(f==60.e9)[0][0]
i68_f = np.where(f==76.e9)[0][0]
i78_i = np.where(f==69.e9)[0][0]
i78_f = np.where(f==87.e9)[0][0]
i89_i = np.where(f==79.e9)[0][0]
i89_f = np.where(f==99.e9)[0][0]
i100_i = np.where(f==88.5e9)[0][0]
i100_f = np.where(f==101.5e9)[0][0]
i119_i = np.where(f==101.e9)[0][0]
i119_f = np.where(f==137.e9)[0][0]
i140_i = np.where(f==119.e9)[0][0]
i140_f = np.where(f==161.e9)[0][0]

eff = np.zeros(steps) # initialize efficiency vector
phi = np.zeros(steps) # initialize phase vector
avg_eff = np.zeros(9) # initialize band-averaged efficiency vector

# Keep looping till band-averaged efficiency vector satisfies requirement (> 0.98)
while avg[0] <= EFF or avg[1] <= EFF or avg[2] <= EFF or avg[3] <= EFF or avg[4] <= EFF or avg[5] <= EFF or avg[6] <= EFF or avg[7] <= EFF or avg[8] <= EFF:
    # Random pair of angles 0 < a < 180
  a = np.random.randint(0, 1800, 2) / 10. / 180. * np.pi
  a1 = a[1] # First plate angle
  a2 = a[0] # Second plate angle
  a3 = np.deg2rad(0.) # Central plate (third) fixed
  a4 = a[1] # Fourth plate angle
  a5 = a[0] # Fifth plate angle

  # Loop over all frequency steps
  for i in range(steps):
    delta_0 = delta(f[i], no, ne, t0) # Single pplate retardance
    biref_0 = birefringent(delta_0) # Single plate birefringent matrix

    # Single plate HWP matrix for different orientation
    gamma_5=np.matmul(rotation(-1.*a5), np.matmul(biref_0, rotation(1.*a5)))
    gamma_4=np.matmul(rotation(-1.*a4), np.matmul(biref_0, rotation(1.*a4)))
    gamma_3=np.matmul(rotation(-1.*a3), np.matmul(biref_0, rotation(1.*a3)))
    gamma_2=np.matmul(rotation(-1.*a2), np.matmul(biref_0, rotation(1.*a2)))
    gamma_1=np.matmul(rotation(-1.*a1), np.matmul(biref_0, rotation(1.*a1)))
```

```
            # Combining plates:
        gamma_tot = np.matmul(gamma_5, gamma_4)
        gamma_tot = np.matmul(gamma_tot, gamma_3)
        gamma_tot = np.matmul(gamma_tot, gamma_2)
        gamma_tot = np.matmul(gamma_tot, gamma_1)

        # AHWP modulation efficiency
        eff_num = np.sqrt((gamma_tot[1, 1] - gamma_tot[2, 2])**2. + (gamma_tot[1, 2] + gamma_tot[2, 1])**2.) / 4.
        eff_den = gamma_tot[0, 0]/2. + (gamma_tot[1, 1] + gamma_tot[2, 2]) / 4.
        eff[i] = eff_num / eff_den

        # AHWP phase
        phi[i] = np.arctan((gamma_tot[1, 2] + gamma_tot[2, 1]) / (gamma_tot[1, 1] - gamma_tot[2, 2])) / 4.

        # LFT band-averaged modulation efficiency
        avg[0]=sum(eff[i40_i:i40_f+1])/(i40_f+1-i40_i)
        avg[1]=sum(eff[i50_i:i50_f+1])/(i50_f+1-i50_i)
        avg[2]=sum(eff[i60_i:i60_f+1])/(i60_f+1-i60_i)
        avg[3]=sum(eff[i68_i:i68_f+1])/(i68_f+1-i68_i)
        avg[4]=sum(eff[i78_i:i78_f+1])/(i78_f+1-i78_i)
        avg[5]=sum(eff[i89_i:i89_f+1])/(i89_f+1-i89_i)
        avg[6]=sum(eff[i100_i:i100_f+1])/(i100_f+1-i100_i)
        avg[7]=sum(eff[i119_i:i119_f+1])/(i119_f+1-i119_i)
        avg[8]=sum(eff[i140_i:i140_f+1])/(i140_f+1-i140_i)
```

Listing E.1: A sample of the code used to optimize the HWP configuration.

F

Runge-Kutta 4th order method

The Runge-Kutta 4th order method (RK4 from now on) is the most well known method of the Runge-Kutta methods family developed by Carl Runge and Wilhelm Kutta, to solve ordinary differential equations.
For an initial value problem specified as:

$$\begin{aligned} \frac{dy}{dx} &= f(x,y) && \text{(F.1)} \\ y_0 &= y(x_0), && \text{(F.2)} \end{aligned}$$

and step size h, RK4 finds a numerical approximation of the function $y(x)$ at position x_{n+1} as:

$$\begin{aligned} y_{n+1} &= y_n + h\frac{1}{6}(k_1 + 2k_2 + 2k_3 + k_4) + \mathcal{O}(h^5) && \text{(F.3)} \\ x_{n+1} &= x_n + h, && \text{(F.4)} \end{aligned}$$

where at each step n the coefficient k_i $(i = 1, 2, 3, 4)$ are:

$$\begin{aligned} k_1 &= f(x_n, y_n) && \text{(F.5)} \\ k_2 &= f(x_n + \frac{h}{2}, y_n + h\frac{k_1}{2}) && \text{(F.6)} \\ k_3 &= f(x_n + \frac{h}{2}, y_n + h\frac{k_2}{2}) && \text{(F.7)} \\ k_4 &= f(x_n + h, y_n + hk_3). && \text{(F.8)} \end{aligned}$$

At each step x_{n+1} the procedure estimates the value of the function $y(x)$ by dividing the interval h in half and estimating the slope of the function as a weighted mean of the estimation at the beginning of the interval x_n (k_1), in the middle of the interval $x_n + \frac{h}{2}$ (k_2 and k_3) and at the end of the interval $x_{n+1} = x_n + h$ (k_4). As it is clear from Equation F.3 the weighted mean gives more importance to the value estimated in the middle of the interval.

As written in Equation F.3 the local error is expected to be of the order of $\mathcal{O}(h^5)$, therefore a smaller step size leads to smaller error.

RK4 can be generalized to higher orders by subdividing the interval h in sub-intervals smaller than $h/2$.

References

[1] Tommaso Ghigna et al. “Permittivity and permeability of epoxy-magnetite powder composites at microwave frequencies”. In: *Journal of Applied Physics* 127.4 (2020), p. 045102. URL: https://doi.org/10.1063/1.5128519.

[2] Tommaso Ghigna et al. “Design of a Testbed for the Study of System Interference in Space CMB Polarimetry”. In: *Journal of Low Temperature Physics* (Jan. 2020). URL: 10.1007/s10909-020-02359-9.

[3] Tommaso Ghigna et al. *Requirements for future CMB satellite missions: photometric and band-pass response calibration.* 2020. arXiv: 2004.11601 [astro-ph.IM].

[4] Kunimoto Komatsu et al. “Demonstration of the broadband half-wave plate using the nine-layer sapphire for the cosmic microwave background polarization experiment”. In: *Journal of Astronomical Telescopes, Instruments, and Systems* 5.4 (2019), pp. 1–14. URL: https://doi.org/10.1117/1.JATIS.5.4.044008.

[5] H. Sugai et al. “Updated Design of the CMB Polarization Experiment Satellite LiteBIRD”. In: *Journal of Low Temperature Physics* (Jan. 2020). URL: http://dx.doi.org/10.1007/s10909-019-02329-w.

[6] A. A. Penzias and R. W. Wilson. “A Measurement of Excess Antenna Temperature at 4080 Mc/s.” In: *ApJ* 142 (July 1965), pp. 419–421.

[7] R. H. Dicke et al. “Cosmic Black-Body Radiation.” In: *Astrophysical Journal Supplement* 142 (July 1965), pp. 414–419.

[8] D. J. Fixsen. “THE TEMPERATURE OF THE COSMIC MICROWAVE BACKGROUND”. In: *The Astrophysical Journal* 707.2 (Nov. 2009), pp. 916–920. URL: https://doi.org/10.1088%5C%2F0004-637x%5C%2F707%5C%2F2%5C%2F916.

[9] J. C. Mather et al. “Measurement of the Cosmic Microwave Background Spectrum by the COBE FIRAS Instrument”. In: *Astrophysical Journal Supplement* 420 (Jan. 1994), p. 439.

[10] J. Chluba et al. *Spectral Distortions of the CMB as a Probe of Inflation, Recombination, Structure Formation and Particle Physics.* 2019. arXiv: 1903.04218 [astro-ph.CO].

[11] J. Chluba et al. *New Horizons in Cosmology with Spectral Distortions of the Cosmic Microwave Background.* 2019. arXiv: 1909.01593 [astro-ph.CO].

[12] Martin White, Douglas Scott, and Joseph Silk. “Anisotropies in the Cosmic Microwave Background”. In: *Annual Review of Astronomy and Astrophysics* 32 (Jan. 1994), pp. 319–370.

[13] Wayne Hu and Scott Dodelson. “Cosmic Microwave Background Anisotropies”. In: *Annual Review of Astronomy and Astrophysics* 40.1 (2002), pp. 171–216. eprint: https://doi.org/10.1146/annurev.astro.40.060401.093926. URL: https://doi.org/10.1146/annurev.astro.40.060401.093926.

[14] Anthony Challinor and Hiranya Peiris. “Lecture notes on the physics of cosmic microwave background anisotropies”. In: *AIP Conference Proceedings* 1132.1 (2009), pp. 86–140. eprint: https://aip.scitation.org/doi/pdf/10.1063/1.3151849. URL: https://aip.scitation.org/doi/abs/10.1063/1.3151849.

[15] G. F. Smoot et al. “Structure in the COBE Differential Microwave Radiometer First-Year Maps”. In: *Astrophysical Journal Letter* 396 (Sept. 1992), p. L1.

[16] S. Hanany et al. “MAXIMA-1: A Measurement of the Cosmic Microwave Background Anisotropy on Angular Scales of 10[arcmin]–5°”. In: *The Astrophysical Journal* 545.1 (Dec. 2000), pp. L5–L9. URL: https://doi.org/10.1086%2F317322.

[17] Andrew H Jaffe et al. “Recent results from the MAXIMA experiment”. In: *New Astronomy Reviews* 47.8 (2003). Proceedings of the 2nd CMBNet workshop on Science and Parameter Extraction, pp. 727–732. URL: http://www.sciencedirect.com/science/article/pii/S1387647303001556.

[18] J. E. Ruhl et al. “Improved Measurement of the Angular Power Spectrum of Temperature Anisotropy in the Cosmic Microwave Background from Two New Analyses of BOOMERANG Observations”. In: *The Astrophysical Journal* 599.2 (Dec. 2003), pp. 786–805. URL: https://doi.org/10.1086%2F379345.

[19] W. C. Jones et al. “A Measurement of the Angular Power Spectrum of the CMB Temperature Anisotropy from the 2003 Flight of BOOMERANG”. In: *Astrophysical Journal Supplement* 647.2 (Aug. 2006), pp. 823–832. arXiv: astro-ph/0507494 [astro-ph].

[20] C. L. Bennett et al. “First-Year Wilkinson Microwave Anisotropy Probe (WMAP) Observations: Preliminary Maps and Basic Results”. In: *Astrophysical Journal Supplement* 148.1 (Sept. 2003), pp. 1–27. arXiv: astro-ph/0302207 [astro-ph].

[21] N. Jarosik et al. “Three-Year Wilkinson Microwave Anisotropy Probe (WMAP) Observations: Beam Profiles, Data Processing, Radiometer Characterization, and Systematic Error Limits”. In: *Astrophysical Journal Supplement* 170.2 (June 2007), pp. 263–287. arXiv: astro-ph/0603452 [astro-ph].

[22] G. Hinshaw et al. “Five-Year Wilkinson Microwave Anisotropy Probe Observations: Data Processing, Sky Maps, and Basic Results”. In: *Astrophysical Journal Supplement* 180.2 (Feb. 2009), pp. 225–245. arXiv: 0803.0732 [astro-ph].

[23] N. Jarosik et al. “Seven-year Wilkinson Microwave Anisotropy Probe (WMAP) Observations: Sky Maps, Systematic Errors, and Basic Results”. In: *Astrophysical Journal Supplement* 192.2, 14 (Feb. 2011), p. 14. arXiv: 1001.4744 [astro-ph.CO].

[24] C. L. Bennett et al. “Nine-year Wilkinson Microwave Anisotropy Probe (WMAP) Observations: Final Maps and Results”. In: *Astrophysical Journal Supplement* 208.2, 20 (Oct. 2013), p. 20. arXiv: 1212.5225 [astro-ph.CO].

[25] Planck Collaboration et al. “Planck 2013 results. I. Overview of products and scientific results”. In: *A&A* 571 (2014), A1. URL: https://doi.org/10.1051/0004-6361/201321529.

[26] Planck Collaboration et al. “Planck 2015 results - I. Overview of products and scientific results”. In: *A&A* 594 (2016), A1. URL: https://doi.org/10.1051/0004-6361/201527101.

[27] Y. Akrami et al. “Planck 2018 results. I. Overview and the cosmological legacy of Planck”. In: (2018). arXiv: 1807.06205 [astro-ph.CO].

[28] P. A. R. Ade et al. “Measurements of Degree-Scale B-mode Polarization with the BICEP/Keck Experiments at South Pole”. In: *53rd Rencontres de Moriond on Cosmology La Thuile, Italy, March 17-24, 2018*. 2018. arXiv: 1807.02199 [astro-ph.CO].

[29] P. A. R. Ade et al. “Measurement of the Cosmic Microwave Background Polarization Lensing Power Spectrum with the POLARBEAR Experiment”. In: *Phys. Rev. Lett.* 113 (2 July 2014), p. 021301. eprint: 1312.6646v2. URL: https://link.aps.org/doi/10.1103/PhysRevLett.113.021301.

[30] Blake D. Sherwin et al. “Two-season Atacama Cosmology Telescope polarimeter lensing power spectrum”. In: *Phys. Rev. D* 95 (12 June 2017), p. 123529. eprint: 1611.09753v1. URL: https://link.aps.org/doi/10.1103/PhysRevD.95.123529.

[31] A. van Engelen et al. “A Measurement of Gravitational Lensing of the Microwave Background Using South Pole Telescope Data”. In: *The Astrophysical Journal* 756.2 (2012), p. 142. eprint: 1202.0546v1. URL: http://stacks.iop.org/0004-637X/756/i=2/a=142.

[32] Peter Ade et al. “The Simons Observatory: science goals and forecasts”. In: *Journal of Cosmology and Astroparticle Physics* 2019.02 (Feb. 2019), pp. 056–056. URL: https://doi.org/10.1088%5C%2F1475-7516%5C%2F2019%5C%2F02%5C%2F056.

[33] Kevork Abazajian et al. “CMB-S4 Science Case, Reference Design, and Project Plan”. In: 2019. arXiv: 1907.04473 [astro-ph.IM].

[34] M. Hazumi et al. “LiteBIRD: a small satellite for the study of B-mode polarization and inflation from cosmic background radiation detection”. In: *Proc. SPIE* 8442 (2012), pp. 8442 - 8442 –9. URL: https://doi.org/10.1117/12.926743.

[35] T. Matsumura et al. “Mission Design of LiteBIRD”. In: *Journal of Low Temperature Physics* 176.5 (Sept. 2014), pp. 733–740. eprint: 1311.2847v1. URL: https://doi.org/10.1007/s10909-013-0996-1.

[36] Matias Zaldarriaga and Uros Seljak. “All-sky analysis of polarization in the microwave background”. In: *Phys. Rev. D* 55 (4 Feb. 1997), pp. 1830–1840. URL: https://link.aps.org/doi/10.1103/PhysRevD.55.1830.

[37] Uros Seljak and Matias Zaldarriaga. “Signature of Gravity Waves in the Polarization of the Microwave Background”. In: *Phys. Rev. Lett.* 78 (11 Mar. 1997), pp. 2054–2057. URL: https://link.aps.org/doi/10.1103/PhysRevLett.78.2054.

[38] Wayne Hu and Martin White. "CMB anisotropies: Total angular momentum method". In: *Phys. Rev. D* 56 (2 July 1997), pp. 596–615. URL: https://link.aps.org/doi/10.1103/PhysRevD.56.596.

[39] Marc Kamionkowski, Arthur Kosowsky, and Albert Stebbins. "A Probe of Primordial Gravity Waves and Vorticity". In: *Phys. Rev. Lett.* 78 (11 Mar. 1997), pp. 2058–2061. URL: https://link.aps.org/doi/10.1103/PhysRevLett.78.2058.

[40] Marc Kamionkowski, Arthur Kosowsky, and Albert Stebbins. "Statistics of cosmic microwave background polarization". In: *Phys. Rev. D* 55 (12 June 1997), pp. 7368–7388. URL: https://link.aps.org/doi/10.1103/PhysRevD.55.7368.

[41] Matias Zaldarriaga and Uros Seljak. "Gravitational lensing effect on cosmic microwave background polarization". In: *Phys. Rev. D* 58 (2 June 1998), p. 023003. URL: https://link.aps.org/doi/10.1103/PhysRevD.58.023003.

[42] Sara Seager, Dimitar D. Sasselov, and Douglas Scott. "How Exactly Did the Universe Become Neutral?" In: *The Astrophysical Journal Supplement Series* 128.2 (June 2000), pp. 407–430. URL: https://doi.org/10.1086%5C%2F313388.

[43] Antony Lewis, Anthony Challinor, and Anthony Lasenby. "Efficient computation of CMB anisotropies in closed FRW models". In: *Astrophysical Journal* 538 (2000), pp. 473–476. arXiv: astro-ph/9911177 [astro-ph].

[44] Antony Lewis and Sarah Bridle. "Cosmological parameters from CMB and other data: A Monte Carlo approach". In: *Physical Review D* 66 (2002), p. 103511. arXiv: astro-ph/0205436 [astro-ph].

[45] Planck Collaboration et al. "Planck 2018 results. VI. Cosmological parameters". In: *arXiv e-prints*, arXiv:1807.06209 (July 2018), arXiv:1807.06209. arXiv: 1807.06209 [astro-ph.CO].

[46] Suzanne Staggs, Jo Dunkley, and Lyman Page. "Recent discoveries from the cosmic microwave background: a review of recent progress". In: *Reports on Progress in Physics* 81.4 (Feb. 2018), p. 044901. URL: https://doi.org/10.1088%5C%2F1361-6633%5C%2Faa94d5.

[47] S. Adachi et al. "A measurement of the CMB E-mode angular power spectrum at subdegree scales from 670 square degrees of POLARBEAR data". In: *arXiv e-prints*, arXiv:2005.06168 (May 2020), arXiv:2005.06168. arXiv: 2005.06168 [astro-ph.CO].

[48] Dongwon Han et al. "The Atacama Cosmology Telescope: Delensed Power Spectra and Parameters". In: *arXiv e-prints*, arXiv:2007.14405 (July 2020), arXiv:2007.14405. arXiv: 2007.14405 [astro-ph.CO].

[49] and P. A. R. Ade et al. "A Measurement of the Cosmic Microwave BackgroundB-mode Polarization Power Spectrum at Subdegree Scales from Two Years of polarbear Data". In: *The Astrophysical Journal* 848.2 (Oct. 2017), p. 121. URL: https://doi.org/10.3847%5C%2F1538-4357%5C%2Faa8e9f.

[50] J. T. Sayre et al. "Measurements of B-mode polarization of the cosmic microwave background from 500 square degrees of SPTpol data". In: *Phys. Rev. D* 101 (12 June 2020), p. 122003. URL: https://link.aps.org/doi/10.1103/PhysRevD.101.122003.

[51] Steve K. Choi et al. “The Atacama Cosmology Telescope: A Measurement of the Cosmic Microwave Background Power Spectra at 98 and 150 GHz”. In: *arXiv e-prints*, arXiv:2007.07289 (July 2020), arXiv:2007.07289. arXiv: `2007.07289 [astro-ph.CO]`.

[52] P. A. R. Ade et al. “Joint Analysis of BICEP2/Keck Array and Planck Data”. In: *Phys. Rev. Lett.* 114 (10 Mar. 2015), p. 101301. eprint: `1502.00612v2`. URL: `https://link.aps.org/doi/10.1103/PhysRevLett.114.101301`.

[53] P. A. R. Ade et al. “Constraints on Primordial Gravitational Waves Using *Planck*, WMAP, and New BICEP2/*Keck* Observations through the 2015 Season”. In: *Phys. Rev. Lett.* 121 (22 Nov. 2018), p. 221301. URL: `https://link.aps.org/doi/10.1103/PhysRevLett.121.221301`.

[54] Planck Collaboration et al. “Planck 2015 results - X. Diffuse component separation: Foreground maps”. In: *A&A* 594 (2016), A10. URL: `https://doi.org/10.1051/0004-6361/201525967`.

[55] Planck Collaboration et al. “Planck 2018 results. II. Low Frequency Instrument data processing”. In: *arXiv e-prints*, arXiv:1807.06206 (July 2018), arXiv:1807.06206. arXiv: `1807.06206 [astro-ph.CO]`.

[56] N. Aghanim et al. “Planck 2018 results. III. High Frequency Instrument data processing and frequency maps”. In: (2018). arXiv: `1807.06207 [astro-ph.CO]`.

[57] Brandon S. Hensley and Philip Bull. “Mitigating Complex Dust Foregrounds in Future Cosmic Microwave Background Polarization Experiments”. In: *The Astrophysical Journal* 853.2 (Jan. 2018), p. 127. URL: `https://doi.org/10.3847%5C%2F1538-4357%5C%2Faaa489`.

[58] Planck Collaboration et al. “Planck 2015 results - XXV. Diffuse low-frequency Galactic foregrounds”. In: *A&A* 594 (2016), A25. URL: `https://doi.org/10.1051/0004-6361/201526803`.

[59] Kiyotomo Ichiki. “CMB foreground: A concise review”. In: *Progress of Theoretical and Experimental Physics* 2014.6 (June 2014). URL: `https://doi.org/10.1093/ptep/ptu065`.

[60] Y. Akrami et al. “Planck 2018 results. IV. Diffuse component separation”. In: (2018). arXiv: `1807.06208 [astro-ph.CO]`.

[61] Christopher G. R. Wallis et al. “Optimal scan strategies for future CMB satellite experiments”. In: *Monthly Notices of the Royal Astronomical Society* 466.1 (Oct. 2016), pp. 425–442. eprint: `https://academic.oup.com/mnras/article-pdf/466/1/425/10864929/stw2577.pdf`. URL: `https://doi.org/10.1093/mnras/stw2577`.

[62] Josquin Errard et al. “Robust forecasts on fundamental physics from the foreground-obscured, gravitationally-lensed CMB polarization”. In: *Journal of Cosmology and Astroparticle Physics* 2016.03 (Mar. 2016), pp. 052–052. URL: `https://doi.org/10.1088%5C%2F1475-7516%5C%2F2016%5C%2F03%5C%2F052`.

[63] J. Hubmayr et al. “Low-Temperature Detectors for CMB Imaging Arrays”. In: *Journal of Low Temperature Physics* 193.3-4 (Nov. 2018), pp. 633–647. arXiv: `1807.01384 [astro-ph.IM]`.

[64] Planck HFI Core Team et al. “Planck early results. IV. First assessment of the High Frequency Instrument in-flight performance”. In: *A&A* 536 (2011), A4. URL: https://doi.org/10.1051/0004-6361/201116487.

[65] Howard Hui et al. “BICEP Array: a multi-frequency degree-scale CMB polarimeter”. In: *Millimeter, Submillimeter, and Far-Infrared Detectors and Instrumentation for Astronomy IX*. Ed. by Jonas Zmuidzinas and Jian-Rong Gao. Vol. 10708. International Society for Optics and Photonics. SPIE, 2018, pp. 1–15. URL: https://doi.org/10.1117/12.2311725.

[66] Shaul Hanany et al. “PICO: Probe of Inflation and Cosmic Origins”. In: *arXiv e-prints*, arXiv:1902.10541 (Feb. 2019), arXiv:1902.10541. arXiv: 1902.10541 [astro-ph.IM].

[67] Roger O’Brient. *A Log-Periodic Focal-Plane Architecture for Cosmic Microwave Background Polarimetry*. 2010. URL: https://escholarship.org/uc/item/8bh7z0pb.

[68] Aritoki Suzuki et al. “Multichroic dual-polarization bolometric detectors for studies of the cosmic microwave background”. In: *Millimeter, Submillimeter, and Far-Infrared Detectors and Instrumentation for Astronomy VI*. Ed. by Wayne S. Holland. Vol. 8452. International Society for Optics and Photonics. SPIE, 2012, pp. 1038–1047. URL: https://doi.org/10.1117/12.924869.

[69] J. McMahon et al. “Multi-chroic Feed-Horn Coupled TES Polarimeters”. In: *Journal of Low Temperature Physics* 167.5-6 (June 2012), pp. 879–884. arXiv: 1201.4124 [astro-ph.IM].

[70] Roger O’Brient et al. “A dual-polarized broadband planar antenna and channelizing filter bank for millimeter wavelengths”. In: *Applied Physics Letters* 102.6 (2013), p. 063506. eprint: https://doi.org/10.1063/1.4791692. URL: https://doi.org/10.1063/1.4791692.

[71] Aritoki Suzuki. “Multichroic Bolometric Detector Architecture for Cosmic Microwave Background Polarimetry Experiments”. PhD thesis. University of California, Berkeley, Jan. 2013.

[72] Aritoki Suzuki et al. “Commercially Fabricated Antenna-Coupled Transition Edge Sensor Bolometer Detectors for Next-Generation Cosmic Microwave Background Polarimetry Experiment”. In: *Journal of Low Temperature Physics* 199.3-4 (Jan. 2020), pp. 1158–1166. arXiv: 1912.12782 [astro-ph.IM].

[73] S. Walker et al. “Demonstration of 220/280 GHz Multichroic Feedhorn-Coupled TES Polarimeter”. In: *Journal of Low Temperature Physics* 199.3-4 (Jan. 2020), pp. 891–897. arXiv: 1909.11569 [astro-ph.IM].

[74] P A R Ade et al. “Polarization modulators for CMBPol”. In: *Journal of Physics: Conference Series* 155 (Mar. 2009), p. 012006. URL: https://doi.org/10.1088%5C%2F1742-6596%5C%2F155%5C%2F1%5C%2F012006.

[75] G. Pisano et al. “Development of large radii half-wave plates for CMB satellite missions”. In: *Millimeter, Submillimeter, and Far-Infrared Detectors and Instrumentation for Astronomy VII*. Ed. by Wayne S. Holland and Jonas Zmuidzinas. Vol. 9153. International Society for Optics and Photonics. SPIE, 2014, pp. 385–400. URL: https://doi.org/10.1117/12.2056380.

[76] S. Oguri et al. “GroundBIRD Experiment: Detecting CMB Polarization Power in a Large Angular Scale from the Ground”. In: *Journal of Low Temperature Physics* 176.5-6 (Sept. 2014), pp. 691–697.

[77] Maximilian H. Abitbol et al. “CMB-S4 Technology Book, First Edition”. In: *arXiv e-prints*, arXiv:1706.02464 (June 2017), arXiv:1706.02464. arXiv: `1706.02464 [astro-ph.IM]`.

[78] B. R. Johnson et al. “MAXIPOL: Cosmic Microwave Background Polarimetry Using a Rotating Half-Wave Plate”. In: *The Astrophysical Journal* 665.1 (Aug. 2007), pp. 42–54. URL: `https://doi.org/10.1086%5C%2F518105`.

[79] R. H. Dicke. “The Measurement of Thermal Radiation at Microwave Frequencies”. In: *Review of Scientific Instruments* 17.7 (1946), pp. 268–275. eprint: `https://doi.org/10.1063/1.1770483`. URL: `https://doi.org/10.1063/1.1770483`.

[80] A. Kusaka et al. “Modulation of cosmic microwave background polarization with a warm rapidly rotating half-wave plate on the Atacama B-Mode Search instrument”. In: *Review of Scientific Instruments* 85.2 (2014), p. 024501. eprint: `https://doi.org/10.1063/1.4862058`. URL: `https://doi.org/10.1063/1.4862058`.

[81] Satoru Takakura et al. “Performance of a continuously rotating half-wave plate on the POLARBEAR telescope”. In: *Journal of Cosmology and Astroparticle Physics* 2017.05 (May 2017), pp. 008–008. URL: `https://doi.org/10.1088%5C%2F1475-7516%5C%2F2017%5C%2F05%5C%2F008`.

[82] Duc Thuong Hoang et al. “Bandpass mismatch error for satellite CMB experiments I: estimating the spurious signal”. In: *Journal of Cosmology and Astroparticle Physics* 2017.12 (Dec. 2017), pp. 015–015. URL: `https://doi.org/10.1088%5C%2F1475-7516%5C%2F2017%5C%2F12%5C%2F015`.

[83] S. Pancharatnam. “Achromatic combinations of birefringent plates. Part I. An achromatic circular polarizer”. In: *Proc. Indian Acad. Sci.* 41 (1955), pp. 130–136. URL: `https://doi.org/10.1007/BF03047097`.

[84] S. Pancharatnam. “Achromatic combinations of birefringent plates. Part II. An achromatic quarter-wave plate”. In: *Proc. Indian Acad. Sci.* 41 (1955), pp. 137–144. URL: `https://doi.org/10.1007/BF03047098`.

[85] Yuki Inoue et al. “Cryogenic infrared filter made of alumina for use at millimeter wavelength”. In: *Appl. Opt.* 53.9 (Mar. 2014), pp. 1727–1733. URL: `http://ao.osa.org/abstract.cfm?URI=ao-53-9-1727`.

[86] Charles A. Hill et al. “Design and development of an ambient-temperature continuously-rotating achromatic half-wave plate for CMB polarization modulation on the POLARBEAR-2 experiment”. In: *Millimeter, Submillimeter, and Far-Infrared Detectors and Instrumentation for Astronomy VIII.* Ed. by Wayne S. Holland and Jonas Zmuidzinas. Vol. 9914. International Society for Optics and Photonics. SPIE, 2016, pp. 699–716. URL: `https://doi.org/10.1117/12.2232280`.

[87] R. Datta et al. “Large-aperture wide-bandwidth antireflection-coated silicon lenses for millimeter wavelengths”. In: *Appl. Opt.* 52.36 (Dec. 2013), pp. 8747–8758. URL: `http://ao.osa.org/abstract.cfm?URI=ao-52-36-8747`.

[88] A. Nadolski et al. “Broadband, millimeter-wave antireflection coatings for large-format, cryogenic aluminum oxide optics”. In: *Appl. Opt.* 59.10 (Apr. 2020), pp. 3285–3295. URL: http://ao.osa.org/abstract.cfm?URI=ao-59-10-3285.

[89] Tomotake Matsumura et al. “Millimeter-wave broadband antireflection coatings using laser ablation of subwavelength structures”. In: *Appl. Opt.* 55.13 (May 2016), pp. 3502–3509. URL: http://ao.osa.org/abstract.cfm?URI=ao-55-13-3502.

[90] Karl Young et al. “Broadband millimeter-wave anti-reflection coatings on silicon using pyramidal sub-wavelength structures”. In: *Journal of Applied Physics* 121.21 (2017), p. 213103. eprint: https://doi.org/10.1063/1.4984892. URL: https://doi.org/10.1063/1.4984892.

[91] Yuki Sakurai et al. “Design and development of a polarization modulator unit based on a continuous rotating half-wave plate for LiteBIRD”. In: *Millimeter, Submillimeter, and Far-Infrared Detectors and Instrumentation for Astronomy IX*. Ed. by Jonas Zmuidzinas and Jian-Rong Gao. Vol. 10708. International Society for Optics and Photonics. SPIE, 2018, pp. 28–39. URL: https://doi.org/10.1117/12.2312391.

[92] R. Takaku et al. “Broadband, millimeter-wave anti-reflective structures on sapphire ablated with femto-second laser”. In: *arXiv e-prints*, arXiv:2007.15262 (July 2020), arXiv:2007.15262. arXiv: 2007.15262 [astro-ph.IM].

[93] G. Pisano et al. *Development and application of metamaterial-based Half-Wave Plates for the NIKA and NIKA2 polarimeters*. 2020. arXiv: 2006.12081 [astro-ph.IM].

[94] Jean-Marc Duval et al. “LiteBIRD Cryogenic Chain: 100 mK Cooling with Mechanical Coolers and ADRs”. In: *Journal of Low Temperature Physics* 199.3-4 (Feb. 2020), pp. 730–736.

[95] Y. Minami et al. “Irradiation Tests of Superconducting Detectors and Comparison with Simulations”. In: *J. Low Temp. Phys.* 199.1-2 (2020), pp. 118–129.

[96] J. T. Ward et al. “The Effects of Bandpass Variations on Foreground Removal Forecasts for Future CMB Experiments”. In: *The Astrophysical Journal* 861.2 (July 2018), p. 82. URL: https://doi.org/10.3847%5C%2F1538-4357%5C%2Faac71f.

[97] Ranajoy Banerji et al. “Bandpass mismatch error for satellite CMB experiments II: correcting for the spurious signal”. In: *Journal of Cosmology and Astroparticle Physics* 2019.07 (July 2019), pp. 043–043. URL: https://doi.org/10.1088%5C%2F1475-7516%5C%2F2019%5C%2F07%5C%2F043.

[98] Akito Kusaka et al. “Results from the Atacama B-mode Search (ABS) experiment”. In: *Journal of Cosmology and Astroparticle Physics* 2018.09 (Sept. 2018), pp. 005–005. URL: https://doi.org/10.1088%5C%2F1475-7516%5C%2F2018%5C%2F09%5C%2F005.

[99] Clive Dickinson et al. “The State-of-Play of Anomalous Microwave Emission (AME) research”. In: *New Astronomy Reviews* 80 (2018), pp. 1–28. URL: http://www.sciencedirect.com/science/article/pii/S1387647317300842.

[100] J. S. Greaves et al. “Polarized CO Emission from Molecular Clouds”. In: *The Astrophysical Journal* 512.2 (Feb. 1999), pp. L139–L142. URL: https://doi.org/10.1086%5C%2F311888.

[101] G. Puglisi, G. Fabbian, and C. Baccigalupi. "A 3D model for carbon monoxide molecular line emission as a potential cosmic microwave background polarization contaminant". In: *Monthly Notices of the Royal Astronomical Society* 469.3 (May 2017), pp. 2982–2996. eprint: https://academic.oup.com/mnras/article-pdf/469/3/2982/17644667/stx1029.pdf. URL: https://doi.org/10.1093/mnras/stx1029.

[102] C. H. Lineweaver et al. "The Dipole Observed in the COBE DMR 4 Year Data". In: *ApJ* 470 (Oct. 1996), p. 38. eprint: astro-ph/9601151.

[103] Piat, M. et al. "Cosmic background dipole measurements with the Planck-High Frequency Instrument". In: *A&A* 393.1 (2002), pp. 359–368. URL: https://doi.org/10.1051/0004-6361:20021093.

[104] Radek Stompor et al. "Maximum likelihood algorithm for parametric component separation in cosmic microwave background experiments". In: *Monthly Notices of the Royal Astronomical Society* 392.1 (2009), pp. 216–232. eprint: 0804.2645v2. URL: http://dx.doi.org/10.1111/j.1365-2966.2008.14023.x.

[105] J. Errard, F. Stivoli, and R. Stompor. "Framework for performance forecasting and optimization of CMB B-mode observations in the presence of astrophysical foregrounds". In: *Phys. Rev. D* 84 (6 Sept. 2011), p. 063005. URL: https://link.aps.org/doi/10.1103/PhysRevD.84.063005.

[106] Radek Stompor, Josquin Errard, and Davide Poletti. "Forecasting performance of CMB experiments in the presence of complex foreground contaminations". In: *Phys. Rev. D* 94 (8 Oct. 2016), p. 083526. URL: https://link.aps.org/doi/10.1103/PhysRevD.94.083526.

[107] B. Thorne et al. "The Python Sky Model: software for simulating the Galactic microwave sky". In: *Monthly Notices of the Royal Astronomical Society* 469.3 (2017), pp. 2821–2833. eprint: 1608.02841v1. URL: http://dx.doi.org/10.1093/mnras/stx949.

[108] Josquin Errard and Radek Stompor. "Characterizing bias on large scale CMB B-modes after Galactic foregrounds cleaning". In: *Phys. Rev. D* 99 (4 Feb. 2019), p. 043529. URL: https://link.aps.org/doi/10.1103/PhysRevD.99.043529.

[109] Samira Hamimeche and Antony Lewis. "Likelihood analysis of CMB temperature and polarization power spectra". In: *Phys. Rev. D* 77 (10 May 2008), p. 103013. arXiv: 0801.0554v4 [astro-ph.CO]. URL: https://link.aps.org/doi/10.1103/PhysRevD.77.103013.

[110] Nobuhiko Katayama and Eiichiro Komatsu. "SIMPLE FOREGROUND CLEANING ALGORITHM FOR DETECTING PRIMORDIAL B-MODE POLARIZATION OF THE COSMIC MICROWAVE BACKGROUND". In: *The Astrophysical Journal* 737.2 (Aug. 2011), p. 78. URL: https://doi.org/10.1088%5C%2F0004-637x%5C%2F737%5C%2F2%5C%2F78.

[111] F. Matsuda et al. "The POLARBEAR Fourier transform spectrometer calibrator and spectroscopic characterization of the POLARBEAR instrument". In: *Review of Scientific Instruments* 90.11 (Nov. 2019), p. 115115. URL: http://dx.doi.org/10.1063/1.5095160.

[112] Bradley R. Johnson et al. "A CubeSat for Calibrating Ground-Based and Sub-Orbital Millimeter-Wave Polarimeters (CalSat)". In: *Journal of Astronomical Instrumentation* 04.03n04 (2015), p. 1550007.

[113] G. Patanchon et al. "SANEPIC: A Mapmaking Method for Time Stream Data from Large Arrays". In: *The Astrophysical Journal* 681.1 (July 2008), pp. 708–725. URL: https://doi.org/10.1086%5C%2F588543.

[114] de Gasperis, G. et al. "Optimal cosmic microwave background map-making in the presence of cross-correlated noise". In: *A&A* 593 (2016), A15. URL: https://doi.org/10.1051/0004-6361/201628143.

[115] Mark Heyer and T.M. Dame. "Molecular Clouds in the Milky Way". In: *Annual Review of Astronomy and Astrophysics* 53.1 (2015), pp. 583–629. eprint: https://doi.org/10.1146/annurev-astro-082214-122324. URL: https://doi.org/10.1146/annurev-astro-082214-122324.

[116] Adriaan J Duivenvoorden, Jon E Gudmundsson, and Alexandra S Rahlin. "Full-sky beam convolution for cosmic microwave background applications". In: *Monthly Notices of the Royal Astronomical Society* 486.4 (May 2019), pp. 5448–5467. eprint: https://academic.oup.com/mnras/article-pdf/486/4/5448/32394296/stz1143.pdf. URL: https://doi.org/10.1093/mnras/stz1143.

[117] Meir Shimon et al. "CMB polarization systematics due to beam asymmetry: Impact on inflationary science". In: *Phys. Rev. D* 77 (8 Apr. 2008), p. 083003. URL: https://link.aps.org/doi/10.1103/PhysRevD.77.083003.

[118] D. A. Crocker and W. R. Scott. "Exploiting Polarization Wobble in Sinuous Antennas for the Detection of Linear Scatterers in Ground Penetrating Radar Applications". In: *2018 IEEE International Symposium on Antennas and Propagation USNC/URSI National Radio Science Meeting*. 2018, pp. 837–838.

[119] Tomotake Matsumura et al. "Performance of three- and five-stack achromatic half-wave plates at millimeter wavelengths". In: *Appl. Opt.* 48.19 (July 2009), pp. 3614–3625. URL: http://ao.osa.org/abstract.cfm?URI=ao-48-19-3614.

[120] C. Bao et al. "THE IMPACT OF THE SPECTRAL RESPONSE OF AN ACHROMATIC HALF-WAVE PLATE ON THE MEASUREMENT OF THE COSMIC MICROWAVE BACKGROUND POLARIZATION". In: *The Astrophysical Journal* 747.2 (Feb. 2012), p. 97. URL: https://doi.org/10.1088%5C%2F0004-637x%5C%2F747%5C%2F2%5C%2F97.

[121] Jonas Zmuidzinas. "Thermal noise and correlations in photon detection". In: *Appl. Opt.* 42.25 (Sept. 2003), pp. 4989–5008. URL: http://ao.osa.org/abstract.cfm?URI=ao-42-25-4989.

[122] Kent Irwin and Gene Charles Hilton. "Transition-Edge Sensors". In: *Cryogenic Particle Detection*. Vol. 99. Springer, 2005. URL: https://doi.org/10.1007/10933596_3.

[123] Jonas Zmuidzinas. "Superconducting Microresonators: Physics and Applications". In: *Annual Review of Condensed Matter Physics* 3.1 (2012), pp. 169–214. eprint: https://doi.org/10.1146/annurev-conmatphys-020911-125022. URL: https://doi.org/10.1146/annurev-conmatphys-020911-125022.

[124] P. D. Mauskopf. “Transition Edge Sensors and Kinetic Inductance Detectors in Astronomical Instruments”. In: *Publications of the Astronomical Society of the Pacific* 130.990 (June 2018), p. 082001. URL: https://doi.org/10.1088%2F1538-3873%2Faabaf0.

[125] Joy Didier et al. “Intensity-coupled Polarization in Instruments with a Continuously Rotating Half-wave Plate”. In: *The Astrophysical Journal* 876.1 (May 2019), p. 54. URL: https://doi.org/10.3847%5C%2F1538-4357%5C%2Fab0f36.

[126] Dominic J. Benford. “Transition Edge Sensor Bolometers for CMB Polarimetry”. In: 2008.

[127] John C. Mather. “Bolometers: ultimate sensitivity, optimization, and amplifier coupling”. In: *Appl. Opt.* 23.4 (Feb. 1984), pp. 584–588. URL: http://ao.osa.org/abstract.cfm?URI=ao-23-4-584.

[128] P. L. Richards. “Bolometers for infrared and millimeter waves”. In: *Journal of Applied Physics* 76.1 (1994), pp. 1–24. eprint: https://doi.org/10.1063/1.357128. URL: https://doi.org/10.1063/1.357128.

[129] Shih-Fu Lee et al. “Voltage-biased superconducting transition-edge bolometer with strong electrothermal feedback operated at 370 mK”. In: *Appl. Opt.* 37.16 (June 1998), pp. 3391–3397. URL: http://ao.osa.org/abstract.cfm?URI=ao-37-16-3391.

[130] John Clarke et al. “SQUID Voltmeters and Amplifiers”. In: *The SQUID Handbook*. John Wiley & Sons, Ltd, 2006. Chap. 8, pp. 1–93. eprint: https://onlinelibrary.wiley.com/doi/pdf/10.1002/9783527609956.ch8. URL: https://onlinelibrary.wiley.com/doi/abs/10.1002/9783527609956.ch8.

[131] Dietmar Drung, Colmar Hinnrichs, and Henry-Jobes Barthelmess. “Low-noise ultra-high-speed dc SQUID readout electronics”. In: *Superconductor Science and Technology* 19.5 (Feb. 2006), S235–S241. URL: https://doi.org/10.1088%5C%2F0953-2048%5C%2F19%5C%2F5%5C%2Fs15.

[132] D. Drung et al. “Highly Sensitive and Easy-to-Use SQUID Sensors”. In: *IEEE Transactions on Applied Superconductivity* 17.2 (2007), pp. 699–704.

[133] R. Kleiner et al. “Superconducting quantum interference devices: State of the art and applications”. In: *Proceedings of the IEEE* 92.10 (2004), pp. 1534–1548.

[134] John C. Butcher. “Runge-Kutta Methods”. In: *Numerical Methods for Ordinary Differential Equations*. John Wiley & Sons, Ltd, 2008. Chap. 3, pp. 137–316. eprint: https://onlinelibrary.wiley.com/doi/pdf/10.1002/9780470753767.ch3. URL: https://onlinelibrary.wiley.com/doi/abs/10.1002/9780470753767.ch3.

[135] Amy N. Bender et al. “Digital frequency domain multiplexing readout electronics for the next generation of millimeter telescopes”. In: *Millimeter, Submillimeter, and Far-Infrared Detectors and Instrumentation for Astronomy VII*. Ed. by Wayne S. Holland and Jonas Zmuidzinas. Vol. 9153. International Society for Optics and Photonics. SPIE, 2014, pp. 430–444. URL: https://doi.org/10.1117/12.2054949.

[136] Maximilian H. Abitbol et al. “CMB-S4 Technology Book, First Edition”. In: (June 2017). arXiv: 1706.02464 [astro-ph.IM].

[137] M Dobbs et al. “Multiplexed readout of CMB polarimeters”. In: *Journal of Physics: Conference Series* 155 (Mar. 2009), p. 012004. URL: https://doi.org/10.1088%5C%2F1742-6596%5C%2F155%5C%2F1%5C%2F012004.

[138] A. Cukierman et al. “Microwave Multiplexing on the Keck Array”. In: *Journal of Low Temperature Physics* 199.3-4 (Dec. 2019), pp. 858–866. arXiv: 1909.01305 [astro-ph.IM].

[139] Mayuri Sathyanarayana Rao et al. “Simons Observatory Microwave SQUID Multiplexing Readout: Cryogenic RF Amplifier and Coaxial Chain Design”. In: *Journal of Low Temperature Physics* 199.3-4 (Mar. 2020), pp. 807–816. arXiv: 2003.08949 [astro-ph.IM].

[140] K. D. Irwin and K. W. Lehnert. “Microwave SQUID multiplexer”. In: *Applied Physics Letters* 85.11 (2004), pp. 2107–2109. eprint: https://doi.org/10.1063/1.1791733. URL: https://doi.org/10.1063/1.1791733.

[141] Amy E. Lowitz et al. “Digital frequency multiplexing with sub-Kelvin SQUIDs”. In: *Millimeter, Submillimeter, and Far-Infrared Detectors and Instrumentation for Astronomy IX*. Ed. by Jonas Zmuidzinas and Jian-Rong Gao. Vol. 10708. International Society for Optics and Photonics. SPIE, 2018, pp. 170–178. URL: https://doi.org/10.1117/12.2311984.

[142] T. de Haan et al. “Recent Advances in Frequency-Multiplexed TES Readout: Vastly Reduced Parasitics and an Increase in Multiplexing Factor with Sub-Kelvin SQUIDs”. In: *Journal of Low Temperature Physics* 199.3-4 (Feb. 2020), pp. 754–761. arXiv: 1908.07642 [astro-ph.IM].

[143] Y. Sekimoto et al. “Concept design of the LiteBIRD satellite for CMB B-mode polarization”. In: *Space Telescopes and Instrumentation 2018: Optical, Infrared, and Millimeter Wave*. Ed. by Makenzie Lystrup et al. Vol. 10698. International Society for Optics and Photonics. SPIE, 2018, pp. 613–629. URL: https://doi.org/10.1117/12.2313432.

[144] M.C. Runyan and W.C. Jones. “Thermal conductivity of thermally-isolating polymeric and composite structural support materials between 0.3 and 4K”. In: *Cryogenics* 48.9 (2008), pp. 448–454. URL: http://www.sciencedirect.com/science/article/pii/S0011227508000933.

[145] E. M. Vavagiakis et al. “Magnetic Sensitivity of AlMn TESes and Shielding Considerations for Next-Generation CMB Surveys”. In: *Journal of Low Temperature Physics* 193.3-4 (Nov. 2018), pp. 288–297. arXiv: 1710.08456 [astro-ph.IM].

[146] Axel Murk et al. “Blackbody Calibration Targets with Ultralow Reflectivity at Submillimeter Wavelengths”. In: 2006.

[147] A. Murk et al. “Development of microwave calibration targets for upcoming ESA missions”. In: *2012 IEEE International Geoscience and Remote Sensing Symposium*. July 2012, pp. 2949–2952.

[148] R. Wylde et al. “The need for and development of MM-wave radiometer calibration targets with very low coherent backscatter”. In: *2012 Conference on Precision electromagnetic Measurements*. July 2012, pp. 260–261.

[149] A. Schröder et al. “Brightness Temperature Computation of Microwave Calibration Targets”. In: *IEEE Transactions on Geoscience and Remote Sensing* 55.12 (Dec. 2017), pp. 7104–7112.

[150] E. J. Wollack, R. E. Kinzer, and S. A. Rinehart. “A cryogenic infrared calibration target”. In: *Review of Scientific Instruments* 85.4 (2014), p. 044707. eprint: `https://doi.org/10.1063/1.4871108`. URL: `https://doi.org/10.1063/1.4871108`.

[151] I. Zivkovic and A. Murk. “Characterization of Magnetically Loaded Microwave Absorbers”. In: *Progress In Electromagnetics Research B* 33 (2011), pp. 277–289.

[152] Irena Zivkovic and Axel Murk. “Free-Space Transmission Method for the Characterization of Dielectric and Magnetic Materials at Microwave Frequencies”. In: *Microwave Materials Characterization*. Ed. by Sandra Costanzo. Rijeka: IntechOpen, 2012. Chap. 5. URL: `https://doi.org/10.5772/51596`.

[153] I. Zivkovic and A. Murk. “Extraction of dielectric and magnetic properties of carbonyl iron powder composites at high frequencies”. In: *Journal of Applied Physics* 111.11 (2012), p. 114104.

[154] Ruey-Bin Yang and Wen-Fan Liang. “Microwave properties of high-aspect-ratio carbonyl iron/epoxy absorbers”. In: *Journal of Applied Physics* 109.7 (2011), 07A311. eprint: `https://doi.org/10.1063/1.3536340`. URL: `https://doi.org/10.1063/1.3536340`.

[155] Sung-Soo Kim et al. “Magnetic, dielectric, and microwave absorbing properties of iron particles dispersed in rubber matrix in gigahertz frequencies”. In: *Journal of Applied Physics* 97.10 (2005), 10F905. eprint: `https://doi.org/10.1063/1.1852371`. URL: `https://doi.org/10.1063/1.1852371`.

[156] Ari Sihvola. *Electromagnetic Mixing Formulas and Applications*. Electromagnetic Waves. Institution of Engineering and Technology, 1999. URL: `https://digital-library.theiet.org/content/books/ew/pbew047e`.

[157] R. B. Yang, S. D. Hsu, and C. K. Lin. “Frequency-dependent complex permittivity and permeability of iron-based powders in 2-18 GHz”. In: *Journal of Applied Physics* 105.7 (2009), 07A527. eprint: `https://doi.org/10.1063/1.3068039`. URL: `https://doi.org/10.1063/1.3068039`.

[158] W. M. Merrill et al. “Effective medium theories for artificial materials composed of multiple sizes of spherical inclusions in a host continuum”. In: *IEEE Transactions on Antennas and Propagation* 47.1 (Jan. 1999), pp. 142–148.

[159] Shibing Ni et al. “Hydrothermal synthesis and microwave absorption properties of Fe3O4 nanocrystals”. In: *Journal of Physics D: Applied Physics* 42.5 (Feb. 2009), p. 055004. URL: https://doi.org/10.1088%5C%2F0022-3727%5C%2F42%5C%2F5%5C%2F055004.

[160] Kun Jia et al. “Preparation and microwave absorption properties of loose nanoscale Fe3O4 spheres”. In: *Journal of Magnetism and Magnetic Materials* 322.15 (2010), pp. 2167–2171. URL: http://www.sciencedirect.com/science/article/pii/S0304885310000697.

[161] Yao-Feng Zhu et al. “Synthesis and microwave absorption properties of electromagnetic functionalized Fe3O4-polyaniline hollow sphere nanocomposites produced by electrostatic self-assembly”. In: *Journal of Nanoparticle Research* 15.1988 (2013).

[162] I. S. Unver and Z. Durmus. “Magnetic and Microwave Absorption Properties of Magnetite (Fe3O4)@Conducting Polymer (PANI, PPY, PT) Composites”. In: *IEEE Transactions on Magnetics* 53.10 (Oct. 2017), pp. 1–8.

[163] D.M. Pozar. *Microwave Engineering, 4th Edition.* Wiley, 2011. URL: https://books.google.co.jp/books?id=JegbAAAAQBAJ.